Tuning the Magnetic Properties of Prussian Blue Analogues:

Size Control and the Effects of External Stimuli

Lindsay Egan

Doctor of Philosophy
University of Edinburgh
2009

Declaration

I hereby declare that I composed this thesis myself and that all research detailed within it, unless otherwise stated, is my own. This work has not been submitted for any other degree or professional qualification.

Signed:

Date:

Abstract

The hetero-bimetallic mixed valence metal polycyanides (Prussian Blue analogues (PBAs)) with formula $A_xM^{II}[M'^{III}(CN)_6]_y$ (where A= alkali-metal cation and M, M'= transition-metal cations respectively) are archetypal examples of molecule-based magnets, exhibiting a wealth of exotic electronic and magnetic behaviours. Similar intriguing electronic and magnetic properties are anticipated in nanoscale structures employing the PBA molecular building block. Herein investigations of multifunctional molecular magnets based on the PBA building block, with varying dimensionalities, are reported.

Synthesis and characterisation of a novel family of mixed ferri-ferromagnets, $RbNi_zMn_{(1-z)}[Fe(CN)_6]$ ($0<z<1$), illustrates how relatively minor changes in chemical composition can induce significant changes in the magnetic properties. Selected members of this series show photo-induced electronic transitions and pressure-induced magnetic pole inversions. The rare phenomenon of a double magnetic pole inversion is observed when Fe^{II} is introduced as a third M^{II} ion.

PBAs incorporating the Cu^{2+} ion are studied with the aim of establishing the influence of Jahn-Teller distortions on the photo-induced electron transfer which has been observed in a number of PBAs. X-ray powder diffraction and absorption measurements of $CsCu[Fe(CN)_6]$ under laser illumination reveal an unusual and unexpected behaviour, with photo-irradiation initiating a simultaneous reduction of both transition metal centres, which is proposed to occur via a chemical reaction.

Superparamagnetic nanoparticles based on the Cu^{II}-NC-Cr^{III} and Mn-NC-Cr^{III} moieties are prepared by polymer protected synthesis, a method based upon spatial confinement. Control over the particle size, and consequently magnetic properties, of the isolated polymer-capped nanoparticles is achieved by altering the polymer concentration. The relaxation dynamics of the polymer-capped nanoparticles are studied using AC susceptibility.

Acknowledgements

First and foremost, I would like to express my deepest gratitude to Dr Serena Margadonna for her unwavering support, guidance, encouragement and patience over the past few years. I could not have wished for a better supervisor.

I wish to acknowledge several other individuals who have greatly assisted me in conducting the research detailed within this thesis. I am extremely grateful to my collaborators from the University of Durham - particularly Dr Dionisis Papanikolaou and Dr Yasuhiro Takabayashi - who were fundamental to obtaining the results described in Chapters 3 and 4. I would also like to thank Prof Petra Rudolf and Régis Gengler from the University of Groningen, whose resources and expertise facilitated the XPS measurements discussed in Chapter 5. I am similarly indebted to Peter Bruce and Dr Feng Jiao, of the University of St Andrews, for the extensive TEM measurements presented within this chapter. From the University of Edinburgh, I want to thank: Dr Javier Sanchez-Benetiz and Dr Konstantin Kamenev for their time and perseverance with SQUID measurements, Dr Anna Tamai for her participation in the XANES measurements reported in Chapter 4 and Dr Lorna Eades for all her help with elemental analysis.

To Mum & Dad

Contents

Chapter 1

Introduction

1.1 Background

Magnetic materials underpin many of the modern technologies which are now integral to life in the 21st century. Advances in technology demand increasingly sophisticated magnetic materials and over the past two decades scientists have looked towards molecule-based materials to meet these demands. Molecule-based magnets have proven capable of matching, and in fact often surpass, the magnetic properties commonly exhibited by conventional magnetic materials. What is more, the electronic and magnetic properties of molecule-based materials can be tailored to meet specific requirements by introducing subtle changes in molecular precursor composition or connectivity, thus giving them an advantage over classical magnets such as metals and metal oxides. Molecule based materials also offer the opportunity to combine magnetism with other technologically important properties to produce multifunctional materials.

The hetero-bimetallic mixed valence metal polycyanides, known as the Prussian Blue analogues (PBAs), with the general formula $A_xM^{II}[M'^{III}(CN)_6]_y$ (where A= alkali metal cation and M, M'= transition-metal cations) are exemplary molecular magnets. The PBA molecular building blocks are ideal for the rational design of innovative magnetic materials for several reasons: 1) their flexible network structures can accommodate a range of transition metal ions, with varying oxidation and spin states, without structural distortion; 2) the relatively long distances between second nearest neighbour TM ions (~ 10 Å) facilitates accurate theoretical prediction of their magnetic properties from simple orbital symmetry rules, since the only significant magnetic interactions are superexchange interactions between nearest neighbour spin sources; 3) the availability of quasidegenerate electronic states makes them ideal systems with which to explore magnetic switching phenomena.[1] The work described in this thesis exploits these attributes to synthesise and explore novel multifunctional

molecular magnetic materials based on the PBA building block with varying dimensionality.

1.2 Prussian Blue Analogues

Prussian Blue ($Fe^{III}_4[Fe^{II}(CN)_6]_3 \cdot 14H_2O$) was serendipitously discovered by a Berlin draper in 1704 and subsequently found widespread applications as a pigment due to its vibrant and durable colour.[2] The commercial value of this pigment stimulated intense research efforts by chemists keen to establish the nature of Prussian Blue (and crucially the origin of its intense colour). Subsequently, the chemical formula, metal oxidation states and solid state structure of Prussian Blue were successfully established. Chemists' fascination with Prussian Blue was, and continues to be, further perpetuated by the discovery of intriguing electronic and magnetic properties. In the 20th century research efforts in this field were extended by replacing one or both of the Fe sites with an alternative transition metal, giving rise to analogues of Prussian Blue which in time came to be regarded as archetypal molecule based magnets.

1.2.1 Structure

The solid state structure of Prussian Blue was first proposed in 1936; more than 200 years after its discovery.[3, 4] Keggin and Miles proposed a face-centred cubic structure in which alternating ferrous and ferric irons are bridged by cyanide ligands to form a three-dimensional framework, with "excess" Fe^{III} ions (note that Fe^{III} / Fe^{II} = 4/3) accommodated in the interstitial sites. This tentative structure was subsequently modified by Ludi et al who found that the interstitial sites are, in fact, occupied by zeolitic water molecules and that "excess" Fe^{III} ions are actually a consequence of Fe^{II} vacancies, with water molecules completing the coordination spheres of Fe^{III} ions adjacent to such vacancies. Analogues of Prussian Blue ($AM^{II}[M'^{III}(CN)_6]$ where A is an alkali metal) generally adopt cubic structures - similar to that of the parent compound - which can be likened to those of ABO_3 perovskites, with the oxide bridges of the perovskite replaced by the cyanide bridges of the PBA. Figure 1.1 overleaf shows a schematic of the $AM^{II}[M'^{III}(CN)_6]$ unit cell, in which first-row transition metals M and M′ linked by cyanide groups along all

three Cartesian directions to form a 3-D structure in which alkali metal cations (A) reside in the interstitial sites.[1]

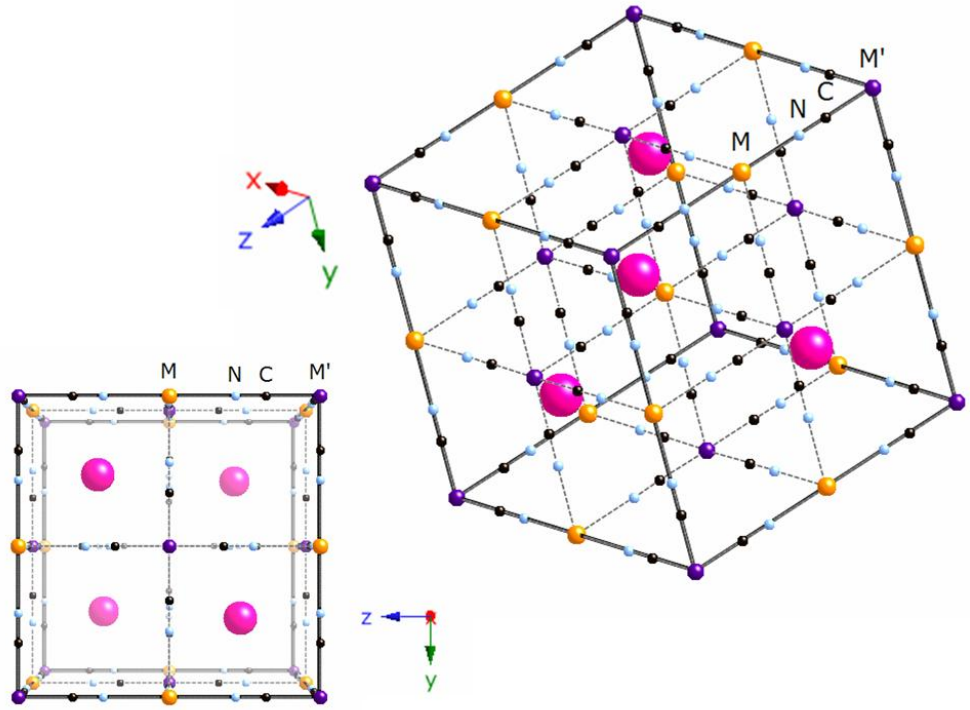

Figure 1.1 Schematic crystallographic structure of $AM^{II}[M'^{III}(CN)_6]$. Pink, orange, purple, black and light blue spheres represent A, M, M', C and N atoms respectively.

The precise architecture comprising a PBA framework is strongly related to its stoichiometry, nonetheless these cubic structures can usually be classified according to one of three types (Figure 1.2 overleaf). The first being the $AM^{II}[M'^{III}(CN)_6]$ type structure, as shown above in Figure 1.1 and overleaf in Figure 1.2a, where each M^{II} centre is surrounded by six M'^{III} in a octahedral geometry and vice versa (it is worth noting that the structures depicted here are somewhat idealized and in many cases a small fraction of the $[M'^{III}(CN)_6]$ moieties are replaced by water molecules). The second type of cubic PBA structure is observed for those compounds with M:M' > 1, such as Prussian Blue itself in which ¼ of the $[Fe(CN)_6]^{4-}$ sites are vacant. One such structure is depicted in Figure 1.2b, in this case M:M' = 3:2 and 1/3 of the $[M'^{III}(CN)_6]$ moieties are replaced by water molecules giving M a mean coordination sphere of $[M(NC)_4(H_2O)_2]$.

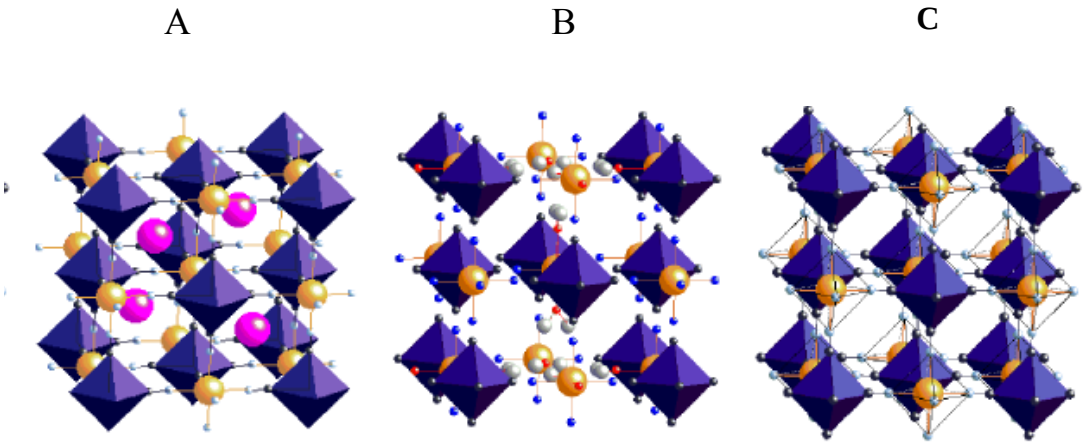

Figure 1.2 Classification of cubic PBAs on the basis of stoichiometry: a) $A^{I}M^{II}[M'^{III}(CN)_6]$, b) $M^{II}_3[M'^{III}(CN)_6]_2 \cdot zH_2O$ and c) M^{III} $[M'^{III}(CN)_6]$. Purple octahedra represent $[M'(CN)_6]$ moieties, orange spheres represent M ions and pink spheres (where present) represent A ions. The water molecules in b) are represented by small red spheres. *(Taken from reference 2).*

The compositions, and thus structures, of PBAs are highly dependent upon synthetic conditions. Minor variations in variables such as temperature, concentration and rate of precipitation have been proven to give rise to materials which differ considerably in stoichiometry and physical properties.[5] Complexation of the M^{II} and $M'^{III}(CN)_6$ components of the PBAs is rapid and irreversible thus making controllable synthesis and the growth of single crystals difficult.

One may anticipate that the initial PBA produced by this reaction of a substitution-inert hexacyanometalate with a labile hexaaquo transition metal will retain the M'-C bonding of the original hexacyanometalate. However, some combinations of M and M' may give rise to PBAs which are metastable with respect to interchange of the transition metal ions between the carbon and nitrogen sites (or flipping of the CN ligand) and thus exhibit linkage isomerization.[6] This phenomenon may occur spontaneously, as is the case for the transformation of ferrous chromicyanide and manganicyanide into Cr^{3+} ferrocyanide and Mn^{2+} ferrocyanide,[7] or be triggered by the application of an external stimulus, e.g. the reversible pressure induced transformation of Cr^{III}-CN-Fe^{II} moieties in $K_{0.4}Fe_4[Cr(CN)_6]_{2.8} \cdot 16H_2O$ to Cr^{III}-NC-Fe^{II}.[8]

1.2.2 Magnetic Exchange

The bridging cyanide ligands of PBAs provide extremely efficient pathways for the exchange of magnetic information between adjacent paramagnetic spin centres. The magnetic susceptibility of Prussian Blue was first reported by Davidson and Welo in 1928.[9] However, no information about the nature of magnetic ordering could be obtained at this time because measurements were restricted to temperatures above 200 K. It was not until 40 years later that a Mossbauer study by Ito et al determined Prussian Blue to be a ferromagnet with $T_C = 5.5 \pm 0.5$ K.[10] Inspired by the Davidson and Welo's pioneering work, scientists began to investigate the magnetic properties of Prussian Blue's analogues. Initial research efforts focused on establishing the nature of long range magnetic ordering in these systems; ultimately with a view to uncovering PBAs exhibiting spontaneous magnetization at or near room temperature. Low-temperature studies in the 1950s by Bozorth et al. were successful in uncovering several magnetic PBAs (including the nominal $Mn^{II}[Mn^{III}(CN)_6]$ which orders at 50 K). These results clearly demonstrated the direct relationship between magnetic ordering temperatures and fraction of paramagnetic TM centres, as demonstrated by the rather low magnetic ordering temperature of PB in which only half the TM ions are paramagnetic.[11, 12] Despite these key findings progress in the development of magnetic PBAs remained slow until the 1980s when Babel et al discovered $CsMn[Cr(CN)_6]$, a ferrimagnet with $T_N = 90$ K, and proposed a *superexchange* mechanism to account for the magnetic properties of PBAs.

Superexchange refers to the magnetic coupling of next-to-nearest paramagnetic neighbours through a non-magnetic anion**.** Superexchange interactions are usually explained in terms of the Goodenough-Kanamori-Anderson rules.[13] On the basis of these rules a magnetic ion-ligand-magnetic ion angle of 90°, where the singly occupied d-orbitals of the paramagnetic ions are orthogonal to one another and there is zero orbital overlap, is anticipated to give rise to weak ferromagnetic exchange interactions. This mechanism of superexchange is referred to as potential exchange. For a magnetic ion-ligand-magnetic ion angle of 180° the singly occupied d-orbitals of the paramagnetic ions are non-orthogonal to one another and there is direct orbital

overlap. Consequently, the unpaired electrons of the magnetic ions align anti-parallel to one another, in accordance to the Pauli exclusion principle, giving rise to strong antiferromagnetic exchange interactions in a superexchange mechanism known as kinetic exchange.

The face-centred cubic (FCC) structures typically adopted by PBAs facilitate prediction of their magnetic properties, which arise from superexchange interactions, since the magnetic orbital symmetries of both the metals and ligands are identical throughout the structure. The M' ions of PBAs are octahedrally coordinated to six cyanide ligands via the C atoms and hence experience a large ligand field splitting of the d-orbitals. Consequently, the M' ions in these systems are always low spin. Furthermore, only transition metals with less than six d-electrons can assume the role of the M' site ion since occupation of the e_g orbitals is energetically unfavourable. The ligand field strength of nitrogen, and also water, is much lower than that of C and consequently the M ions of PBAs experience weak field splitting and are almost always high spin.[14] In instances where M only has paramagnetic orbitals of e_g symmetry there will be zero overlap with the paramagnetic t_{2g} orbitals of M' (Figure 1.3a) and all exchange interactions will be ferromagnetic, and the magnetic coupling constant (J) assumes a positive value.

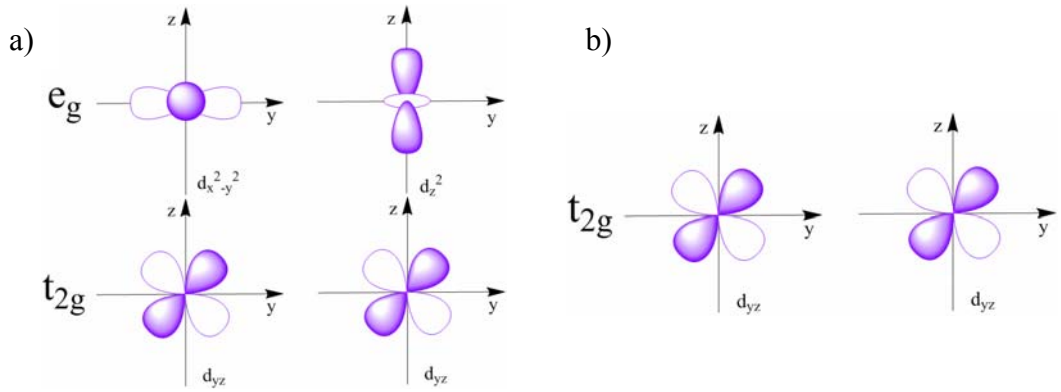

Figure 1.3 Orientations of d-orbitals on adjacent transition metal centres, giving rise to a) potential exchange and b) kinetic exchange.

Conversely, where the paramagnetic orbitals of M are all of t_{2g} symmetry there will be significant orbital overlap with the paramagnetic t_{2g} orbital of M' (Figure 1.3b) and all exchange interactions will be antiferromagnetic, resulting in a negative J

value. If M possesses both e_g and t_{2g} paramagnetic orbitals, ferromagnetic and antiferromagnetic exchange interactions with the t_{2g} orbitals of M' coexist and compete. In such instances, J is the sum of the ferromagnetic (J_F) and antiferromagnetic (J_{AF}) exchange contributions and ferrimagnetism results.

The orbital model outlined above facilitates prediction of the nature and number of magnetic exchange pathways between any given combination of paramagnetic metal ions in PBAs, and consequently it has proven to be an extremely useful tool in the design of novel magnets. Take for example the $Cu_3[Cr(CN)_6]_2$ analogue: the singly occupied e_g orbital of Cu^{II} (d^9, $t_{2g}^6e_g^3$, S = ½) may interact with any of the Cr^{III} (d^3, $t_{2g}^3e_g^0$, S = 3/2) ion's t_{2g} orbitals and thus we predict three possible exchange pathways, all of which are ferromagnetic. Whereas, for $Co_3[Cr(CN)_6]_2$ we predict that interaction of Co^{II} (d^7, $t_{2g}^5e_g^2$, S = 3/2) with Cr^{III} (d^3, $t_{2g}^3e_g^0$, S = 3/2) creates nine superexchange pathways, six of which are ferromagnetic and three of which are antiferromagnetic. The paramagnetic Fe^{III} ions of PB are interspersed by diamagnetic Fe^{II} ions and, the magnetic exchange interactions between spin centres separated by distances of more than 10 Angstroms are very weak. Thus, for PBAs containing only paramagnetic ions the magnetic exchange interactions between second-nearest neighbour spin centres are considered negligible.

In the 1980s, armed with a basic understanding of the origin of magnetism in hetero-bimetallic mixed valence metal polycyanides, materials scientists eventually adopted a rational approach to obtaining PBAs with magnetic ordering temperatures above 90 K. The research groups of Verdaguer and Girolami were key players in achieving this objective. They recognized that the mean field theory employed by Néel to account for the magnetic properties of ferrimagnetic ABO_3 pervoskites was equally applicable to PBAs and consequently their strategies for optimizing the magnetic ordering temperature were founded upon on the following equation:

$$T_N = z|J|\frac{C_A C_B}{N_A g^2 \mu_B^2} \qquad (1.1)$$

where z is the number of nearest neighbors, J is the exchange integral, C_A and C_B are the Curie constants of the metal centers in the two different magnetic sublattices of the perovskite, N_A is Avogadro's number, g is the Landé g factor, and μ_B is the Bohr magneton.[11, 15] The Curie constants may be expressed in terms of the metal ion spin values, S_A and S_B:[15]

$$C_A = (N_A\mu_B^2 / 3k_B)g^2S_A(S_A + 1) \qquad (1.2)$$

$$C_B = (N_B\mu_B^2 / 3k_B)g^2S_B(S_B + 1) \qquad (1.3)$$

Thus, allowing for the possibility of vacancies, Equation 1.1 can be rewritten for $A_xM^{II}[M'^{III}(CN)_6]_y$ type PBAs as follows:[16]

$$T_N = \frac{\sqrt{z_M z_{M'}}\left|J_{MM'}\right|\sqrt{S_M(S_M+1)yS_{M'}(S_{M'}+1)}}{3k_B} \qquad (1.4)$$

It is clear from Equation 1.4 that it should be possible to enhance the magnetic ordering temperatures of PBAs by increasing the number of nearest neighbours, the magnitude of the magnetic exchange integral or the spin values of the transition metal ions. With this in mind, PBAs comprising $[V^{II}(CN)_6]$ and $[Cr^{III}(CN)_6]$ molecular units were targeted because the three singly occupied orbitals ($t_{2g}^3e_g^0$) of the metal ions offer the potential for magnetic interactions in all three directions of space since S = 3/2, whereas all other $[M'(CN)_6]$ molecular building blocks have S < 3/2 and thus magnetic interactions are restricted to a maximum of one or two spatial directions. Moreover, early 1st row transition metals such as Ti, V and Cr offer better non-orthogonal orbital overlap than those further to the right (a consequence of radial expansion of the t_{2g} orbitals with decreasing effective nuclear charge), which in turn gives rise to stronger antiferromagnetic exchange interactions (J_{AF}) and higher values of T_N.

For more than 10 years, the magnetic ordering temperature of Babel's ferrimagnetic $CsMn[Cr(CN)_6]$ (T_N = 90 K) remained unsurpassed in the field of molecule-based materials. Verdaguer et al equaled this record in 1992 when they succeeded in

synthesising the ferromagnetic $CsNi[Mn(CN)_6]$ (T_C = 90 K). This discovery was preceded by the synthesis of several $M^{II}_3[M'^{III}(CN)_6]_2$ type nickel hexayanochromates PBAs. However, the presence of $[Cr^{III}(CN)_6]$ vacancies in these systems acts as an obstacle to high temperature magnetic ordering and consequently the highest T_C observed was limited to 53 K (for $Ni^{II}[Cr^{III}(CN)_6]_{2/3}\cdot 4H_2O$). Incorporating Cs to obtain a stoichiometric $A^IM^{II}[M'^{III}(CN)_6]$ type PBA, in which each Ni cation is surrounded by six $[Cr(CN)_6]$ molecular units as opposed to four, exploited the direct relationship between Z and T_C (as outlined in Equation 1.4) and enabled the magnetic ordering temperatures of nickel hexacyanochromates to be pushed to 90 K. On the basis of molecular orbital theory, nickel hexacyanochromates offer the highest number of solely ferromagnetic superexchange pathways (six) of all the first-row transition metal PBAs. Consequently, the synthesis of $CsNi[Mn(CN)_6]$, with its T_C of 90 K, stimulated a change of focus in the quest to obtain higher magnetic ordering temperatures of PBA magnets. Researchers understood that in order to increase the ordering temperature a ferrimagnetic strategy had to be adopted.

The |J| values, and hence magnetic ordering temperatures, of ferrimagnetic PBAs may be enhanced by decreasing the ferromagnetic contributions (J_F) or increasing the antiferromagnetic contributions (J_{AF}), since $J = J_{AF} + J_F$. Replacing the Mn ($t_{2g}^3\ e_g^2$) ions of $CsMn[Cr(CN)_6]$ with divalent Cr ($t_{2g}^3\ e_g^1$) implements both strategies, reducing the number of ferromagnetic superexchange pathways from six to three and shortening the distance between paramagnetic neighbours. In 1993 Verdaguer et al reported their synthesis of $Cs_{0.75}[Cr_{2.125}\ (CN)_6]\cdot 5H_2O$ (or $Cs_{0.75}Cr^{II}_{1.125}[Cr^{III}(CN)_6]\cdot 5H_2O$ from charge balance analysis), a ferrimagnet with T_N = 190 K.[17] The same study revealed, somewhat surprisingly, that this magnetic ordering temperature is surpassed by the cation-free $[Cr_5(CN)_{12}]\cdot 10H_2O$ (or $Cr^{II}_3[Cr^{III}(CN)_6]_2\cdot 10H_2O$ from charge analysis), which orders at 240 K. The authors proposed two hypotheses to account for this unexpected result: i) a non-ideal value of z, i.e. less than six, in $Cs_{0.75}[Cr_{2.125}\ (CN)_6]\cdot 5H_2O$ due to $[Cr^{III}(CN)_6]$ vacancies; or ii) the presence of low-spin $[Cr^{II}(CN)_6]$ moieties.

The first PBA to exhibit spontaneous magnetization above 273 K was discovered - again by Verdaguer et al - in 1995. The $V^{II}_{0.42}V^{III}_{0.58}[Cr^{III}(CN)_6]_{0.86}\cdot 2.8H_2O$ analogue is a ferrimagnet with an ordering temperature of 315 K.[18] The e_g orbitals of vanadium are unoccupied, thus this material comprises solely antiferromagnetic exchange interactions and the ferromagnetic contribution to J is zero. Furthermore, the orbital overlap between the t_{2g} orbitals of second nearest neighbours is enhanced relative to that of the Cr-Cr analogues discussed above because the vanadium orbitals are more diffuse. The groups of Miller and Girolami both sought to raise the magnetic ordering temperature of PBAs even higher by addressing the major weaknesses of $V^{II}_{0.42}V^{III}_{0.58}[Cr^{III}(CN)_6]_{0.86}\cdot 2.8H_2O$, which were poor crystallinity and a non-stoichiometric composition. Miller et al modified the stoichiometry and increased z by inserting an alkali cation into the interstitial sites to obtain $K_{0.5}V^{II}_{0.65}V^{III}_{0.35}[Cr^{III}(CN)_6]_{0.95}\cdot 1.7H_2O$ with T_N = 350 K.[19] Combining this approach with a sol-gel synthesis to improve crystallinity, Girolami et al. achieved a magnetic ordering temperature of 376 K with the stoichiometric $KV^{II}[Cr^{III}(CN)_6]\cdot 2H_2O$ analogue.[20] This high magnetic ordering temperature is attributed to: i) the eradication of V^{III} ions, with d-orbitals which are radially contracted compared to those of V^{II} ions, ii) the average number of Cr ions coordinated to each V ion is optimized to six and iii) the slow crystal growth afforded by the sol-gel synthesis technique produces a crystalline material.

Titanium, being the earliest first-row transition metal, should give rise to magnets with exceptionally high ordering temperatures. The $[Ti^{III}(CN)_6]^{3-}$ ion is instantly hydrolyzed in water, thus attempts to synthesis PBAs incorporating this ion are restricted to non-aqueous media. The hexacyanotitanate(III) ion is soluble in acetonitrile. However, this solvent is poorly coordinating and addition of divalent TM cations to solutions of $[Ti^{III}(CN)_6]^{3-}$ in acetronitrile results in the rapid precipitation of poorly crystalline, non-magnetic solids. To date, all efforts to prepare magnetic materials in which Ti^{III} occupies the carbon sites of the Prussian Blue structure have failed. Thus, the magnetic ordering temperature of 376 K observed for $KV^{II}[Cr^{III}(CN)_6]\cdot 2H_2O$ is unsurpassed and preparation of molecular

magnets from hexacyanotitanate(III) building blocks remains to be considered, by some at least, the holy grail of PBA research.[21]

1.2.3 Bistability

The intense blue colour which originally brought Prussian Blue to the attention of scientists is the consequence of an intervalence charge transfer, centred at approximately 680 nm, from low spin Fe^{II} to high spin Fe^{III} through a cyanide bridge.[22] Intermetallic charge transfer is also responsible for many of the intriguing phenomena observed in Prussian Blue's transition metal analogues. For example, $Co^{II}_x[Fe^{III}(CN)_6]_y \cdot nH_2O$ and its alkali-doped analogues have been observed to undergo photo-induced magnetization, thermally induced demagnetization[23] and pressure-induced structural phase transitions[24] – all of which are the consequence of an externally driven electron transfer between the Co and Fe sites. Prussian Blue analogues such as these - that is those which can be switched between electronic states upon application of an external stimulus - may be referred to as *switchable* or *tunable*.

Tunable PBAs hold particular promise for the burgeoning field of molecular electronics, since systems which undergo reversible and controlled changes of their physical properties in response to external perturbations may find applications in novel information storage and electronic devices. The switching phenomena observed for selected PBAs arise as a consequence of molecular bistability. Olivier Kahn defined molecular bistability as follows: "*the property of a molecular system able to evolve from a stable electronic state to another stable electronic state in a reversible and detectable fashion when applying an appropriate and controllable perturbation*".[25] Electronic interactions between the oxidized and reduced sites in PBAs are relatively weak, thus despite a degree of charge delocalization the oxidation states of the metal centres remain distinguishable (valence trapped). Systems such as this are categorized as Class II mixed-valence compounds and can be described by two degenerate or quasi-degenerate parabolic potential energy curves, i.e. a double well potential.[26] In the ground state the mobile electron is trapped in one of the minima; however, the probability of an externally driven

transfer from one metal centre to another is non-zero and consequently the system may be described as switchable or bistable.[27]

A variety of external stimuli have been successfully employed to switch between the metastable electronic states of PBAs. Photoirradiation is a particularly attractive means of control because the photon mode allows access to a range of different types of materials with high speed and superior resolution.[28] The Co-Fe analogues referred to in the opening paragraph of this section were the first PBA systems to exhibit photomagnetism. In 1996 Hashimoto et al reported that irradiation of $K_{0.2}Co_{1.4}[Fe(CN)_6]\cdot 6.9H_2O$ at 5 K with red light brings about a significant augmentation of the magnetization and an increase of the magnetic ordering temperature from 16 to 19 K.[23] This compound is comprised of both paramagnetic $Fe^{III}(d^5, t_{2g}^5e_g^0, S = 1/2)$-CN-$Co^{II}(d^7, t_{2g}^5e_g^2, S = 3/2)$ (HS0) and diamagnetic $Fe^{II}(d^6, t_{2g}^6e_g^0, S = 0)$-CN-$Co^{III}(d^6, t_{2g}^6e_g^0, S = 0)$ (LS0) units (the presence of the latter subsequently being proven to be a prerequisite for observation of photomagnetic phenomena). Red light excitation stimulates an electron transfer from Fe^{II} to Co^{III}, in the diamagnetic moieties, thereby increasing the fraction of the paramagnetic units and giving rise to a macroscopically observable increase in magnetization and T_N. The reverse intramolecular charge transfer can be accessed, and hence the ground state recovered, by blue light irradiation or by heating to 150 K. In the absence of such perturbations the photoinduced state may persist in the dark at 5 K for several days.[29, 30, 31] Kawamoto et al. summarized the elementary processes involved in this photoinduced magnetization/demagnetization cycle with the following schematic:[32]

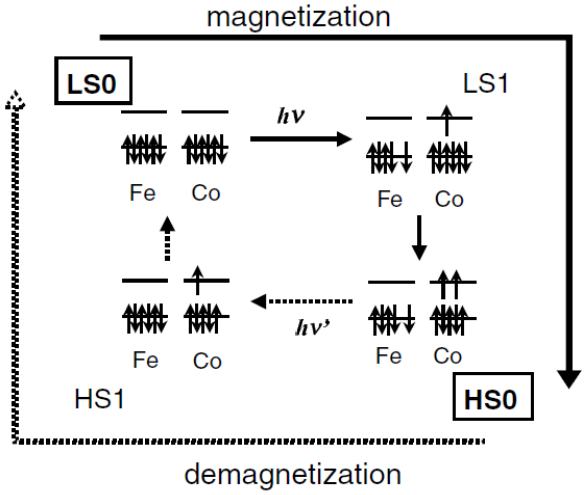

Figure 1.4 The elementary processes of photoinduced magnetization/demagnetization in $K_{0.2}Co_{1.4}[Fe(CN)_6]\cdot 6.9H_2O$. *(Taken from reference 32)*

Photoinduced charge transfer between Fe and Co initially converts the LS0 and HS0 states to the intermediate $Fe^{III}(d^5, t_{2g}^5e_g^0, S = ½)$-CN-$Co^{II}(d^7, t_{2g}^6e_g^1, S = 1/2)$ (LS1) and $Fe^{II}(d^6, t_{2g}5e_g^0, S = ½)$-CN-$Co^{III}(d^6, t_{2g}^5e_g^1, S = 1)$ (HS1) states, respectively. These states are subsequently transformed to the final HS0 and LS0 states by intersystem crossing. The Co-N bond of the LS0 state is contracted by ~ 0.2 Å compared to that of the HS0 state, due to occupation of the sigma antibonding 3d e_g orbitals in the latter, while the Fe-C bond is relatively unaltered by the charge transfer process driving this spin change. Consequently, the transition between LS0 and HS0 states is accompanied by a volume change, which is thought to make a significant contribution to the large energy barrier which exists between the two states and precludes thermally activated relaxation at low temperatures.[33, 34]

Studies of related Co-Fe PBAs revealed that the redox, optical and magnetic properties of these compounds can be tuned via modification of the alkali metal cation fraction. The $M^{II}_3[M'^{III}(CN)_6]_2\cdot nH_2O$ type analogue $Co^{II}_{1.5}[Fe^{III}(CN)_6]\cdot 6H_2O$, which is free from alkali cations, is comprised entirely of paramagnetic $Fe^{III}(d^5, t_{2g}^5e_g^0, S = 1/2)$-CN-$Co^{II}(d^7, t_{2g}^5e_g^2, S = 3/2)$ moieties and is unperturbed by photoirradiation. However, electroneutrality dictates that insertion of interstitial alkali metal cations in this compound is accompanied by a reduction in the number of $[Fe(CN)_6]$ vacancies, which in turn strengthens the ligand field around Co (CN

lies slightly higher in the spectrochemical series than H_2O) causing the low-spin Fe^{II}-CN-Co^{III} state to be favoured. Thus the efficiency of photoinduced magnetization in these systems can be controlled at will via judicious selection of the alkali metal ions.

Following more than a decade of research, the oxidation and spin states of the stable and metastable phases involved in the photoswitching processes of Co-Fe PBAs are now well characterized and some understanding of the conditions necessary for the observation of such phenomena has been gained. However, several unanswered questions remain on the atomic arrangement of the Co-NC-Fe linkages, water molecules, and alkali cations in the structure and their role in photoswitching properties. Thus Co-Fe systems continue to be actively studied because resolution of these issues is of fundamental importance for the rational design of new systems with improved photomagnetic properties. The cobalt hexacyanoferrates are now joined by several other Prussian Blue type systems, constructed from both hexa- and octacyanometalate building blocks, which exhibit light-induced metal-to-metal charge transfer. These systems will be discussed further in the following chapters.

The energy of radiation employed in the photoswitching of Co-Fe PBAs and related systems is typically comparable to the Franck-Condon energies of the charge transfer excitations which drive the observed magnetization/demagnetization effects, that is, light which lies in the near-IR, visible, or UV regions. Photoswitching by means of X-ray irradiation has, until recently, been disregarded within the field of PBAs since the energy of X-ray light exceeds the energy difference separating the ground and metastable electronic states of bistable PBAs by a factor of 1000.[35] The synchrotron X-ray powder diffraction studies of $CsFe^{II}[Cr^{III}(CN)_6]$ performed by Papanikolaou et al demonstrate a rare example of X-ray induced photoswitching within a PBA system. This compound exhibits a thermally induced, hysteretic reversible spin-crossover which is uncharacteristic of the PBAs because it occurs in the absence of an electron transfer or linkage isomerism.[36, 37] The crossover of the Fe^{II} spin state from Fe^{II}(HS, S = 2, $t_{2g}^4e_g^2$)-Cr^{III}(S = 3/2, $t_{2g}^3e_g^0$) to Fe^{II}(LS, S = 0, $t_{2g}^6e_g^0$)-Cr^{III}(S = 3/2, $t_{2g}^3e_g^0$) which occurs at 212 K upon cooling is observed macroscopically as an abrupt structural phase collapse and a dramatic decrease of the magnetization. The reverse transformation is observed at 241 K upon warming. The low-temperature

phase is weakly ferromagnetic due to double exchange interaction of the Cr^{III} ions via the diamagnetic low-spin Fe^{II} centres. The high- to low-spin transition of the Fe centres in $CsFe^{II}[Cr^{III}(CN)_6]$ can also be triggered outwith the thermal hysteresis loop, i.e. at temperatures above 241 K, via X-ray irradiation. Thus X-ray light is proven to be an effective means of switching between the ground and hidden or inaccessible excited states in PBAs. Furthermore, this study illustrates how X-ray irradiation can simultaneously act a probe and source of perturbation, thereby demonstrating that X-ray irradiation is an extremely useful tool for the study of photosensitive PBAs.

1.2.4 Multifunctionality

The majority of research performed on PBAs over the past 20 years (and indeed within the scope of this thesis) has focused on their magnetic properties. However, it is important to acknowledge that magnetic ordering belongs to a vast array of appealing functionalities associated with the PBAs. Therefore PBAs are ideal systems in which to explore multifunctionality – the coexistence of two or more useful properties within a single system.

Electrochromism, the process whereby the loss or gain of an electron gives rise to an observable colour change, is observed in several PBA systems, e.g. nickel hexacyanoferrate thin films are grey in the reduced state and green in the oxidized state.[38] Various external stimuli (including voltage, light, temperature and pressure) have been employed to drive the redox reactions responsible for the colour switching phenomena of PBAs. Indeed, the $Cs_{0.75}Co[Fe(CN)_6]_y$ analogue is reported to be both photo- and thermo-chromic, that is, its purple colour changes in response to light irradiation and thermal pertubations.[39] Electrochromic materials such as these hold commercial promise for the development of electrochromic windows – the prospect of darkening of windows in cars and buildings at the flick of a switch is particularly appealing – and electrochromically controlled information display devices.

The porosity of PBAs – a consequence of their open-channel framework structures – acts as a further source of commercial appeal. Cavities which exist within the PBA structure due to systematic $[M'^{III}(CN)_6]$ vacancies are typically occupied by zeolitic

water molecules hydrogen bonded to the water molecules of the M site ion's coordination sphere, $[M(NC)_4(H_2O)_2]$. The water molecules of PBAs (both coordinated and zeolitic) may be removed by heating or storage over a dehydrating agent to form channels.[40] Thus, PBAs are appropriate materials for the separation and storage of small molecules and may be employed as aluminosilicate alternatives in absorbent and molecular sieve applications. The molecular sieving properties of PBAs were first demonstrated in 1985 by Boxhoorn et al, who successfully used $Zn[Co(CN)_6]$ to separate C_6 isomers. The dimensions of pore openings in the $Zn[Co(CN)_6]$ structure, which measure approximately 0.56 x 0.86 nm, permit the adsorption of n-hexane and 3-methylpentane molecules, whereas 2,2-dimethylbutane molecules are excluded due to their larger size.[41]

Recent research has proven PBAs, and $Cu_3[Co(CN)_6]_2$ in particular, to be effective hydrogen storage materials.[42] The development of appropriate means of storage is essential if hydrogen is to replace fossil fuels in mobile applications. Hydrogen molecules bind side-on to the open coordination sites of nitrogen-bound M ions through sigma-donation to vacant metal d-orbitals to form coordination bonds which are stabilized by metal-to-ligand back-bonding interactions.[43] Elucidation of the nature of hydrogen uptake in PBAs illustrated just how accessible the electronic structures of metals at the surface of structural cavities are to adsorbed species. Consequently, the adsorption of guest species becomes a feasible means of tuning the electronic and magnetic properties and is currently an active line of research in the field of PBAs.

1.2.5 Future Directions

In the 20th century the major challenges in the field of magnetic PBA research were the realization of room temperature ordering and preparation of tunable compounds. The coexistence of these phenomena within a single system, i.e. the preparation of PBAs exhibiting bistability at room temperature, is now likely to be one of the key objectives of the 21st century. That, however, is not to say that low temperature bistable PBAs will cease to be pursued; exploration of the way in which their

magnetic properties react to external stimuli provides valuable insight into their intrinsic nature of these systems.

The vast majority of PBA research performed over the past two decades has focused on the relationship between the unit-cell structure and magnetic properties; however, before these properties can be fully exploited in functional devices further processing of the PBAs - beyond the length scale of the unit cell - is required. It is envisaged that PBAs will be integrated into such devices as arrays of nano-objects ordered on surfaces or within thin-films. However, relatively few efforts have been made towards controlling the particle size, morphology, surface texture and higher order organization of PBAs. Work within this thesis seeks to address this issue and consequently detailed discussions on the state-of-the-art are reserved for ensuing chapters.

1.3 Bibliography

1. M. Verdaguer, A. Bleuzen, V. Marvaud, J. Vaissermann, M. Seuleiman, C. Desplanches, A. Scuiller, C. Train, R. Garde, G. Gelly, C. Lomenech, I. Rosenman, P. Veillet, C. Cartier and F. Villain, *Coordination Chemistry Reviews*, 1999, **192**, 1023-1047.
2. J. S. Miller and M. Drillon, *Magnetism: molecules to materials*, Weinheim; [Great Britain]: Wiley-VCH, 2001.
3. D. F. Shriver and D. B. Brown, *Inorganic Chemistry*, 1969, **8**, 42.
4. A. Ludi, *Journal of Chemical Education*, 1981, **58**, 1013-1013.
5. E. J. M. Vertelman, E. Maccallini, D. Gournis, P. Rudolf, T. Bakas, J. Luzon, R. Broer, A. Pugzlys, T. T. A. Lummen, P. H. M. van Loosdrecht and P. J. van Koningsbruggen, *Chemistry of Materials*, 2006, **18**, 1951-1963.
6. D. B. Brown and D. F. Shriver, *Inorganic Chemistry*, 1969, **8**, 37.
7. E. Reguera, J. F. Bertran and L. Nunez, *Polyhedron*, 1994, **13**, 1619-1624.
8. E. Coronado, M. C. Gimenez-Lopez, T. Korzeniak, G. Levchenko, F. M. Romero, A. Segura, V. Garcia-Baonza, J. C. Cezar, F. M. F. de Groot, A. Milner and M. Paz-Pasternak, *Journal of the American Chemical Society*, 2008, **130**, 15519-15532.
9. D. Davidson and L. A. Welo, *Journal of Physical Chemistry*, 1928, **32**, 1191-1196.
10. A. Ito, M. Suenaga and K. Ono, *Journal of Chemical Physics*, 1968, **48**, 3597.
11. W. R. Entley, C. R. Treadway and G. S. Girolami, *Molecular Crystals and Liquid Crystals Science and Technology Section a-Molecular Crystals and Liquid Crystals*, 1995, **273**, 153-166.
12. R. M. Bozorth, H. J. Williams and D. E. Walsh, *Physical Review*, 1956, **103**, 572-578.
13. J. Curely, *Monatshefte Fur Chemie*, 2005, **136**, 1013-1036.
14. D. F. Shriver, S. A. Shriver and S. E. Anderson, *Inorganic Chemistry*, 1965, **4**, 725.
15. S. Ferlay, T. Mallah, R. Ouahes, P. Veillet and M. Verdaguer, *Inorganic Chemistry*, 1999, **38**, 229-234.
16. E. Ruiz, A. Rodriguez-Fortea, S. Alvarez and M. Verdaguer, *Chemistry-A European Journal*, 2005, **11**, 2135-2144.
17. T. Mallah, S. Thiebaut, M. Verdaguer and P. Veillet, *Science*, 1993, **262**, 1554-1557.
18. S. Ferlay, T. Mallah, R. Ouahes, P. Veillet and M. Verdaguer, *Nature*, 1995, **378**, 701-703.

19. O. Hatlevik, W. E. Buschmann, J. Zhang, J. L. Manson and J. S. Miller, *Advanced Materials*, 1999, **11**, 914.

20. S. M. Holmes and G. S. Girolami, *Journal of the American Chemical Society*, 1999, **121**, 5593-5594.

21. S. M. Holmes, A. S. Whelpley and G. S. Girolami, *Polyhedron*, 2007, **26**, 2291-2298.

22. A. S. Wills, *Annual Reports Section "A" (Inorganic Chemistry)*, 2005, **101**, 472-488.

23. O. Sato, T. Iyoda, A. Fujishima and K. Hashimoto, *Science*, 1996, **272**, 704-705.

24. A. Bleuzen, J. D. Cafun, A. Bachschmidt, M. Verdaguer, P. Munsch, F. Baudelet and J. P. Itie, *J Phys Chem C*, 2008, **112**, 17709-17715.

25. O. Kahn, in *Engineering in Medicine and Biology Society, 1990., Proceedings of the Twelfth Annual International Conference of the IEEE*, 1990, pp. 1683-1685.

26. B. S. Brunschwig, C. Creutz and N. Sutin, *Chemical Society Reviews*, 2002, **31**, 168-184.

27. J. Ribas Gispert, *Coordination chemistry*, Wiley-VCH; Chichester: John Wiley [distributor], Weinheim, 2008.

28. O. Sato, Y. Einaga, A. Fujishima and K. Hashimoto, *Inorganic Chemistry*, 1999, **38**, 4405-4412.

29. P. Gutlich, Y. Garcia and T. Woike, *Coordination Chemistry Reviews*, 2001, **219**, 839-879.

30. M. Verdaguer, *Science*, 1996, **272**, 698-699.

31. D. F. Li, R. Clerac, O. Roubeau, E. Harte, C. Mathoniere, R. Le Bris and S. M. Holmes, *Journal of the American Chemical Society*, 2008, **130**, 252-258.

32. T. Kawamoto, Y. Asai and S. Abe, *Physical Review Letters*, 2001, **86**, 348-351.

33. T. Yokoyama, T. Ohta, O. Sato and K. Hashimoto, *Physical Review B*, 1998, **58**, 8257-8266.

34. A. Dei, *Angewandte Chemie-International Edition*, 2005, **44**, 1160-1163.

35. D. Papanikolaou, S. Margadonna, W. Kosaka, S. Ohkoshi, M. Brunelli and K. Prassides, *Journal of the American Chemical Society*, 2006, **128**, 8358-8363.

36. W. Kosaka, K. Nomura, K. Hashimoto and S. Ohkoshi, *Journal of the American Chemical Society*, 2005, **127**, 8590-8591.

37. D. Papanikolaou, W. Kosaka, S. Margadonna, H. Kagi, S. Ohkoshi and K. Prassides, *J Phys Chem C*, 2007, **111**, 8086-8091.

38. N. R. de Tacconi, K. Rajeshwar and R. O. Lezna, *Chemistry of Materials*, 2003, **15**, 3046-3062.

39. A. Goujon, F. Varret, V. Escax, A. Bleuzen and M. Verdaguer, *Polyhedron*, 2001, **20**, 1339-1345.

40. J. Balmaseda, E. Reguera, J. Rodriguez-Hernandez, L. Reguera and M. Autie, *Microporous and Mesoporous Materials*, 2006, **96**, 222-236.

41. G. Boxhoorn, J. Moolhuysen, J. G. F. Coolegem and R. A. Vansanten, *Journal of the Chemical Society-Chemical Communications*, 1985, 1305-1307.

42. L. Reguera, C. P. Krap, J. Balmaseda and E. Reguera, *J Phys Chem C*, 2008, **112**, 15893-15899.

43. S. S. Kaye and J. R. Long, *Catalysis Today*, 2007, **120**, 311-316.

Chapter 2

Experimental Theory & Techniques

2.1 Introduction

The experimental techniques used to characterize the PBA materials investigated in this work are described within this chapter. Magnetic SQUID measurements and X-ray powder diffraction (XRPD) were the principal characterization methods used and consequently they are described in detail, together with the theories upon which they are based. In the case of PBA nanoparticles, the additional technique of transmission electron microscopy (TEM) was used to determine particle size distribution and dispersion. Selected cases, where oxidation states of the PBAs could not be confidently assigned from the susceptibility and XRPD data alone, necessitated the use of either X-ray photoelectron spectroscopy (XPS) or X-ray absorption near edge structure (XANES) spectroscopy. Inductively coupled plasma (ICP) spectrometry is a standard analytical technique which was routinely employed to determine the exact stoichiometry of the materials. The three aforementioned spectroscopic methods and their relevant theories will be briefly outlined in this chapter.

2.2 Magnetic Materials

A magnetic field (**H**) produces lines of force, the density of which are referred to as the magnetic flux density (**B**) or magnetic induction. The flux density changes when the field is applied to a magnetic material. If the material is paramagnetic **B** will increase, while if it is diamagnetic **B** will decrease. Paramagnetism is associated with the presence of unpaired electrons and diamagnetism with the presence of electron pairs. The actual field experienced by the magnetic material is referred to as its magnetization (**M**), defined as the magnetic moment per unit volume, and related to the flux density and applied field by:

$$\mathbf{B} = \mu_0 (\mathbf{H} + \mathbf{M}) \qquad (2.1)$$

where μ_0 is the permeability of free space. Magnetic properties are usually discussed in terms of magnetic susceptibility, a dimensionless parameter which is derived from the magnetization using the following relationship:

$$\chi = \frac{M}{H} \qquad (2.2)$$

Magnetic susceptibilities are often given in terms of the molar magnetic susceptibilities (χ_m) where

$$\chi_m = \frac{\chi}{V_m} \qquad (2.3)$$

and V_m is the molar volume (the relative atomic mass of the substance divided by its density). Alternatively, magnetic interactions may be discussed in terms of the effective magnetic moment (μ_{eff}):

$$\mu_{eff} = 2.828\sqrt{\chi_m T} \qquad (2.4)$$

where 2.828 is a number of fundamental constants in cgs units. Paramagnetic materials exhibit temperature dependent behaviour. In cases where unpaired electrons on different atoms remain randomly orientated to one another down to absolute zero this temperature dependence is described by the Curie law:

$$\chi = \frac{C}{T} \qquad (2.5)$$

where C is the Curie constant and T is the temperature in Kelvin. Different temperature dependent behaviours are observed when cooperative behaviour exists between unpaired electrons on different atoms.[1] The Hamiltonian

$$H = -J\, S_1 \cdot S_2 \qquad (2.6)$$

is used to describe the magnetic interactions between cooperating centres carrying spins S_1 and S_2, with J being the strength of the interaction.[2] Ferromagnetic materials, in which unpaired electrons on adjacent spin centres are aligned parallel to one another, have $J > 0$. In cases where the ferromagnetic coupling between two spin centres is interjected by a diamagnetic neighbour J will be smaller due to longer-range coupling. Antiferromagnetic materials, in which two identical spins align antiparallel to one another giving overall zero spin, have $J < 0$. Ferrimagnetism arises when non-identical spins align antiparallel to one another to give a nonzero spin. In instances where cooperative magnetic phenomena exist at low temperatures the behaviour in the high temperature region, where cooperative ordering is disrupted by thermal fluctuations and paramagnetism results, is best described by the Curie-Weiss law:

$$\chi = \frac{C}{T - \theta} \qquad (2.7)$$

where θ is the Weiss constant.

The temperature dependence of χ is used to distinguish different types of magnetic materials (Figure 2.1 overleaf). The magnetic ordering temperature, the point at which Curie-type paramagnetic behaviour switches to cooperative behaviour, is termed the Curie temperature (T_C) in the case of ferromagnetism and the Néel temperature (T_N) in the case of antiferromagnetism. At low temperatures ferromagnets exhibit very large susceptibilities which decrease rapidly upon approaching T_C whereas the susceptibilities of antiferromagnets are small at low temperatures but increase upon approaching T_N. In both cases Curie-Weiss behaviour is generally observed above the magnetic ordering temperature. The Weiss constant (θ) is determined by plotting the temperature dependence of the inverse susceptibility (χ^{-1}) in the paramagnetic regime and extrapolating to y = 0, with θ being given by the temperature at which the plot intercepts the abscissa.[3] A plot which extrapolates to 0 K giving θ = 0 is indicative of simple paramagnetism.

For ferromagnetic substances, since there is already some alignment of spins above T_C and χ is higher than for the simple paramagnetic case at the same temperature, the plot extrapolates to give $\theta > 0$. Conversely, for antiferromagnetic substances χ is lower than for the simple paramagnetic case at the same temperature and $\theta < 0$.

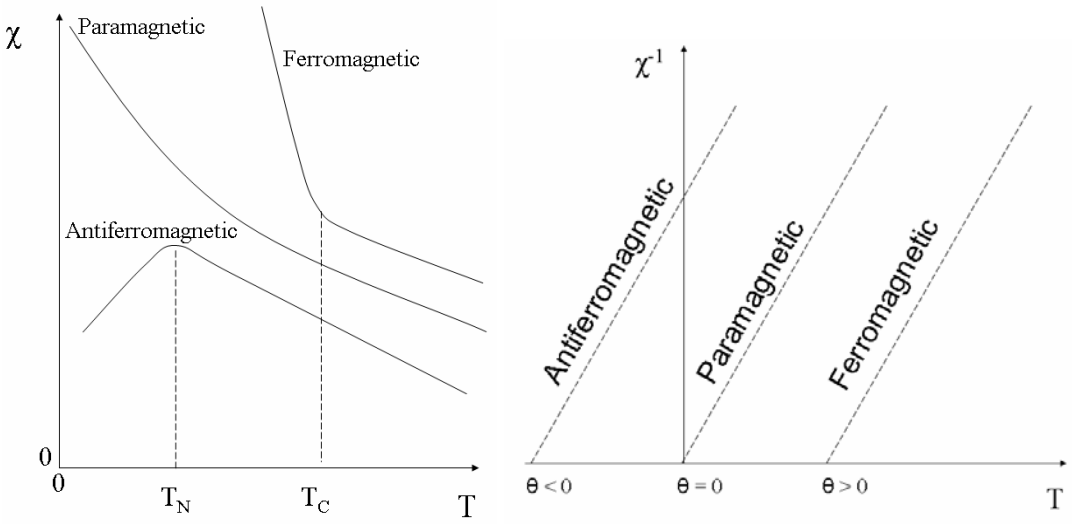

Figure 2.1 a) Variation of magnetic susceptibility with temperature. b) Plot of reciprocal susceptibility in the high temperature paramagnetic regime extrapolated to y = 0.

2.2.1 SQUID Magnetometry

One of the most sensitive devices for the measurement of bulk magnetic properties is the Quantum Design Magnetic Measurement System (MPMS), a magnetometer which comprises several superconducting components including a radio-frequency Superconducting Quantum Interference Device (RF SQUID).[4] The SQUID is essentially a flux-to-voltage transducer which employs the quantum-mechanical effects of superconductivity, Josephson tunneling and flux quantization to convert changes in magnetic flux into voltages.[5]

The RF SQUID consists of a superconducting loop, which is interrupted by a Josephson junction and coupled to both a radio-frequency circuit and a superconducting pick-up coil (Figure 2.2 overleaf).[6]

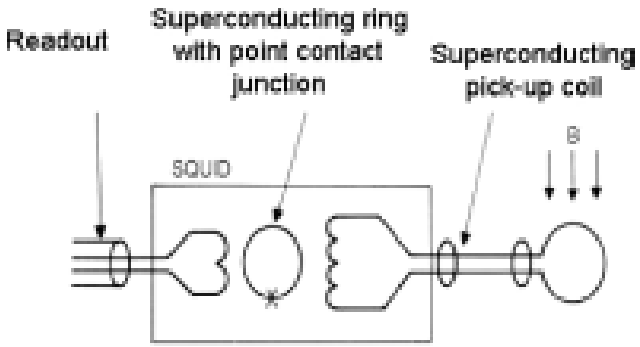

Figure 2.2 Schematic of the RF SQUID. *(Taken from reference 7).*

A line of magnetic flux threading through the loop will induce a current in the ring, the magnitude of which is a sensitive indicator of flux density.[7] Cooper pairs tunnel through the insulating material of the Josephson junction as supercurrents - oscillating functions related to the magnetic flux quanta (Φ_0) threading through the loop. Progressively increasing or decreasing the applied magnetic field causes the current in the loop to oscillate between a maximum and minimum value (which correspond to integral and half-integral numbers of flux quanta respectively). This in turn alters the resonant frequency of the RF circuit, which simultaneously acts a supplier of a known bias field and a detector output. This effect is exploited in the MPMS by moving the sample to be measured through the superconducting pick-up coils to generate a magnetic flux in the coil which in turn changes the current in the loop, which is connected to the coils via superconducting wires. The output of the SQUID is recorded as a function of sample position and the response curve analyzed by a computer to derive a corresponding magnetic moment. The solenoidal superconducting magnet employed by the MPMS allows large magnetic fields to be applied to the sample, while a superconducting shield is used to protect the sensitive SQUID assembly from fluctuations in the ambient magnetic field and from those produced by the superconducting magnet.

Direct-current (DC) magnetometry, in which the sample is magnetized by a constant magnetic field, is used to establish the equilibrium value of the magnetization in a sample. The principal DC measurements used in the characterization of magnetic

materials are magnetization as a function of temperature, M(T), and magnetization as a function of applied field, M(H). Alternating-current (AC) magnetic measurements, in which an AC field is applied to the sample, provide information on magnetization dynamics since the sample moment is time dependent. At sufficiently high measurement frequencies the magnetization of the sample may lag behind the drive field, resulting in a susceptibility measurement which is comprised of two components: the magnitude of the susceptibility (χ) and the phase shift relative to the drive signal (φ).

Two types of cell were employed for high pressure MPMS susceptibility measurements, a piston-cylinder cell and a long symmetric cell. Both cells were designed in-house. The cross-sectional view of the piston-cylinder cell, its key components and the overall dimensions are shown in Figure 2.3.

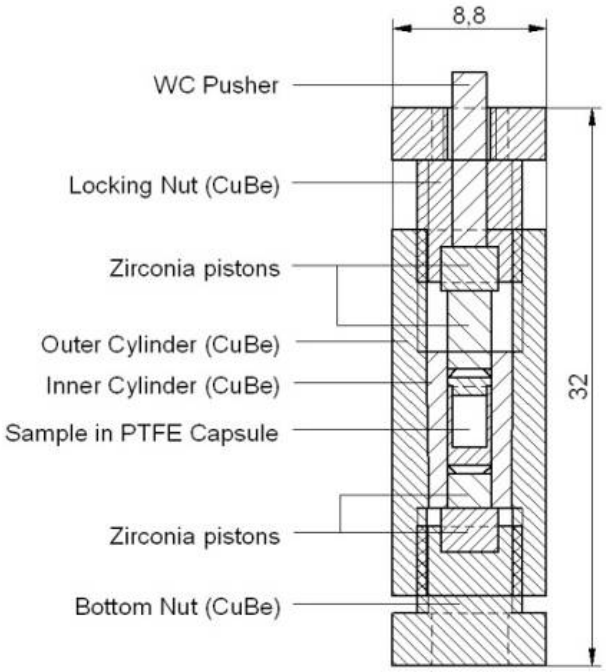

Figure 2.3 Cross-sectional view of the MPMS high pressure cell (dimensions are in mm). The outer and inner diameters of the cell are 8.8 mm and 2.5 mm respectively.

The cell is made from two non-magnetic BERYLCO-25 alloy cylinders with interference fit and is capable of reaching pressures in excess of 10 kbar. The sample is contained inside a polytetrafluoroethylene (PTFE) capsule and Daphne 7373 oil (IDEMITSU-ILS)[8] used as the pressure transmitting medium. Pressure is applied in a hydraulic press with a tungsten carbide (WC) pusher and monitored by using a calibrated load cell. The capsule sealed by two anti-extrusion copper rings is squeezed between zirconia rods used as pistons. Once the desired pressure is achieved the pistons are locked in their position by the locking nut. The cell is removed from the press and attached to the SQUID sample rod using an internal thread on the upper locking nut. The pressure is then measured at low temperature using the superconducting transition in a small piece of tin placed inside the PTFE capsule next to the sample.[9]

Pressure inside the long-symmetric cell is induced by means of screws, rather than with the use of an external press, and pressure changes are determined from mechanical micrometry measurements of the external dimensions of the cell. Again the cell is made of BERYLCO-25 alloy, the body of the cell consisting of two coaxial cylinders with interference fit.

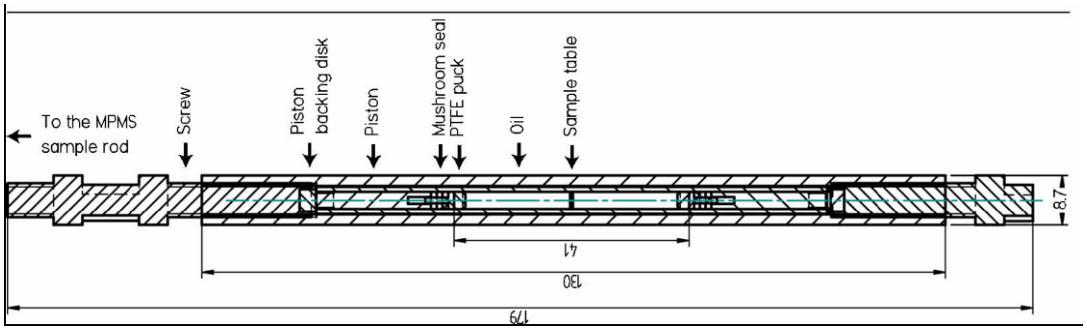

Figure 2.4 Cross sectional view of the long symmetric cell.

The cell is assembled by positioning a mushroom seal with tin and copper washers inside the bore so that the mushroom assembly just enters the bore of the cell. The piston is then backed up with a backing disk and the screw. The cell is filled with Daphne 7373 oil just above the midpoint of the bore. Powdered samples are pressed into pellets and mounted on a PTFE puck which is inserted into the cell and

positioned in the centre. The cell is then filled with oil almost to the top of the bore and the oil stirred with a wire rod to remove any trapped air bubbles. The second piston assembly is inserted and the cell is now at ambient pressure and fully symmetric with respect to the sample. As the pressure is increased the overall length of the cell decreases. Once the required pressure is achieved the pressure cell is attached to the standard sample rod by means of an M6_1 thread on the top screw and a simple two-way threaded adapter.

2.3 Crystalline Materials

Solid state crystalline materials are ordered arrays of regularly repeating structural motifs – which may be atoms, molecules, or groups of atoms, molecules, or ions. The position of each structural motif may be represented by a point and the resultant pattern of points defined as the crystal lattice. The simplest repeating unit in this pattern is referred to as the unit cell, an imaginary parallelepiped containing one unit of the translationally repeating pattern. The macroscopic crystal is reproduced via stacking (translational displacements) of the unit cell in three dimensions. The unit cell parallelepiped is generated from the vectors **a**, **b**, and **c** which lie along the x, y and z axes respectively. Similarly, the lengths of the unit cell vectors along the x, y and z axes are respectively defined as *a, b* and *c*. The angle between the unit cell vector **b** and **c** is represented by α, likewise β is the angle between **a** and **c** and γ is the angle between **a** and **b**.

Three-dimensional unit cells may be termed primitive (P), body-centred (I) or face-centred (F). A P-type unit cell normally only has lattice points located at the corners, an I-type cell has lattice points at its corners and an additional lattice point at the centre of the unit cell, a F-type cell has lattice points at its corners and at the centre of each of its faces. The term face-centred may also refer to a unit cell with a lattice point at just one of its faces. Such cells are termed A-type if the lattice point exists at the centre of the face defined by the *b* and *c* directions, B-type if it exists at the face defined by the *a* and *c* directions or C-type if the lattice point is found at the face defined by the *a* and *b* directions.

Unit cells may also be classified into seven crystal classes according to the relationships between the unit cell parameters *(Table 2.1)*.

Table 2.1 The seven crystal lattice systems.[10]

Unit cell dimensions	Crystal class	Bravais Lattices
$a = b = c \quad \alpha = \beta = \gamma = 90^o$	Cubic	P, I, F
$a = b \neq c \quad \alpha = \beta = \gamma = 90^o$	Tetragonal	P, I
$a \neq b \neq c \quad \alpha = \beta = \gamma = 90^o$	Orthorhombic	P, C, I, F
$a \neq b \neq c \quad \alpha = \gamma = 90^o \quad \beta \neq 90^o$	Monoclinic	P, C
$a \neq b \neq c \quad \alpha \neq \beta \neq \gamma \neq 90^o$	Triclinic	P
$a = b \neq c \quad \alpha = \beta = 90^o \gamma \neq 120^o$	Hexagonal	P
$a = b = c \quad \alpha = \beta = \gamma \neq 90^o$	Trigonal	P

Combining the seven crystal classes with the six lattice types (P, I, F, A, B, C) gives rise to the Bravais lattices[11] - fourteen distinct ways of arranging lattice points in three-dimensional space. Several of the possible combinations (there are 6 x 7 = 42) are equivalent to one another.

Points within a three-dimensional lattice may be connected via lattice planes. These planes are labelled with Miller indices, triplets of integers *(h k l)* derived from the intercepts of the plane with the three crystal axes. In cases where axes intercepts are expressed as fractions of the unit cell length the Miller indices are simply the reciprocals of these fractions. However, a plane parallel to a crystal axis will never intercept it, that is the intercept is formally at infinity, and consequently the Miller index is zero (the reciprocal of infinity).

2.3.1 X-ray Powder Diffraction

Powder diffraction is an extremely powerful technique for the characterization of polycrystalline materials which harnesses the scattering of X-rays by electrons bound to atoms.[12] Consider the diffraction from atoms on the set of lattice planes shown overleaf[13] (Figure 2.5).

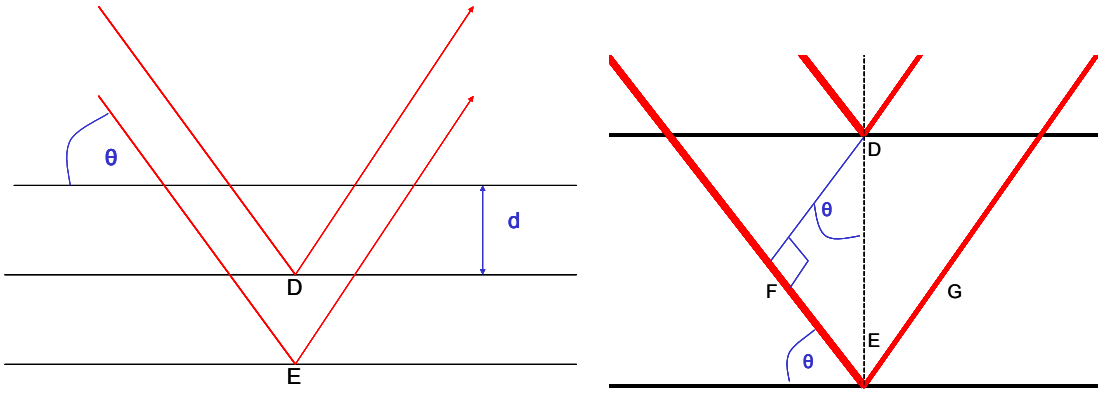

Figure 2.5 a) diffraction from atoms D and E on a set of lattice planes. b) illustration of the geometry used for the derivation of Bragg's law.

X-rays impinging on D and E are scattered in the same direction and thus superposition of the scattered waves occurs. The additional distance traveled by the X-ray impinging on and scattered by E (FE + EG) is referred to as the path difference, Δ. From Figure 2.5 it is clear that, geometrically:

$$\Delta = 2d_{hkl}\sin\theta \qquad (2.8)$$

where d_{hkl} is the separation of the lattice planes and θ is the angle between the incident beam and the family of lattice planes with indices *h ,k, l.* If Δ is an integral number of λ ($n = 0, \pm 1, \pm 2, \ldots$) the waves are in phase and interfere constructively. Thus interference maxima, observed as bright reflections, are observed when θ satisfies the Bragg equation:

$$n\lambda = 2d_{hkl}\sin\theta \qquad (2.9)$$

If the Δ is a non integral number of wavelengths, λ, ($n = \pm 1/2 , \pm 3/2 , \ldots$) the waves interfere destructively and the Bragg equation is not verified. In general *n* is always taken to be unity since a n^{th} order reflection from the family of lattice planes with indices *h ,k, l* can be interpreted as first order reflection from the family of lattice planes with indices *nh, nk, nl.*[10, 12, 14]

It is clear from rearrangement of Equation 2.9 that an indirect relationship exists between sinθ (which is indicative of the extent to which the diffracted beam deviates

from the direct beam) and the interplanar spacing $d_{hkl.}$ The interpretation of diffraction patterns is aided by replacing this with a direct relationship,[15] which is attained by constructing a reciprocal lattice. Vectors normal to the planes of the direct lattice radiate from some lattice point taken as the origin with each normal terminating at a point at a distance of $1/d_{hkl}$ from the origin, where d_{hkl} is the separation between the family of planes *(h k l)*. The resultant set of points comprises the reciprocal lattice. The following relationships exist between the reciprocal and real lattice parameters:[12]

$$a^* = bc\sin\alpha / V \qquad (2.10)$$

$$b^* = ac\sin\beta / V \qquad (2.11)$$

$$c^* = ab\sin\gamma / V \qquad (2.12)$$

$$\cos\alpha^* = (\cos\beta\cos\gamma - \cos\alpha) / \sin\beta\sin\gamma \qquad (2.13)$$

$$\cos\beta^* = (\cos\alpha\cos\gamma - \cos\beta) / \sin\alpha\sin\gamma \qquad (2.14)$$

$$\cos\gamma^* = (\cos\alpha\cos\beta - \cos\gamma) / \sin\alpha\sin\beta \qquad (2.15)$$

The Bragg equation is satisfied when the scattering vector $\mathbf{h = s - s_0}$ (which is determined by experimental geometry) equals a reciprocal lattice vector, which is dependent upon crystal orientation and lattice parameters. The Ewald sphere, a geometric construct, highlights the reciprocal lattice vectors which verify the Bragg equation (Figure 2.6, overleaf).

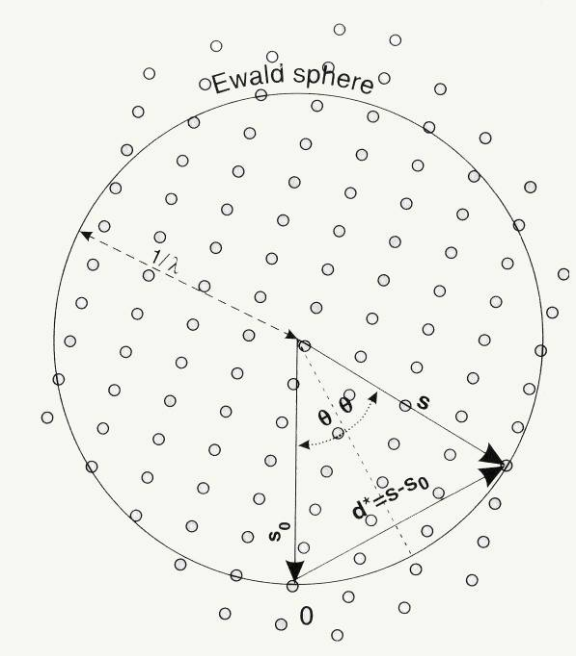

Figure 2.6 Geometrical construction of the Ewald sphere, with the origin of reciprocal space marked by "0". (*Taken from reference 12*).

Consider a beam of wavelength λ incident upon the origin of a reciprocal lattice, a sphere of radius 1/λ drawn through the origin will only intersect lattice points which correspond to the reflecting planes of a stationary structure. In single crystal diffraction different reciprocal lattice points are brought onto the surface of the Ewald sphere via reorientation of the crystal. In the case of powder diffraction each crystallite presents its own orientation of the reciprocal lattice and consequently each reciprocal lattice point is smeared onto a spherical shell on the surface of the Ewald sphere due to the averaging of crystallite orientation. The appearance of the resulting reciprocal lattice is that of a series of concentric shells as opposed to the distinct array of spots observed in single crystal diffraction.

2.3.2 The Rietveld Method

The fundamental difference between single crystal and powder diffraction methods is the loss of information, due to peak overlap, that occurs upon projection of the three-dimensional grid of lattice points on to the single dimension of a powder diffraction pattern.[16, 17] Peak overlap is exacerbated with increasing angle because the number of diffraction points varies as d^{*3}, where $d^* = 2\sin\theta / \lambda$. Thus extracting the

intensities of individual reflections, which are essential for structure determination, is problematic. The Rietveld method is a crystal structure refinement technique which minimises the detrimental effect of overlapping peaks. Rietveld recognized that a neutron powder diffraction pattern essentially consists of Gaussian peaks on top of a smooth background and that the following mathematical expression could be used to represent the observed intensity (Y_c) at each step of the diffraction pattern:

$$Y_c = Y_b + \Sigma Y_{\mathbf{h}} \qquad (2.16)$$

where Y_b is a background contribution and $Y_{\mathbf{h}}$ (are contributions from nearby steps). The powder diffraction pattern of a trial structure is calculated, taking into account various peak broadening effects, and compared with the experimental pattern. Structural model parameters such as unit cell, atomic positions and thermal displacement values are refined to minimize the residual

$$M = \Sigma w (Y_o - Y_c)^2 \qquad (2.17)$$

by least squares, where Y_o is the observed intensity, Y_c is the calculated profile intensity and w is a suitable weight which is calculated from the variance in Y_o. Agreement between the observations and models are estimated by the weighted profile (R_{wp}), expected (R_{exp}) and the reduced χ^2 (goodness of fit) indices:

$$R_{exp} = [(N- P) / (\Sigma wY^2_o)]^{1/2} \qquad (2.18)$$

$$R_{wp} = [M / \Sigma wY^2_o]^{1/2} \qquad (2.19)$$

$$\chi^2 = (R_{wp}/R_{exp}) \qquad (2.20)$$

where N is the number of profile points and P is the number of refined parameters.

The peak shapes observed in a powder diffraction pattern are dependent upon both the sample and the instrument. Accurate descriptions of these shapes are crucial for a successful Rietveld refinement. Peak shapes encountered in X-ray diffraction

studies are somewhat more complex than the Gaussian peak shapes characteristic of neutron data and subsequently alternative peak-shape functions are required. The Pseudo-Voigt approximation of the Voigt function – a linear combination of Lorentzian and Gaussian components in the ratio η / (1- η), where η is the pseudo-Voigt mixing parameter – is often used to provide a satisfactory description of X-ray diffraction peaks.[18] The pseudo-Voigt function is given as follows:

$$pV(x, \eta, W) = \eta\, L(x, W_L) + (1- \eta)G(x, W_G) \qquad (2.21)$$

where L and G are normalised Lorentzian and Gaussian functions respectively, while W_L and W_G are the full-width at half maxima (FWHM).[19] The FWHM of the Gaussian and Lorentzian components vary with scattering angle and are given as by Equations 2.22 and 2.23 respectively (U, V, W, X and Y are variable parameters in the profile refinement)[14].

$$W_G = (U \tan^2 \theta + V \tan \theta + W)^{1/2} \qquad (2.22)$$

$$W_L = X \tan \theta + Y/\cos \theta \qquad (2.23)$$

An infinite number of lattice planes exist in crystalline materials, each family of planes having a particular separation d_{hkl}, and consequently X-ray beams impinging on these materials scatter to produces a large number of reflections. The positions of these reflections are related to the X-ray wavelength, lattice parameters and Miller indices thus analysis of powder diffraction patterns provides a wealth of structural information. Consequently, the process of fitting structural models to X-ray powder diffraction data necessitates the use of crystallographic software packages. All analyses of the synchrotron X-ray diffraction profiles were performed with the Generalized Structure and Analysis Software (GSAS) suite of Rietveld analysis programs.[20]

2.3.3 Instrumentation

Preliminary powder diffraction data were collected from flat-plate mounted samples using a Bruker AXS D8 powder diffractometer in reflection mode. The X-rays are produced inside a sealed tube where a copper source is bombarded with high energy electrons, inducing multiple electronic transitions in the Cu atoms which are accompanied by the emission of X-rays. The resultant X-ray spectrum exhibits several sharp maxima which correspond to quantised electron transitions and are labelled according to the electron shells involved in producing the X-ray. The single X-ray wavelength required for diffraction experiments is selected by means of a Ge single crystal monochromator, orientated such that the $K\alpha_1$ (1.54056 Å) wavelength satisfies Bragg's Law and hence is the only wavelength diffracted. A position sensitive detector (PSD) enables rapid data acquisition.

High resolution powder diffraction data were collected on beam line ID31 at the European Synchrotron Radiation Facility, Grenoble. The high intensity and collimation of synchrotron radiation permits much higher 2θ resolution than can be achieved with laboratory X-ray sources. Furthermore, the wide continuous spectrum of synchrotron radiation permits selection an appropriate wavelength, e.g. for limiting radiation or observing X-ray induced phenomena. Synchrotron radiation is produced when charged particles moving at speeds close to the speed of light, *c*, (299792458 m s^{-1}) change velocity. At the ESRF this change in velocity is achieved by applying a magnetic field to electrons travelling at relativistic speed, forcing them to follow a curved trajectory. Electrons are discharged by an electron gun and accelerated to 6 GeV, first by a linear accelerator (linac) and then by a circular accelerator (booster synchrotron). The resultant high energy electrons are injected into the storage ring, which has a circumference of 844.4 m, and kept circulating under vacuum. The ring is comprised of alternating straight and curved sections. Electrons are guided from curved sections into straight sections by bending magnets, resulting in the emission of X-rays. The straight sections of the storage ring can also act as a source of X-rays. Arrays of magnets (known as insertion devices) produce alternating magnetic fields, causing the path of electrons to oscillate and emit synchrotron radiation. The X-ray source at beam line ID31 is an insertion device.

The X-rays produced at the ID31 beam line range from 5 to 60 keV. The beam is monochromated by a double-crystal monochromator with Si 111 crystals. Samples are loaded in glass capillaries and mounted on the diffractometer axis and spun to minimise preferred orientation. A bank of nine detectors is scanned vertically and the diffracted intensity measured as a function of 2θ (Figure 2.7).

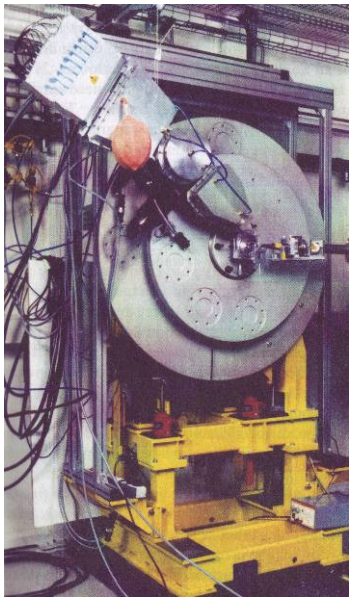

Figure 2.7 High resolution powder diffraction beam line ID31 at the ESRF *(taken from reference 12)*

Each detector is preceded by a Si 111 analyser crystal. Only radiation which impinges on the crystal with an angle satisfying the Bragg equation is reflected into the detector. A complete range of 2θ angles is measured by scanning the 2θ circle on which the analyser and detector are mounted.

2.4 X-ray Absorption Near Edge Structure (XANES)

X-ray absorption spectroscopy is a powerful means of investigating the short-range environment of an atomic species.[21] The energy of a monochromatic X-ray impinging onto a sample is scanned to the desired absorption 'edge' of the chosen element. Below the absorption edge the energy of the photons cannot excite the electrons of the desired atomic level and absorption is low. However, when the photon energy becomes sufficient to excite these electrons a large increase in

absorption, known as the absorption edge, occurs and a core level photoelectron is generated. This photoelectron is scattered by the surrounding matter producing interference effects visible in the absorption cross-section. At X-ray energies just sufficient to excite a core level the resultant photoelectron leaps into unoccupied states; this is the region that is explored by X-ray absorption near edge structure (XANES) spectroscopy. The near-edge structure region corresponds to an energy approximately 50 eV above the edge.[22] The absolute position of the edge contains information about the oxidation state of the absorbing atom.

2.5 X-ray Photoelectron Spectroscopy (XPS)

X-ray photoelectron spectroscopy (XPS) is based upon the photoelectric effect. A monochromatic beam of X-rays impinging on a powdered PBA sample may induce electron emission from the core level of a transition metal ion provided that the photon energy ($h\nu$) exceeds the work function (Φ). The work function is characteristic of the transition metal and is defined as the energy required for removal an electron from the metal to infinity.[13] The kinetic energies (E_K) of the emitted photoelectrons are determined using Einsten's photoelectric equation:

$$E_K = h\nu - \Phi \qquad (2.24)$$

Since the photon energy is fixed the E_K of the photoelectron is diagnostic of the metal. Atoms with a high oxidation state give XPS peaks with high binding energy relative to the same atom in a low oxidation state.[23] The increase in positive charge leads to a shift of the core levels to higher binding energies due to the increased Coulombic attraction between the core electrons and the nucleus. The precise binding energy of the core level is also highly dependent upon the species to which it is bonded. Thus X-ray photoelectron spectroscopy (XPS) is a useful probe of the chemical environment and oxidation states of transition metal ions in PBAs.

2.6 Transmission Electron Microscopy (TEM)

Transmission electron microscopy (TEM) is an extremely powerful means of studying the internal structure of solids at the atomic scale. Electron wavelengths are in the range of 0.001 and 0.01 nm, many magnitudes smaller than those of visible light (400 – 700 nm). Consequently electron microscopes are capable of imaging at higher resolution than light microscopes since resolving power (r) is directly related to the wavelength (λ) of the impinging radiation, as shown by:

$$r_1 = \frac{0.61\lambda}{NA} \qquad (2.25)$$

where NA is the numerical aperture.[24] A beam of electrons passing through a solid specimen in a transmission electron microscope will interact with the sample and may be elastically or inelastically scattered. By measuring the phase and amplitude of the modified beam of the electrons it is possible to gather information about the about the specimen's structure.[25]

2.6.1 Instrumentation

The Jeol JEM 2011, a high resolution TEM (HRTEM) with a resolution of 0.18 nm and a magnification up to 1 200 000 x, employs a LaB_6 filament as an electron source. The filament is heated by the passage of current resulting in the thermionic emission of electrons. The emitted electrons are accelerated through a potential difference (80 – 200 kV) by an electric potential and focused towards the specimen by electromagnetic lenses. The initial image produced by the first of the magnifying lenses, the objective lens, is magnified 50 - 100 times. This is further magnified by a series of intermediate and projector lenses before being projected onto a fluorescent screen which is viewed through a lead glass window. The optical paths of the TEM must be evacuated to low pressures to prevent the scattering of electrons by gas molecules. Specimens are dispersed in solvent and deposited onto 3 mm copper grids for TEM imaging. An ultra thin specimen is imperative for the transmission of electrons.

2.7 Elemental Analysis

The stoichiometries of all compounds were established by a combination of CHN analysis and inductively coupled plasma (ICP) spectrometry techniques. Multimetal optical emission spectrometry (ICP-OES) analyses were performed using a Perkin Elmer Optima 5300 DV ICP-OES while inductively coupled plasma mass spectrometry (ICP-MS) analyses were performed on an Agilent 7500ce ICP-MS. Analysis by ICP spectrometry necessitates that samples are completely dissolved into solution. This was achieved by nitric acid digestion and subsequent dilution with H_2O. Carbon, hydrogen, and nitrogen fractions were determined via combustion of solid samples using a Carlo Erba CHNS analyser.

2.8 Bibliography

1. L. Smart and E. Moore, *Solid state chemistry: an introduction*, Chapman & Hall, London, 1995.
2. J. S. Miller and M. Drillon, *Magnetism: molecules to materials*, Weinheim ; [Great Britain] : Wiley-VCH, 2001.
3. R. L. Carlin, *Magnetochemistry*, Springer, Berlin, 1986.
4. M. McElfresh, Purdue University, Quantum Design Inc., 1994.
5. J. Clarke, *Scientific American*, 1994, **271**, 46-53.
6. R. Kleiner, D. Koelle, F. Ludwig and J. Clarke, *Proceedings of the IEEE*, 2004, **92**, 1534-1548.
7. J. Lenz and A. S. Edelstein, *IEEE Sens J*, 2006, **6**, 631-649.
8. K. Murata, H. Yoshino, H. O. Yadav, Y. Honda and N. Shirakawa, *Review of Scientific Instruments*, 1997, **68**, 2490-2493.
9. A. Eiling and J. S. Schilling, *Journal of Physics F-Metal Physics*, 1981, **11**, 623-639.
10. M. T. Weller, *Inorganic materials chemistry*, Oxford University Press, Oxford, 1994.
11. M. Pitteri and G. Zanzotto, *Acta Crystallogr A*, 1996, **52**, 830-838.
12. R. E. Dinnebier and S. J. L. Billinge, *Powder diffraction: theory and practice*, Royal Society of Chemistry, Cambridge, 2008.
13. P. W. Atkins, *Physical chemistry*, Oxford University Press, Oxford, 1998.
14. C. Giacovazzo, *Fundamentals of crystallography*, International Union of Crystallography [and] Oxford University Press, Oxford, 1992.
15. G. H. Stout and L. H. Jensen, *X-ray structure determination: a practical guide*, Wiley, New York, 1989.
16. W. I. F. David, *Structure determination from powder diffraction data*, Oxford University Press, Oxford, 2002.
17. H. M. Rietveld, *J Appl Crystallogr*, 1969, **2**, 65-71.
18. L. B. McCusker, R. B. Von Dreele, D. E. Cox, D. Louer and P. Scardi, *J Appl Crystallogr*, 1999, **32**, 36-50.
19. W. David, *J Appl Crystallogr*, 1986, **19**, 63-64.
20. A. C. Larson and R. B. V. Dreele, Los Alamos National Laboratory Report, LAUR , 86-748 , 2004.
21. A. Filipponi, M. Borowski, D. T. Bowron, S. Ansell, A. Di Cicco, S. De Panfilis and J. P. Itie, *Review of Scientific Instruments*, 2000, **71**, 2422-2432.

22. D. C. Koningsberger and R. Prins, *X-ray absorption: principles, applications, techniques of exafs, sexafs and xanes*, Wiley, New York, 1988.

23. G. Attard and C. Barnes, *Surfaces*, Oxford University Press, Oxford, 1998.

24. P. J. Goodhew, R. Beanland and F. J. Humphreys, *Electron microscopy and analysis*, Taylor & Francis, London, 2001.

25. DoITPoMS (Dissemination of IT for the promotion of Materials Science) Teaching and Learning Packages, http://www.msm.cam.ac.uk/doitpoms/tlplib/index.php, Accessed 03/01/09, 2009.

26. W. E. Buschmann, J. Ensling, P. Gutlich and J. S. Miller, *Chem-Eur J*, 1999, **5**, 3019-3028.

Chapter 3

Chemical, Thermal, Photo & Piezo Control in a New Family of Prussian Blue Analogue Mixed Ferro-ferrimagnets

3.1 Introduction

Rubidium manganese hexacyanoferrates are amongst some of the most extensively studied Prussian Blue analogue systems. A multitude of intriguing electronic and magnetic functionalities have been observed within this family of PBAs, many of which are derived from the inherent bistability of these systems. The rubidium manganese hexacyanoferrates first attracted attention when stoichiometric $Rb^{I}Mn^{II}[Fe^{III}(CN)_6]$ was reported as the first octahedrally coordinated Mn^{II} complex to under go a spin transition.[1] The temperature dependence of $\chi_m T$ reveals a sharp decrease at 231 K upon cooling and abrupt increase at 304 K upon warming, that is, a large thermal hysteresis is observed. X-ray absorption and emission spectroscopies (XAS and XES) confirm that these thermal variations are driven by a reversible internal charge transfer between the Mn^{II} and Fe^{III} ions and a corresponding interconversion between high-spin and low-spin Mn: Mn^{II}(S = 5/2)-NC-Fe^{III}(S = 1/2) [high-temperature (HT) phase] to Mn^{III}(S = 2)-NC-Fe^{II}(S = 0) [low-temperature (LT) phase].[2] The thermally driven electron transfer from Mn^{II} to Fe^{III} is accompanied by a structural transition from cubic ($F\bar{4}3m$) to tetragonal ($I\bar{4}m2$) which arises from the Jahn-Teller distortion of the resultant $Mn^{III}N_6$ octahedra.[3] The LT phase of $RbMn[Fe(CN)_6]$ exhibits spontaneous magnetization below 11.3 K. Specific heat measurements confirm that this magnetic ordering is a consequence of long range coupling between the Mn^{III} sites due to a partial delocalization of the electrons occupying the Fe^{II} t_{2g} orbitals to the neighbouring high-spin Fe^{III} sites - analogous to the ferromagnetic ordering of Prussian Blue ($Fe^{III}_4[Fe^{II}(CN)_6]_3$).[4]

Light has proven a powerful means of reversing the thermally driven phase transitions of rubidium manganese hexacyanoferrates. For example, the spontaneous magnetization of the LT phase of $RbMn[Fe(CN)_6]$ can be completely quenched via

visible light irradiation (650 nm).[5] X-ray absorption studies reveal that the photoinduced phase is structurally and electronically identical to the HT phase and that the LT phase is recoverable after irradiation. Analogous demagnetization effects are observed upon laser irradiation (532 nm) of the LT phases of $Rb_{0.91}Mn_{1.05}[Fe(CN)_6]\cdot 0.6H_2O$ and $Rb_{0.88}Mn[Fe(CN)_6]_{0.96}\cdot 0.5H_2O$ at 3 K.[6, 7] The photomagnetism of $Rb_{0.88}Mn[Fe(CN)_6]_{0.96}\cdot 0.5H_2O$ can be reversibly switched between ferromagnetic and antiferromagnetic states by alternate irradiation with 532 and 410 nm radiation. Such photoinduced demagnetization effects are not limited to sub liquid helium temperatures; $Rb_{0.98}Mn_{1.01}[Fe(CN)_6]\cdot 0.2H_2O$ can be switched from the LT to HT phase at 295 K (inside the thermal hysteresis loop) with a one-shot laser pulse (532 nm).[8]

Thermal hysteresis loops of varying widths are observed within the $Rb^{I}Mn^{II}[Fe^{III}(CN)_6]$ family. These variations are attributed to differences in the precise stoichiometry of the rubidium manganese hexacyanoferrates.[9] The water content of a rubidium manganese hexacyanoferrate varies directly with the extent to which it deviates from the ideal Rb:Mn:Fe stoichiometry of 1:1:1. Water molecules occupy the $Fe(CN)_6$ vacancies, giving rise to $Mn(NC)_{6-a}(H_2O)_a$ moieties. Replacement of the relatively strong N-donating cyano ligands with weaker aqua donors brings about a reduction in the ligand field strength and consequently the redox potential of the Mn moiety is considerably altered. Thus significant deviation from the ideal Rb:Mn:Fe ratio of 1:1:1 may preclude the observation of metal-to-metal charge transfer processes, as illustrated by $Rb_{0.59}Mn[Fe(CN)_6]_{0.86}\cdot 2.63H_2O$ which fails to exhibit the thermal hysteresis loop associated with the charge driven interconversion between high- and low-temperature configurations.

Ohkoshi et al recently utilized blue light irradiation to stimulate Mn^{II}(S = 5/2)-NC-Fe^{III}(S = 1/2) to Mn^{III}(S = 2)-NC-Fe^{II}(S = 0) intercoversion in $Rb_{0.43}Mn^{II}[Fe^{III}(CN_6)]_{0.81}\cdot 3H_2O$, a rubidium manganese hexacyanoferrate in which the Mn^{II}–Fe^{III} "high temperature" phase is maintained from 320 K down to 20 K.[10] Previously, photoinduced phase transition phenomena had only been observed in materials which also undergo a thermal phase transition. Blue light irradiation of $Rb_{0.43}Mn^{II}[Fe^{III}(CN_6)]_{0.81}\cdot 3H_2O$ in the 100 to 200 K temperature range triggers a

sudden collapse from the initial thermodynamically metastable Mn^{II}–Fe^{III} phase into the photo-generated Mn^{III}–Fe^{II} phase – a hidden stable phase. This material holds promise for the development of optical memory devices based on blue laser irradiation.

Pressure may also prove an effective means of modulating structural and magnetic properties of the rubidium manganese hexacyanoferrates, with $RbMn[Fe(CN)_6]$ having been shown to transform to a metastable phase upon the application of 2 GPa at room temperature.[11]

Herein the synthesis and characterization of a novel series of closely related $Rb_xA^{II}_zMn_{(1-z)}[Fe(CN)_6]\cdot yH_2O$ (where A^{II} = Ni^{II} and/or Fe^{II}) mixed ferro-ferrimagnets is described.

3.2 Chemical Modification

In addition to the methods outlined in the previous section, the fine tuning of Prussian Blue analogue properties may also be achieved via subtle chemical modifications. Ohkoshi et al successfully used this approach to design the novel $(Ni^{II}_{b}Mn^{II}_{c})_{1.5}[Cr(CN)_6]\cdot zH_2O$[12] and $(Fe^{II}_{a}Ni^{II}_{b}Mn^{II}_{c})_{1.5}[Cr(CN)_6]\cdot zH_2O$[13] ($a + b + c = 1$) families of mixed ferro-ferrimagnets. Mixed ferro-ferrimagnetic PBAs incorporate two or more different transition metal M^{II} ions (or sublattices) with opposing spin alignments, giving rise to the coexistence of ferromagnetic and antiferromagnetic exchange interactions with the M'^{III} ion. The spontaneous magnetization of such a PBA below T_N is the sum of the magnetic contributions from each of its constituent sublattices. While the magnetization curves of ferromagnets usually increase monotonically with decreasing temperature,[14] anomalous thermomagnetic behaviour arises in ferrimagnets and mixed ferro-ferrimagnets due to differences in the thermodynamics of the constituent antiparallel sublattices. Thus a variety of thermomagnetic behaviours may be accessed via subtle changes in stoichiometry. These thermomagnetic behaviours, and a number of other magnetic properties, are accurately predicted by molecular field theory - a fact which is well illustrated by studies of the $(Ni^{II}_{b}Mn^{II}_{c})_{1.5}[Cr(CN)_6]\cdot zH_2O$ and $(Fe^{II}_{a}Ni^{II}_{b}Mn^{II}_{c})_{1.5}[Cr(CN)_6]\cdot zH_2O$ series.

The temperature-dependent spontaneous magnetization of a PBA mixed ferro-ferrimagnet may be designated Q-, R-, P- or N-type, according to Néel's system of classification for ferrimagnetic materials (Figure 3.1 overleaf).[15] Those magnetizations which decrease monotonically as the temperature is raised above 0 K may be classified as Q-type if a sharp decline occurs only in the vicinity of the magnetic ordering temperature; or R-type if a rapid drop in magnetization has already occurred in the temperature region intermediate between 0 K and T_C. Thermomagnetic curves displaying a single maximum are defined as P-type, while those exhibiting a point of zero overall magnetization accompanied by either a magnetic pole inversion or 2 maxima are labelled N-type. The point at which sublattice magnetizations cancel to give zero overall magnetization is known as the

compensation temperature, T_{comp}. More complex temperature dependencies may be observed for mixed ferro-ferrimagnets comprising more than two sublattices, e.g. multiple compensation temperatures.

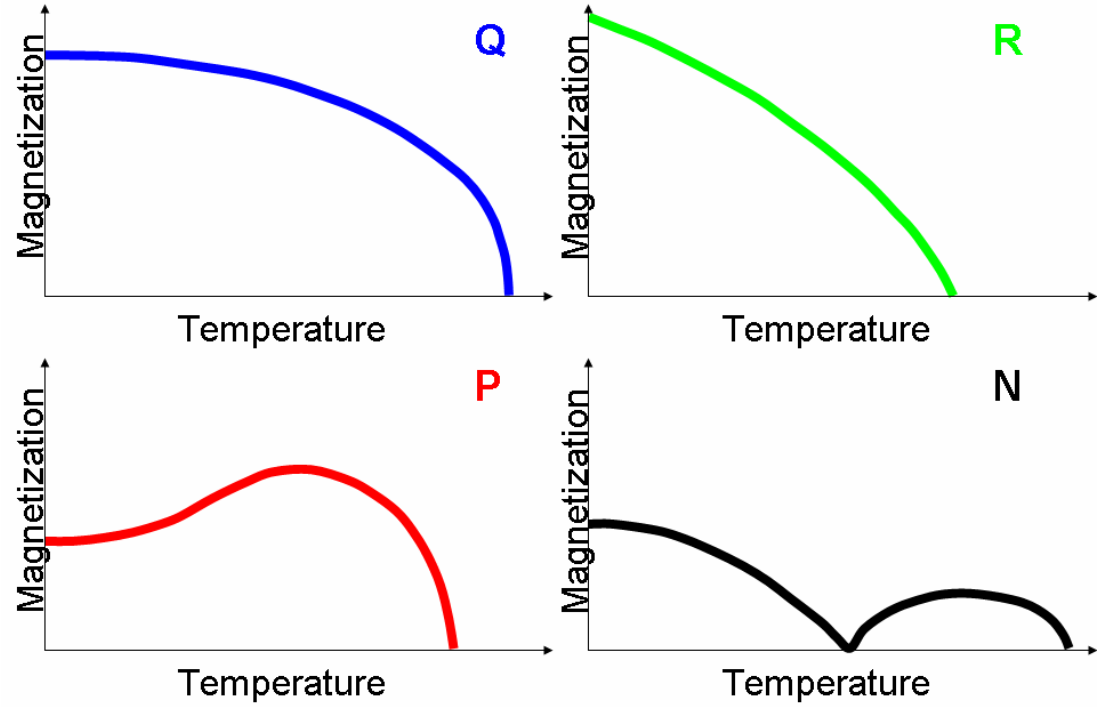

Figure 3.1 The principal types of temperature-dependent spontaneous magnetization exhibited by PBA mixed ferro-ferrimagnets

Within the $(Ni^{II}_{b}Mn^{II}_{c})_{1.5}[Cr(CN)_6]\cdot zH_2O$ and $(Fe^{II}_{a}Ni^{II}_{b}Mn^{II}_{c})_{1.5}[Cr(CN)_6]\cdot zH_2O$ series of mixed ferro-ferrimagnets, all four types of thermomagnetic behaviour predicted by Néel are observed. The various thermomagnetic behaviours observed as M^{II} site of $Mn_{1.5}[Cr(CN)_6]$ is progressively doped with Ni^{II} and Fe^{II} ions closely follow those predicted by molecular field theory. Take for example the $(Ni^{II}_{b}Mn^{II}_{c})_{1.5}[Cr(CN)_6]\cdot zH_2O$ series, the molecular fields H_{Ni}, H_{Mn} and H_{Cr} acting upon the three sublattice sites in this family of compounds are as follows:[16, 17]

$$H_{Ni} = H_0 + n_{Ni\text{-}Cr}M_{Cr} \qquad (3.1)$$

$$H_{Mn} = H_0 + n_{Mn\text{-}Cr}M_{Cr} \qquad (3.2)$$

$$H_{Cr} = H_0 + n_{Cr\text{-}Ni}M_{Ni} + n_{Cr\text{-}Mn}M_{Mn} \qquad (3.3)$$

where H_0 is the external magnetic field, the n_{ij} values are molecular field coefficients, while M_{Ni}, M_{Mn} and M_{Cr} are the sublattice magnetizations per unit volume for the Ni, Mn and Cr sites respectively. Molecular field coefficients are derived from the exchange coefficients J_{ij} using the following equation:

$$n_{ij} = 2Z_{ij}J_{ij} / \lambda_j N(g\mu_B)^2 \qquad (3.4)$$

where μ_B is the Bohr magneton, Z_{ij} are the numbers of the nearest neighbour j-site ions surrounding i-site ions, g is the g factor, N is the total number of all types of metal ions per unit volume, and λ_j is the mole fraction for each metal ion per unit volume. The J_{ij} values are derived from the magnetic ordering temperatures of the end members of the $(Ni^{II}_bMn^{II}_c)_{1.5}[Cr(CN)_6]\cdot zH_2O$ series, $Ni_{1.5}[Cr(CN)_6]\cdot zH_2O$ and $Mn_{1.5}[Cr(CN)_6]\cdot zH_2O$. Sublattice magnetizations are determined from:

$$M_i = \lambda_i N g \mu_B \langle S_i \rangle \qquad (3.5)$$

where $\langle S_i \rangle$ parameters are the thermally averaged values of the Mn, Ni and Cr spins in their respective sites in the direction of each sublattice magnetization. The $\langle S_i \rangle$ value is calculated by setting $H_0 = 0$:

$$\langle S_i \rangle = S_{i_0} B_{S_i} (g\mu_B H_i S_{i_0} / k_B T) \qquad (3.6)$$

where B_{S_i} is the Brillouin function, S_{i_0} is the value of $\langle S_i \rangle$ at T = 0 K and k_B is the Boltzmann constant. Substitution of Equations 3.4 and 3.5 into Equations 3.1-3.3 gives:

$$H_{Ni} = H_0 + (2\, Z_{Ni\text{-}Cr}\, J_{Ni\text{-}Cr}\, \langle S_{Cr} \rangle) / g\mu_B \qquad (3.7)$$

$$H_{Mn} = H_0 + (2\, Z_{Mn\text{-}Cr}\, J_{Mn\text{-}Cr}\, \langle S_{Cr} \rangle) / g\mu_B \qquad (3.8)$$

$$H_{Cr} = H_0 + (2\, Z_{Cr\text{-}Ni}\, x\, J_{Cr\text{-}Ni}\, \langle S_{Ni} \rangle) / g\mu_B + (2\, Z_{Cr\text{-}Mn}\, (1\text{-}x)\, J_{Cr\text{-}Ni}\, \langle S_{Ni} \rangle) / g\mu_B \qquad (3.9)$$

Thus the total magnetization at any particular temperature can be derived from the following equation:

$$M_{total} = M_{Ni} - M_{Mn} + M_{Cr} \qquad (3.10)$$

The theoretical magnetic ordering temperatures (T_C or T_N) of these ternary PBAs are given by:

$$T_C = \sqrt{1.5 S_{Cr}(S_{Cr}+1)\left\{ x S_{Fe}(S_{Fe}+1) n_{FeCr}{}^2 + (1-x) S_{Mn}(S_{Mn}+1) n_{MnCr}{}^2 \right\}} \qquad (3.11)$$

Combining molecular field theory with chemical modifications has proven an extremely powerful strategy for the design of new PBAs exhibiting novel functionalities, as illustrated by the $(Ni^{II}_bMn^{II}_c)_{1.5}[Cr(CN)_6]\cdot zH_2O$ and $(Fe^{II}_aNi^{II}_bMn^{II}_c)_{1.5}[Cr(CN)_6]\cdot zH_2O$ series. Take for example, $(Ni^{II}_{0.22}Mn^{II}_{0.60}Fe^{II}_{0.18})_{1.5}[Cr^{III}CN_6]\cdot 7.6H_2O$, the first PBA to exhibit two compensation temperatures. Molecular field theory was employed to calculate the ratio of M^{II} site ions and balance of ferromagnetic and antiferromagnetic interactions necessary for observation of this unusual phenomenon. Similarly, the first PBA to exhibit a photoinduced magnetic pole inversion, $(Fe^{II}_{0.40}Mn^{II}_{0.60})_{1.5}[Cr^{III}(CN)_6]\cdot 7.5H_2O$,[18] was derived from the $(Ni^{II}_bMn^{II}_c)_{1.5}[Cr(CN)_6]\cdot zH_2O$ series which was designed on the basis of molecular field theory, as outlined above.

The following section details the synthesis of the $Rb_xA^{II}_zMn_{(1-z)}[Fe(CN)_6]\cdot yH_2O$ (where $A^{II} = Ni^{II}$ and/or Fe^{II}) series, which follows a chemical modification approach analogous to that employed by Ohkoshi et al. Progressive doping of $RbMn[Fe(CN)_6]$ with Ni^{II} and/or Fe^{II}, and subsequent tuning of the competing ferromagnetic and

antiferromagnetic interactions, produces a novel series of mixed ferro-ferrimagnets exhibiting a variety of magnetic behaviours. Study of this series provides the opportunity to determine the influence of dopant ions on the thermo- and photo-induced charge transfer processes that have been reported for the parent $RbMn^{II}[Fe^{III}(CN)_6]$ systems.

3.2.1 Experimental

Members of the $Rb_xNi^{II}_zMn_{(1-z)}[Fe(CN)_6]\cdot yH_2O$ series were synthesised according to the following general procedure. A mixed aqueous solution (10 ml) comprising RbCl (1 M), $MnCl_2$ and $NiCl_2\cdot 6H_2O$ (where $[Ni^{II}] + [Mn^{II}] = 0.1$ M) was added dropwise - via a burette - to a beaker containing aqueous $K_3[Fe(CN)_6]$ (0.1 M, 10 ml). The temperature of the latter was maintained at 5°C using an ice bath, as was that of the subsequent reaction solution. Addition took place over approximately 40 minutes, with mechanical stirring throughout. The resultant precipitate was recovered by filtration and washed with several portions of de-ionised H_2O to remove excess RbCl. Preparation of $Fe_{0.12}Ni_{0.28}Mn[Fe(CN)_6]\cdot 1.94H_2O$ followed a method similar to that outlined above. However, in this instance the mixed aqueous solution comprised RbCl (1 M), $MnCl_2$, $NiCl_2\cdot 6H_2O$ and $FeCl_2\cdot 4H_2O$, with $[Fe^{II}] + [Ni^{II}] + [Mn^{II}] = 0.1$ M.

3.2.2 Results

3.2.2.1 Structural Characterization

Nominal compositions, actual stoichiometries and cubic lattice parameters for members of the $Rb_xNi^{II}_zMn_{(1-z)}[Fe(CN)_6]\cdot yH_2O$ series are shown in Table 3.1.

Table 3.1 Compositions and lattice constants of $Rb_xNi^{II}_zMn_{(1-z)}[Fe(CN)_6]\cdot yH_2O$ series

Sample	Nominal z	Observed Composition	a (Å)
1	0.1	$Rb_{0.59}Ni_{0.13}Mn_{0.97}[Fe(CN)_6]\cdot 1.72H_2O$	10.4955(1)
2	0.2	$Rb_{0.78}Ni_{0.23}Mn_{0.88}[Fe(CN)_6]\cdot 1.46H_2O$	10.4666(1)
3	0.25	$Rb_{0.64}Ni_{0.31}Mn_{0.87}[Fe(CN)_6]\cdot 2.8H_2O$	10.4538(3)
4	0.3	$Rb_{0.54}Ni_{0.34}Mn_{0.75}[Fe(CN)_6]\cdot 3.28H_2O$	10.4365(2)
5	0.4	$Rb_{0.64}Ni_{0.45}Mn_{0.66}[Fe(CN)_6]\cdot 2.33H_2O$	10.4038(2)
6	0.5	$Rb_{0.67}Ni_{0.52}Mn_{0.53}[Fe(CN)_6]\cdot 2.22H_2O$	10.3706(3)
7	0.6	$Rb_{0.64}Ni_{0.62}Mn_{0.42}[Fe(CN)_6]\cdot 2.56H_2O$	10.3518(4)
8	1	$Rb_{0.65}Ni_{1.06}[Fe(CN)_6]\cdot 3.13H_2O$	10.2589(3)

The results of elemental analysis reveal relatively good agreement between nominal and actual Ni content. Infrared spectra of samples 1-8, were recorded as Nujol mulls and examined in the CN stretching frequency region (2000-2300 cm^{-1}). All exhibit a sharp, intense absorption around 2150 cm^{-1} together with a relatively broad band composed of two absorptions around 2100 cm^{-1} and 2075 cm^{-1} (see Appendix 1). Absorptions at ca. 2150 cm^{-1} correspond to CN stretching of the Fe^{III}-CN-$Mn^{II}(Ni^{II})$ linkages; while those around 2100 cm^{-1} and 2075 cm^{-1} are attributed to CN stretching of Fe^{II}-CN-Mn^{III} linkages.

Synchrotron X-ray powder diffraction profiles were collected on beamline ID31 at the European Synchrotron Radiation Facility (ESRF), Grenoble, France. Rietveld refinement of all room temperature data shows that the lattice parameters of the $Rb_xNi^{II}_zMn_{(1-z)}[Fe(CN)_6]\cdot yH_2O$ series vary linearly as a function of Ni content, with lattice parameters ranging from a = 10.4955(1) Å for **1** down to a =10.2589(3) Å for the manganese-free end member **8** (Figure 3.2).

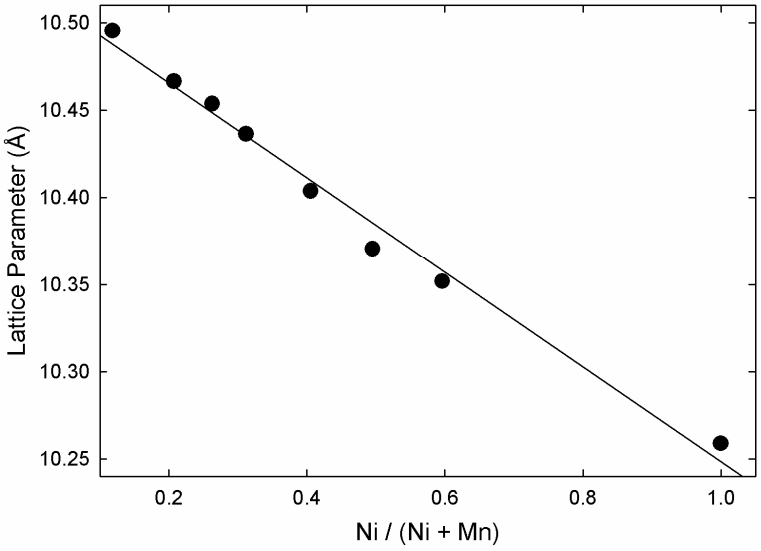

Figure 3.2 Lattice constants of $Rb_xNi^{II}_zMn_{(1-z)}[Fe(CN)_6]\cdot yH_2O$ series as a function of nickel content. The error bars, being significantly smaller, are hidden by the data markers.

All members of the series adopt face-centred cubic structures and remain strictly cubic upon cooling to 10 K. The powder diffraction data of **1** collected at 295 K necessitate that individual Rietveld refinements are performed for each detector because, although the structure remains cubic, the peak positions rapidly shift to higher angles (that is within the duration of a single scan) with increasing irradiation time. Similarly, the powder diffraction pattern of **2** at 295 K necessitates a two phase Rietveld refinement because there is a very gradual shift of diffraction peaks to higher angles within the scan period. Rietveld refinements for all other members of the series employed a single cubic phase. The Rietveld refinements of **2, 3, 5** and **6** at 295 K, shown overleaf (Figures 3.3 to 3.6), illustrate peak broadening associated with increasing nickel fraction.

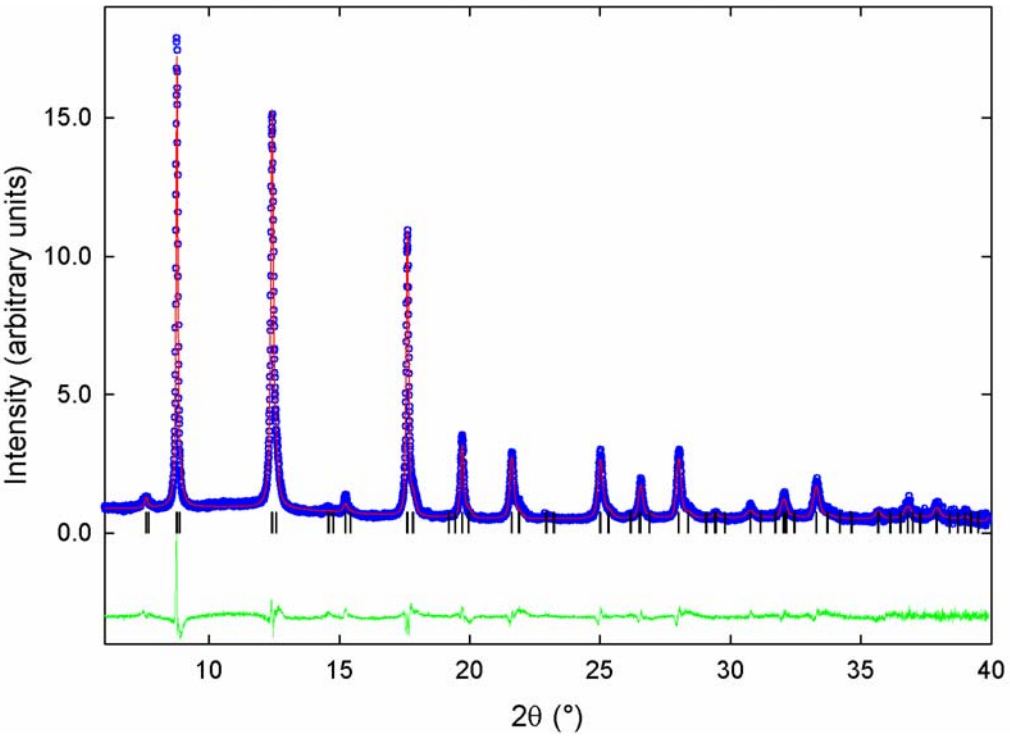

.

Figure 3.3 Final observed (blue circles), calculated (red solid line), and difference (lower green solid line) plots for the two -phase Rietveld refinement of **2** at 295 K. Tick marks show the reflection positions for both phases. The refinement was performed with both phases in the $Fm\bar{3}m$ space group. The refined lattice constant of the majority phase (88%) is a = 10.4666(1) Å and of the minority phase (12%) is a = 10.337(1) Å. The agreement factors are R_1 = 4.78 %, R_{wp} = 6.31 %, R_{exp} = 1.91 %. The X-ray wavelength is 0.8016 Å.

Table 3.2 Refined structure parameters of the major (a) and minor (b) phases of **2** at 295K. Estimated errors in the last digits are given in parentheses.

a) Major Phase

	n	x	y	z	Wyckoff Position	B_{iso} (Å^2)
Fe	0.893(6)	0	0	0	4a	1.22(5)
Ni	0.2072	1/2	1/2	1/2	4b	1.22(5)
Mn	0.7928	1/2	1/2	1/2	4b	1.22(5)
Rb	0.311(1)	1/4	1/4	1/4	8c	9.0(2)
C	0.893(6)	0.1695(6)	0	0	24e	4.1(1)
N	0.893(6)	0.2795(6)	0	0	24e	4.1(1)
O1	0.107(6)	0.190(3)	0	0	24e	4.1(1)
O2	0.122(2)	0.215(1)	0.215(1)	0.215(1)	32f	17(2)

b) Minor Phase

	n	x	y	z	Wyckoff Position	B_{iso} (Å^2)
Fe	0.893(6)	0	0	0	4a	1.22(5)
Ni	0.2072	1/2	1/2	1/2	4b	1.22(5)
Mn	0.7928	1/2	1/2	1/2	4b	1.22(5)
Rb	0.311(1)	1/4	1/4	1/4	8c	9.0(2)
C	0.893(6)	0.189(2)	0	0	24e	4.1(1)
N	0.893(6)	0.290(2)	0	0	24e	4.1(1)
O1	0.107(6)	0.19(2)	0	0	24e	4.1(1)
O2	0.122(2)	0.202(5)	0.202(5)	0.202(5)	32f	17(2)

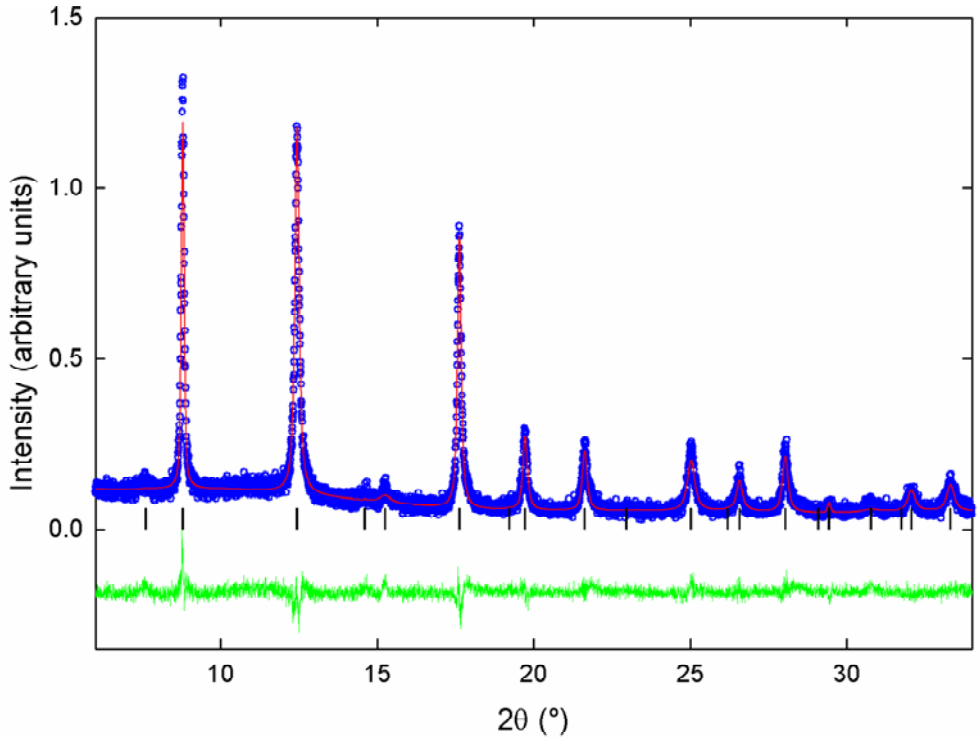

Figure 3.4 Final observed (blue circles), calculated (red solid line), and difference (lower green solid line) plots for the single-phase Rietveld refinement of **3** at 295 K. Tick marks show the reflection positions. The refinement was performed using the $Fm\bar{3}m$ space group. Refined lattice constant is *a* = 10.4538(3) Å. The agreement factors are R_1 = 5.75 %, R_{wp} =8.93 %, R_{exp} = 3.01 %. The X-ray wavelength is 0.8010 Å.

Table3.3 Refined structure parameters of **3**. Estimated errors in the last digits are given in parentheses.

	n	x	y	z	Wyckoff Position	B_{iso} (Å^2)
Fe	0.90(1)	0	0	0	4a	1.29(7)
Ni	0.263	1/2	1/2	1/2	4b	1.29(7)
Mn	0.737	1/2	1/2	1/2	4b	1.29(7)
Rb	0.292(1)	1/4	1/4	1/4	8c	11.7(3)
C	0.90(1)	0.183(1)	0	0	24e	2.7(2)
N	0.90(1)	0.290 (1)	0	0	24e	2.7(2)
O1	0.10(1)	0.206(3)	0	0	24e	2.7(2)
O2	0.287(3)	0.228(1)	0.228(1)	0.228(1)	32f	14.2(5)

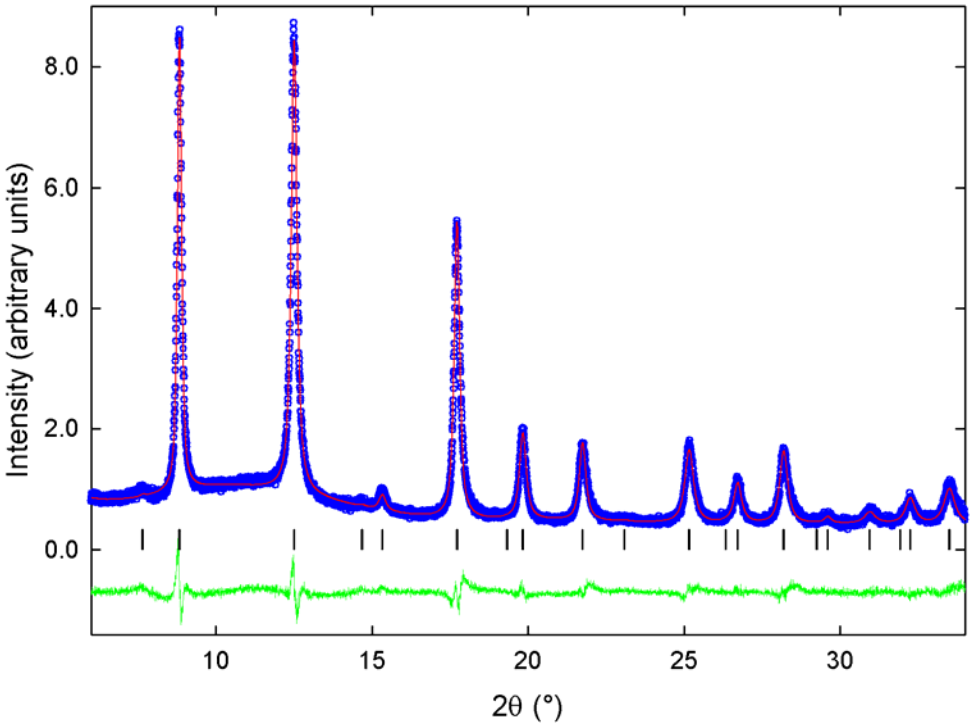

Figure 3.5 Final observed (blue circles), calculated (red solid line), and difference (lower green solid line) plots for the single-phase Rietveld refinement of **5** at 295 K. Tick marks show the reflection positions. The refinement was performed using the $Fm\bar{3}m$ space group. The refined lattice constant is a = 10.4038(2) Å. The agreement factors are R_I = 4.78 %, R_{wp} = 6.31 %, R_{exp} = 1.91 %. The X-ray wavelength is 0.8016 Å.

Table 3.4 Refined structure parameters of **5**. Estimated errors in the last digits are given in brackets.

	n	x	y	z	Wyckoff Position	B_{iso} (Å^2)
Fe	0.896(5)	0	0	0	4a	1.37(3)
Ni	0.405	1/2	1/2	1/2	4b	1.37(3)
Mn	0.595	1/2	1/2	1/2	4b	1.37(3)
Rb	0.286(1)	1/4	1/4	1/4	8c	7.52(10)
C	0.896(5)	0.1821(8)	0	0	24e	3.00(8)
N	0.896(5)	0.2914(7)	0	0	24e	3.00(8)
O1	0.104(5)	0.187(2)	0	0	24e	3.00(8)
O2	0.205(2)	0.1982(4)	0.1982(4)	0.1982(4)	32f	16.1(6)

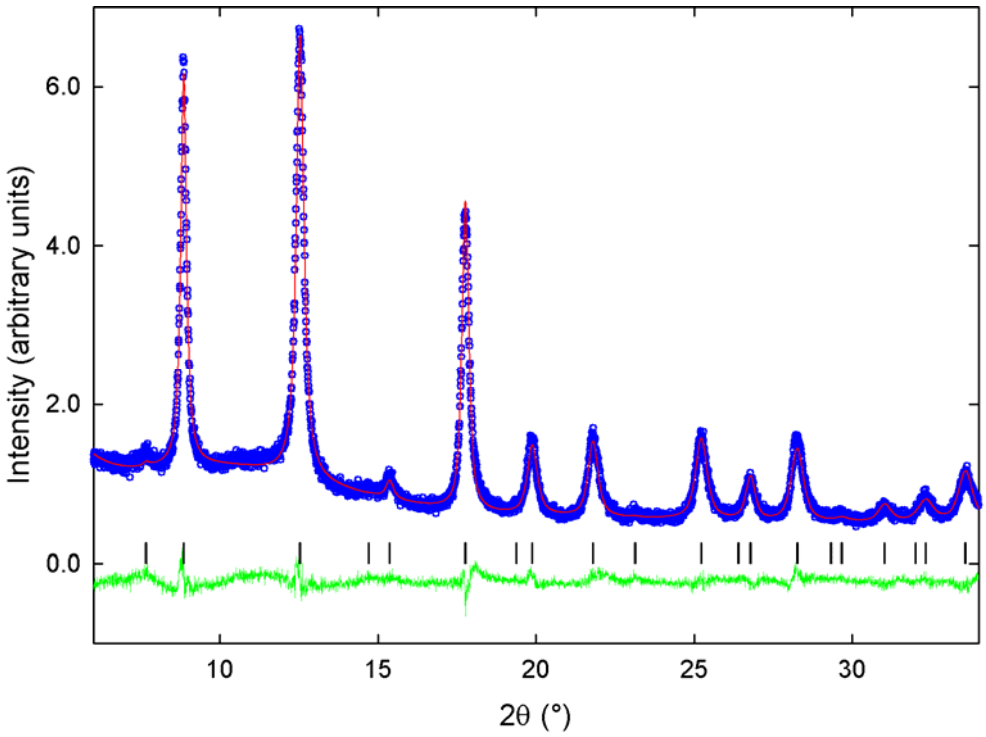

Figure 3.6 Final observed (blue circles), calculated (red solid line), and difference (lower green solid line) plots for the single-phase Rietveld refinement of **6** at 295 K. Tick marks show the reflection positions. The refinement was performed in the $Fm\bar{3}m$ space group. Error bars, being significantly smaller, are hidden by the data markers. The refined lattice constant is a = 10.3706(3) Å. The agreement factors are R_I = 4.13%, R_{wp} = 5.08%, R_{exp} = 1.53%. The X-ray wavelength is 0.8010 Å.

Table 3.5 Refined structure parameters of **6**. Estimated errors in the last digits are given in brackets.

	n	x	y	z	Wyckoff Position	B_{iso} (Å^2)
Fe	0.980(6)	0	0	0	4a	1.33(3)
Ni	0.495	1/2	1/2	1/2	4b	1.33(3)
Mn	0.505	1/2	1/2	1/2	4b	1.33(3)
Rb	0.315(1)	1/4	1/4	1/4	8c	4.78(9)
C	0.980(6)	0.1792(7)	0	0	24e	2.49(10)
N	0.980(6)	0.2915(7)	0	0	24e	2.49(10)
O1	0.020(6)	0.17(2)	0	0	24e	2.49(10)
O2	0.235(3)	0.1852(4)	0.1852(4)	0.1852(4))	32f	15.1(8)

3.2.2.2 Magnetic Characterization

The spontaneous magnetizations of the $Rb_xNi^{II}_zMn_{(1-z)}[Fe(CN)_6]\cdot yH_2O$ series, recorded in low magnetic fields, show that the onset of magnetic ordering occurs at progressively higher temperatures with increasing Ni fraction (Table 3.6).

Table 3. 6 Magnetic ordering temperatures of the $Rb_xA^{II}_zMn_{(1-z)}[Fe(CN)_6].yH_2O$ series

Sample	1	2	3	4	5	6	7	8
T_N (K)	12.5	14.5	15.0	16.0	18.5	20.0	20.0	23.0

Members of this series exhibit a variety of temperature dependent behaviours below the magnetic ordering temperature, T_N (or T_C in the case of **8**). Below $T_N(T_C)$ the spontaneous magnetizations of samples **1, 2, 3**, and **8** increase with decreasing temperature while in all other cases a single maximum is observed (Figure 3.7). Furthermore, samples **4** and **5** exhibit magnetic pole inversions with compensation temperatures (T_{comp}) of 5.7 and 7.8 K respectively.

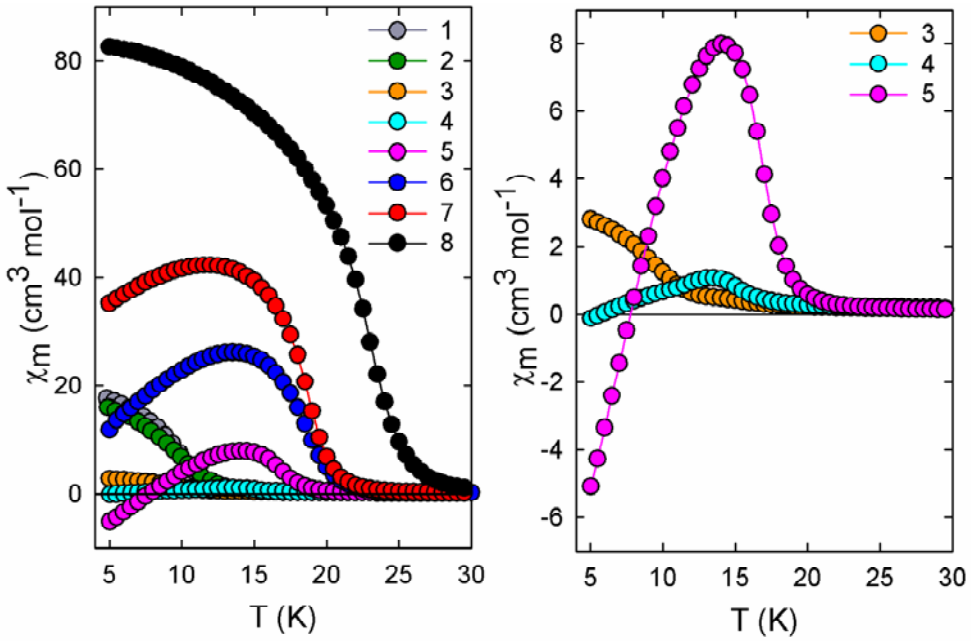

Figure 3.7 Field-cooled (FC) magnetizations of the $RbNi^{II}_zMn_{(1-z)}[Fe(CN)_6]\cdot yH_2O$ series in a 1 mT field.

Above the magnetic ordering temperature paramagnetic behaviour prevails, with magnetizations obeying the Curie-Weiss law. It is interesting to note that, none of the compounds in this series undergo the thermally induced reversible electron transfer from Fe^{III}(S = 1/2)-CN-Mn^{II}(S = 5/2) to Fe^{II}(S = 0)-CN-Mn^{III}(S = 2) which is frequently observed in the $RbMn[Fe(CN)_6]$ family from which these materials are derived.

Expansion of the $Rb_xNi^{II}_zMn_{(1-z)}[Fe(CN)_6]\cdot yH_2O$ series to include Fe^{II} as a third M^{II} ion produced a mixed ferro-ferrimagnet, $RbFe_{0.12}Ni_{0.28}Mn[Fe(CN)_6]\cdot 1.94H_2O$, which exhibits two compensation temperatures (Figure 3.8).

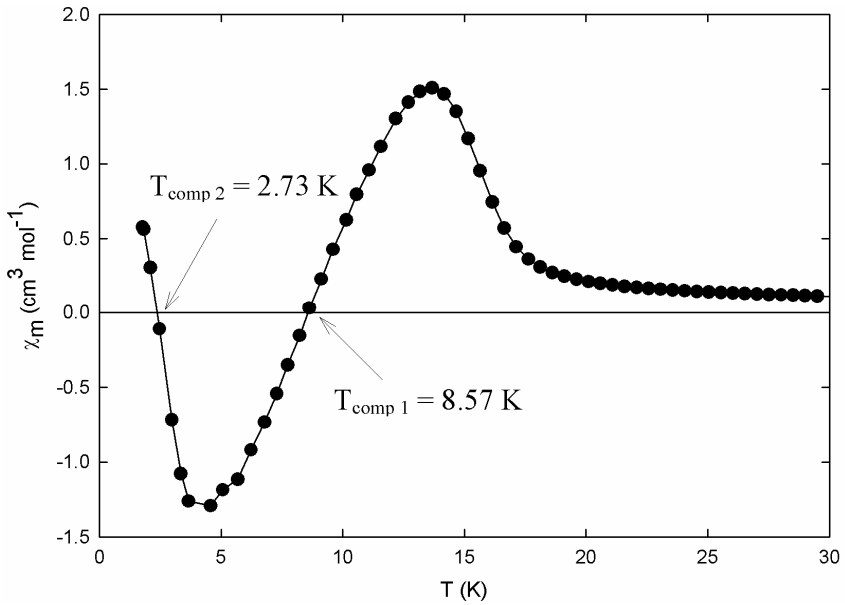

Figure 3.8 Field-cooled (FC) magnetization of $RbFe_{0.12}Ni_{0.28}Mn[Fe(CN)_6]\cdot 1.94H_2O$ in a 1mT field.

The spontaneous magnetization of $RbFe_{0.12}Ni_{0.28}Mn[Fe(CN)_6]\cdot 1.94H_2O$ is positive from the magnetic ordering temperature (T_C) of 17.1 K down to 8.6 K. Upon reaching 8.6 K the magnetization switches to negative and remains so until reaching 2.4 K where it switches back to positive. The diffraction pattern of this compound indicates that it adopts the *fcc* structure typical of PBAs with a lattice parameter of 10.32 Å. The IR spectrum exhibits a strong absorption at 2154 cm^{-1} accompanied by a weaker, broader absorption centred at 2072 cm^{-1}.

3.2.3 Discussion

Synchrotron powder diffraction studies confirm that members of the $Rb_xNi^{II}_zMn_{(1-z)}[Fe(CN)_6]\cdot yH_2O$ series are ternary transition metal complexes rather than physical mixtures of $RbNi[Fe(CN)_6]$ and $RbMn[Fe(CN)_6]$. The absence of peaks arising from both the $RbNi[Fe(CN)_6]$ and $RbMn[Fe(CN)_6]$ components clearly shows the successful synthesis of solid solutions. The progressive contraction of lattice parameters within the $Rb_xNi^{II}_zMn_{(1-z)}[Fe(CN)_6]\cdot yH_2O$ family with increasing z is attributed to the smaller ionic radius of the Ni^{II} ion (0.69 Å) as compared to Mn^{II} (0.83 Å), since the Rb fraction remains approximately constant in all members of the series. The peak broadening observed at higher nickel fractions could be explained by the increased disorder. Only two members of the $Rb_xNi^{II}_zMn_{(1-z)}[Fe(CN)_6]\cdot y\ H_2O$ series exhibit X-ray sensitivity at 295 K. The progressive lattice contractions of **1** and **2** under X-ray irradiation at 295 K are attributed to photo-induced internal charge transfer and will be discussed further in Section 3.5.3.

The end members of the $RbNi^{II}_zMn_{(1-z)}[Fe(CN)_6]\cdot yH_2O$ series, $RbNi[Fe(CN)_6]$ and $RbMn[Fe(CN)_6]$, incorporate only two transition metal ions and therefore cannot possibly exhibit mixed ferro-ferrimagnetism. Parallel alignment of the transition metal spins in $RbNi[Fe(CN)_6]$ gives rise to ferromagnetism ($J_{Ni\text{-}Fe} > 0$) with a magnetic ordering temperature of 22.50 K. Whereas in the parent compound, $RbMn[Fe(CN)_6]$, anti-parallel alignment of the non-compensating spins produces ferrimagnetism ($J_{MnFe} < 0$) with a magnetic ordering temperature of 11.59 K. Incorporating Ni^{II} (HS, $t_{2g}^6\ e_g^2$, S=1) into the A site ion position of the $RbMn^{II}[Fe^{III}(CN)_6]$, gives rise to compounds accommodating both ferromagnetic ($J_{Ni\text{-}Fe} > 0$) and antiferromagnetic exchange ($J_{Mn\text{-}Fe} < 0$) (Figure 3.9), i.e. mixed ferro-ferrimagnets.

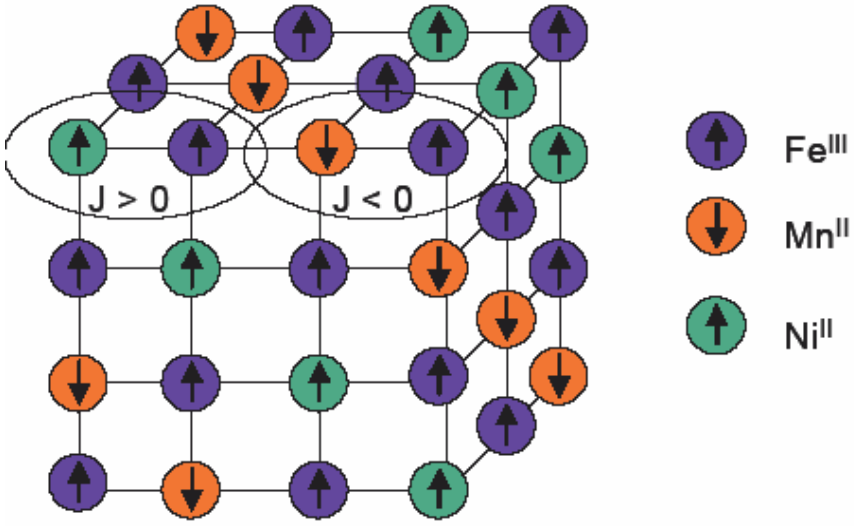

Figure 3.9 Illustration of the exchange interactions within the $Rb_xNi^{II}_zMn_{(1-z)}[Fe(CN)_6]\cdot yH_2O$ family.

The magnetic ordering temperatures (T_C or T_N) of the $RbNi^{II}_zMn_{(1-z)}[Fe(CN)_6]\cdot_yH_2O$ mixed ferro-ferrimagnets vary directly with z, as predicted by the following equation:

$$T_N = \sqrt{1.5S_{Fe}(S_{Fe}+1)\left\{xS_{Ni}(S_{Ni}+1)n_{NiFe}{}^2 + (1-x)S_{Mn}(S_{Mn}+1)n_{MnFe}{}^2\right\}} \qquad (3.12)$$

since ordering of the Ni sublattice occurs at higher temperature than that of the Mn sublattice. The spontaneous magnetization observed below T_N in these mixed ferro-ferrimagnets - the sum of the magnetic contributions from each sublattice – is extremely sensitive to chemical modifications, i.e. the replacement of Mn^{II} centres with Ni^{II}. Hence subtle changes in stoichiometry can produce a variety of thermomagnetic behaviours. The R-, N- and P-type thermomagnetic curves predicted by Néel, can be accessed by varying the stoichiometric factor z from 0 to 1.

The $RbNi^{II}_zMn_{(1-z)}[Fe(CN)_6]\cdot yH_2O$ family members **1, 2, 3** and **8** exhibit R-type spontaneous magnetizations below T_N because the magnetic contribution of one of the sublattices dominates over the entire temperature range, although the double hump in the thermomagnetic curve of **3** indicates that it lies on the R-N boundary. In contrast, **4** and **5** display N-type behaviour with a magnetic pole inversion upon

cooling. The magnetic contribution of the nickel sublattice, which aligns parallel to the applied field, dominates the spontaneous magnetizations of these materials at higher temperatures. However, as the temperature falls the manganese sublattice begins to order, aligning antiparallel to the nickel sublattice and causing the overall magnetization to tend towards zero. The contribution of the manganese sublattice continues to grow, eventually eliminating the effect of the nickel sublattice and causing the magnetization to switch from positive to negative (Figure 3.10).

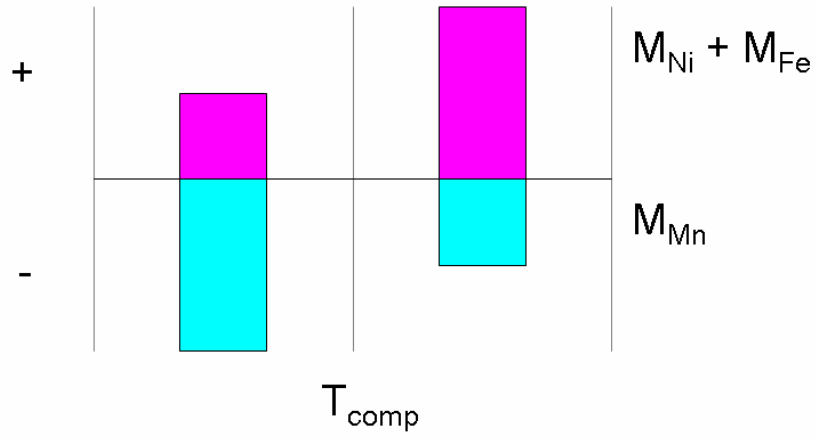

Figure 3.10 Illustration of the positive ($M_{Ni} + M_{Fe}$) and negative (M_{Mn}) magnetizations versus the direction of the external magnetic field at $T > T_{comp}$ and $T < T_{comp}$.

The effects of competition between the manganese and nickel sublattices continue to be observed as z increases to 0.52 (**6**) and 0.62 (**7**), with the thermomagnetic curves exhibiting maxima. Here the overall magnetizations remain positive over the entire temperature range, and hence are classified as P-type, because the antiparallel contribution of the manganese sublattice has been diminished by increasing z.

The $\chi_m T$ vs T plots of **1** shown below (Figure 3.11) are typical of $\chi_m T$ vs T plots in the $Rb_xM^{II}_zMn_{(1-z)}[Fe(CN)_6]\cdot yH_2O$ series. The absence of thermal hysteresis loops in the $\chi_m T$ vs T plots suggests that the introduction of even a minimal fraction of Ni^{II} into the $RbMn[Fe(CN)_6]$ system precludes the observation of thermally induced charge transfer. The 1T limit of the MPMS magnetometer failed to saturate the magnetizations of selected members of the $Rb_xM^{II}_zMn_{(1-z)}[Fe(CN)_6]\cdot yH_2O$ family.

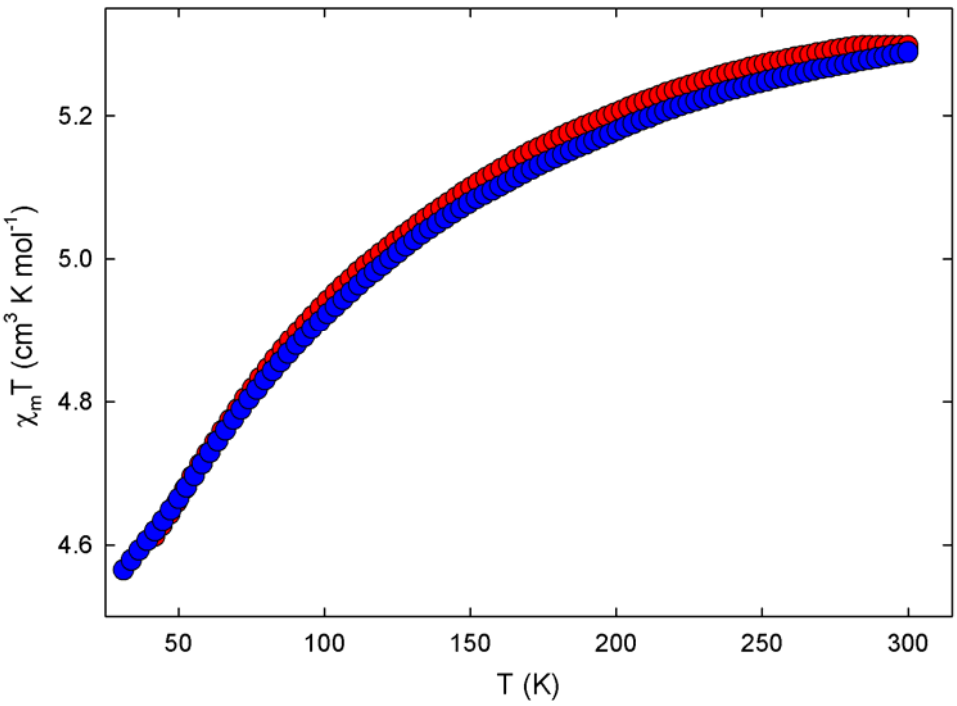

Figure 3.11 $\chi_m T$ vs T plots of **1** upon cooling (blue circles) and warming (red circles) in a 1 T field.

The flexible nature of the Prussian Blue analogue framework allows synthesis of Prussian Blue analogues incorporating three different types of A^{II} ion. Consequently we were able to expand our investigation of mixed ferri-ferromagnets to include $RbFe_{0.12}Ni_{0.28}Mn[Fe(CN)_6]\cdot 1.94H_2O$. The spontaneous magnetization of this material passes through zero twice when cooled below T_C, i.e. exhibits two compensation temperatures. This is an extremely rare phenomenon, having been reported only once before by Ohkoshi et al,[13] and can again be explained in terms of the different temperature dependencies of the constituent transition metal sublattices. As with N-type materials of the $RbNi^{II}_zMn_{(1-z)}[Fe(CN)_6]\cdot yH_2O$ series the prevailing sublattice contribution switches from Ni^{II} to Mn^{II} upon cooling. However, in this case the magnetization reverts back to positive at very low temperatures due to the ferromagnetic ordering of the Fe^{II} sublattice which aligns parallel to the applied field.

3.3 Hydrostatic Pressure

The magnetic pole inversions reported in Section 3.2 were accessed through chemical modifications but the sign of the spontaneous magnetization may also be controlled via application of an external stimulus, such as humidity or light irradiation.[16, 19] A humidity-induced pole inversion has been observed for the ternary PBA, $(Co^{II}_{0.41}Mn^{II}_{0.59})[Cr^{III}(CN)_6]_{2/3}\cdot zH_2O$. At 80% relative humidity (RH) this material is a mixed ferro-ferrimagnet with a magnetic ordering temperature of 52 K and a compensation temperature of 42 K, below which the sign of the spontaneous magnetization is negative. The compensation temperature and magnitude of the negative magnetization decrease as the RH falls until at 5% RH the compensation point vanishes, with the spontaneous magnetization remaining positive over the entire temperature range. These humidity-induced changes in the magnetic pole inversion are attributed to a conversion of the Co coordination environment from 6-Co^{II} to 4-Co^{II} due to the desorption of ligand water molecules. The change in the coordination geometry is accompanied by a switch from a ferromagnetic (6-Co^{II}–NC–Cr^{III}) to an antiferromagnetic (4-Co^{II}–NC–Cr^{III}) exchange interaction. Consequently, the negative sublattice magnetization of the 6-Co^{II} sublattice is replaced by that of the 4-Co^{II}, the positive sublattice magnetizations of the Mn^{II} and 4-Co^{II} sublattices dominate over that of 6-Co^{II} and the compensation point ceases to exist.

The mechanism responsible for the photoinduced magnetic pole inversion observed in $(Fe^{II}_{0.40}\ Mn^{II}_{0.60})_{1.5}[Cr^{III}(CN)_6]$ is quite distinct from the humidity-induced effects of $(Co^{II}_{\ 0.41}Mn^{II}_{0.59})[Cr^{III}(CN)_6]_{2/3}\cdot zH_2O$. This N-type mixed ferro-ferrimagnet, exhibits a spontaneous magnetization which is initially positive upon cooling below T_C, due to the dominating contributions of the positively aligned Fe^{II} and Cr^{II}, but diminishes towards zero as the sample is cooled towards 19 K. Below 19 K (T_{comp}) the contribution of the Mn^{II} sublattice dominates and the magnetization switches to become negative. A photoinduced magnetic pole inversion is observed under visible light irradiation (360 – 450 nm) due to suppression of the Fe^{II} sublattice magnetization. The mechanism responsible for this suppression is thought to be a

change in the iron spin state via an excited charge transfer state from Fe^{II} S = 2 to Fe^{II} S = 0.

The proceeding study of appropriately chosen members of the $Rb_xM^{II}_zMn_{(1-z)}[Fe(CN)_6]\cdot yH_2O$ series, $Rb_{0.64}Ni_{0.31}Mn_{0.87}[Fe(CN)_6]\cdot 2.8H_2O$ (**3**) and $Rb_{0.64}Ni_{0.45}Mn_{0.66}[Fe(CN)_6]\cdot 2.33H_2O$ (**5**)**,** illustrates that hydrostatic pressure is an equally powerful means of inducing sequential magnetic pole inversions in PBAs**.**

3.3.1 Experimental

Pressure dependent magnetic measurements of **3** employed the long symmetric high pressure cell described in Chapter 2. The pressure applied to **3** was increased incrementally and the temperature dependent susceptibility, in both 1 mT and 0.1 T applied fields, recorded at each pressure. The field dependent susceptibility at 4 K was recorded at selected pressures. Temperature and field dependent susceptibilities were also measured subsequent to complete pressure release.

Susceptibility measurements of **5** under hydrostatic pressure employed the piston cylinder cell, which is also outlined in Chapter 2. The temperature dependent susceptibility of **5** in a 1 mT applied field was mapped upon pressurization and depressurization, both of which proceeded incrementally.

3.3.2 Results

3.3.2.1 $Rb_{0.64}Ni_{0.31}Mn_{0.87}[Fe(CN)_6]\cdot 2.8H_2O$

At ambient pressure the field-cooled spontaneous magnetization of **3** below the magnetic ordering temperature of 16 K exhibits a double hump, indicating that **3** lies near Néel's R-N phase boundary for exhibiting a magnetic pole inversion (Figure 3.12a overleaf). A saturation magnetization of 2.63 μ_B is derived from the magnetic hysteresis loop of **3** recorded at 4 K under ambient pressure conditions (Figure 3.12b overleaf).

a)

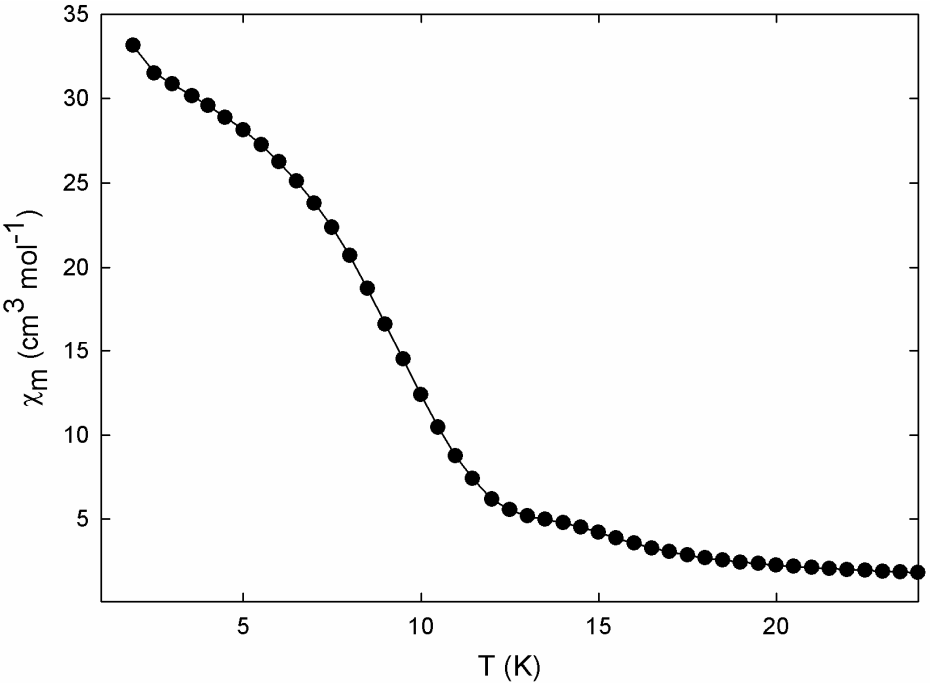

b)

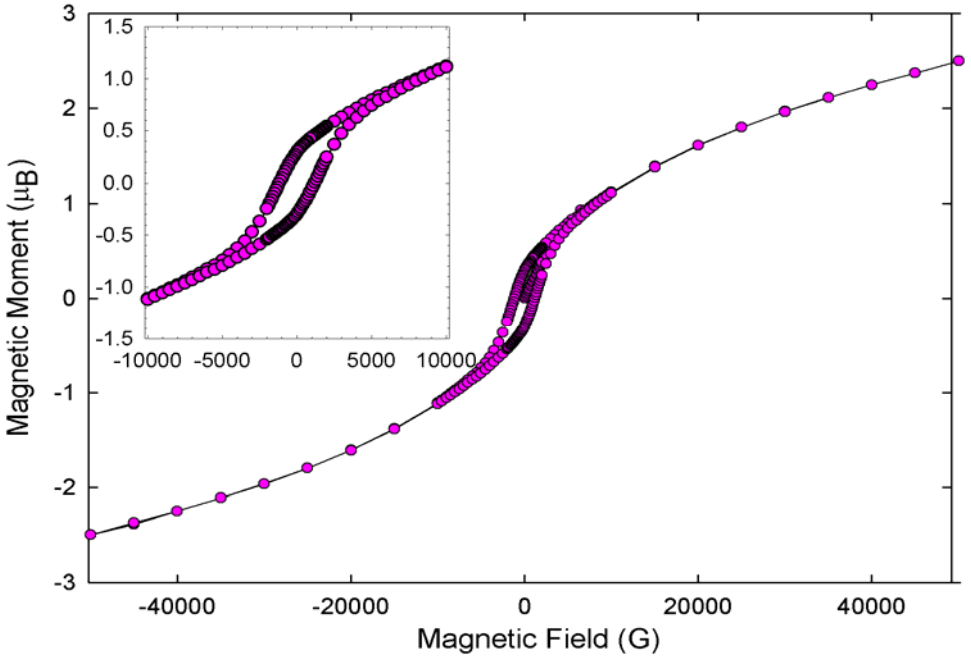

Figure 3.12 a) Temperature dependence of the magnetization of **3 (**1 mT field, field-cooling). b) Magnetic hysteresis loop of **3** at 4 K.

The value of $\chi_m T$ is 4.53 cm^3 K mol^{-1}at 300 K and ambient pressure (Figure 3.13a overleaf), while the Weiss temperature (θ), derived from the temperature dependence of the inverse molar susceptibility of **3,** is -7.5(1) K (Figure 3.13b overleaf).

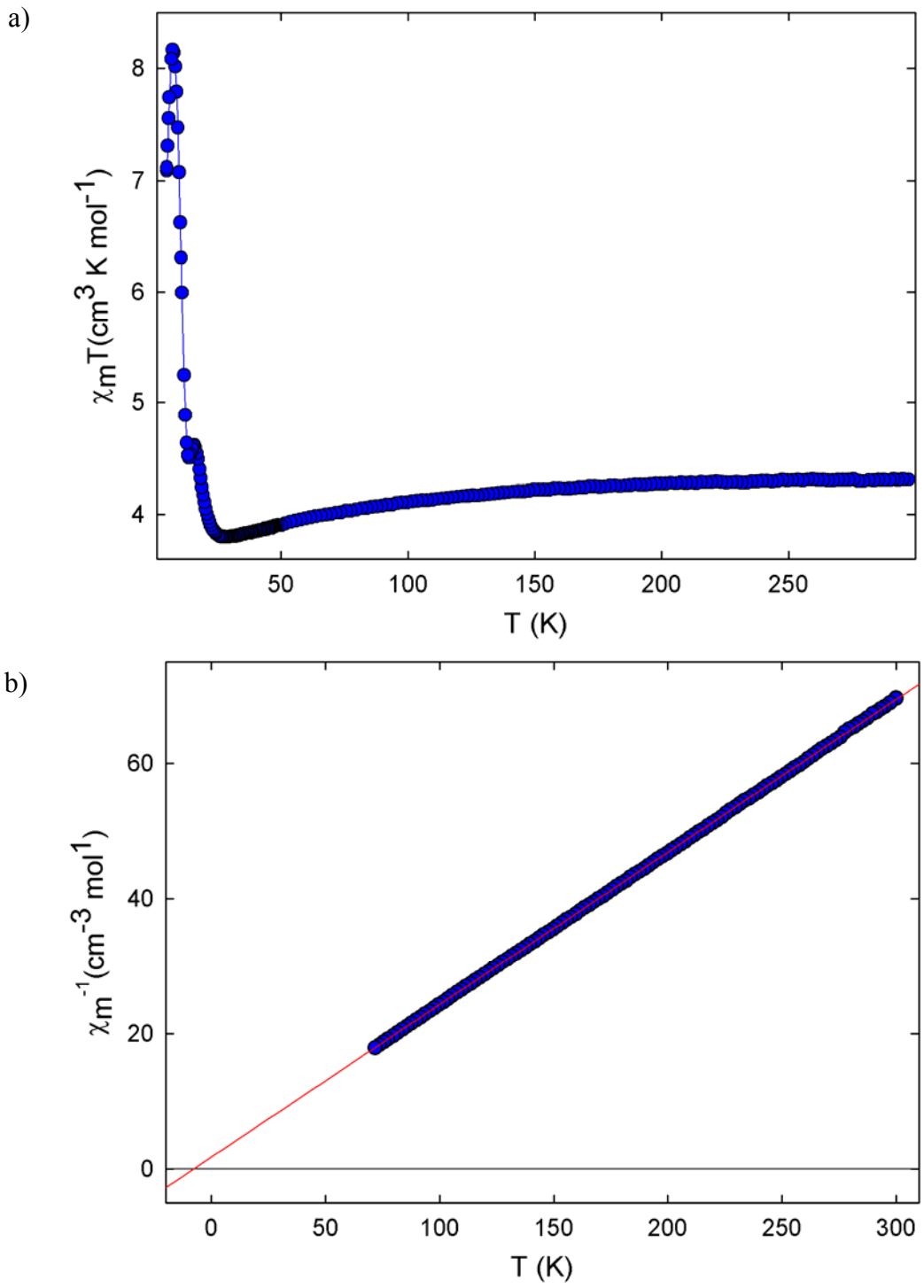

Figure 3.13 a) Temperature dependence of $\chi_m T$ for **3** (0.1 T). b) Curie-Weiss plot of **3** (0.1 T).

Upon application of 0.2 kbar of hydrostatic pressure, **3** exhibits a magnetic pole inversion with the spontaneous magnetization reversing its sign to negative below T_{comp} = 13 K (Figure 3.14a overleaf).

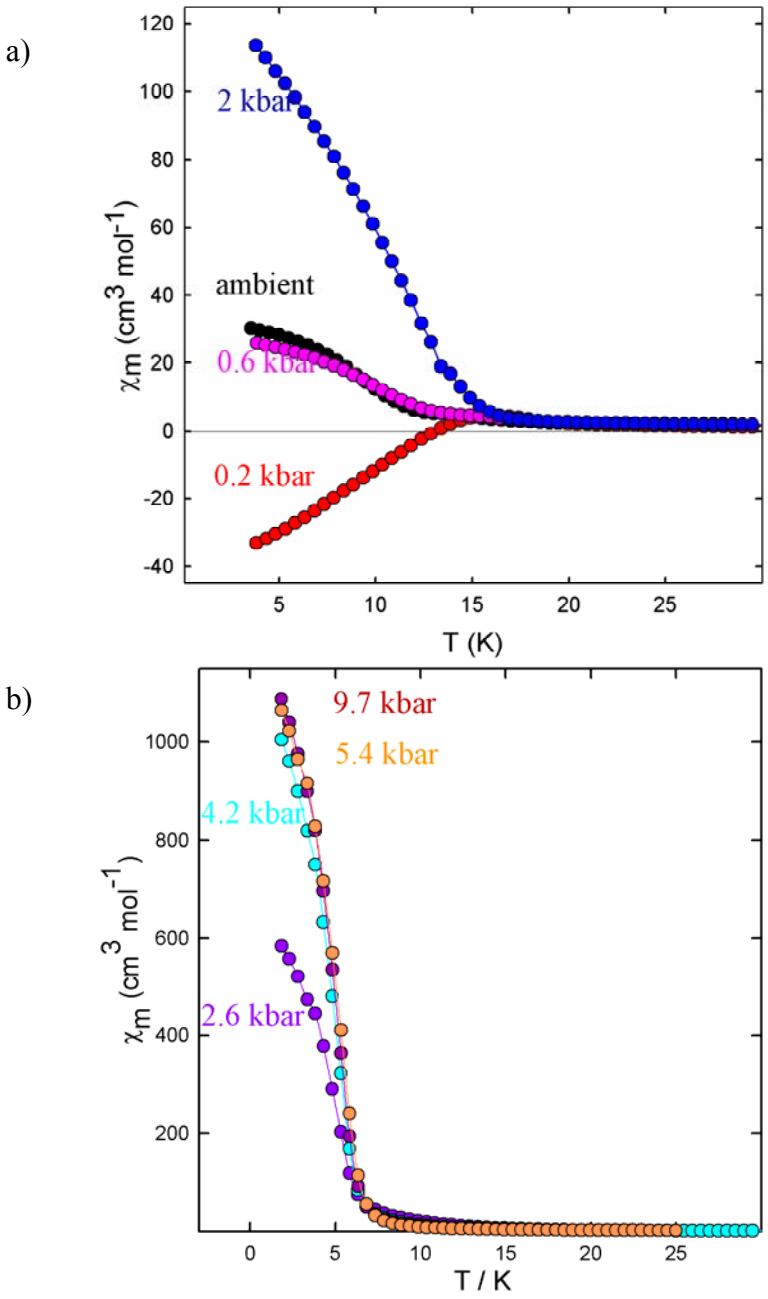

Figure 3.14 Temperature dependence of the magnetization of **3** (1 mT, field cooling) as a function of pressure.

The low-field magnetization switches back to positive as the pressure is increased further to 0.6 kbar, and the material crosses the N-P boundary. The spontaneous magnetization continues to increase rapidly on further raising the pressure to 2.0 kbar. A dramatic increase in the spontaneous magnetization is observed upon reaching 2.6 kbar (Figure 3.14b). This pressure-induced transformation is virtually

complete upon pressurizing to 4.2 kbar, when the spontaneous magnetization approaches a value 40 times larger than that at ambient pressure.

The magnetic pole inversion observed at 0.2 kbar is accompanied by an increase of the magnetic ordering temperature to 17.5 K while the magnitude of $\chi_m T$ at 300 K and θ decrease to 4.32 cm^3 K mol^{-1} and -5.9(1) K, respectively. Upon further pressurization the magnetic ordering temperature continues to increase, $\chi_m T$ at 300 K continues to fall and θ becomes increasingly less negative and finally assumes a small positive value at 2.0 kbar (Figure 3.15).

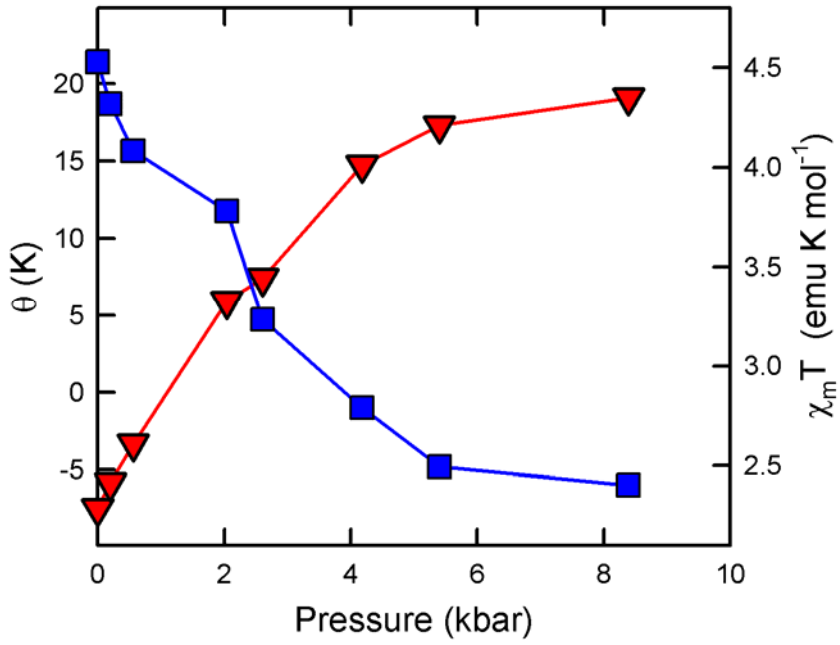

Figure 3.15 Pressure dependence of $\chi_m T$ at 300 K (blue squares) and of the Weiss temperature, *θ* (red triangles) deduced by Curie-Weiss fits to χ_m^{-1} vs T between 50 and 300 K.

A considerable decrease in $\chi_m T$ at 300 K and a magnetic ordering temperature of 5 K accompany the dramatically enhanced spontaneous magnetization observed at 2.6 kbar. The magnetic ordering temperature continues to decrease slowly at a rate of ~ 0.1 K/kbar as **3** is pressurized further to 9.7 kbar but no other major changes are observed. The Weiss temperature of the fully transformed material is +16.4(2) K while the value its value of $\chi_m T$ at 300 K is 2.6 cm^3 K.

All pressure induced transformations of **3** are fully reversible upon release of the pressure and are accompanied by hysteretic behaviour (Figure 3.16). A dramatic reduction in the magnitude of the spontaneous magnetization is observed below 2.2 kbar while the sign of the spontaneous magnetization reverses just above atmospheric pressure.

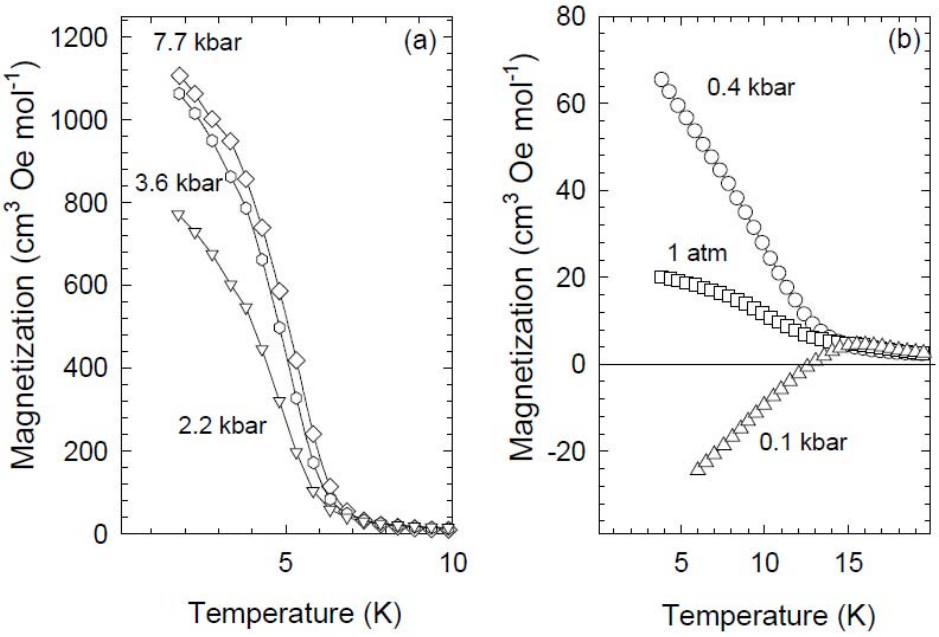

Figure 3.16 Temperature dependence of the magnetization (H = 1 mT, field cooling) of **3** as a function of pressure. Data were collected upon release of pressure from 9.7 kbar to ambient. (7.7 kbar = diamonds, 3.6 kbar = hexagons, 2.2 kbar = downwards triangles, 0.4 kbar = circles, 0.1 kbar = upwards triangles, squares = complete release of pressure).

3.3.2.2 $Rb_{0.64}Ni_{0.45}Mn_{0.66}[Fe(CN)_6]\cdot 2.33H_2O$

At ambient pressure **5** exhibits N-type behaviour, with a spontaneous magnetization displaying a single maximum at 14.9 K and a magnetic pole inversion at T_{comp} = 8.3 K in its temperature dependence. Pressurization to 3.5 kbar causes a decrease in the magnitude of the spontaneous magnetization observed below T_{comp} and a shift in the point of maximum magnetization to 16.9 K (Figure 3.17 overleaf). Increasing the pressure further to 6.4 kbar induces a magnetic pole inversion from negative to positive with the temperature dependence of resultant spontaneous magnetization displaying a double hump, indicating that at this pressure **5** lies near

Néel's R-N phase boundary. The magnitude of the spontaneous magnetization is further enhanced until the upper pressure limit of the cell (8 kbar) is reached.

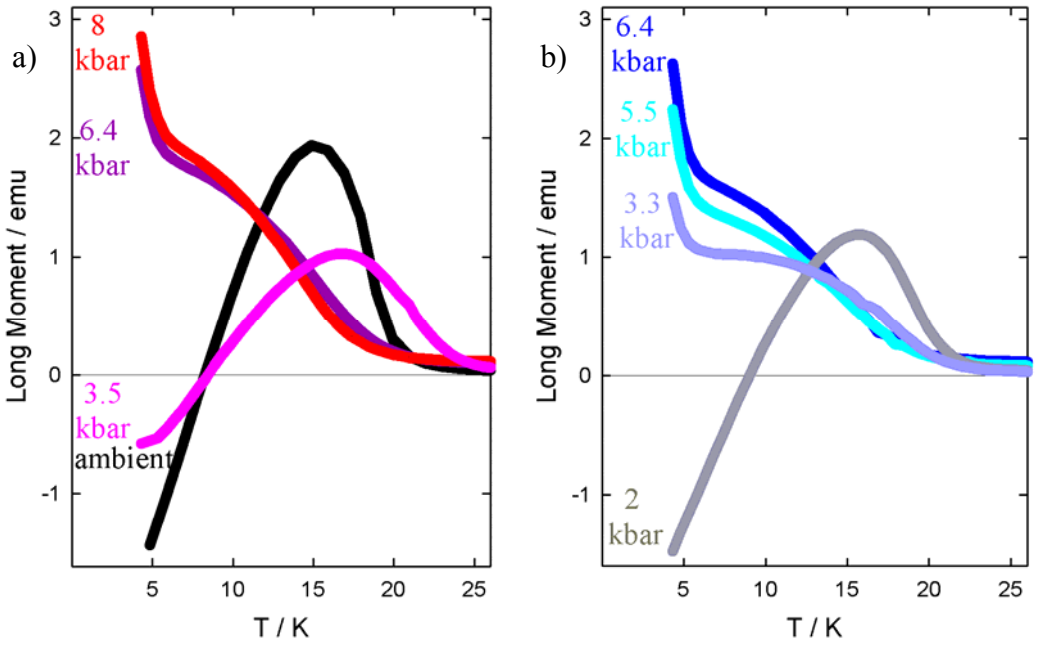

Figure 3.17 Field-cooled (FC) magnetizations of $Rb_{0.64}Ni_{0.45}Mn_{0.66}[Fe(CN)_6]\cdot 2.33H_2O$ as a function of pressure upon a) pressurization b) depressurization in a 1 mT field.

The spontaneous magnetization of **5** - like that of **3** - displays a hysteretic effect during depressurization. At 3.5 kbar in the pressurization sequence **5** exhibits a single maximum and a magnetic pole inversion whereas the piezo-transformed state displaying a double hump persists to 3.3 kbar upon pressure release. However, the pressure induced transformation is fully reversible as seen by the spontaneous magnetization recorded at 2.0 kbar in the depressurization sequence.

3.3.3 Discussion

The negative Weiss temperature derived from the magnetic response of **3** in a 0.1 T applied field at ambient pressure is consistent with overall antiferromagnetic exchange interactions. Both the measured $\chi_m T$ at 300 K and the saturation magnetization are consistent with parallel alignment of the Ni^{II} (S = 1) and antiparallel alignment of Mn^{II} (HS, S = 5/2) spins with those of the Fe^{II} (LS, S = 1/2) centres, thus **3** is ferrimagnetic under ambient conditions. The response of **3** upon pressurization to 0.2 kbar indicates that the application of pressure enhances the

ferromagnetic interactions of Ni^{II} sublattice relative to the antiferromagnetic interactions of the Mn^{II} sublattice, that is $[(dJ|Ni\text{-}Fe|/dP) > (dJ|Mn\text{-}Fe|/dP)]$. Consequently, **3** is shifted across the R-N phase boundary to become a N-type material. The magnetic response of **3** upon further pressurization to 2.0 kbar is consistent with further enhancement of the ferromagnetic interactions.

The only possible scenario which can explain the dramatically enhanced spontaneous magnetization and suppressed effective magnetic observed at 2.6 kbar is an internal metal-to-metal charge transfer from Mn^{II}-(HS, d5, S = 5/2)-NC-Fe^{III}(LS, d5, S = 1/2) to Mn^{III}(HS, d4, S = 2)-NC-Fe^{II}(LS, d6, S = 0). This metal-to-metal transfer cannot be accessed thermally or via X-ray irradiation. Alternative scenarios, such as metal-centered spin transitions and cyanide ligand flips, can be unambiguously excluded. This piezo-induced electronic transformation is also responsible for the switch to bulk ferromagnetism. At low pressures, the Mn^{II}(HS) and Fe^{III}(LS) centers couple antiferromagnetically. In contrast, the exchange coupling between near-neighbour Mn^{III}(HS, $t_{2g}^{3}e_{g}^{1}$) ions in the piezotransformed material - as mediated by the Fe^{II}(LS, $t_{2g}^{6}e_{g}^{0}$) t_{2g} orbitals - is ferromagnetic in nature. The slow increase in the magnetic ordering temperature, T_C, at higher pressures is due to further enhancement of the ferromagnetic exchange interactions (Figure 3.18 overleaf).

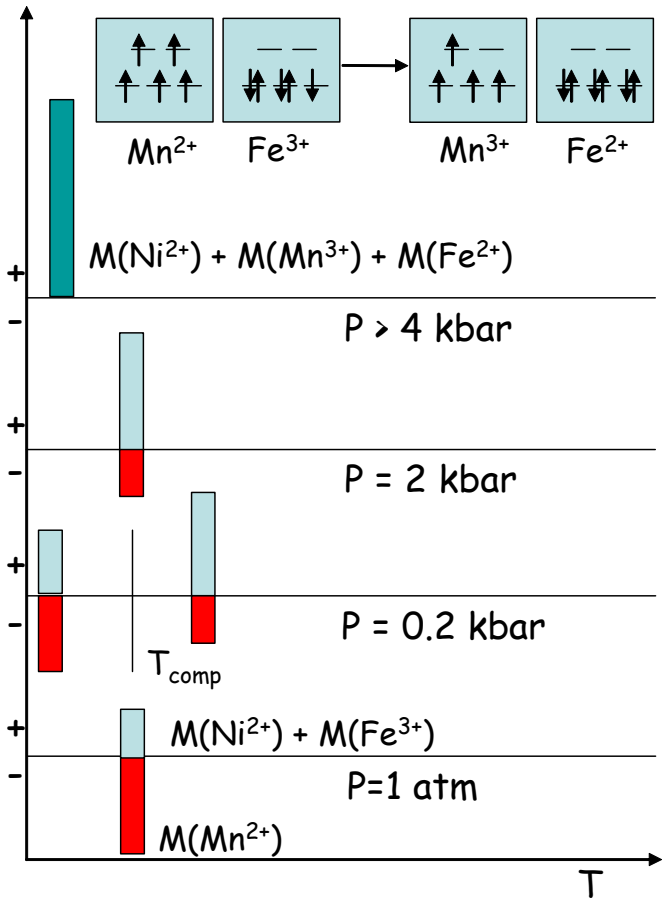

Figure 3.18 Schematic diagram illustrating positive, $M(Ni^{2+})+M(Fe^{3+})$,and negative, $M(Mn^{2+})$, magnetizations versus the direction of the external magnetic field as a function of temperature and pressure.

We propose that enhancement of Ni sublattice exchange interactions relative to those of the Mn sublattice is also responsible for the pressure-induced conversions of **5.** The spontaneous magnetization of **5** at ambient pressure indicates that it is a mixed N-type mixed ferri-ferromagnet, however the double hump in the spontaneous magnetization observed upon pressurization to 6.4 K suggests that **5** has been shifted to the boundary of Néel's R and N ferrimagnetic phases. Observation of the double hump in the spontaneous magnetization upon further compression suggests that R-N boundary phase of **5** persists. Subtle increases in the magnitude of the magnetization upon pressurization to 8 kbar (the limit of the cell) suggests that metal-to-metal charge transfer does not occur, in contrast to the behaviour of **3** which undergoes a pressure induced electron transfer. The pressure sensitivity of **5** is much reduced compared to that of **3.** Absence of an electron transfer within the range of

technically feasible pressures is attributed to the decreased concentration redox-active Fe^{III}(S = 1/2)-CN-Mn^{II}(S = 5/2) units relative to non redox-active Fe^{III}(S = 1/2)-CN-Ni^{II}(S = 4) units.

3.4 Photoirradiation

The photosensitivity of rubidium manganese hexacyanoferrates is not confined to visible region of the electromagnetic spectrum. Synchrotron X-ray radiation proved useful as both a structural probe and a means of external perturbation in the study of $Rb_{0.7}Mn_{1.15}[Fe(CN)_6]\cdot 2H_2O$.[20] At 295 K X-ray irradiation of this PBA stimulates metal-to-metal charge transfer and the subsequent evolution of Fe^{III}-CN-Mn^{II} centres to Fe^{II}-CN-Mn^{III}. Oxidation of Mn^{2+} to Mn^{3+} causes the Mn-N bond to shrink while the Fe-C bond length remains relatively unchanged by the reduction process, consequently a rapid lattice contraction of 0.238(3) $Å^3$ min^{-1} is observed under X-ray illumination at 295 K. At 100 K this photoinduced charge transfer occurs more efficiently and an abrupt structural phase transition takes place, indicated by a dramatic collapse of the unit cell dimensions and the appearance of a discrete minority phase. This collapsed phase is unstable at 10 K and further photoirradiation reverses the charge transfer process, as indicated by expansion of the lattice parameters to a value intermediate between those of the photo-transformed phase and non-irradiated phase.

The proceeding synchrotron X-ray powder diffraction studies on selected members of the $Rb_xM^{II}_zMn_{(1-z)}[Fe(CN)_6]\cdot yH_2O$ series explores the effects of Ni doping on the photosensitivity of the rubidium manganese hexacyanoferrates.

3.4.1 Experimental

Synchrotron X-ray powder diffraction data were collected at the high-resolution powder X-ray diffraction beamline ID31 at the European Synchrotron Radiation Facility (ESRF), Grenoble, France. Diffraction profile analysis was performed using the GSAS suite of Rietveld analysis programs.[21]

3.4.2 Results

Synchrotron X-ray (λ = 0.80160 Å) powder diffraction studies of **1** over a range of temperatures show that the crystal structure remains cubic down to 10 K. Rietveld analyses employed the generic structural model of mixed-valence metal cyanides comprising a three-dimensional network of $\{M^{II}(NC)_6\}$ and $\{Fe^{III}(CN)_6\}$ octahedra linked by the CN ligands (space group $Fm\bar{3}m$).[22] The $Fe(CN_6)$ vacancy positions (9 %) are occupied by H_2O molecules completing the coordination sphere of neighbouring M^{II} cations while the Rb^+ ions are disordered in the tetrahedral interstices of the framework structure. The positions of the diffraction peaks rapidly shift to higher angles with increasing irradiation time (Figure 3.19), corresponding to a volume contraction rate of 0.3463 $Å^3$ min^{-1}.

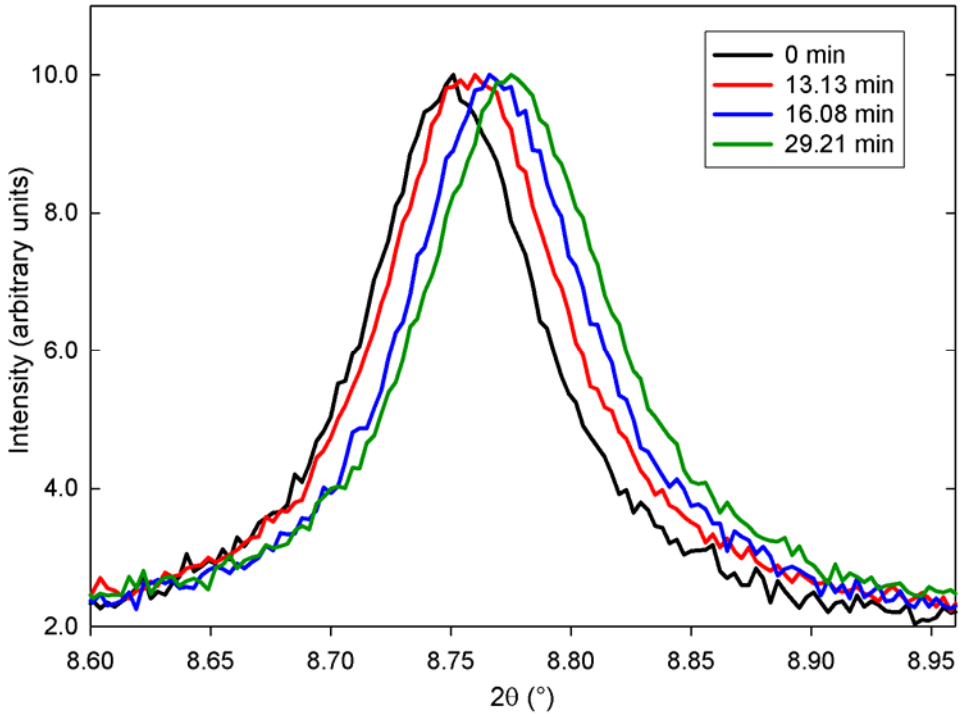

Figure 3.19 Evolution of the (200) Bragg reflection of **1** with increasing illumination time at 295 K.

The photo-induced lattice contraction of **1** resumes at 100 K after cooling in the absence of illumination and continues steadily for 31 minutes, with the lattice parameter shrinking from an initial value of 10.4666(1) to 10.3487(4) Å. An abrupt collapse of the lattice parameter to 10.2032(2) Å is subsequently observed, indicating

a first-order phase transition (Figure 3.20a overleaf). The contraction of the lattice parameter which occurs during the period of irradiation (53 min) is accompanied by a decrease of the M-N bond length from 2.224(5) to 2.04065(4) Å, consistent with the generation of M^{III}-NC-Fe^{II} centres. In contrast the iron coordination sphere changes only marginally from 1.902(3) to 1.9002(8) Å as a consequence of the metal-to-metal charge transfer.

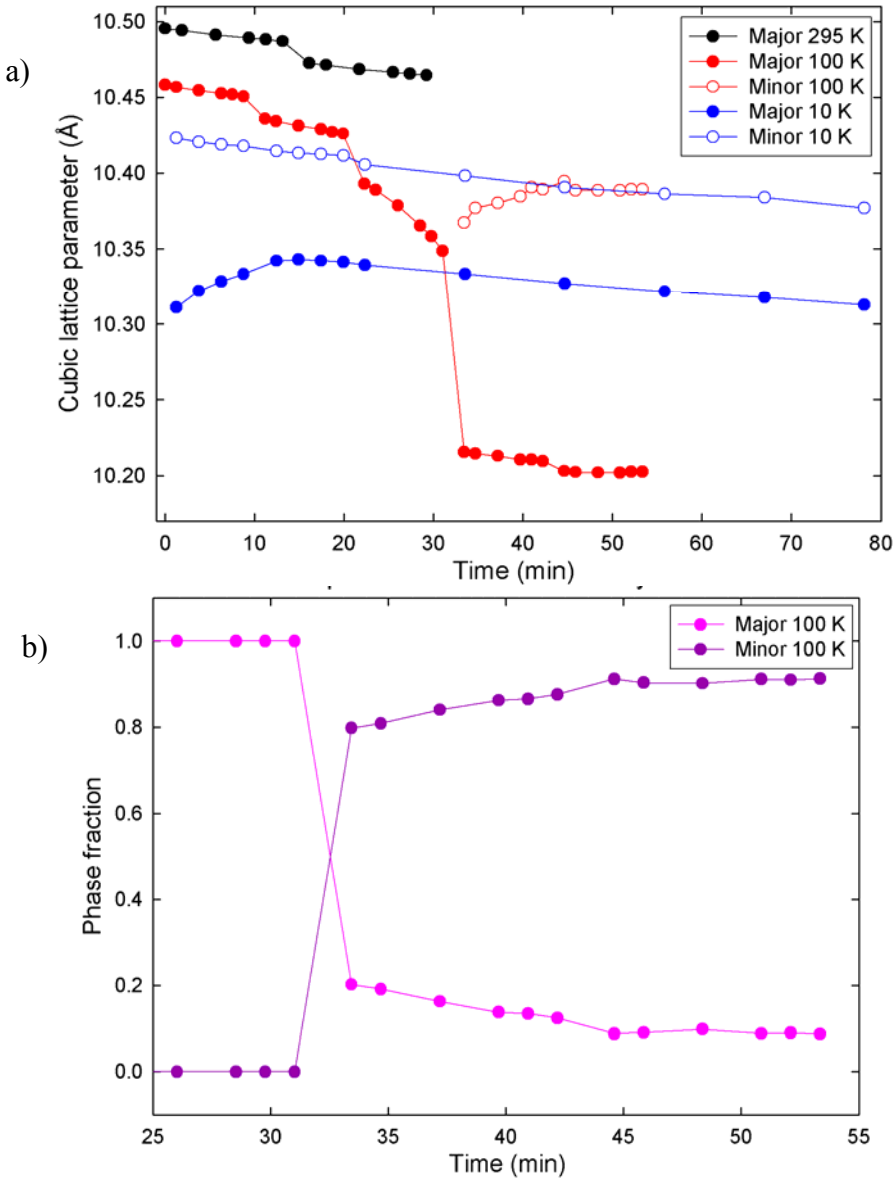

Figure 3.20 a) Evolution of the lattice constants of **1** with illumination time at 295 K (black), 100 K (red) and 10 K (blue). Open symbols indicate the lattice constants of the minority phase at 100 and 10 K. b) Evolution of the phase fractions of the majority (pink) and minority (purple) phases at 100 K. (Error bars in a) and b), being considerably smaller, are hidden by data markers).

This dramatic lattice collapse is accompanied by the emergence of a minor secondary phase, the lattice constants of which correspond to that of the untransformed material at 100 K. X-ray irradiation of the photo-transformed material after cooling to 10 K triggers a rapid lattice expansion, which progresses at a rate 2.93 $Å^3$ min^{-1} during the first 5 minutes of illumination. The photo-induced expansion is virtually complete after 11 minutes of illumination, as signified by stabilization of the lattice dimensions at 10.3123(3) Å. This value is intermediate between those of the original and photo-transformed phases.

Photosensitivity analogous to that of **1** has been detected in other members of the $Rb_xNi^{II}_zMn_{(1-z)}[Fe(CN)_6]\cdot yH_2O$ series. Synchrotron powder diffraction studies reveal that members of the series with $z > 0.13$ are unperturbed by X-ray irradiation at room temperature. However, several of these compounds do exhibit photo-induced lattice contraction upon cooling to 100 K; the rate of transformation being inversely related to fraction of nickel present (Figures 3.21 – 3.24 overleaf).

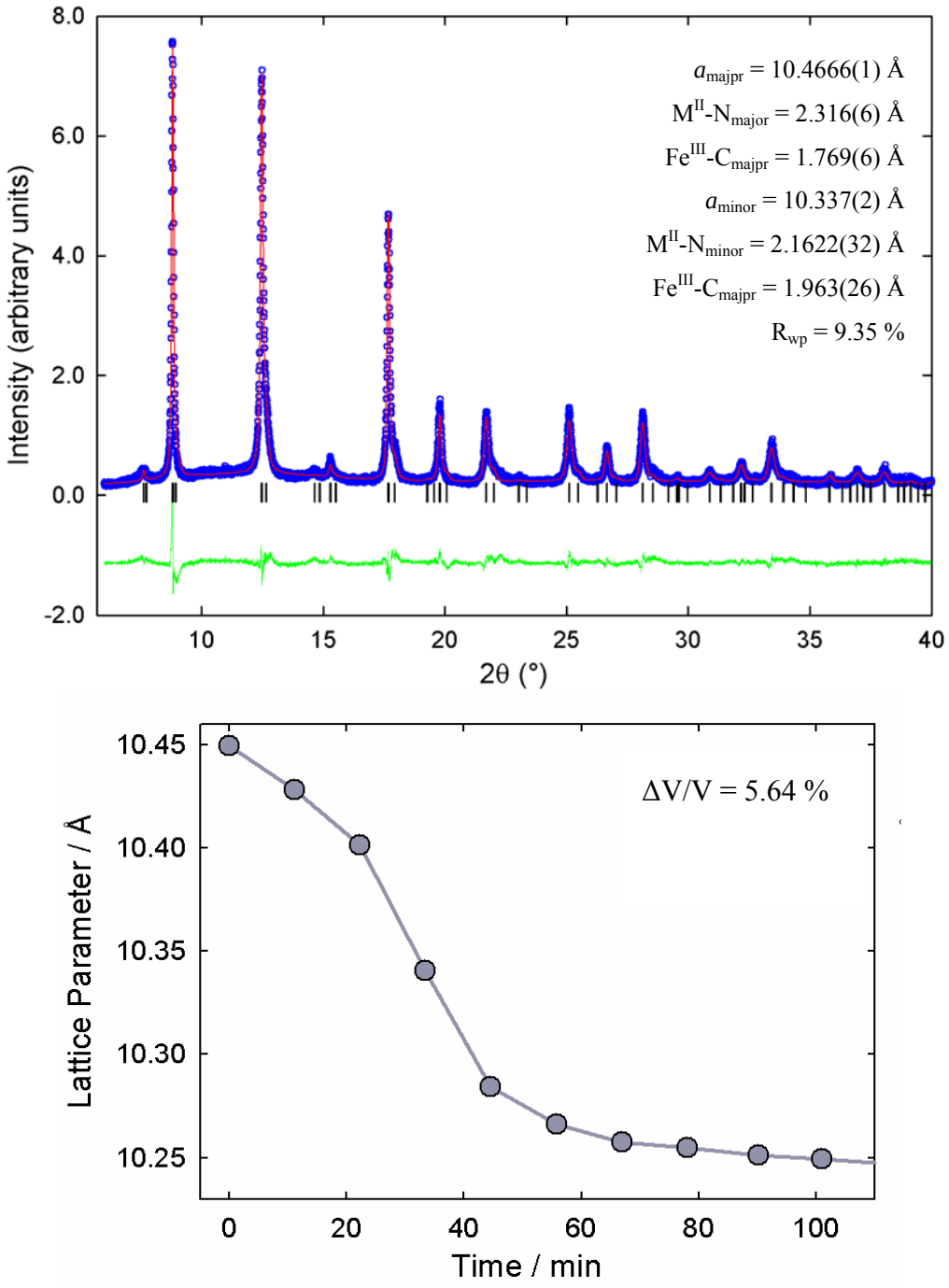

Figure 3.21 Upper: Final observed (blue circles), calculated (red solid line), and difference (lower green solid line) plot for the two phase Rietveld refinement of the synchrotron X-ray powder diffraction profile of **2** at 100 K. The tick marks show the reflection positions for both phases. The refinement included with both phases in the $Fm\bar{3}m$ space group. Lower: Evolution the lattice constant with increasing illumination time. (Error bars, being significantly smaller, are hidden by the data markers).

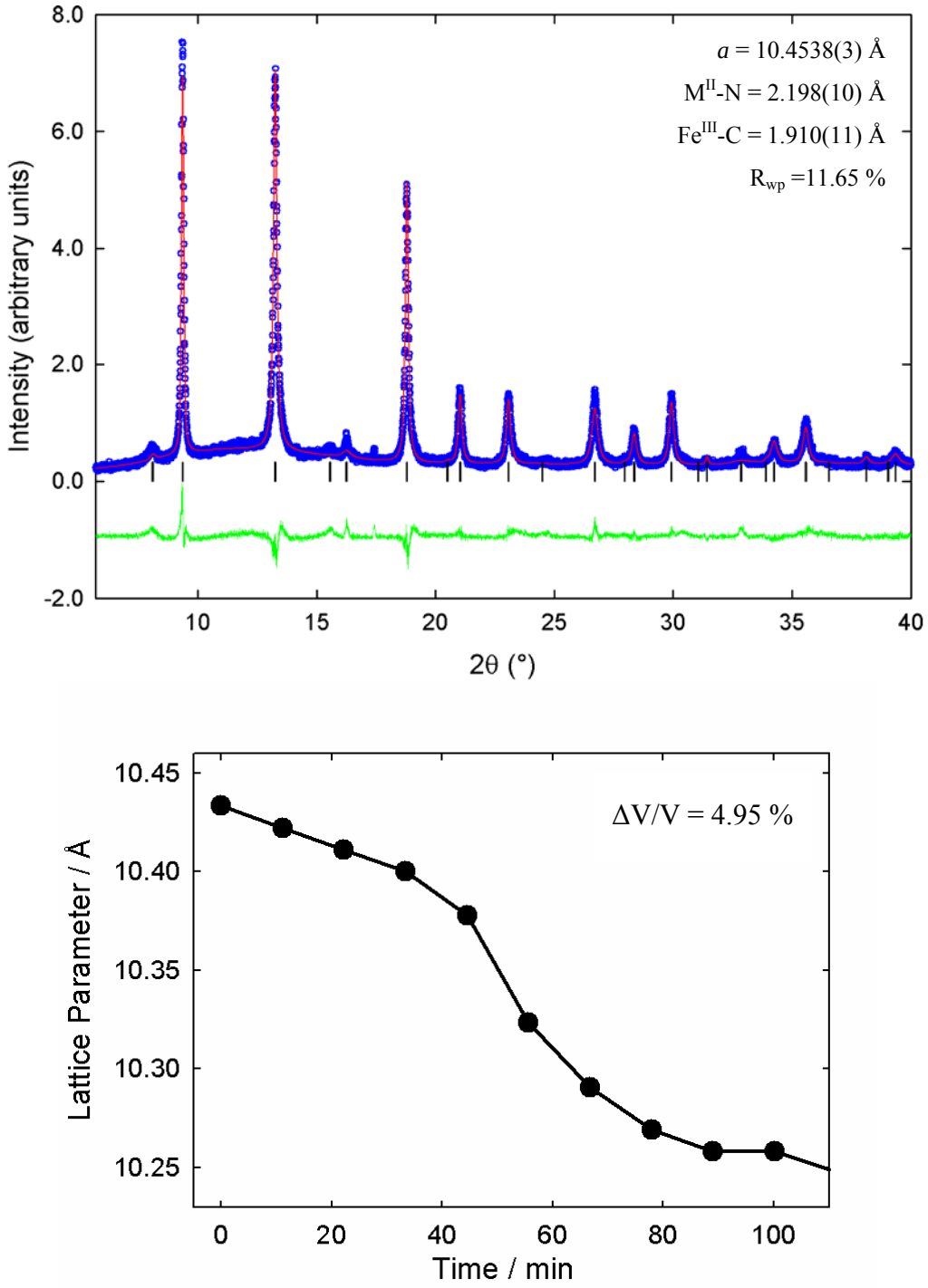

Figure 3.22 Upper: Final observed (blue circles), calculated (red solid line), and difference (lower green solid line) plot for the phase Rietveld refinement of the synchrotron X-ray powder diffraction profile of **3** at 100 K. The tick marks show the reflection positions. The refinement we performed using a single phase in the $Fm\bar{3}m$ space group. Lower: Evolution the lattice constant with increasing illumination time. (Error bars, being significantly smaller, are hidden by the data markers).

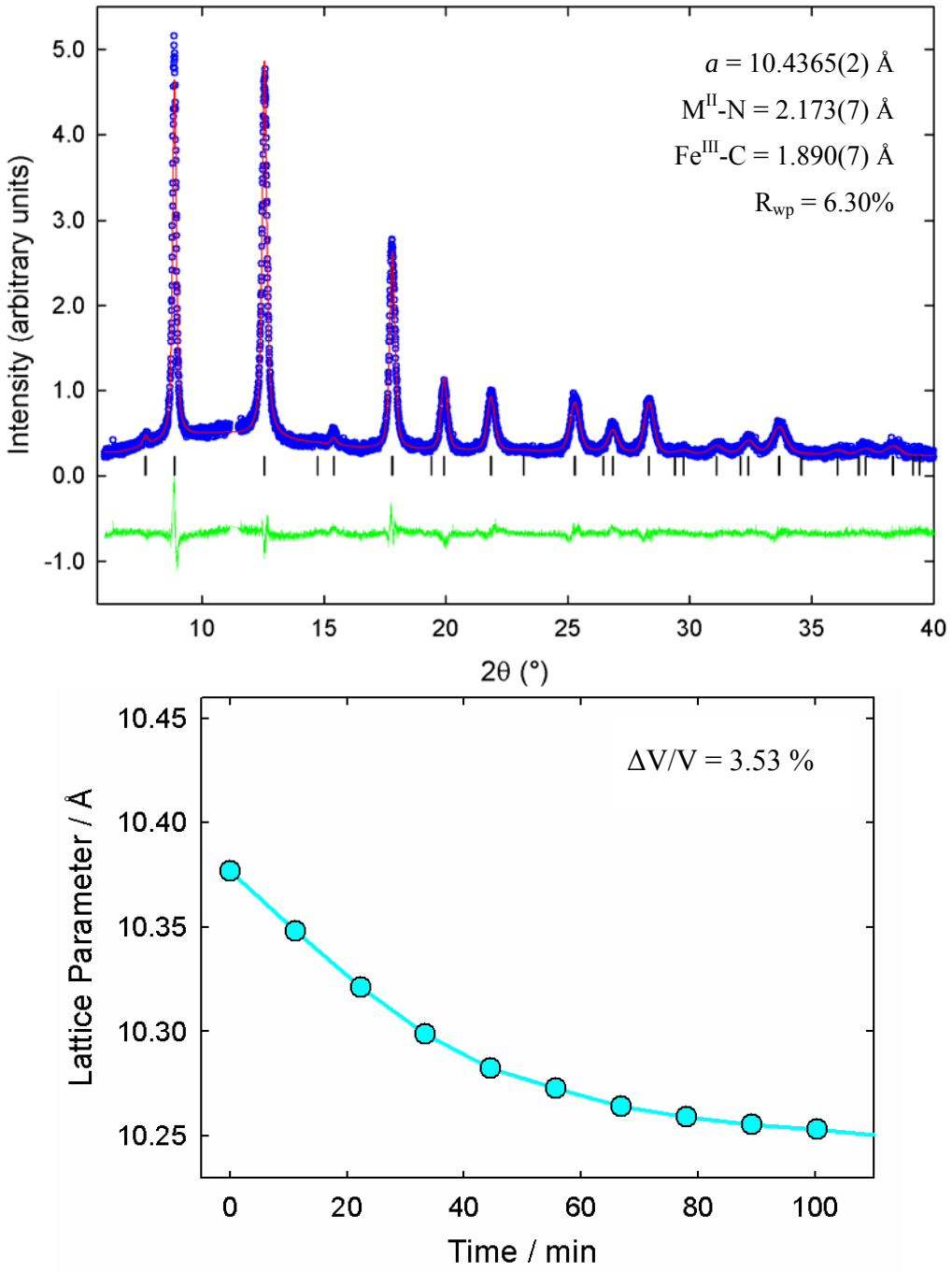

Figure 3.23 Upper: Final observed (blue circles), calculated (red solid line), and difference (lower green solid line) plot for the Rietveld refinement of the synchrotron X-ray powder diffraction profile of **4** at 100 K. The tick marks show the reflection positions. The refinement was performed using a single phases in the $Fm\bar{3}m$ space group. Lower: Evolution the lattice constant with increasing illumination time. (Error bars, being significantly smaller, are hidden by the data markers).

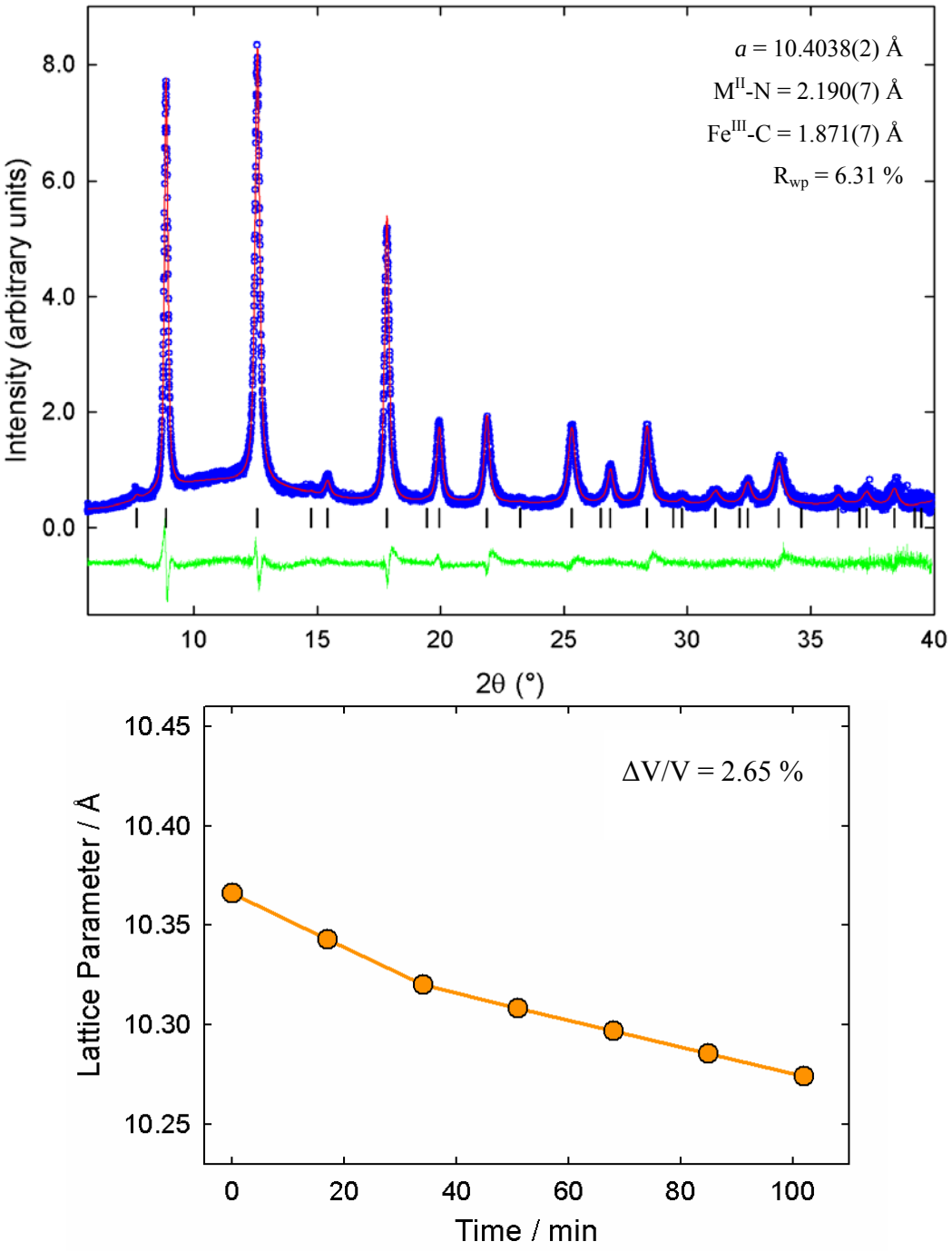

Figure 3.24 Upper: Final observed (blue circles), calculated (red solid line), and difference (lower green solid line) plot for the phase Rietveld refinement of the synchrotron X-ray powder diffraction profile of **4** at 100 K. Tick marks show the reflection positions. The refinement was performed using a single phase in the $Fm\bar{3}m$ space group. Lower: Evolution the lattice constant with increasing illumination time. (Error bars, being significantly smaller, are hidden by the data markers).

3.4.3 Discussion

The photo-induced electron transfer observed in $Rb_{0.7}Mn_{1.15}[Fe(CN)_6]\cdot 2H_2O$ at 295 K is not precluded by replacing a small fraction of Mn^{II} with Ni^{II}, as demonstrated by **1** which contracts at a rate of 0.3901 $Å^3$ min^{-1} under X-ray illumination (λ = 0.8016 Å). At 100 K **1** undergoes an abrupt photoinduced collapse of the unit cell, reminiscent to that of the parent material, due to cooperativity between phototransformed domains or "islands". Thus, despite the inclusion of Fe^{III}(S = 1/2)-CN-Ni^{II}(S = 4) centres, sufficient photoconversion from Fe^{III}-CN-Mn^{II} to Fe^{II}-CN-Mn^{III} occurs to overcome the percolation threshold which elicits a first-order phase transformation. The photo-transformed phase becomes unstable at 10 K and the reverse redox reaction is triggered upon photoirradiation.

As the value of z increases within the $Rb_xNi^{II}_zMn_{(1-z)}[Fe(CN)_6]\cdot yH_2O$ series the periodicity of the redox-active Fe^{III}(S=1/2)-CN-Mn^{II}(S=5/2) units is progressively disrupted with non redox-active Fe^{III}(S=1/2)-CN-Ni^{II}(S=4) units and the effects of internal electron transfer are diminished, thus family members with z > 0.23 are unperturbed by X-ray irradiation at 295 K (see Section 3.2.3). However, photoefficiency improves upon cooling and photoinduced charge transfer is observed at 100 K for **2**, **3**, **4** and **5**. Instinctively the rate of conversion varies inversely with the nickel fraction since the extent of photoconversion is limited by fraction of redox-active units present. These proceed as continuous transitions (as indicated by steady unit cell contractions and overlapping phases) since replacement of redox-active Fe^{III}(S=1/2)-CN-Mn^{II}(S=5/2) units with inactive Fe^{III}(S=1/2)-CN-Ni^{II}(S=4) units prohibits attainment of the percolation threshold necessary for a cooperative abrupt phase transformation to occur.

3.5 Conclusions

We have exploited the flexible nature of the Prussian Blue analogue framework structure and employed rational design to synthesis the novel $Rb_xNi^{II}_zMn_{(1-z)}[Fe(CN)_6]\cdot yH_2O$ family of ternary transition metal mixed ferro-ferrimagnets and in turn demonstrated control over their physical properties via chemical modifications, hydrostatic pressure, and X-ray irradiation. A variety of thermomagnetic behaviours are observed within this series, illustrating the control of magnetic properties via minor changes in chemical composition and reinforcing the suitability of PBAs as candidates for the molecular design of mixed ferro-ferrimagnets. Expansion of this series to include a fourth transition metal ion produces the mixed ferro-ferrimagnet $RbFe_{0.12}Ni_{0.28}Mn[Fe(CN)_6]\cdot 1.94H_2O$, the spontaneous magnetization of which changes sign twice as the sample is cooled from T_N to absolute zero – that is it exhibits two compensation temperature.

Hydrostatic pressure is a powerful tool for tuning the magnetic interactions of PBAs, as demonstrated by the spontaneous magnetization of **3** and **5** which can be reversibly switched from positive and negative directions (and vice versa) via the application of minimal pressures. Pressure is also an effective means of trapping novel inaccessible states, as illustrated by the piezo-induced electron transfer of **3**. The piezo-sensitivity of the $Rb_xNi^{II}_zMn_{(1-z)}[Fe(CN)6]\cdot yH_2O$ series appears to be intrinsically linked to the extent of Ni^{II} doping.

Synchrotron X-ray powder diffraction studies of **1** reveal reversible photoinduced metal-to-metal charge transfers occurring over a range of temperatures, analogous to those of $Rb_{0.7}Mn_{1.15}[Fe(CN)_6]\cdot 2H_2O$. However, photosensitivity in the $Rb_xNi^{II}_zMn_{(1-z)}[Fe(CN)_6]\cdot yH_2O$ series diminishes as the extent of Ni doping increases - electron transfer from Mn^{II} to Fe^{III} only being at 100 K for higher doping levels.

3.6 Bibliography

1. S. I. Ohkoshi, H. Tokoro, M. Utsunomiya, M. Mizuno, M. Abe and K. Hashimoto, *Journal of Physical Chemistry B*, 2002, **106**, 2423-2425.
2. H. Osawa, T. Iwazumi, H. Tokoro, S. Ohkoshi, K. Hashimoto, H. Shoji, E. Hirai, T. Nakamura, S. Nanao and Y. Isozumi, *Solid State Communications*, 2003, **125**, 237-241.
3. Y. Moritomo, K. Kato, A. Kuriki, M. Takata, M. Sakata, H. Tokoro, S. Ohkoshi and K. Hashimoto, *Journal of the Physical Society of Japan*, 2002, **71**, 2078-2081.
4. H. Tokoro, S. Ohkoshi, T. Matsuda, T. Hozumi and K. Hashimoto, *Chemical Physics Letters*, 2004, **388**, 379-383.
5. T. Yokoyama, H. Tokoro, S. Ohkoshi, K. Hashimoto, K. Okamoto and T. Ohta, *Physical Review B*, 2002, **66**, 184111.
6. H. Tokoro, S. Ohkoshi and K. Hashimoto, *Applied Physics Letters*, 2003, **82**, 1245-1247.
7. H. Tokoro, T. Matsuda, T. Nuida, Y. Moritomo, K. Ohoyama, E. D. L. Dangui, K. Boukheddaden and S. I. Ohkoshi, *Chemistry of Materials*, 2008, **20**, 423-428.
8. H. Tokoro, T. Matsuda, K. Hashimoto and S. Ohkoshi, *Journal of Applied Physics*, 2005, **97**, 10M508.
9. E. J. M. Vertelman, E. Maccallini, D. Gournis, P. Rudolf, T. Bakas, J. Luzon, R. Broer, A. Pugzlys, T. T. A. Lummen, P. H. M. van Loosdrecht and P. J. van Koningsbruggen, *Chemistry of Materials*, 2006, **18**, 1951-1963.
10. H. Tokoro and S. I. Ohkoshi, *Applied Physics Letters*, 2008, **93**, 021906.
11. Y. Moritomo, M. Hanawa, Y. Ohishi, K. Kato, M. Takata, A. Kuriki, E. Nishibori, M. Sakata, S. Ohkoshi, H. Tokoro and K. Hashimoto, *Physical Review B*, 2003, **68**, 144106.
12. S. Ohkoshi, T. Iyoda, A. Fujishima and K. Hashimoto, *Physical Review B*, 1997, **56**, 11642-11652.
13. S. Ohkoshi, Y. Abe, A. Fujishima and K. Hashimoto, *Physical Review Letters*, 1999, **82**, 1285-1288.
14. K. Hashimoto and S. Ohkoshi, *Philos T Roy Soc A*, 1999, **357**, 2977-3003.
15. L. Néel, *Annales De Physique*, 1948, **3**, 137-198.
16. S. Ohkoshi and K. Hashimotoi, *Journal of the American Chemical Society*, 1999, **121**, 10591-10597.
17. S. Ohkoshi, O. Sato, T. Iyoda, A. Fujishima and K. Hashimoto, *Inorg Chem*, 1997, **36**, 268.
18. S. Ohkoshi, S. Yorozu, O. Sato, T. Iyoda, A. Fujishima and K. Hashimoto, *Applied Physics Letters*, 1997, **70**, 1040-1042.

19. S.-i. Ohkoshi, K.-i. Arai, Y. Sato and K. Hashimoto, *Nat Mater*, 2004, **3**, 857-861.

20. S. Margadonna, K. Prassides and A. N. Fitch, *Angewandte Chemie-International Edition*, 2004, **43**, 6316-6319.

21. A. C. Larson and R. B. V. Dreele, Los Alamos National Laboratory Report LAUR 86-748, 2004.

22. H. J. Buser, D. Schwarzenbach, W. Petter and A. Ludi, *Inorganic Chemistry*, 1977, **16**, 2704-2710.

Chapter 4

Light-Induced Phase Transitions & Chemical Modifications in a Prussian Blue Analogue Containing Jahn-Teller Active Cu^{2+} Ions

4.1 Introduction

Instances of Prussian Blue analogues which depart from the typical face centred cubic type structure are rare. Unconventional PBA structural symmetries may be accessed via the incorporation of Jahn-Teller active ions, such as Cu^{II}, low spin Co^{II} or high spin Mn^{III}.[1] For example, both $CsCu[Cr(CN)_6]_2 \cdot 2.1H_2O$ and $Cu[Pt(CN)_6]$ adopt tetragonal crystal structures with the $I\bar{4}m2$ and $I4mm$ space groups respectively.[2] High-spin (HS) Mn^{II} ions in PBAs can be converted to Jahn-Teller active HS Mn^{III} ions via the application of an external stimulus - as demonstrated by the $Rb_xA^{II}_zMn_{(1-z)}[Fe(CN)6] \cdot yH_2O$ series discussed in Chapter 3. The structural implications of such a transformation are well illustrated by $RbMn[Fe(CN)_6]$, which undergoes a cubic ($F\bar{4}3m$) to tetragonal ($I\bar{4}m2$) phase transition as a consequence of a thermally induced metal-to-metal charge transfer from Mn^{II} to Fe^{III}.[3] Similar structural cubic to tetragonal structural transitions are impeded in the $Rb_xA^{II}_zMn_{(1-z)}[Fe(CN)_6] \cdot yH_2O$ series because the substitution of Mn^{II} with A^{II} ions disrupts cooperativity.

The Jahn-Teller effect is observed in nonlinear coordination compounds with electronic configurations which are orbitally degenerate in the ground state, the degeneracy arising from the combination of an unfilled d-orbital and a high symmetry environment.[4, 5] Such a nuclear configuration is unstable with respect to nuclear displacements that lower the symmetry and lift the degeneracy.[6] Take, for example, the case of Cu^{II} ion coordinated in an octahedral environment where an elongation or compression of the Cu-ligand bonds parallel to one of the three molecular axes acts to remove the degeneracy of the ^2E_g orbitals (Figure 4.1):[7]

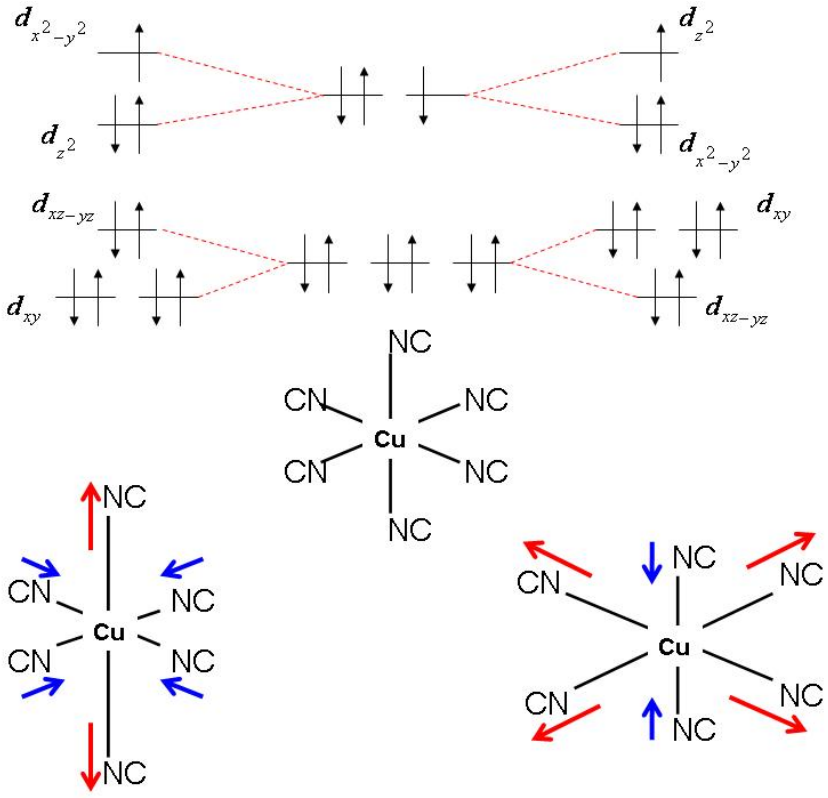

Figure 4.1 Diagram showing the two possible Jahn–Teller splittings of the d-energy levels in an octahedral [$Cu(CN_6)$] complex, and the structural distortions that result from them.

Tetragonal Cu^{II} PBAs arise because the elongation of the Cu-N bonds occurs in a single lattice direction. The Mn^{3+} electronic configuration (t^3_{2g} e^1_g) in the low temperature phase of $RbMn[Fe(CN)_6]$ is degenerate and thus it too undergoes a Jahn-Teller distortion, inducing a cubic to tetragonal structural phase transition in a cooperative manner.

In addition to offering a route to tetragonal symmetries, copper PBAs attract interest because they present several intriguing properties related to the exceptional strength of Cu-NC interaction. This bonding interaction is particularly strong because of the Cu^{2+} ion's tendency to accept electrons from the 5σ orbital of the CN ligand (which is slightly antibonding in character) into its singly occupied 3d orbital in order to approach the optimal $3d^{10}$ configuration.[2, 8] The effects of the strong Cu-NC bond are exemplified by a study of four $M'_3[M(CN)_6]_2$ series (where M' = Mn, Fe, Co, Ni, Cu, Zn, Cd and M = Fe,Co, Rh) in which the copper containing PBAs consistently exhibited atypical behaviours, e.g. shortest unit cell lengths, highest υ(CN)

vibrational frequencies, largest J values (i.e. strongest magnetic exchange interactions) and lowest thermal decomposition temperatures.[2, 8] In a separate study the thermal decomposition of $Cu_3[Fe(CN)_6]\cdot 10H_2O$ was observed to involve the release of CN^- moieties which subsequently participate in the irreversible reduction of ferricyanide units to ferrocyanides:[9] $[Fe(CN)_6]^{3+} + CN^- \rightarrow [Fe(CN)_6]^{4-} + \frac{1}{2} C_2N_2$.

As previously mentioned there are limited examples of PBAs which adopt tetragonal structures in the ground state at room temperature, and to the best of our knowledge the photo-responsiveness of such materials is yet to be reported. Two types of photoinduced transformations are typically encountered in PBAs: (i) internal metal (M^{II})–to–metal (M^{III}) charge transfer and (ii) spin crossover of the M^{II} ions. As discussed in the introductory chapter, the former process may be observed upon photoirradiation of $CsFe^{II}[Cr^{III}(CN)_6]$. The photoinduced internal spin rearrangement, from Fe^{II}(HS, S = 2 , $t_{2g}^4e_g^0$)-Cr^{III}(S = 3/2, $t_{2g}^3e_g^0$) to Fe^{II}(LS, S = 2, $t_{2g}^6e_g^0$)-Cr^{III}(S = 3/2, ^{3}is $t_{2g}^3e_g^0$), is notable because it occurs without any charge transfer. Internal charge transfer is responsible for many of the photomagnetic effects observed in photoswitchable molecule-based magnets. For example, the enhancement of magnetization which occurs upon red light irradiation of $K_{0.2}Co_{1.4}[Fe(CN)_6]\cdot 6.9H_2O$ at 5K (as detailed in Chapter 1) is driven by an internal electron transfer. Herein, the preparation and characterization of Jahn-Teller active caesium copper hexacyanoferrates is described. The aim of this work was to establish the influence of structural distortions on the photomagnetic phenomenona which have been observed in other PBAs.

4.2 Experimental

The target compounds were prepared by slow, dropwise addition of a mixed aqueous solution (10 ml) of CsCl (1 M) and $FeCl_2$ (0.1 M) to a mixed aqueous solution (10 ml) of CsCl (1 M) and $K_3[Cr(CN)_6]$. The resultant precipitates were recovered by filtration and dried under vacuum. The quality of the final product was found to gradually deteriorate on standing at ambient temperatures, thus it was necessary to use a freshly prepared sample for each round of synchrotron X-ray irradiation experiments. Elemental compositions were determined using inductively coupled plasma optical emission spectroscopy (ICP-OES) in combination with thermogravimetric analyses. Magnetic properties were measured using a Quantum Design SQUID magnetometer. Synchrotron X-ray powder diffraction (XRPD) and X-ray absorption near edge structure (XANES) spectroscopy measurements were collected, on beamlines ID31 and BM29 respectively, at the European Synchrotron Radiation Facility (ESRF), Grenoble, France. Diffraction profile analyses were performed using the GSAS suite of Rietveld analysis programs.[10]

4.3 Results

4.3.1 Structure Determination

Stoichiometries of the resultant compounds, as determined from elemental analysis, are $CsCu[Fe(CN)_6]\cdot 0.3H_2O$ **(1)** and $Cs_{0.84}Cu_{1.08}[Fe(CN)_6]\cdot 0.48H_2O$ **(2)**. Rietveld analysis of XRPD data collected at 295 K were performed using the generic structural model of mixed valence metal cyanides, comprising a three-dimensional network of $\{Cu(CN)_6\}$ and $\{Fe(CN)_6\}$ octahedra linked by CN ligands. Powder diffraction patterns of **1** indicate that it adopts the body-centred tetragonal lattice *I4/mmm* (Figure 4.2 overleaf). The lattice parameters of **1** are $a = b = 7.16233(7)$ Å and $c = 10.9740(5)$ Å (these values correspond to $\sqrt{a^2 + b^2} = 10.1291(1)$ Å and $c = 10.9740(5)$ Å in the cubic lattice of a Prussian Blue structure). The two long and four short Cu-N bonds of the Jahn-Teller active $[Cu(NC)_6]$ octahedra refine to 2.48(1) and 2.5205(2) Å respectively, while the Fe-C bonds of $[Fe(CN)_6]$ octahedra

refine to 1.8989(1) and 1.95295(2) Å. The agreement factors are R_1 = 9.94 %, R_{wp} = 11.57 %, R_{exp} = 2.51 %.

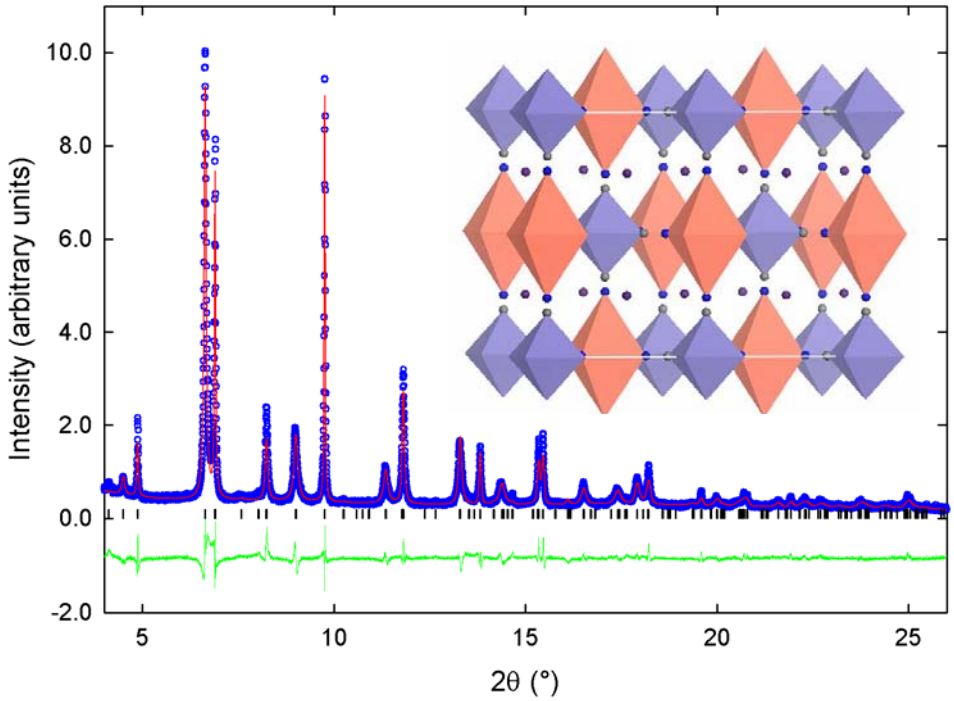

Figure 4.2 Final observed (blue circles), calculated (red solid line), and difference (lower green solid line) plots for the single-phase Rietveld refinement of **1** at 295 K (λ = 0.4309 Å). Tick marks show the reflection positions. Inset: Building block of the tetragonal framework structure of **1**. Alternating Jahn-Teller distorted $[Cu(NC)_6]$ (peach) and $[Fe(CN)_6]$ (lilac) octahedra are bridged by CN ligands.

Table 4.1 Refined structure parameters of the major phase of **1** at 295 K. Estimated errors in the last digits are given in parentheses.

	n	**x**	**y**	**z**	**Wyckoff Position**	**B_{iso} (Å^2)**
Fe	0.951(4)	0	0	0	2a	1.7(1)
Cu	1	0	0	1/2	2b	1.7(1)
Cs	0.951(4)	0	1/2	1/4	4d	2.35(8)
C3	0.951(4)	0	0	0.174 (1)	4e	3.2(2)
N4	0.951(4)	0	0	0.274(1)	4e	3.2(2)
C5	0.951(4)	0.191(1)	0.191(1)	0	8h	3.2(2)
N6	0.951(4)	0.298(1)	0.298(1)	0	8h	3.2(2)

Rietveld analysis of **2** employed a two-phase structural model (Figure 4.3). The space group of the major (83.95(3) %) tetragonal phase is *I4/mmm*. The refined tetragonal lattice parameters are $a = b = 7.1618(1)$ Å and $c = 10.852(1)$ Å (these values correspond to $\sqrt{a^2 + b^2} = 10.1283(2)$ Å and $c = 10.852(1)$ Å in the cubic lattice of a Prussian Blue structure). In the major phase the two long and four short Cu-N bonds of the Jahn-Teller active $[Cu(NC)_6]$ octahedra refine to 2.5108(3) and 1.97308(4) Å respectively, while the Fe-C bonds of the $[Fe(CN)_6]$ octahedra refine to 1.98371(4) and 1.8048(2) Å. The space group of the minor (16.0(3) %) cubic phase is $Fm\bar{3}m$. The cubic lattice parameter refines to $a = 10.258(3)$ Å. The Cu-N bond of the minor phase refines to 2.2116(6) Å, while the Fe-C bond refines to 1.8106(5) Å. The agreement factors are $R_1 = 11.42$ %, $R_{wp} = 10.86$ %, $R_{exp} = 4.54$ %.

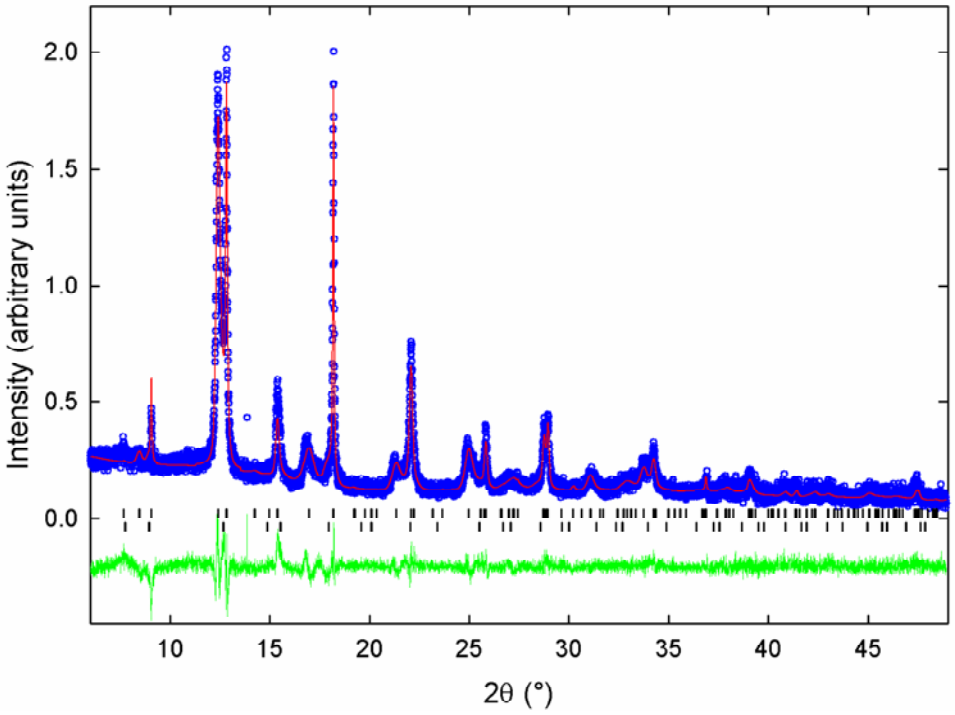

Figure 4.3 Final observed (blue circles), calculated (red solid line), and difference (lower green solid line) plots for the two-phase Rietveld refinement of **2** at 295 K (λ = 0.8010 Å). Tick marks show the reflection positions, the upper row and lower rows correspond to the *I4/mmm* and phases $Fm\bar{3}m$ respectively.

Table 4.2 Refined structure parameters of the major (a) and minor (b) phases of **2** at 295 K. Estimated errors in the last digits are given in parentheses.

a) Major Phase

	n	**x**	**y**	**z**	**Wyckoff Position**	**B_{iso} (Å^2)**
Fe	0.931(6)	0	0	0	2a	4.3(1)
Cu	1	0	0	1/2	2b	4.3(1)
Cs	0.487(3)	0	1/2	1/4	4d	0.86(9)
C3	0.931(6)	0	0	0.1663(7)	4e	4.1(2)
N4	0.931(6)	0	0	0.2686(7)	4e	4.1(2)
C5	0.931(6)	0.1959(8)	0.1959(8)	0	8h	4.1(2)
N6	0.931(6)	0.3052(8)	0.2876(7)	0	8h	4.1(2)

b) Minor Phase

	n	**x**	**y**	**z**	**Wyckoff Position**	**B_{iso} (Å^2)**
Fe	0.931	0	0	0	4a	1.97
Cu	1	1/2	1/2	1/2	4b	1.97
Cs	0.487	1/4	1/4	1/4	8c	1.97
C	0.931	0.1765(1)	0	0	24e	1.97
N	0.931	0.284(5)	0	0	24e	1.97

4.3.2 Photoirradiation Studies of $CsCu[Fe(CN)_6]\cdot 0.3H_2O$ (1)

Synchrotron X-ray powder diffraction studies (λ = 0.4309 Å) of $CsCu[Fe(CN)_6]\cdot 0.3H_2O$ **(1)** at several temperatures show that the tetragonal (*I4/mmm*) crystal structure is retained down to 80 K. Monitoring the evolution of the diffraction profiles with exposure time under laser (532 nm) illumination at 80 K reveals that **1** undergoes a continuous laser induced tetragonal to cubic phase transformation (Figure 4.4).

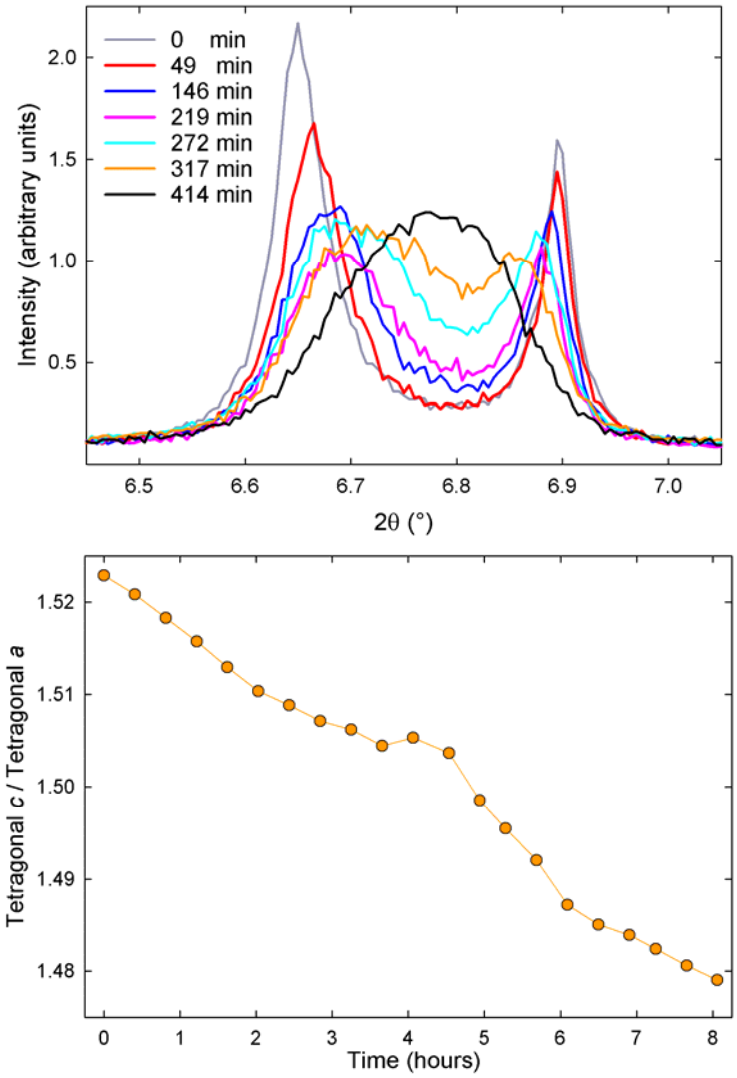

Figure 4.4 a) Time evolution of the tetragonal reflections, (112) and (200), of **1** as they collapse into the cubic reflection (220) under laser (532 nm) illumination at 80 K (λ = 0.4309 Å). b) Ratio of the tetragonal lattice parameters (c/a) as a function of time. Error bars, being considerably smaller, are hidden by data markers.

The collapse of the two tetragonal reflections, (112) and (200), into a single cubic reflection (220) with increasing laser exposure time is shown in Figure 4.4 above. No such structural transition is observed in the analogous study of **1** at 80 K in the absence of laser irradiation, thus allowing laser-induced effects to be confidently decoupled from X-ray induced effects. Plotting the phase fractions and lattice parameters of the original and photo-generated phases as a function of time at 80 K (Figure 4.5) confirms that the tetragonal to cubic phase transformation is a gradual, continuous process.

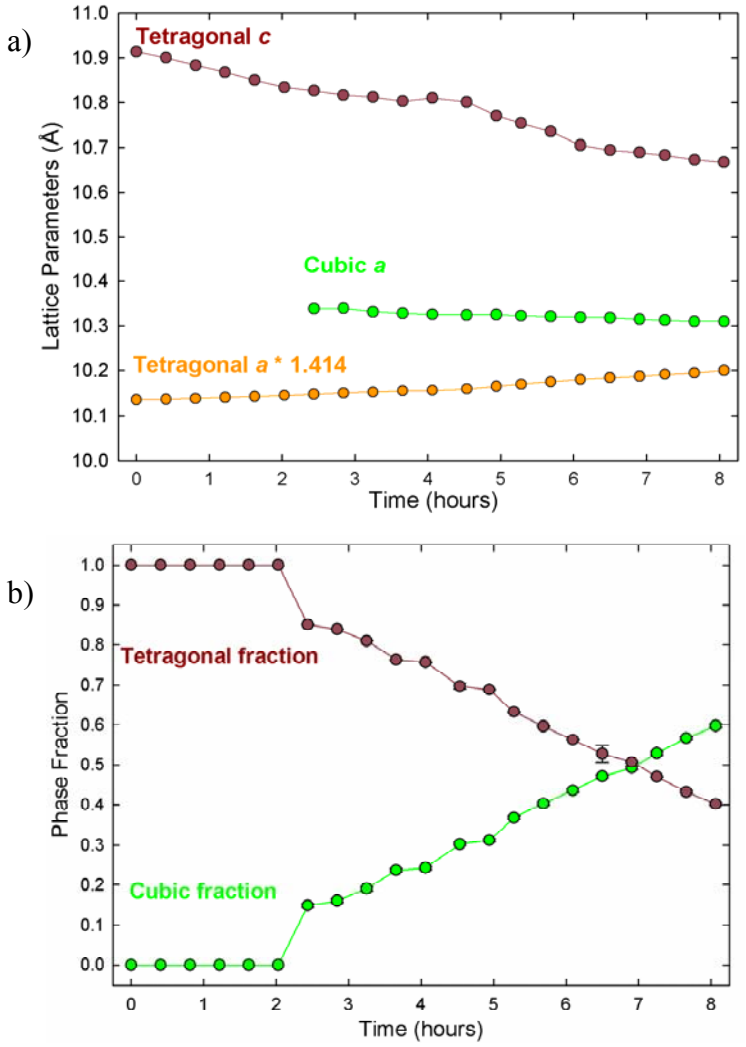

Figure 4.5 a) Evolution of the cubic (green circles) and tetragonal (a = orange circles c = brown circles) lattice parameters of **1** with increasing X-ray irradiation time. b) Evolution of the cubic (green circles) and tetragonal (brown circles) phase fractions with increasing X-ray irradiation time. Some error bars in a) and b), being considerably smaller, are hidden by data markers.

Rietveld analysis of the laser transformed phase of **1** employed a two-phase structural model with a 57.2(4) % cubic ($Fm\bar{3}m$) phase and 42.7(3) % tetragonal (*I4/mmm*) phase (Figure 4.6). The refined lattice constant of the majority cubic phase is a = 10.3091(9) Å, while those of the minority tetragonal phase are a = 7.2075(7) and c = 10.681(6) Å (these values correspond to $\sqrt{a^2 + b^2}$ = 10.1929 Å and c = 10.681(6) Å in the cubic lattice of a Prussian Blue structure). In the major phase the Cu-N and Fe-C bond lengths refine to 2.1627(2) and 1.8951(2) Å respectively. In the minor phase the Cu-N bond lengths of the Jahn-Teller active $[Cu(CN)_6]$ octahedra refine to 2.388(8) and 2.162(7) Å, while the Fe-C bonds of the $[Fe(CN)_6]$ octahedral refine to 1.861(8) and 1.836(6) Å. The agreement factors are R_1 = 8.31 %, R_{wp} = 9.70 % and R_{exp} = 5.63 %.

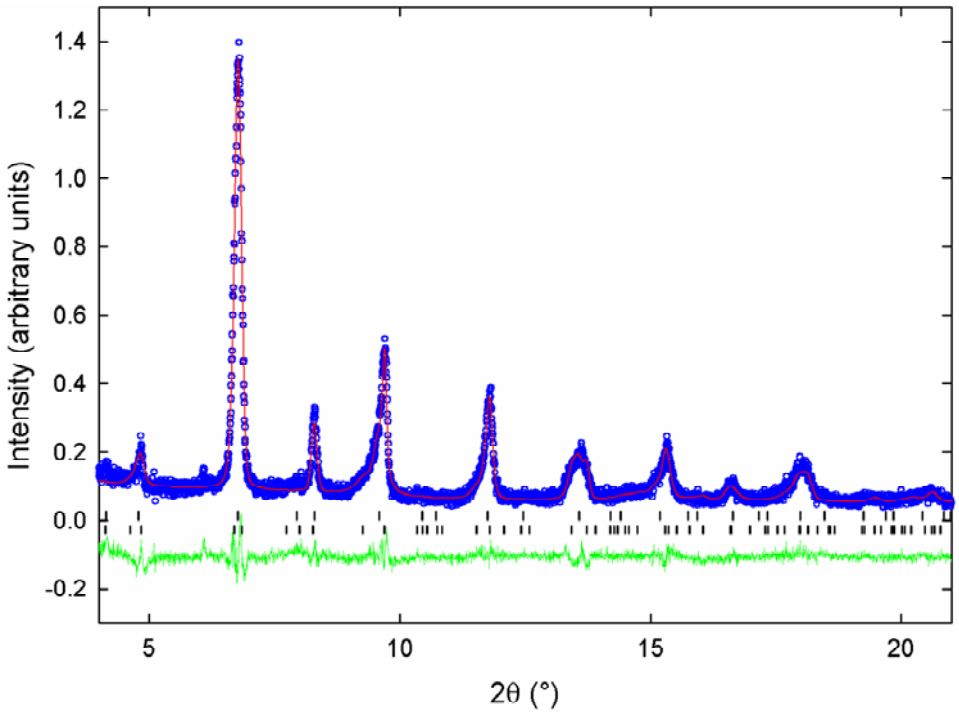

Figure 4.6 Final observed (blue circles), calculated (red solid line), and difference (lower green solid line) plots for the two-phase Rietveld refinement of phototransformed **1** at 80 K (λ = 0.4309 Å). Tick marks show the reflection positions, the upper row and lower rows correspond to the $Fm\bar{3}m$ (57.2(4) %) and *I4/mmm* (42.7(3) %) phases respectively.

Table 4.3 Refined structure parameters of the major (a) and minor (b) phases of phototransformed **1** at 80 K. Estimated errors in the last digits are given in parentheses.

a) Major Phase

	n	**x**	**y**	**z**	**Wyckoff Position**	**B_{iso} (Å^2)**
Fe	1	0	0	0	4a	6.1(3)
Cu	1	1/2	1/2	1/2	4b	6.1(3)
Cs	0.5	1/4	1/4	1/4	8c	3.4(2)
C	1	0.1838(7)	0	0	24e	3.1.(4)
N	1	0.2902(8)	0	0	24e	3.1.(4)

b) Minor Phase

	n	**x**	**y**	**z**	**Wyckoff Position**	**B_{iso} (Å^2)**
Fe	1	0	0	0	2a	1.22(5)
Cu	1	0	0	1/2	2b	1.22(5)
Cs	0.5	0	1/2	1/4	4d	9.0(2)
C3	1	0	0	0.1749(7)	4e	4.1(1)
N4	1	0	0	0.2769(8)	4e	4.1(1)
C5	1	0.1800(6)	0.1800(6)	0	8h	4.1(1)
N6	1	0.2876(7)	0.2876(7)	0	8h	17(2)

cubic phase induced by laser irradiation at 80 K is observed to persist upon warming to 250 K. Synchrotron X-ray powder diffraction studies (λ = 0.4309 Å) of the phototransformed phase of **1** between 80 and 250 K reveal a volume contraction (Figure 4.7 overleaf). The coefficient of thermal expansion (α_V) for **1** is -14.8 x 10^{-6} K^{-1}, as determined from the following equation:

$$\alpha_V = \frac{V_T - V_0}{V_0 (T - T_0)} \qquad (4.1)$$

where V_0 is the initial volume, V_T the final volume, T_0 the initial temperature and T the final temperature.[11]

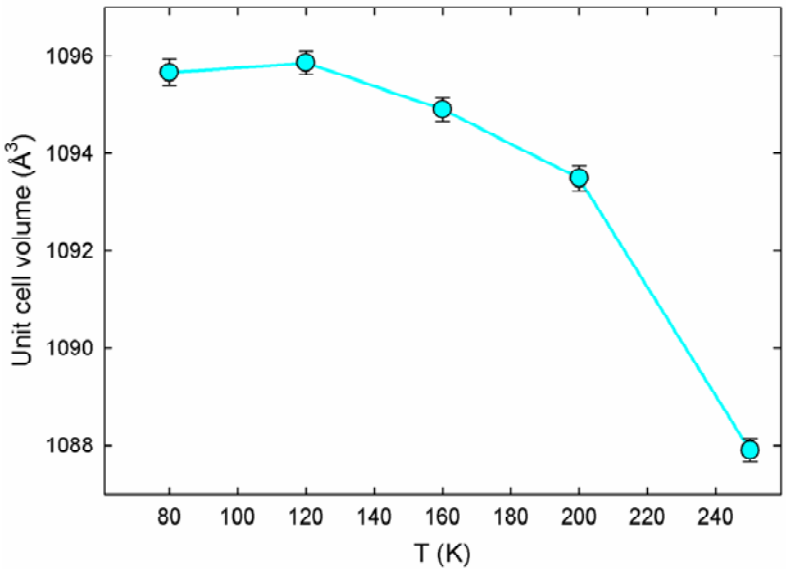

Figure 4.7 Temperature dependency of the unit cell volume of the laser induced cubic phase of **1** (λ = 0.4309 Å).

The oxidation states of the Cu and Fe centres in the tetragonal (untransformed) and cubic (phototransformed) phases were determined from XANES measurements of **1** (Figure 4.8)**.** The Fe K-edge spectra do not show any significant changes upon cooling from room temperature to 2 K, however the 7.130 keV absorption shifts to 7.129 keV upon laser (523 nm) illumination at 2 K. This lower energy absorption peak remains unaltered after 9 hours of laser irradiation and persists on warming to 300 K in the absence of laser irradiation. Comparison with the spectra of reference materials $K_3[Fe(CN)_6]$ and $K_2[Fe(CN)_6]$ reveals that this shift to lower energy corresponds to the reduction of the Fe^{3+} ions to Fe^{2+}. The Cu K-edge spectra also remain unchanged on cooling from room temperature to 2 K. A satellite absorption appears at 8.982 keV upon laser irradiation at 2 K. It too is unchanged by further laser irradiation and warming to 300 K. On the basis of the CuO and Cu_2O reference spectra, the emergence of this peak at 8.982 keV is attributed to the reduction of Cu^{2+} to Cu^{+}.

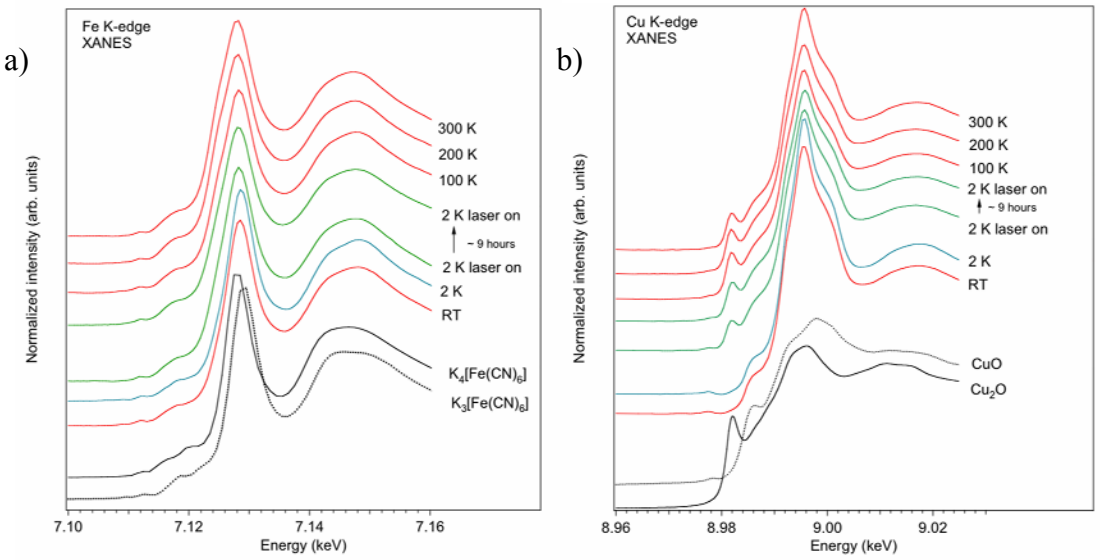

Figure 4.8 Cu (a) and Fe (b) K-edge spectra of **1** at RT and 2 K prior to laser irradiation; at 2 K under laser illumination; at 2 K after 9 hours laser irradiation and warming of the phototransformed phase in the absence of laser illumination . The spectra of the $K_4[Fe(CN)_6]$, $K_3[Fe(CN)_6]$, CuO and Cu_2O reference compounds are also shown.

4.3.3 Photoirradiation Studies of $Cs_{0.84}Cu_{1.08}[Fe(CN)_6]\cdot 0.48H_2O$ (2)

Synchrotron X-ray powder diffraction studies showed that $Cs_{0.84}Cu_{1.08}[Fe(CN)_6]\cdot 0.48H_2O$ **(2)** (λ = 0.8010 Å) retains its tetragonal crystal structure down to 5 K. Monitoring the evolution of the diffraction profiles with increasing X-ray exposure time revealed that **2** undergoes a tetragonal to cubic phase transformation, with the rate of transformation being inversely proportion to temperature. The tetragonal to cubic X-ray induced transformation of **2**, at both 5 and 80 K, proceeds more efficiently than the laser induced transformation of **1** at 80 K (Figure 4.9). The X-ray induced transformations of **2** at 5 K and 100 K are complete after two hours, whereas even after 8 hours of laser irradiation at 80 K only 60% of the tetragonal phase of **1** had been converted to the cubic phase.

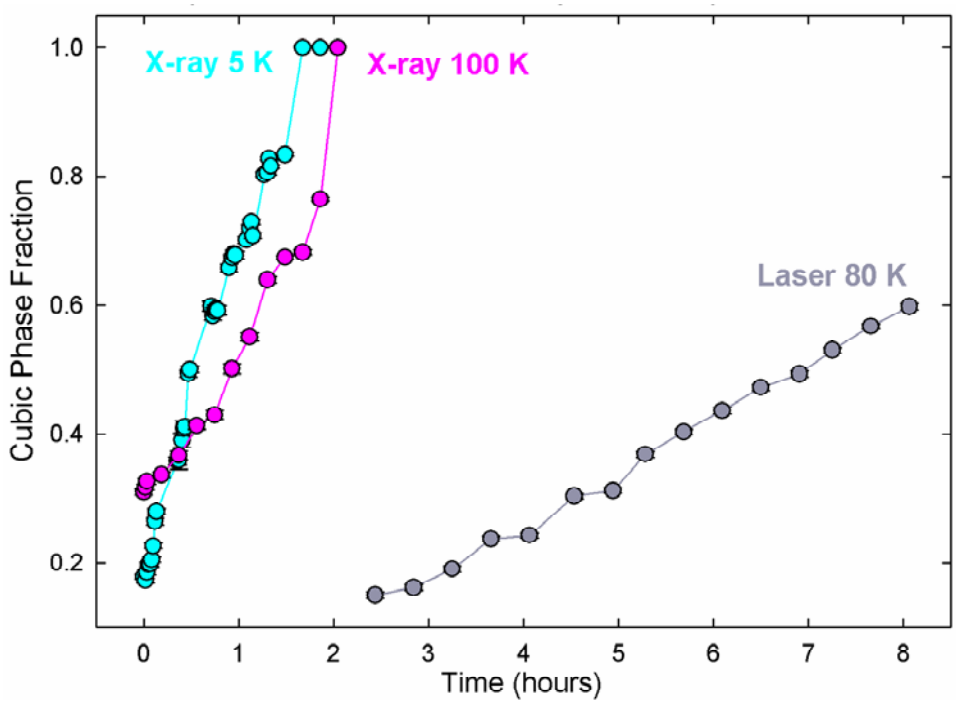

Figure 4.9 a) Evolution of the cubic phase fraction of **2** with increasing X-ray (λ = 0.8010 Å) irradiation time at 5 K (cyan circles) and 100 K (pink circles) compared with that of **1** at 80 K under laser (532 nm) illumination (grey circles). Some error bars, being considerably smaller, are hidden by data markers.

Figure 4.10, overleaf, shows the phase fractions and lattice parameters of the cubic and tetragonal phases of **2** as a function of time at 5 K. The predominant tetragonal phase (82.20(4) %) of **2** is transformed to the cubic phase over 1.5 hours. The X-ray

induced growth of the cubic phase is accompanied by an increase in the cubic unit cell length from 10.257(2) to 10.3108(5) Å. The shorter of the two tetragonal unit cell edges (*a*) progressively lengthens from 7.1781(2) to 7.252(1) Å during the 1.5 hour irradiation period, while the longer cell edge (*c*) gradually contracts from 10.754(2) to 10.431(7) Å with increasing X-ray exposure time.

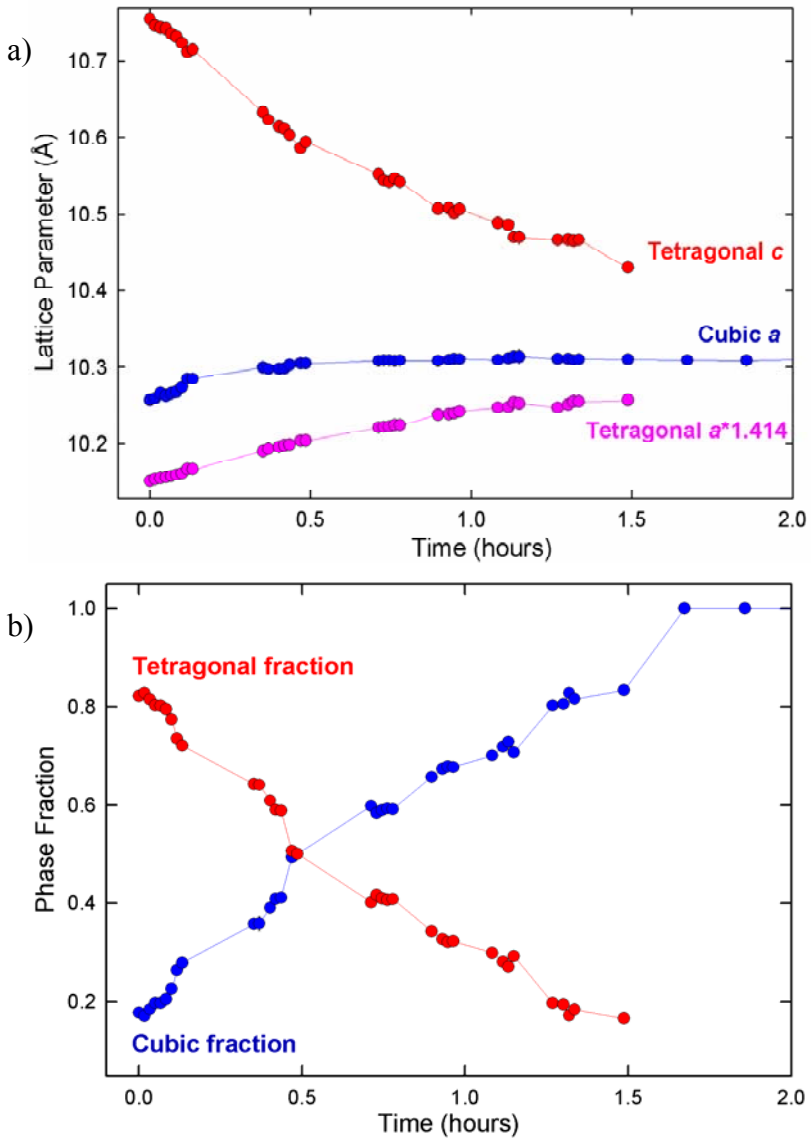

Figure 4.10 a) Evolution of the cubic (blue circles) and tetragonal (a = pink circles c = red circles) lattice parameters of **2** with increasing X-ray irradiation time. b) Evolution of the cubic (blue circles) and tetragonal (red circles) phase fractions with increasing X-ray irradiation time. Some error bars, being considerably smaller, are hidden by data markers.

The Rietveld analysis of **2** after 1.5 hours X-ray irradiation at 5 K was performed with a single cubic phase ($Fm\bar{3}m$) (Figure 4.11).

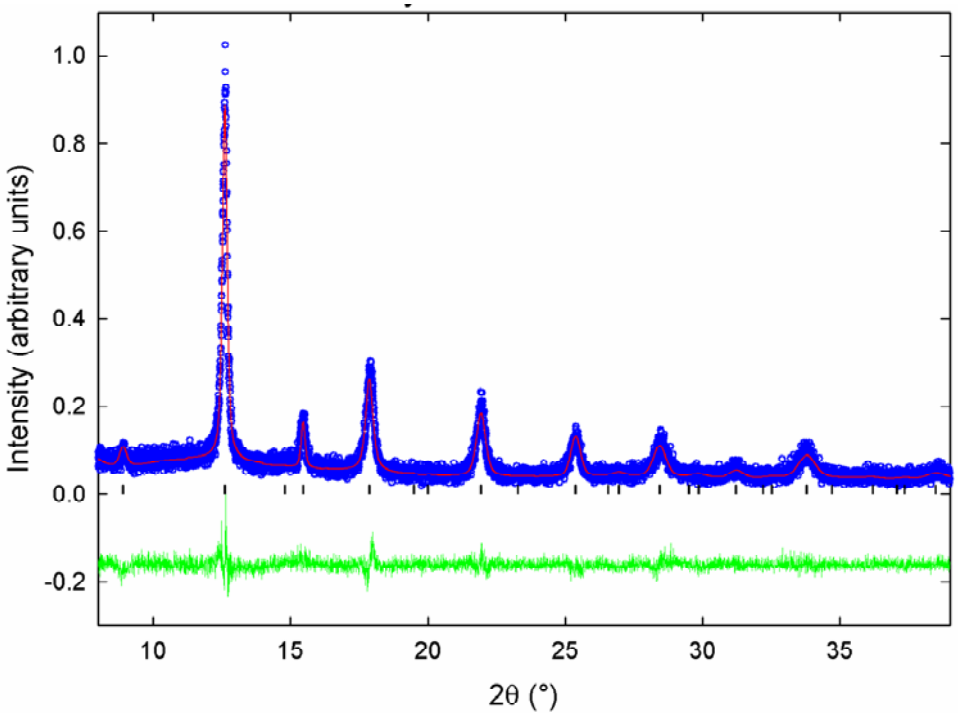

Figure 4.11 Final observed (blue circles), calculated (red solid line), and difference (lower green solid line) plots for the Rietveld refinement of phototransformed **2** at 5 K (λ = 0.8010 Å). Tick marks show the reflection positions.

Table 4.4 Refined structure parameters of phototransformed 2 at 5 K. Estimated errors in the last digits are given in parentheses.

	n	**x**	**y**	**z**	**Wyckoff Position**	**B_{iso} (Å^2)**
Fe	1	0	0	0	4a	6.4(2)
Cu	1	1/2	1/2	1/2	4b	6.4(2)
Cs	0.5	1/4	1/4	1/4	8c	0.4(1)
C	1	0.177(1)	0	0	24e	8.4(4)
N	1	0.284(1)	0	0	24e	8.4(4)

The refined lattice parameter of the final X-ray induced cubic phase is *a* = 10.3109(5) Å. The Cu-N bond lengths refine to 2.23(2) Å, the Fe-C bond length to 1.83(2) Å. The agreement factors are R_1 = 11.86 %, R_{wp} = 14.75 %, R_{exp} = 8.34 %.

Synchrotron X-ray powder diffraction studies (λ = 0.8010 Å) over a range of temperatures reveal that the phototransformed phase of **2,** like that of laser induced phase of **1**, persists upon warming and undergoes a small negative thermal expansion (Figure 4.12). The coefficient of thermal expansion (α_V) for **2** is -36.3 x 10^{-6} K^{-1}.

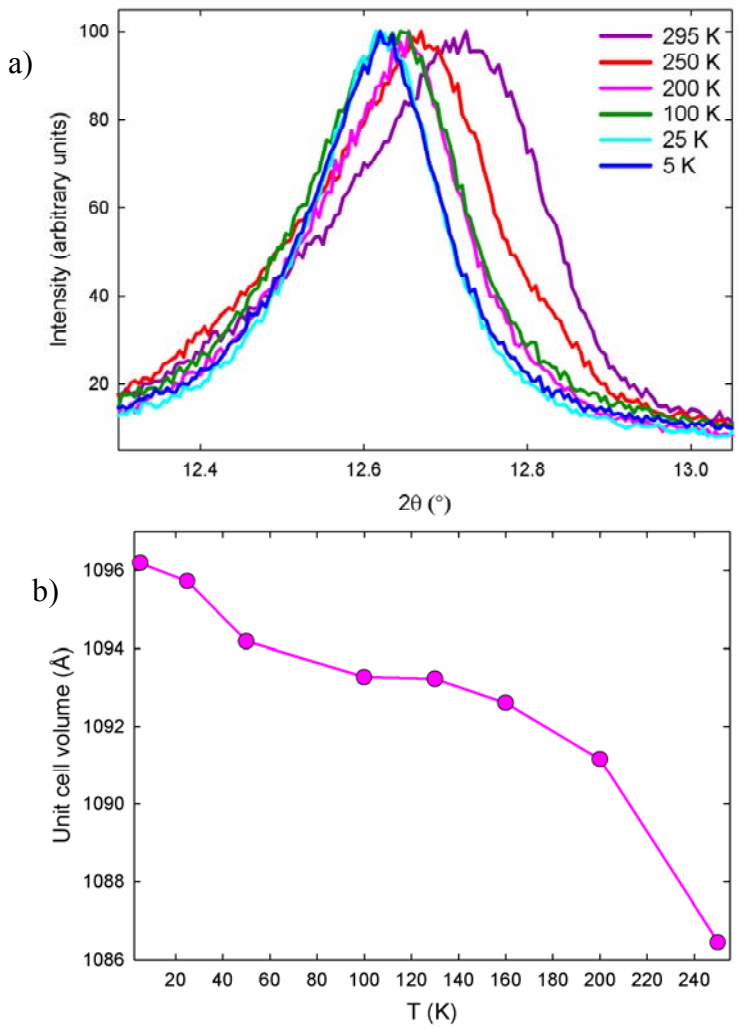

Figure 4.12 Negative thermal expansion of the X-ray induced cubic phase of **2** (λ = 0.8010 Å). a) Shift of the (200) reflection to lower angles with decreasing temperature. b) Plot of unit cell volume versus temperature.

4.3.4 Magnetic Properties of $Cs_{0.84}Cu_{1.08}[Fe(CN)_6]\cdot 0.48H_2O$ (2)

The field-cooled (FC) magnetization curve of $Cs_{0.84}Cu_{1.08}[Fe(CN)_6]\cdot 0.48H_2O$ **(2)** recorded in a 1 mT field shows a rapid increase in the spontaneous magnetization below 20 K, indicating the onset of magnetic ordering (Figure 4.13 overleaf). Plots of $\chi_m T$ versus T recorded upon heating and cooling verify the absence of a temperature induced phase transition.

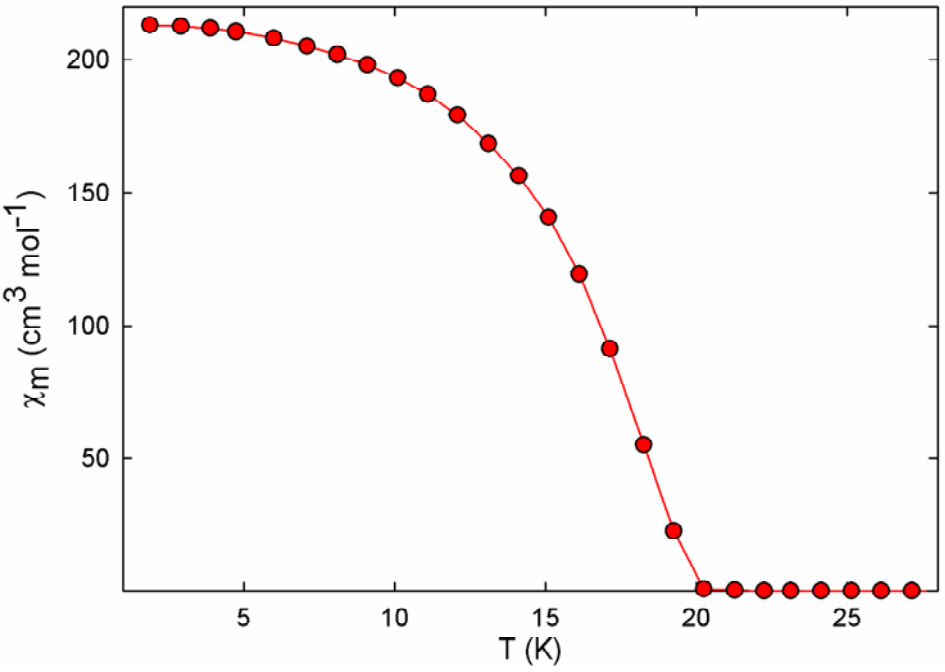

Figure 4.13 Field-cooled (FC) molar susceptibility of **2** in a 1mT field.

Plotting χ_m and χ_m^{-1} as a function of temperature indicates that **2** exhibits Curie-Weiss behaviour in the 100-300 K temperature region (Figure 4.14 overleaf). The positive value of the Weiss temperature (21.2 K), determined from the plot of χ_m^{-1} vs T, is indicative of ferromagnetic exchange interactions between the Cu^{II} and Fe^{III} ions. The effective magnetic moment of **2** as determined from the Curie constant ($\mu_{eff} = 2.828\sqrt{C}\ \mu_B$) is 2.64 μ_B. The magnetization cannot be saturated by the 0.5 T measuring field, as shown by the magnetic hysteresis loop recorded at 2 K (Figure 4.15 overleaf).

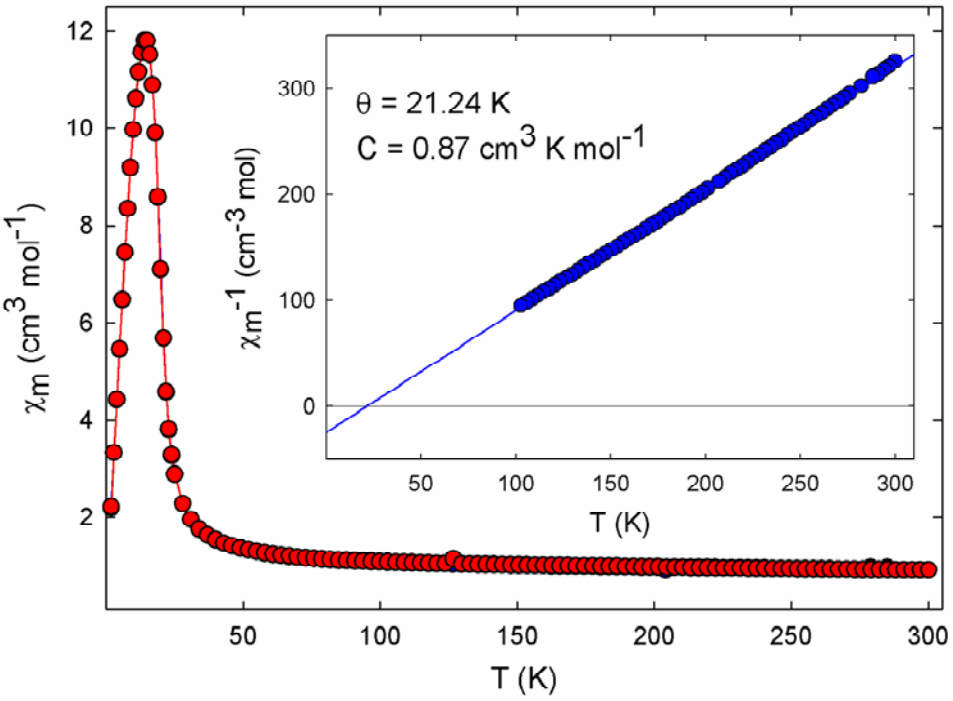

Figure 4.14 Molar susceptibility of **2** upon heating (red circles) and cooling (blue circles, obscured) in a 0.5 T field. Inset: inverse molar susceptibility of **2** in the temperature region 100-300 K, with least squares fitting.

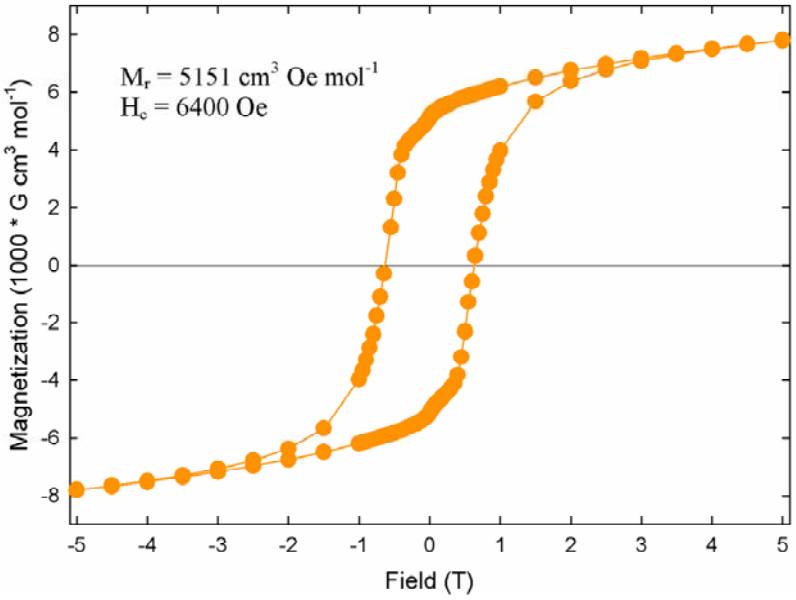

Figure 4.15 Magnetization (M) of **2** versus applied field (T) at 2 K. The magnetization versus applied field data for **2** exhibits a large hysteresis loop with a coercive field of 6400 Oe at 2 K.

4.4 Discussion

Compound **2,** a novel caesium copper hexacyanoferrate, is a ferromagnet with a θ = 21.24 K. There is yet to be a systematic investigation of the influence of the identity of the M ion on the magnetic properties of the $Cs_xM^{II}[Fe'^{III}(CN)_6]_y$ family of PBAs. However, the fact that the T_c of **2** is substantially higher than those of related hexacyanoferrates $Cs_{0.175}Co[Fe(CN)_6]_{0.72}\cdot 4H_2O$[12] and $Cs_{1.51}Mn^{II}[Fe^{II}(CN)_6]_{0.51}[Fe^{III}(CN)_6]_{0.49,}$ which order at 16 K and 5.6 K respectively, may reflect the strong magnetic exchange interactions typically associated with the Cu^{II} ion. The large hysteresis loop (with a coercive field of 6400 Oe) exhibited by **2** at 2 K makes it is one of the hardest ferromagnetic PBAs reported to date and thus shows particular promise for the development of molecule-based magnetic storage devices.

The tetragonal structures of **1** and **2** are a consequence of the strong cooperativity of the Jahn-Teller distorted Cu^{II} ions and the elongation of Cu-N bonds in a single lattice direction. Studies of related caesium copper hexacyanoferrates reveal that a stoichiometry close to the ideal 1:1:1 ratio is key to obtaining a tetragonal, rather than cubic, lattice. The presence of $[Fe(CN)_6]$ vacancies and the subsequent incorporation of water into the coordination sphere of Cu^{II} lifts the orbital degeneracy and disrupts the Cu^{II} cooperativity essential to the observation of a tetragonal lattice. In the absence of any other external stimuli, the structures of both **1** and **2** remain unperturbed by thermal variations.

Photoirradiation studies of **1** and **2** present several intriguing results. Irreversible tetragonal to cubic structural phases transitions – which are not thermally accessible - are observed upon laser (532 nm) irradiation of **1** and X-ray (λ = 0.8010 Å) irradiation of **2.** The X-ray induced transition of **2** proves to be much more efficient than the laser induced transition of **1.** The origin of this difference becomes apparent when we consider that the penetration depth of the green laser is significantly inferior compared to that of the synchrotron generated X-ray beam. Complete laser- induced conversion is observed in XANES studies because **1** is mounted as a very thin sample on tape; rather than densely packed in a capillary.

We can confidently decouple laser (532 nm) and X-ray induced (λ = 0.4309 Å) phenomena in the photoirradiation studies of **1** because powder diffraction data show that the structure remains unperturbed, down to the lowest measuring temperature of 80 K, in the absence of laser irradiation. It is somewhat counter-intuitive that these copper hexacyanochromates are transformed by X-rays with λ = 0.8010 Å but not those with λ = 0.4309 Å since we expect better photoconversion for higher energy (shorter) wavelengths. However, for these copper hexacyanochromates it is the flux at the sample, rather than the energy of the impinging radiation, which is the determining factor in the rate of photoconversion. The flux at the sample on beamline ID31 is directly related to X-ray wavelength. For example, measurements at λ = 0.43 Å show that the flux is 1.5×10^{12} photons mm^{-2} s^{-1}, while at 0.85 Å this value increases to 6.1×10^{12} photons mm^{-2} s^{-1}.[13] Therefore, the rate at which photons impinge upon **1,** when λ = 0.4309 Å, is significantly lower than the rate of photons impinging on **2,** when λ = 0.8010 Å and consequently the longer wavelengths prove to be the more effective stimulus.

Diffraction patterns of the photo-transformed phases of **1** and **2** collected over a range of temperatures indicate that the cubic phase persists up to at least 250 K. These cubic phases exhibit the rare phenomenon of negative thermal expansion (NTE), meaning that – in contrast to the vast majority of materials - they contract upon heating. The contraction of **1** is quantified by a coefficient of thermal expansion of between 5 and 200 K. Negative thermal expansion has been observed in a number of PBA systems and is thought to originate from the population of transverse vibrational modes (which typically lie at lower energies than longitudinal modes) and the subsequent lateral displacement of atoms from their mean positions. Excitation of the transverse vibrational modes responsible for NTE can be likened to plucking a guitar string. Imagine a linear chain of atoms linked by such a string. As the string is stretched by the plucking motion the atoms are drawn closer to one another. The NTE phenomenon is not uncommon amongst the PBAs with the dynamic flexibility of the M'-CN-M building block giving rise to a number of low-energy lattice vibrations which contribute to NTE.[14]

The irreversibility of the photoinduced transformations of **1** and **2** is indicative of a chemical modification rather the metal-to-metal charge transfer process typically associated with PBAs. The absence of such internal electron transfers in these materials is attributed to the high energy of the Frank-Condon excited state, a result of the Jahn-Teller distortions, which means it is not easily accessible – even via X-ray irradiation. XANES measurements reveal that the phase transition is accompanied by the simultaneous reduction of Cu^{2+} to Cu^{+} and Fe^{3+} to Fe^{2+}. We propose the following chemical reaction to explain the reduction of both transition metal centres and tetragonal to cubic structural phase transition: $CsCu^{2+}[Fe^{3+}(CN)_6]$ → $CsCu^{+}[Fe^{2+}(CN)_4] + (CN)_2$. The resultant Cu^{+} ($3d^{10}$, S=0) ion is not Jahn-Teller active and favours tetrahedral coordination geometry, as does the Fe^{2+} ion (Figure 4.16), thereby accounting for the structural properties of the photo-induced disordered cubic phase.

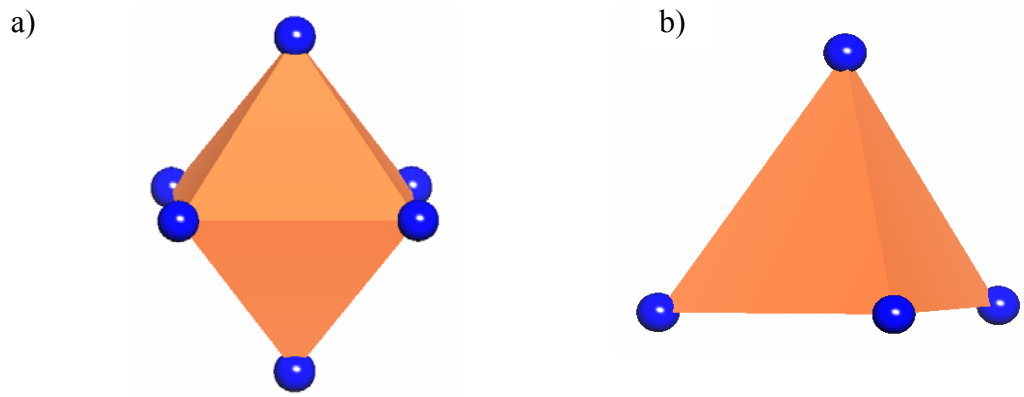

Figure 4.16 a) Octahedral coordination environment in the untransformed tetragonal phase of **1** and **2**. b) Tetrahedral coordination environment in the phototransformed cubic phase of **1** and **2**.

The building block of the cubic framework structure of the phototransformed materials is shown overleaf in Figure 4.17, with alternating $[Cu(NC)_4]$ (peach) and $[Fe(CN)_4]$ (lilac) tetrahedra bridged by CN ligands.

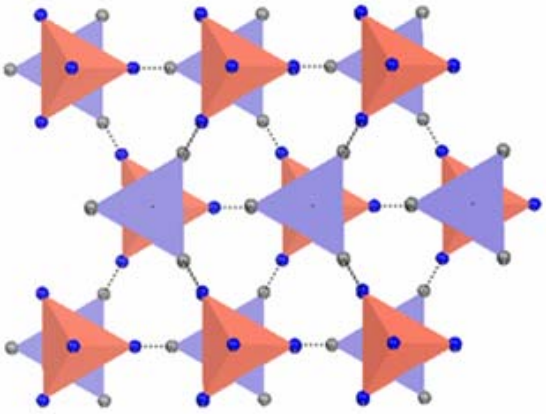

Figure 4.17 Building block of the cubic framework structure of the phototransformed phases of **1** and **2.** Alternating $[Cu(NC)_4]$ (peach) and $[Fe(CN)_4]$ (lilac) tetrahedra bridged by CN ligands.

4.5 Conclusions

Both laser and X-ray irradiation can trigger a tetragonal-to-cubic phase transition, which is not thermally accessible, in caesium copper hexacyanoferrates. XANES measurements reveal that the phase transition is accompanied by the simultaneous reduction of Cu^{2+} to Cu^{+} and Fe^{3+} to Fe^{2+}. Persistence of the photo-transformed phase upon warming is indicative of an irreversible chemical modification, rather than the metal-to-metal charge transfer process typically associated with PBAs. This phototransformed phase exhibits a small negative thermal expansion. The absence of internal electron transfer is due to the high energy of the Frank-Condon excited state, a result of the Jahn-Teller distortions, meaning it is not easily accessed – even via X-ray irradiation. We propose the following chemical reaction:

$$\mathbf{CsCu^{2+}[Fe^{3+}(CN)_6] \rightarrow CsCu^{+}[Fe^{2+}(CN)_4] + (CN)_2}$$

The resultant Cu^{+} ($3d^{10}$, S=0) ion is not Jahn-Teller active and favours tetrahedral coordination geometry, thereby accounting for the structural properties of the photo-induced disordered cubic phase.

4.6 Bibliography

1. W. Kosaka, T. Ishihara, H. Yashiro, Y. Taniguchi, K. Hashimoto and S. Ohkoshi, *Chemistry Letters*, 2005, **34**, 1278-1279.
2. L. Reguera, C. P. Krap, J. Balmaseda and E. Reguera, *Journal of Physical Chemistry C*, 2008, **112**, 15893-15899.
3. Y. Moritomo, K. Kato, A. Kuriki, M. Takata, M. Sakata, H. Tokoro, S. Ohkoshi and K. Hashimoto, *Journal of the Physical Society of Japan*, 2002, **71**, 2078-2081.
4. D. F. Shriver and P. W. Atkins, *Inorganic chemistry*, Oxford University Press, Oxford, 1999.
5. I. B. Bersuker, *Coordination Chemistry Reviews*, 1975, **14**, 357-412.
6. I. B. Bersuker, *Chemical Reviews*, 2001, **101**, 1067-1114.
7. M. A. Halcrow, *Dalton Transactions*, 2003, 4375-4384.
8. E. Reguera, J. Rodriguez-Hernandez, A. Champi, J. G. Duque, E. Granado and C. Rettori, *Zeitschrift Fur Physikalische Chemie-International Journal of Research in Physical Chemistry & Chemical Physics*, 2006, **220**, 1609-1619.
9. J. Balmaseda, E. Reguera, J. Rodriguez-Hernandez, L. Reguera and M. Autie, *Microporous and Mesoporous Materials*, 2006, **96**, 222-236.
10. A. C. L. a. R. B. V. Dreele, *Los Alamos National Laboratory Report LAUR*, 2002, 86-748.
11. J. S. O. Evans, *J Chem Soc Dalton*, 1999, 3317-3326.
12. F. Varret, A. Goujon and A. Bleuzen, *Hyperfine Interactions*, 2001, **134**, 69-80.
13. ESRF, ID31 - The High-resolution Powder-diffraction Beamline http://www.esrf.eu/UsersAndScience/Experiments/MaterialsScience/ID31/Technicaldescription, 2009.
14. K. W. Chapman, P. J. Chupas and C. J. Kepert, *Journal of the American Chemical Society*, 2006, **128**, 7009-7014.

Chapter 5

Prussian Blue Analogue Nanoparticles Based Upon the Hexacyanochromate Building Block

5.1 Introduction

One particularly dynamic area of PBA research is the synthesis and characterisation of nanostructured materials, that is those with length scales in the 1 to 100 nm range.[1] This is driven by the demand for high density data storage and a desire to bridge the knowledge gap which exists for nanoscale magnetic objects with spin states in the 100-1000 range (i.e. intermediate between those of single molecule magnets and metallic nanoparticles). Nanostructured PBAs may give rise to magnetic behaviours quite distinct from those of the corresponding bulk material. Some alterations in the magnetic behaviour, such as the suppression of the magnetic ordering temperature, can be attributed to the increased proportion of paramagnetic TM ions which now lie at the surface (due to the increased surface-to-volume ratio) and have fewer neighbours than those in the bulk. Other behaviours characteristic of nanoscale PBAs, such as superparamagnetism, arise because the very smallest particles may exist as single magnetic domains.

Superparamagnetism can be defined as *"a phenomenon by which magnetic materials may exhibit a behaviour similar to paramagnetism at temperatures below the Curie or the Néel temperature".*[2] Magnetic domain wall formation becomes energetically unfavourable with decreasing particle size and consequently magnetic nanoparticles may exist as single domains and can be viewed as individual large spins or supermoments.[1] The relationship between the internal energy of such a system and the spin direction is referred to as the magnetic anisotropy.[3] Energetically favourable spin alignment is said to occur along the easy axis. Conversely, energetically unfavourable spin alignments are said to occur along the hard axis.

The magnetic anisotropy energy (E_A) of a single domain particle is directly related to its size, as shown by the following equation:

$$E_A = KV\sin^2\theta \qquad (5.1)$$

where K is the effective anisotropy constant, V is the volume of the nanoparticle and θ is the angle between the magnetization direction and the nanoparticle's easy axis.[4] At low temperatures the supermoment of a nanoparticle remains fixed, or *blocked,* in the most energetically favourable direction, i.e. along the easy axis (Figure 5.1).[5]

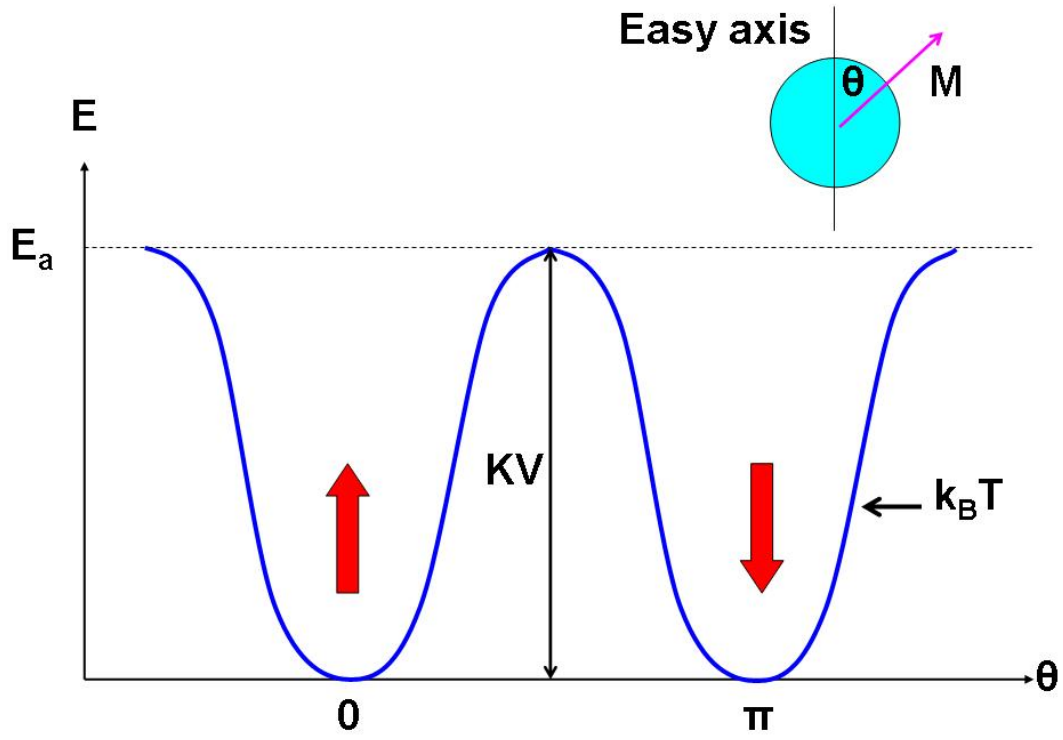

Figure 5.1 Schematic of the free energy of an uniaxial anisotropic single-domain particle as a function of the angle between the magnetization (M) and the easy axis. Note that in this instance there is not enough thermal activation energy (k_BT) to overcome the energy barrier ($E_B = KV$).

At higher temperatures, where there is sufficient thermal energy to overcome the anisotropy energy barrier (E_A), the nanoparticles lose their stable magnetic order as the moment randomly flips with thermal fluctuations. This is what is referred to as the superparamagnetic state, its onset occurring at a temperature known as the blocking temperature (T_B).[6, 7] The blocking temperature is given by the following equation:

$$T_B = \frac{KV}{\ln(\tau_m / \tau_o) k_B} \qquad (5.2)$$

where k_B is the Boltzmann constant, τ_m is the measuring time and τ_o is the characteristic relaxation time. For superparamagnetic materials, the value of τ_o is usually found to lie between 10^{-8} and 10^{-12} s. The superparamagnetic behaviour inherent to many magnetic nanoparticles acts as a barrier to the widespread realisation of their technological potential since most applications require that magnetic ordering remains temporally stable at, or near, room temperature. Thus far the highest blocking temperature reported for a PBA nanoparticle system remains well below room temperature, with $CsNi[Cr(CN)_6]$ nanoparticles (with a mean size of 6.4 nm) ordering at just 9 K.[8]

A key objective of nanoparticle research - other than the augmentation of blocking temperatures - is to achieve synthetic control over particle size, morphology and spatial distribution since magnetic behaviour is strongly dependent upon these properties. A variety of techniques based upon spatial confinement of particle growth have been used to synthesise PBA nanoparticles, e.g. polymer-protection,[9] silica sol-gel mediation[10] and encapsulation within reverse-micelles[11] or Nafion membranes.[12] The superparamagnetic $CsNi[Cr(CN)_6]$ nanoparticles with T_B = 9 K mentioned above were fabricated using polyvinylpyrrolidone (PVP) as a protecting polymer.[8] This polymer has been successfully employed in the spatial confinement of several other PBA systems,[13-15] and indeed facilitated the synthesis of rubidium cobalt hexacyanoferrate nanoparticles - one of the few PBA systems to exhibit photomagnetic behaviour in the nanoregime.[16] The PVP monomer is shown overleaf in Figure 5.2.

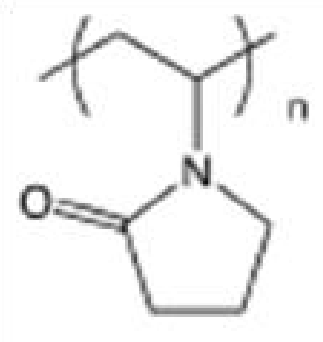

Figure 5.2 Polyvinylpyrrolidone (PVP) monomer.

The amide moieties of PVP are thought to coordinate to the transition metal ions of the PBA during the nucleation and growth processes, providing steric stabilization to confine particle growth and inhibit aggregation.[9, 15] The formation of PVP protected Prussian Blue nanoparticles is depicted below in Figure 5.3.

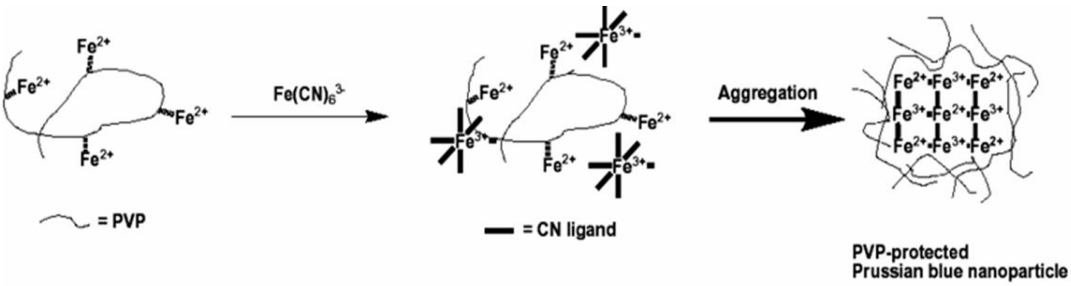

Figure 5.3 Schematic of PVP protected Prussian Blue nanoparticles.[9]

Herein we expand upon the PBA nanostructures outlined above with the synthesis and characterisation of several polymer-stabilized PBA nanoparticles based upon the $[Cr^{3+}(CN)_6]^{3-}$ building block. Magnetometry and TEM provide evidence for the fabrication of the novel PVP protected copper hexacyanochromate ($Cu_3[Cr(CN)_6]_2$) nanoparticles. Consequently we demonstrate systematic control of particle size - and hence magnetic behaviour - within the family of PVP protected $Cu_3[Cr(CN)_6]_2$ nanoparticles. This synthesis method is successfully extended to the preparation of manganese hexacyanochromate ($Mn_3[Cr(CN)_6]_2$) and caesium manganese hexacyanochromate $CsMn[Cr(CN)_6]$ nanoparticles. AC susceptibility measurements show that size dependent superparamagnetism exists within each of the hexacyanochromate families investigated. Finally, XPS measurements are used to

investigate the effects of PVP coordination on metal oxidation states of a caesium manganese hexacyanochromate nanocomposite.

5.2 Copper Hexacyanochromate Nanoparticles

5.2.1 Experimental Section

5.2.1.1 Synthesis

Nanoparticles based upon the ferromagnetic $Cu_3[Cr(CN)_6]_2$ (T_c = 66 K) were prepared by dropwise addition of an aqueous solution of $K_3[Cr(CN)_6]$ (10 mM, 10 ml) to a mixed aqueous solution (10 ml) of $CuCl_2 \cdot 2H_2O$ (15 mM) and PVP. The PVP concentration was varied according to the desired particle size. Each addition took place over a 12 minute period, with mechanical stirring (600 rpm) throughout. In each case, acetone (25 ml) was added dropwise to a 10 ml aliquot of the resultant PVP-$Cu_3[Cr(CN)_6]_2$ solution in order to induce precipitation. As in the previous step, addition took place over 12 min with stirring at a rate of 600 rpm throughout. The resultant precipitate was recovered by centrifuging at 4000 rpm, 4°C for 15 minutes. The solid material was washed several times with de-ionised H_2O (to remove excess PVP) and left to dry under ambient conditions.

5.2.1.2 Characterization

Elemental compositions were determined by ICP-MS and CHN thermogravimetric analysis. Magnetic properties were measured using a Quantum Design MPMS-1 SQUID magnetometer. The PVP-PBA composites were redispersed in de-ionised H_2O then dropped onto copper grids for HRTEM measurements. TEM images of the nanoparticles were obtained using a Jeol JEM 2011 microscope.

5.2.2 Results

5.2.2.1 Elemental Analysis

The chemical formulae of the nanoparticle composites as determined by ICP-MS are shown in the Table 5.1 below.

Table 5.1 Compositions of the PVP protected copper hexacyanochromate PBA nanoparticles.

Sample	Chemical Formula	[PVP]/[Cu^{2+}]
1	$Cu_{1.52}[Cr(CN)_6](C_6H_9NO)_{23.6}$	16
2	$Cu_{1.57}[Cr(CN)_6](C_6H_9NO)_{36.60}(H_2O)_{42.1}$	23
3	$Cu_{1.50}[Cr(CN)_6](C_6H_9NO)_{123.92}(H_2O)_{137.7}$	83

5.2.2.2 TEM

TEM images, and the particle size distributions obtained from them, reveal that the mean particle size of PVP protected $Cu_3[Cr(CN)_6]_2$ decreases as the $[PVP]/[Cu^{2+}]$ ratio increases (Figure 5.4).

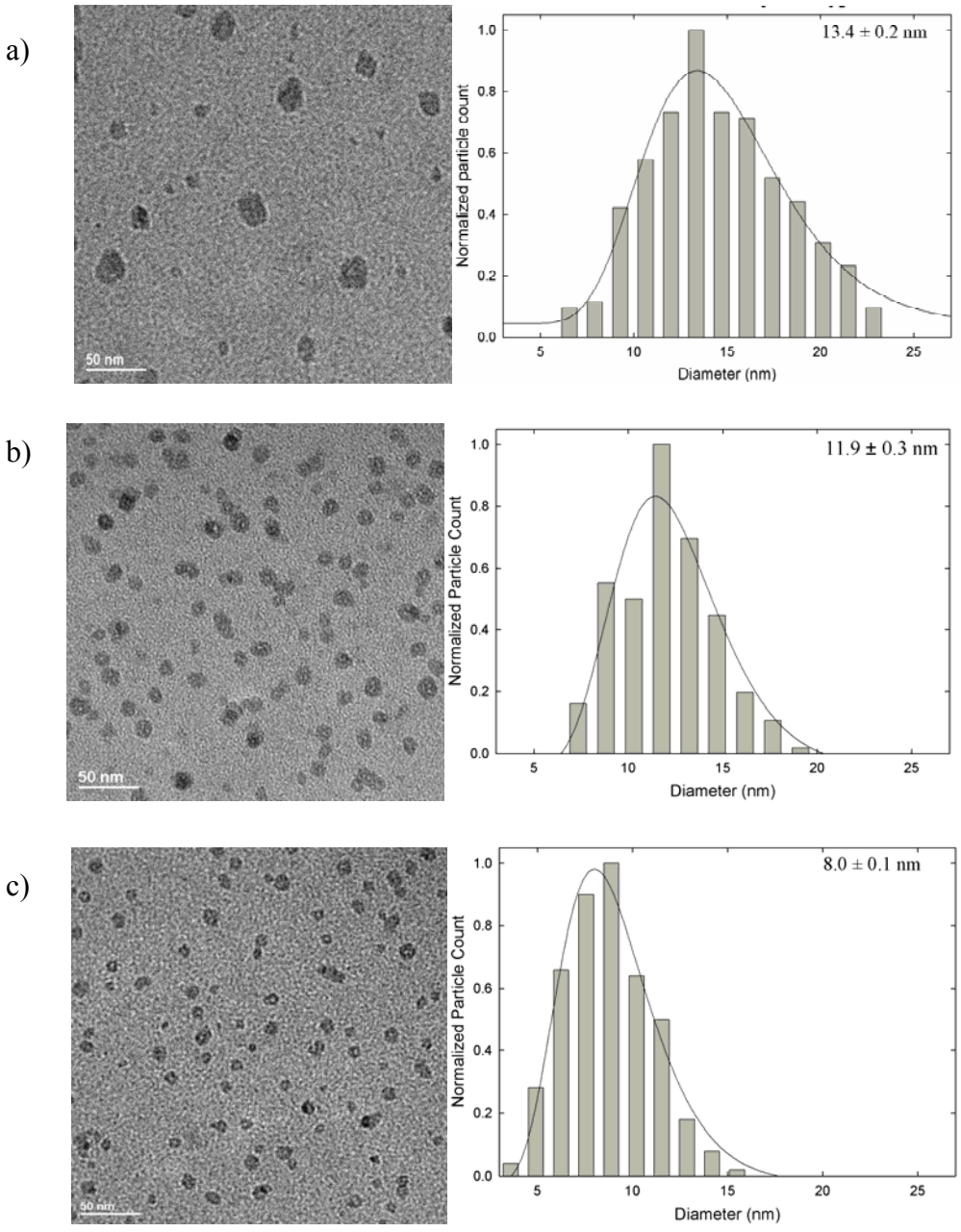

Figure 5.4 The TEM images and particle size distributions (normalized to the largest bin) versus diameter for **1**, **2** and **3** are shown in a), b) and c) respectively. The total number of particles considered for **1**, **2** and **3** are 221, 206 and 215 respectively. The solid lines are the results of log-normal fits that provide the characteristic diameters shown for each distribution.

5.2.2.3 DC Magnetic Characterization

The zero-field cooled (ZFC) and field-cooled (FC) magnetization curves of **1, 2** and **3** are coincident at high temperature but diverge upon cooling, with the ZFC curve exhibiting a peak at low temperature (Figure 5.5).

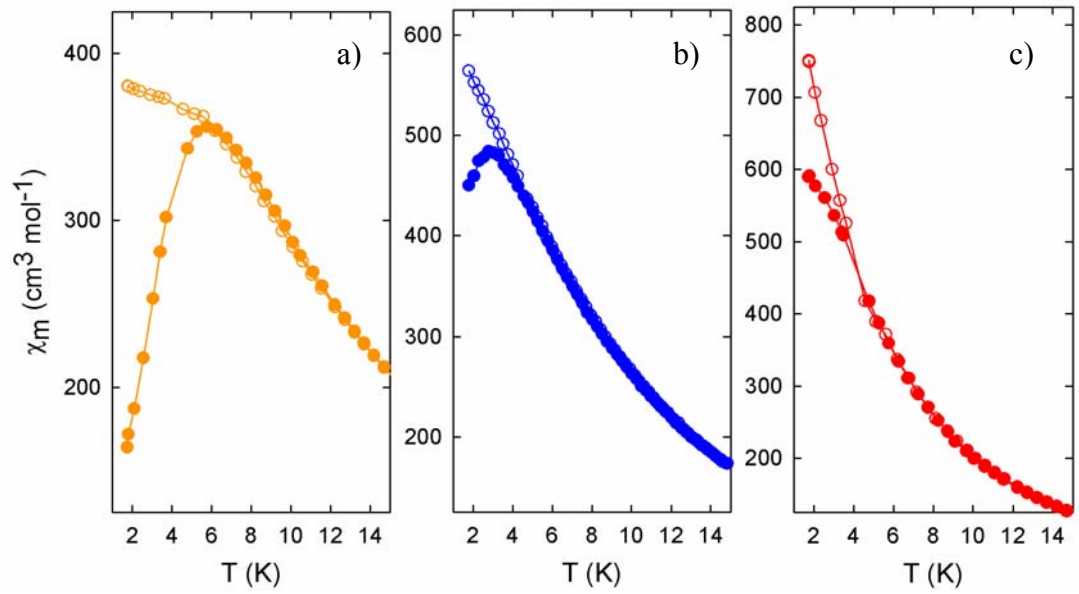

Figure 5.5 The zero-field cooled (ZFC) and field-cooled (FC) magnetization curves of a) **1**, b) **2** and c) **3** in a 1 mT field. Closed and open symbols represent the ZFC and FC magnetizations respectively.

The temperature at which the curves diverge is referred to as the temperature of irreversibility (T_{irr}), while the temperature at which the maximum ZFC magnetization occurs corresponds to T_B. Herein, T_{irr} is taken to be the temperature at which the difference between the ZFC and FC susceptibilities is less than or equal to 1% of the FC susceptibility.[17] The T_{irr} values determined for the copper hexacyanochromate nanoparticles are observed to be directly related to the mean particle size, with the magnetization curves of **1, 2** and **3** diverging at 5.8, 4.3 and 3.6 K respectively. The temperature of the ZFC maximum is similarly related to particle size, with the blocking temperature (T_B) falling from 5.6 K for **1,** to 3.0 K for **2,** to less than 1.7 K for **3**.

5.2.2.4 Detailed Magnetic Characterization of $Cu_{1.57}[Cr(CN)_6](C_6H_9NO)_{36.60}(H_2O)_{42.1}$ (2)

The superparamagnetic properties of $Cu_{1.57}[Cr(CN)_6](C_6H_9NO)_{36.60}(H_2O)_{42.1}$ **(2)** were investigated with further magnetization measurements. The magnetization versus

magnetic field plot of **2** recorded at 1.7 K exhibits a hysteresis loop with a coercive field of 4.5 Oe. The remnant magnetization is 5.32 % of the value at saturation (Figure 5.6). Magnetic hysteresis loops are not observed at temperatures above the blocking temperature of 3.0 K.

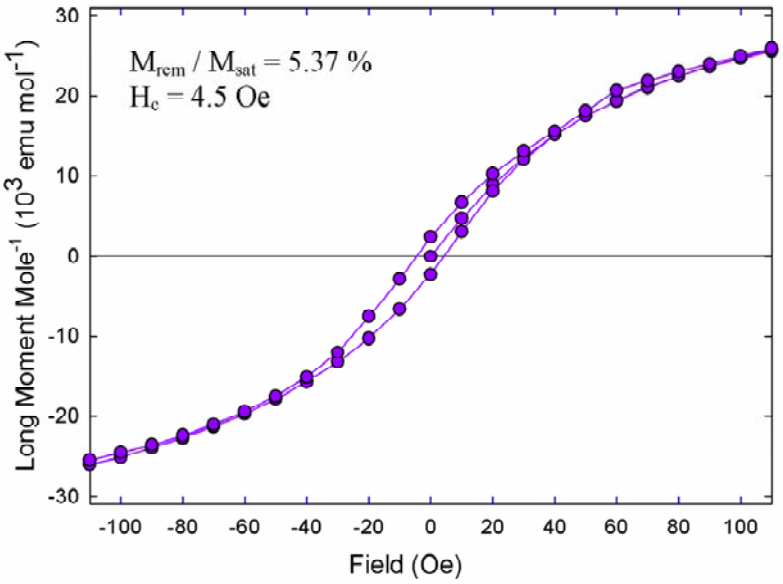

Figure 5.6 The magnetization versus magnetic field plot of **2** recorded at 1.7 K.

The magnetic relaxation of **2** was investigated by means of AC susceptibility measurements performed in zero applied DC field and a 3 Oe oscillating field at 1, 10, 50, 100 and 250 Hz. Both the in-phase (χ'(T)) and out-of-phase (χ''(T)) components show frequency dependence, with the peak susceptibility shifting to higher temperatures as the measuring frequency is increased (Figure 5.7 overleaf). Such frequency dependence is associated with both spin glass and superparamagnetic behaviour. The empirical parameter Φ is used to distinguish between the two phenomena:

$$\phi = \frac{T_{max} - T_{min}}{T_{max}(\log \nu_{max} - \log \nu_{min})} \qquad (5.3)$$

where T_{max} corresponds to the position of the χ''(T) peak at the highest measuring frequency (υ_{max}) and T_{min} corresponds to the position of the χ''(T) peak at the lowest measuring frequency (υ_{min}). A value of Φ in the range $0.01 < \Phi < 0.1$ is

characteristic of spin-glass behaviour; superparamagnetism is characterized by $\Phi > 0.1$. The out-of-phase component of **2** gives rise to $T_{max} = 3.3$ K, $T_{min} = 2.8$ K, $\upsilon_{min} = 1$ Hz and $\upsilon_{max} = 250$ Hz and consequently Φ is calculated to be 0.6.

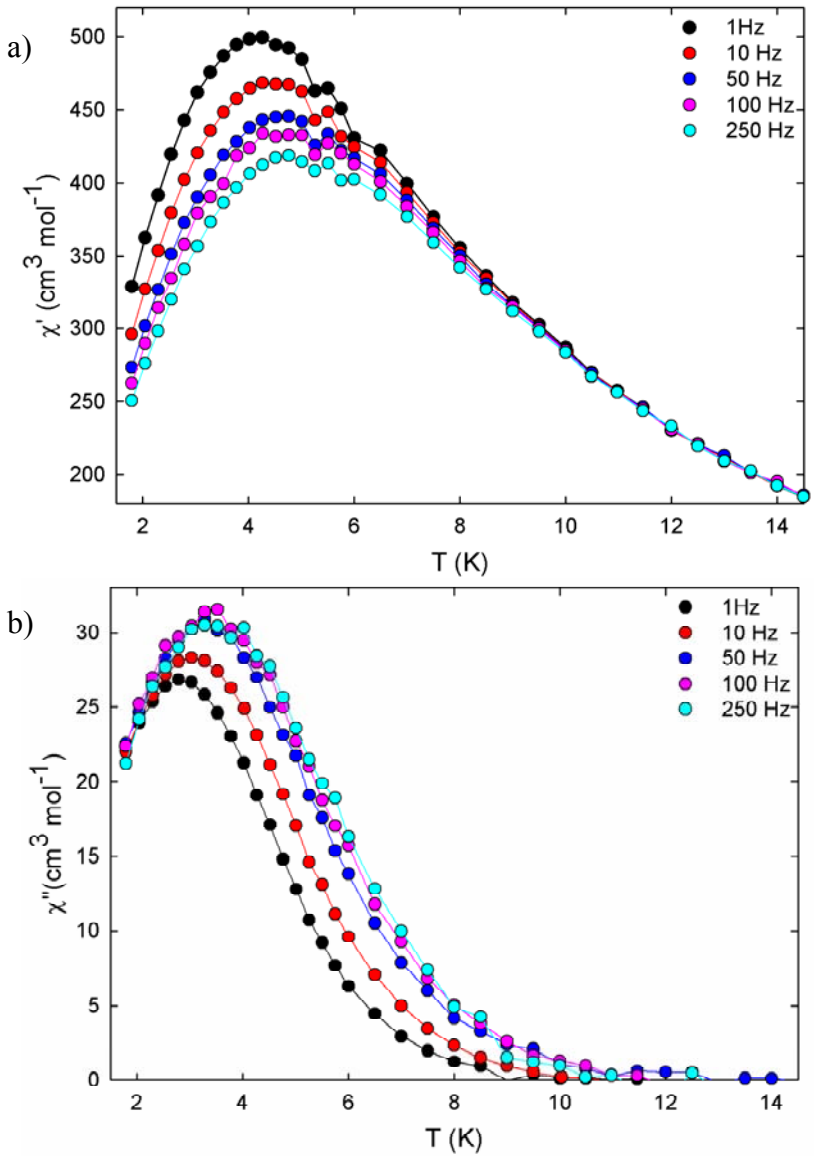

Figure 5.7 Temperature dependence of a) the in-phase (χ'(T)) and b) the out-of-phase (χ''(T)) components of **2** at $H_{DC} = 0$ Oe and $H_{AC} = 3$ Oe.

The frequency dependence of spin-glass and superparamagnetic materials may be further quantified by plotting ln τ as a function of T^{-1} (where T is the temperature of the χ'' maxima) in order to determine the characteristic relaxation time (τ_0), since:

$$\tau = \frac{1}{2\pi f} = \tau_0 \exp \frac{E_A}{k_B T} \qquad (5.4)$$

Superparamagnetic materials typically exhibit characteristic relaxation times which lie in the range $10^{-12} < \tau_0 < 10^{-8}$ s, while substantially lower values of τ_0 are associated with spin glass materials. A characteristic relaxation time of 2.2 x 10^{-12} s is determined from the y-axis intercept of the linear ln τ vs T^{-1} plot of **2**; the gradient corresponds to E_A / k_B = 69.6 K (Figure 5.8).

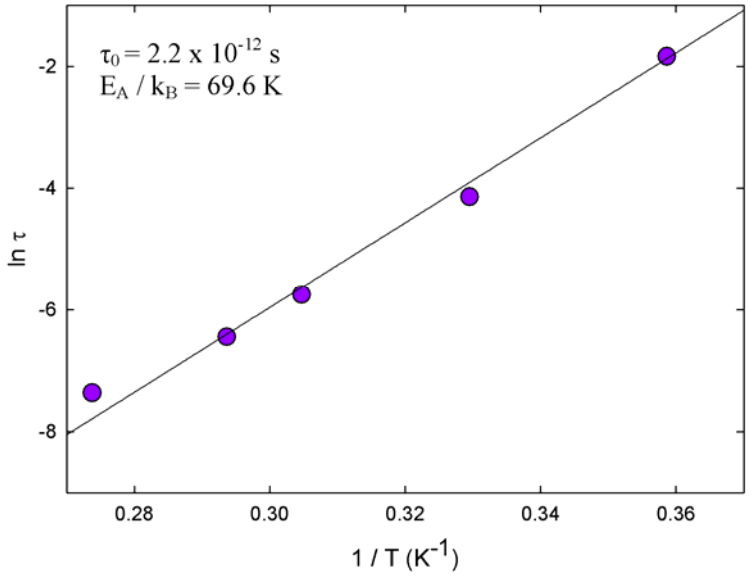

Figure 5.8 Thermal variation of the relaxation time of **2** according to the Arrhenius law.

5.3 Manganese Hexacyanochromate Nanoparticles

5.3.1 Experimental Section

5.3.1.1 Synthesis

Nanoparticles based upon the ferrimagnetic $Mn_3[Cr(CN)_6]_2$ (T_N = 66 K) were prepared by dropwise addition of aqueous solutions (10 ml) of $K_3[Cr(CN)_6]$ (20 mM) to mixed aqueous solutions (10 ml) of $MnCl_2$ (30 mM) and PVP. The PVP concentration was varied according to the desired particle size. Addition took place over 10 minutes, with mechanical stirring at a rate 600 rpm throughout. Subsequently, acetone (25 ml) was added dropwise to a 10 ml aliquot of the resultant PVP-$Mn_3[Cr(CN)_6]_2$ solution. Again, addition took place over 10 minutes with mechanical stirring (600 rpm) throughout. The resultant precipitate was recovered by centrifuging at 4000 rpm, 4°C for 10 minutes. The solid material was washed several times with de-ionised H_2O and left to dry under ambient conditions.

5.3.1.2 Characterization

Inductively coupled plasma mass spectrometry (ICP-MS) and CHN thermogravimetric analysis were used to determine elemental compositions. Magnetic properties were measured using a Quantum Design MPMS-1 superconducting quantum interference device (SQUID) magnetometer. The PVP-$Mn_3[Cr(CN)_6]_2$ composites was redispersed in de-ionised H_2O and dropped onto copper grids for high resolution transmission electron microscopy (TEM) measurements using a Jeol JEM 2011 microscope.

5.3.2 Results

5.3.2.1 Elemental Analysis

Elemental analyses performed on the nominal $Mn_3[Cr(CN)_6]_2$ composites gave the stoichiometries shown below in Table 5.2.

Table 5.2 Compositions of the PVP protected manganese hexacyanochromate PBA nanoparticles.

Sample	Chemical Formula	[PVP]/[Mn^{2+}]
4	$Mn_{1.51}[Cr(CN)_6](C_6H_9NO)_{51.40}(H_2O)_{81.3}$	34
5	$Mn_{1.54}[Cr(CN)_6](C_6H_9NO)_{129.88}(H_2O)_{176.0}$	84
6	$Mn_{1.52}[Cr(CN)_6](C_6H_9NO)_{171.44}(H_2O)_{241.8}$	113

5.3.2.2 DC Magnetic Characterization

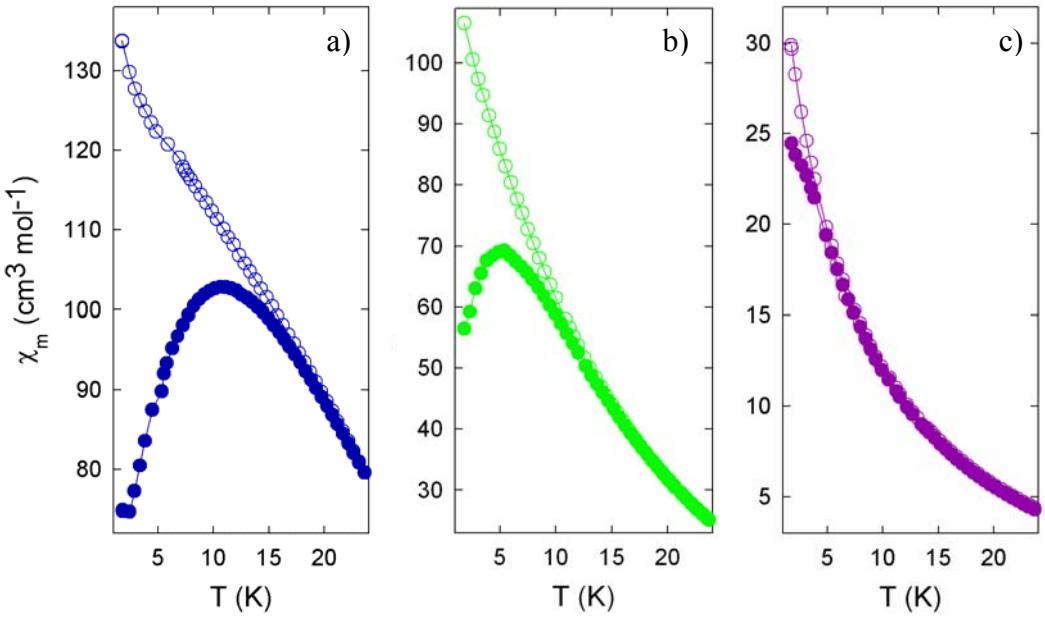

Figure 5.9 The zero-field cooled (ZFC) and field-cooled (FC) magnetization curves of **4**, **5** and **6** in a 2 mT field. Closed and open symbols represent the ZFC and FC magnetizations respectively.

The thermomagnetic behaviours displayed by the manganese hexacyanochromate nanoparticles (Figure 5.9) resembles those observed for compounds **1** to **3.** As was the case with the copper hexacyanochromate nanoparticles, the temperature of ZFC/FC divergence is observed to be directly related to [PVP]/[M^{2+}], with the magnetization curves of **4, 5** and **6** diverging at 16.3, 12.5 and 7.4 K respectively. The temperature of the ZFC maximum is similarly related to [PVP]/[Mn^{2+}] particle size, with the blocking temperature (T_B) falling from 10.6 K for **4,** to 5.4 K for **5,** to less than 1.8 K for **6**.

5.3.2.3 Magnetic Relaxation of $Mn_{1.54}[Cr(CN)_6](C_6H_9NO)_{129.88}(H_2O)_{176.0}$ (5)

AC susceptibility measurements performed in zero applied DC field and a 3 Oe oscillating field at 1, 10, 50, 100, 250 and 1000 Hz were used to characterize the magnetic relaxation of $Mn_{1.54}[Cr(CN)_6](C_6H_9NO)_{129.88}(H_2O)_{176.0}$ **(5)**. Both the in-phase (χ'(T)) and out-of-phase (χ''(T)) components show frequency dependence, with the peak susceptibility shifting to higher temperatures as the measuring frequency is increased (Figure 5.10 overleaf).

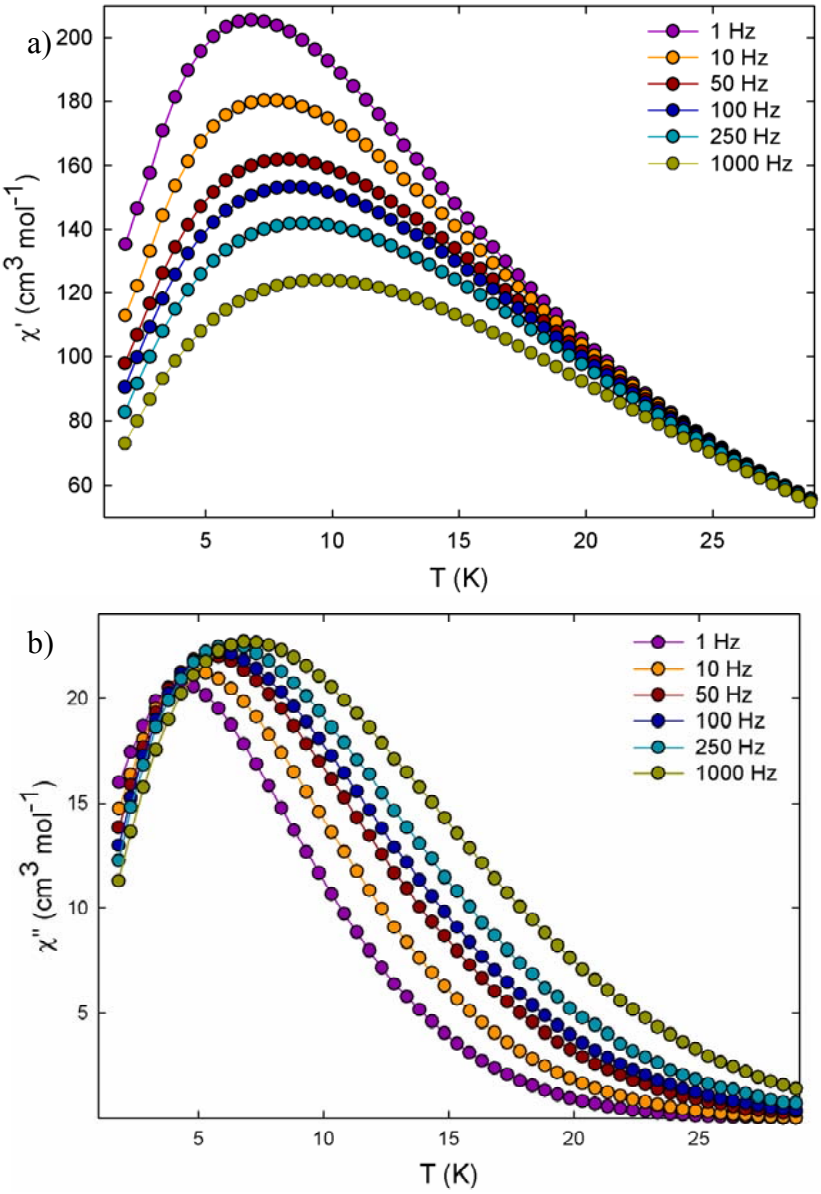

Figure 5.10 Temperature dependence of the a) in-phase (χ'(T)) and b) out-of-phase (χ''(T)) components of **5** at H_{DC} = 0 Oe and H_{AC} = 3 Oe.

The value of Φ = 0.12 derived from the χ''(T) component of **5** (where T_{max} = 6.8 K, T_{min} = 4.3 K, υ_{min} = 1 Hz and υ_{max} = 1000 Hz) is indicative of superparamagnetic behaviour. This is supported by the characteristic relaxation time of 1.3 x 10^{-9} s determined from the Arrhenius fit of the thermal variation of the relaxation time (Figure 5.11 overleaf). The gradient of this plot corresponds to an energy barrier of E_A / k_B = 80.1 K.

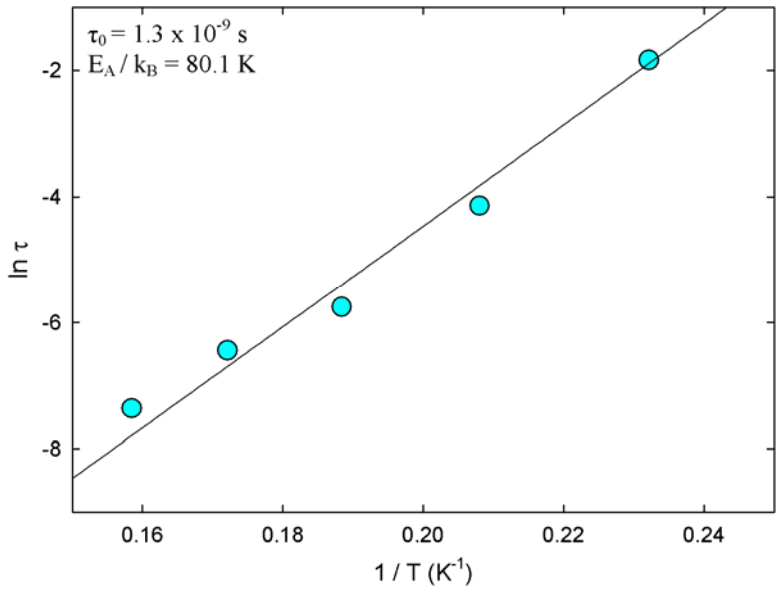

Figure 5.11 Thermal variation of the relaxation time of **5** according to the Arrhenius law.

5.3.2.4 TEM

TEM images of **5** redispersed in de-ionised H_2O show the presence of several pseudo-spherical nanoscale structures with diameters of approximately 15 nm (Figure 5.12).

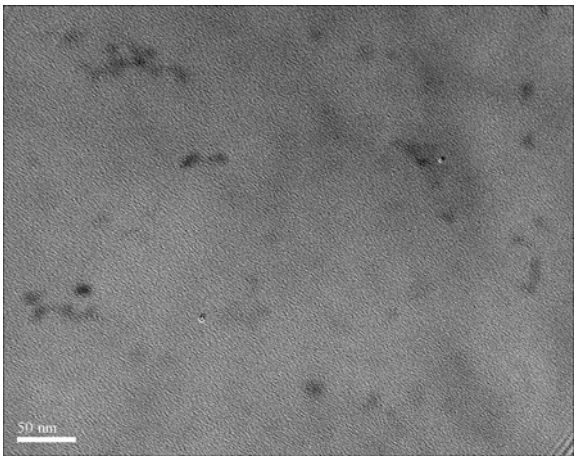

Figure 5.12 TEM image of **5.**

5.4 Caesium Manganese Hexacyanochromate Nanoparticles

5.4.1 Experimental Section

5.4.1.1 Synthesis

Nanoparticles based upon the ferrimagnetic $CsMn[Cr(CN)_6]$ (T_N = 90 K) were prepared by dropwise addition of a mixed aqueous solution (10 ml) of CsCl and $K_3[Cr(CN)_6]$ to a mixed aqueous solution (10 ml) of $MnCl_2{\cdot}2H_2O$ and PVP over 12 minutes, with mechanical stirring at a rate of 600 rpm throughout. The concentration of PVP was varied according to the desired particle size. In each case, acetone (25 ml) was added dropwise over 12 minutes to a 10 ml aliquot of the aqueous PVP-PBA solution, again with mechanical stirring (600 rpm) throughout. The resultant precipitate was recovered by centrifugation at 4000 rpm, 4°C for 10 minutes. The solid material was washed several times with de-ionised H_2O and left to dry under ambient conditions. The concentrations of CsCl, $K_3[Cr(CN)_6]$ and $MnCl_2{\cdot}2H_2O$ solutions employed in the synthesis of samples **7** and **8** were 20 mM, 10 mM and 10 mM respectively. These concentrations were doubled for the preparation of **9** in an attempt to raise T_B and minimise the difference between T_B and T_{irr}.

5.4.1.2 Characterization

Elemental compositions were determined by ICP-MS. Powder X-ray diffraction profiles were recorded, under ambient conditions, on a Bruker AXS D8 diffractometer. Magnetic properties were measured using Quantum Design MPMS-XL and MPMS-1 SQUID magnetometers. The PVP-PBA composites were redispersed in de-ionised H_2O then dropped onto copper grids for HRTEM measurements. TEM images of the nanoparticles were obtained using a Jeol JEM 2011 microscope. X-ray photoemission spectroscopy (XPS) data were collected using a Scienta R4000 spectrometer equipped with a monochromatic Al K_α X-Ray source ($h\nu$ = 1486.6 eV); the photoelectron take-off angle was 90° and the base pressure during measurements was 5.10^{-10} mbar. Powder samples were ground and dispersed in distilled-deionized water (18.2 μS, Milli-Q), stirred, and few drops of the suspension were left to dry in air on a silicon oxide substrate. The samples were

introduced into ultra high vacuum as soon as dry. Binding energies were referenced to the carbon *1s* signal of $-CH_x-C^*H_2-CH_x-$ in polyvinylpyrrolidone (PVP) at 285.00 eV.[18] Although an electron flood gun was used to compensate for sample charging due to the insulating nature of the samples, the full width half-maximum (FWHM) was 1.7 eV as determined from the 4th component (C*=O, see Figure 5.23 below) of the PVP C *1s* spectrum and verified for the Cs *3d* line. No X-ray induced sample degradation was detected. Spectral analysis included a Tougaard[19] (for the transition metal photoemission peaks) or Shirley background subtraction[20] and peak deconvolution employing a Gaussian line shape with the help of the WinSpec program developed at the LISE laboratory, University of Namur, Belgium.

5.4.2 Results

5.4.2.1 Elemental Analysis

The chemical formulae of the nanocomposites determined by ICP-MS and CHN thermogravimetric analysis are shown below in Table 5.3.

Table 5.3 Compositions of the PVP protected caesium manganese hexacyanochromate PBA nanoparticles.

Sample	Chemical Formula	[PVP]/[Mn^{2+}]
7	$Cs_{0.81}Mn_{1.07}[Cr(CN)_6](C_6H_9NO)_{8.35}(H_2O)_{5.80}$	8
8	$Cs_{0.86}Mn_{1.08}[Cr(CN)_6](C_6H_9NO)_{84.35}(H_2O)_{94.40}$	78
9	$Cs_{1.07}Mn_{1.07}[Cr(CN)_6](C_6H_9NO)_{195.54}(H_2O)_{183.14}$	183

5.4.2.2 X-ray Powder Diffraction

Powder diffraction profiles of the cesium manganese hexacyanochromate nanocomposites reveal that they, like the vast majority of bulk PBAs, adopt cubic structures (Figure 5.13 overleaf). Lattice parameters of **7**, **8** and **9 (**as determined from Le Bail profile fits of the data using the $Fm\bar{3}m$ space group) were 10.707(2), 10.682(6) and 10.720(4) Å, respectively. Crystallite sizes may be estimated from the FWHM of diffraction peaks by means of the Scherrer formula:

$$d = \frac{K\lambda}{w\cos\theta} \qquad (5.5)$$

where d is the particle size, λ is the wavelength of the radiation, θ is the angle of the Bragg reflection under consideration, w is the width on a 2θ scale, and K is the Scherrer constant. The value of K is employed in the Scherrer formula depends upon a variety of factors, e.g. crystallite shape and size distribution, but is of the order of unity.[21, 22]

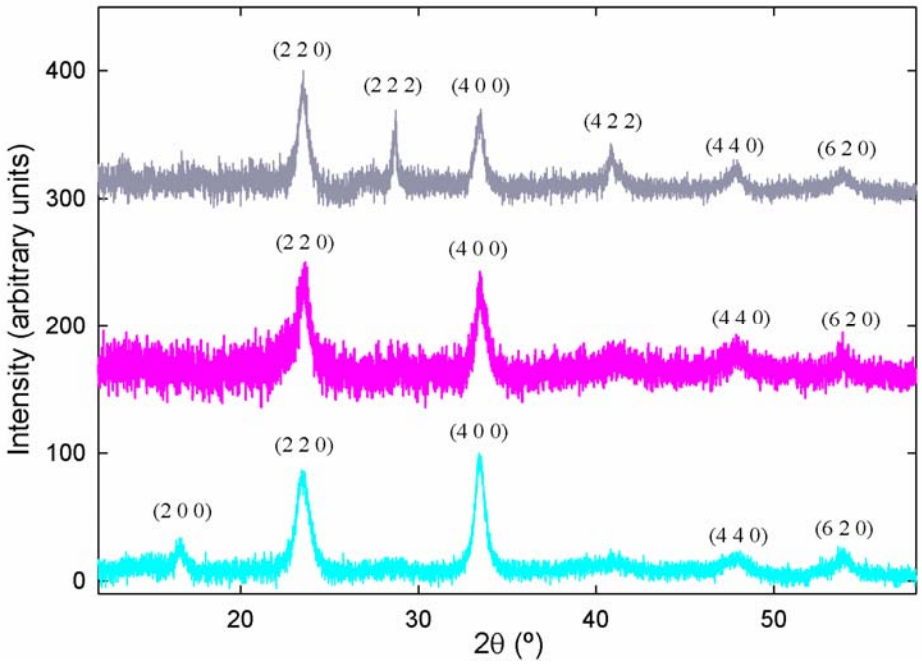

Figure 5.13 Powder X-ray diffraction profiles of **7** (cyan), **8** (pink) and **9** (grey) following background subtraction, with Miller indices of the cubic of the $Fm\bar{3}m$ space group.

Here (following the work of Bochert et al) we use K = 0.9 on the assumption that the powder samples comprise monodisperse, spherical nanoparticles.[21, 22] Consequently, the particle sizes estimated from the FWHM of the (220) reflection in the diffraction patterns of **7**, **8** and **9** were 15.3, 12.8 and 18.6 nm, respectively.

5.4.2.3 TEM

TEM images and particle size distributions of **7, 8** and **9** are shown below in Figure 5.14.

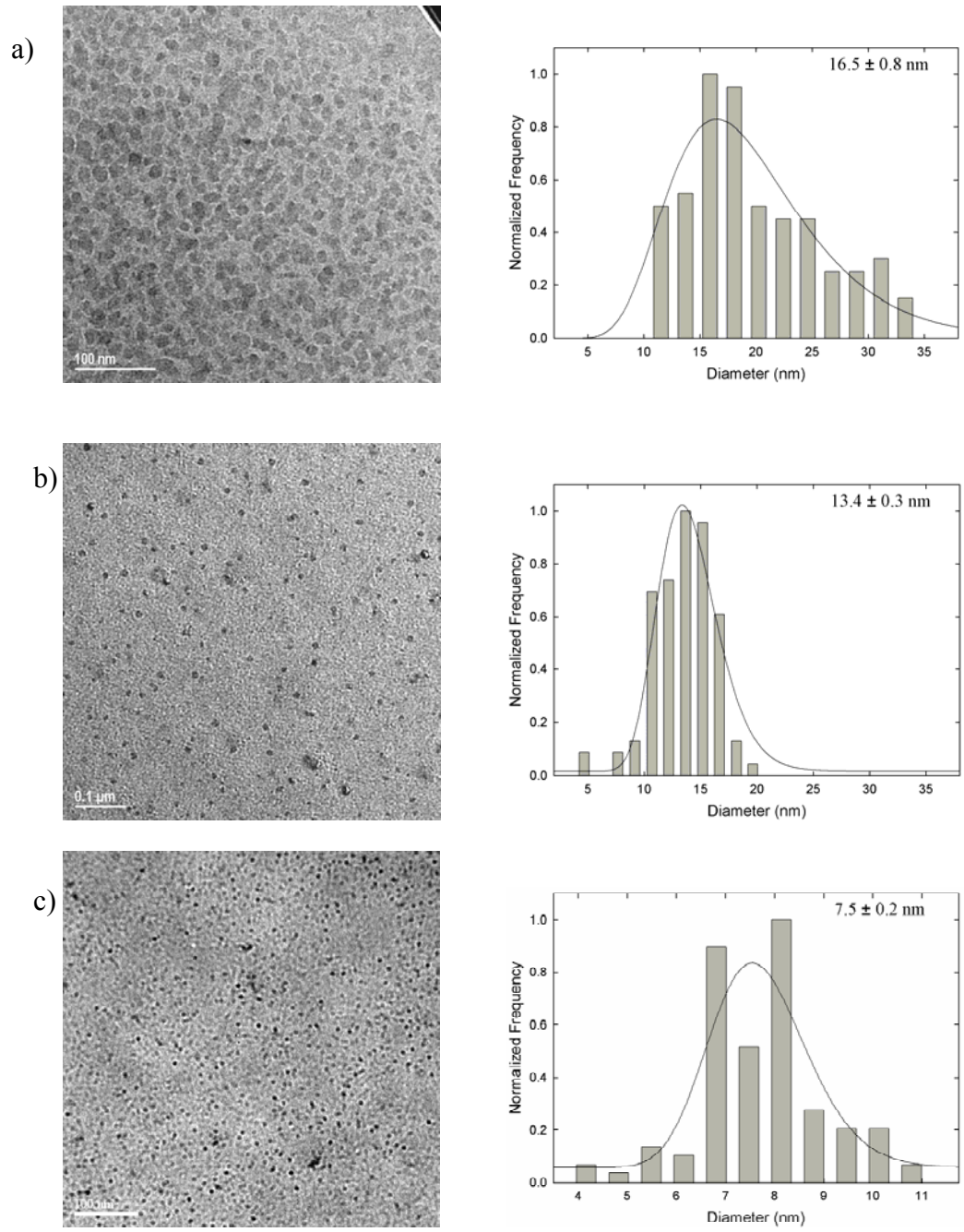

Figure 5.14 The TEM images and particle size distributions (normalized to the largest bin) versus diameter for **7**, **8** and **9** are shown in a), b) and c) respectively. The total number of particles considered for **7**, **8** and **9** are 107, 100 and 102 respectively. The solid lines are the results of log-normal fits that provide the characteristic diameters shown for each distribution.

5.4.2.4 DC Magnetic Characterization

The caesium manganese hexacyanochromate nanoparticles display thermomagnetic behaviours similar to those of **1-6**, that is, the ZFC and FC curves diverge at low temperature with the ZFC magnetization exhibiting a maximum upon subsequent cooling (Figure 5.15).

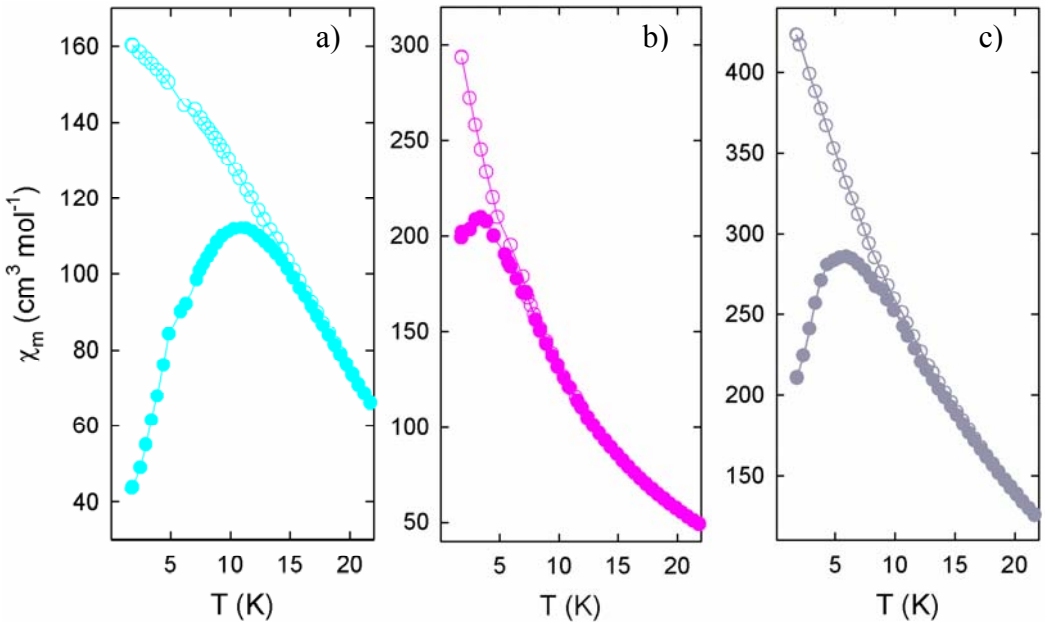

Figure 5.15 The zero-field cooled (ZFC) and field-cooled (FC) magnetization curves of a) **7** b) **8** and c) **9** in a 2 mT field. Closed and open symbols represent the ZFC and FC magnetizations respectively.

The ZFC/FC magnetization curves temperature of **7, 8** and **9** diverge at 20.2, 9.9 and 17.2 K respectively. The temperature of the ZFC maximum, which corresponds to the blocking temperature (T_B), is 10.9 K for **7,** 3.4 K for **8** and 5.6 K for **9.**

5.4.2.5 Magnetic Relaxation of $Cs_{0.81}Mn_{1.07}[Cr(CN)_6](C_6H_9NO)_{8.35}(H_2O)_{5.80}$ (7)

The magnetic relaxation of $Cs_{0.81}Mn_{1.07}[Cr(CN)_6](C_6H_9NO)_{8.35}(H_2O)_{5.80}$ **(7)** was investigated by means of AC susceptibility measurements performed in zero applied DC field and a 3 Oe oscillating field at 10, 50, 150 and 500 Hz. As was observed for samples **1** and **5,** the temperature of maximum susceptibility varies directly with the measuring frequency for both the χ'(T) and χ''(T) magnetization curves (Figure 5.16 overleaf).

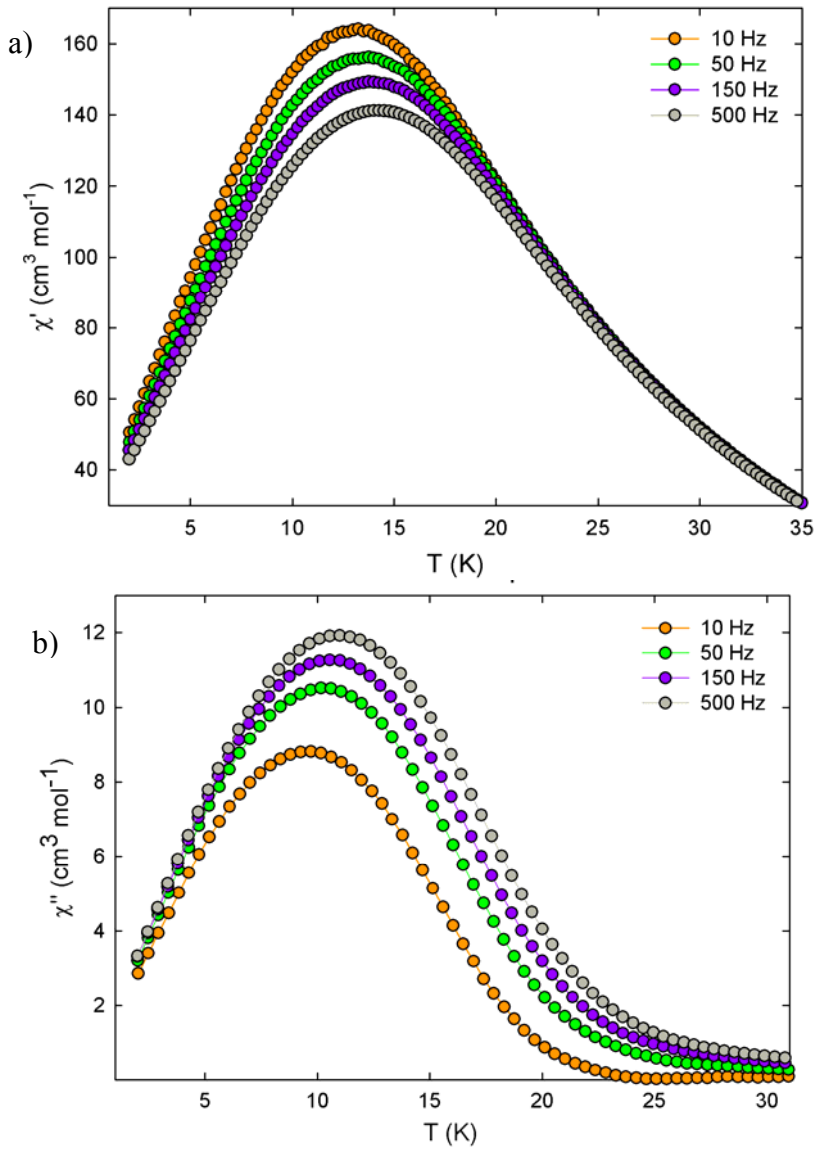

Figure 5.16 Temperature dependence of the a) in-phase (χ'(T)) and b) out-of-phase (χ''(T)) components of **2** at H_{DC} = 0 Oe and H_{AC} = 3 Oe.

The value of Φ = 0.07 derived from the χ''(T) component of **7** (where T_{max} = 11.0 K, T_{min} = 9.7 K, υ_{min} = 10 Hz and υ_{max} = 500 Hz) is characteristic of spin-glass, rather than superparamagnetic, behaviour. This is corroborated by a characteristic relaxation time of 3.3 x 10^{-17} s, as derived from the Arrhenius fit of the thermal variation of the relaxation time (Figure 5.17 overleaf), which is smaller than the values obtained for superparamagnetic systems and has no physical meaning. The energy barrier is E_A / k_B = 328.1 K.

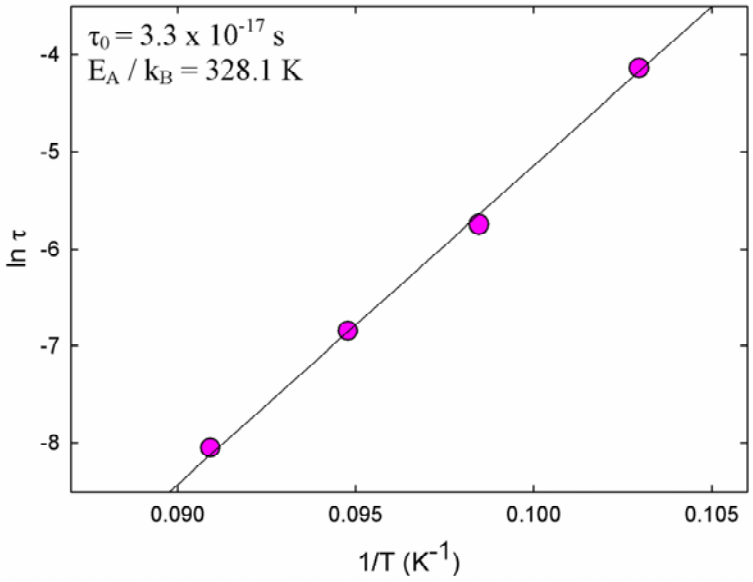

Figure 5.17 Thermal variation of the relaxation time of **7** according to the Arrhenius law

5.4.2.6 Magnetic Relaxation of $Cs_{1.07}Mn_{1.07}[Cr(CN)_6](C_6H_9NO)_{195.54}(H_2O)_{183.14}$ (9)

Frequency dependent behaviour is also observed in AC susceptibility measurements of $Cs_{1.07}Mn_{1.07}[Cr(CN)_6](C_6H_9NO)_{195.54}(H_2O)_{183.14}$ **(9)** recorded in zero applied dc field and a 3 Oe oscillating field at 1, 10, 100, 250 and 1000 Hz (Figure 5.18 overleaf). The temperature of maximum susceptibility varies directly with the measuring frequency for both the $\chi'(T)$ and $\chi''(T)$ components.

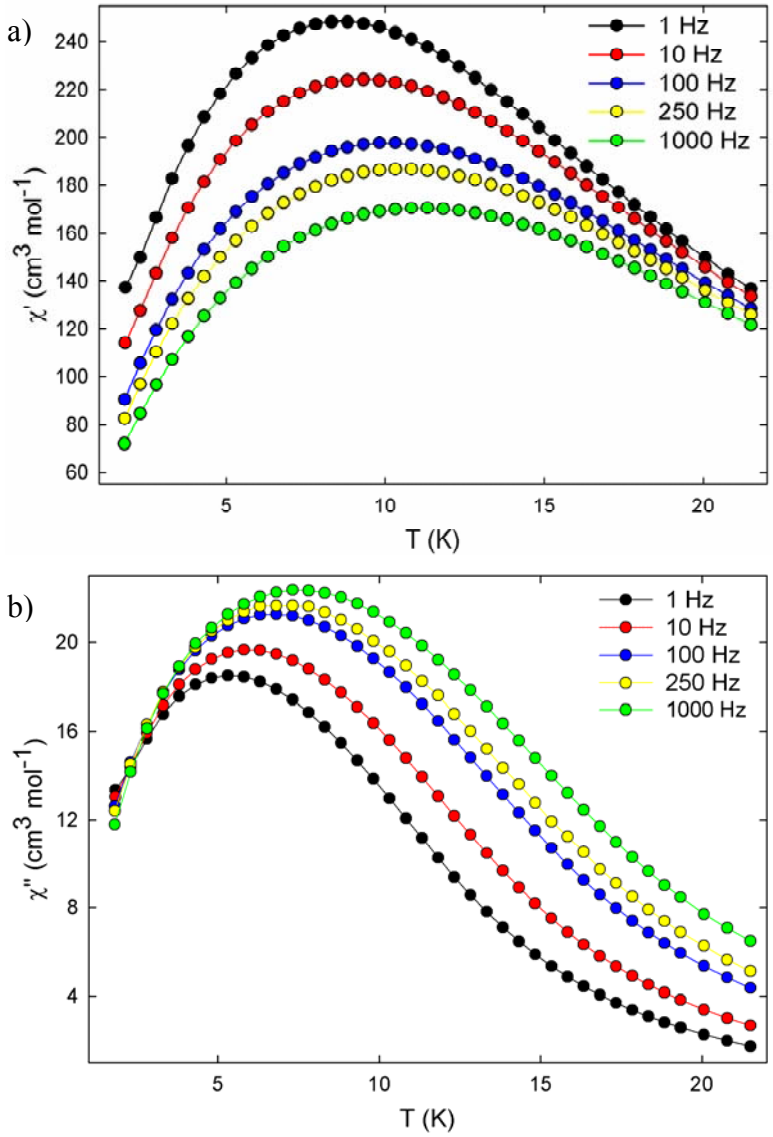

Figure 5.18 Temperature dependence of the a) in-phase (χ'(T)) and b) out-of-phase (χ''(T)) components of **9** at H_{AC} = 0 Oe and H_{DC} = 3 Oe.

The value of Φ = 0.09 derived from the χ''(T) component of **9** (where T_{max} = 7.5 K, T_{min} = 5.4 K, υ_{min} = 1 Hz and υ_{max} = 1000 Hz) is characteristic of superparamagnetic behaviour. This is corroborated by a characteristic relaxation time of 7.6 x 10^{-12} s, as derived from the Arrhenius fit of the thermal variation of the relaxation time (Figure 5.19). The energy barrier E_A / k_B = 126.1 K is significantly smaller than that of **7** and indicative of the decreased mean particle size.

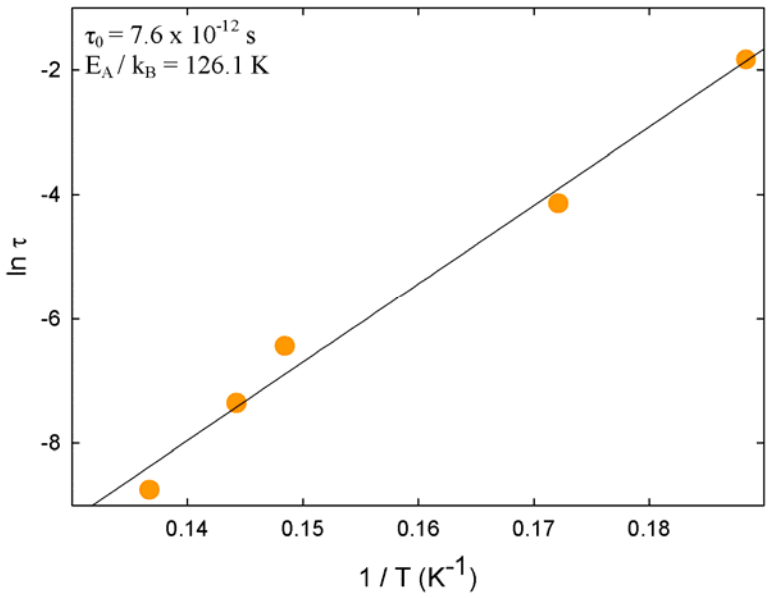

Figure 5.19 Thermal variation of the relaxation time of **9** according to the Arrhenius law

5.4.2.7 X-ray Photoemission Spectroscopy (XPS)

As outlined in Chapter 2, XPS is a direct method for the identification of the surface composition of a compound and the oxidation state of its elements. In addition, due to the so-called multiplet-splitting effect, one can identify the spin state of many (high spin) transition metal elements.[23] This technique was employed to further investigate the caesium manganese hexacyanochromate nanocomposites reported above. However, no peaks arising from elements of the PBA core could be detected for samples **7**-**9**. This indicates that the PVP shells of these nanoparticles are thicker than the probing limit of the XPS, which is limited to between 2 and 2.5 nm. It was therefore necessary to prepare a nominal $CsMn[Cr(CN)_6]$ nanocomposite (**10**) with a reduced $[Mn^{2+}]$/[PVP] ratio, the TEM images and ZFC/FC magnetization of which are shown overleaf in Figures 5.20 and 5.21 respectively. Both nanocubes and psuedospherical nanoparticles are clearly observable in Figure 5.20a, while comparison of a) and b) indicates that a wide range of particle sizes exist within **10**.

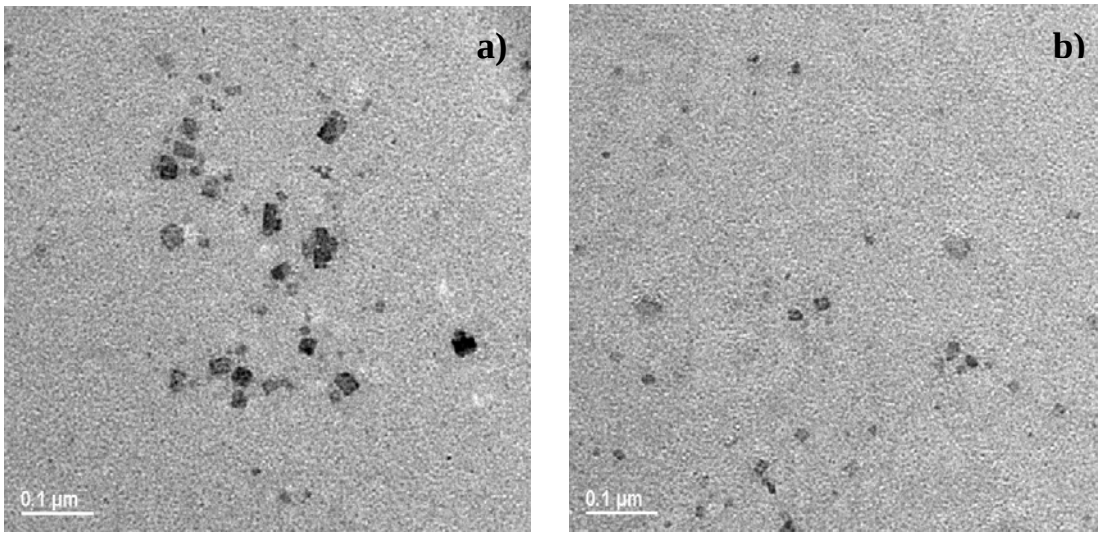

Figure 5.20 TEM images of **10.**

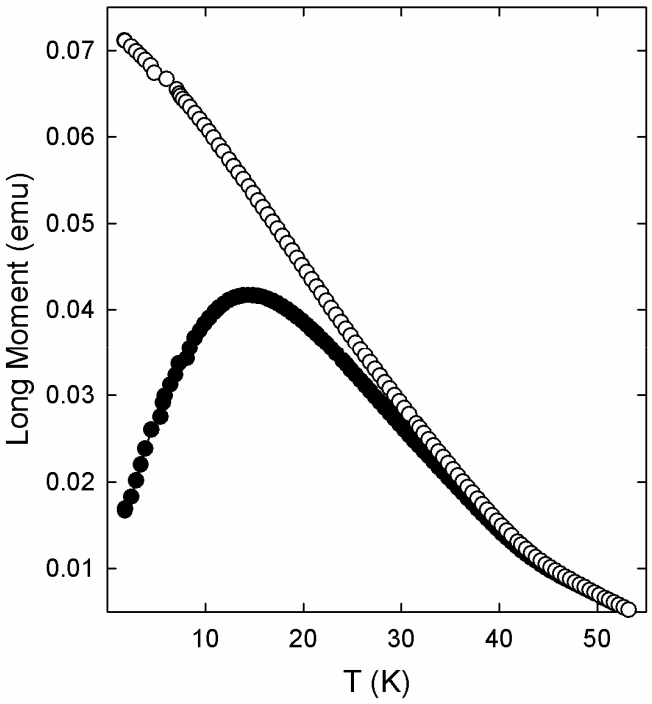

Figure 5.21 The zero-field cooled (ZFC) and field-cooled (FC) magnetization curves of **10** in a 2 mT field. Closed and open symbols represent the ZFC and FC magnetizations respectively.

The ZFC/FC magnetization curves of **10** are also indicative of a broad distribution of particle sizes, with the divergence of the curves occurring gradually (T_{irr} = 51.2 K and T_B = 14.4 K) and the ZFC curve exhibiting a broad peak.

The XPS survey scan of **10** (Figure 5.22) exhibits C *1s*, N *1s*, Cs *2p*, Cr *2p*, Mn *2p* and O *1s* photoemission peaks, thus confirming the presence of these elements within the specimen.

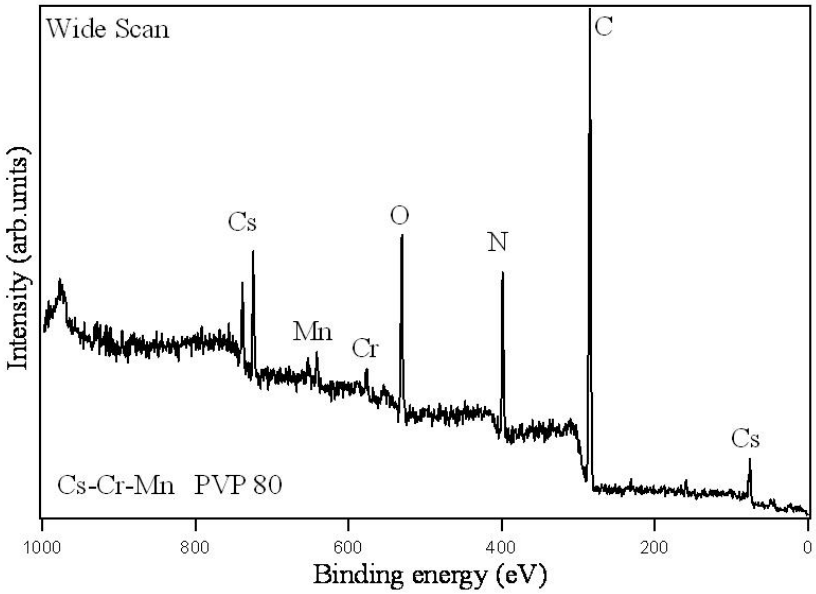

Figure 5.22 XPS survey scan of **10**. Binding energies were referenced to the carbon *1s* signal of $-CH_x-C^*H_2-CH_x-$ in polyvinylpyrrolidone (PVP) at 285.00 eV.[18] The full width half-maximum (FWHM) was 1.7 eV as determined from the 4th component (C*=O, see Figure 5.23 overleaf) of the PVP C *1s* spectrum and verified for the Cs *3d* line. No X-ray induced sample degradation was detected.

Figure 5.23 overleaf shows the photoemission spectra of caesium, chromium and manganese. Peak areas (normalized for the relative cross sections at the photon energy of 1486.6 eV used in the experiments and analyzer transmission) determined from these detailed scans indicate that the Cs:Mn:Cr ratio of **10** is 1.28:1.56: 1. The caesium spectra reveal $3d_{5/2}$ and $3d_{3/2}$ lines, each composed of a single component peak (width of 1.7 eV), at binding energies of 725.3 and 739.4 eV respectively. The chromium *2p* lines are displayed in Figure 5.23b and show that the spin-orbit induced doublet is observed with binding energies of ~ 577.1eV ($2p_{3/2}$) and ~586.7eV ($2p_{1/2}$). A deeper look into the $2p_{3/2}$ photoemission line, as depicted in Figure 5.23c overleaf, shows a broad peak (dotted line) which is due to the assumed presence of two types of chromium, namely Cr^{2+} and Cr^{3+} with corresponding binding energies of 577.0 eV and 578.2 eV.[24] This seems to indicate the existence of two phases, once containing $[Cr^{2+}(CN)_6]^{4-}$ (70%) and the other containing $[Cr^{3+}(CN)_6]^{3-}$ (30%). Detailed analysis of the Mn $2p_{3/2}$ line (fit and raw data) is also

shown in Figure 5.23d. The photoemission peak has been fitted taking into account multiplet splitting: due to multiple possible spin configurations in the *3d* shell of a high spin state compound, several initial and final states can occur. Combination of the various spin configuration and orbital momenta will result in different binding energies of the *2p* core level and therefore various photoemission peaks may be observed. Theoretical and experimental evidence from the work of Gupta[23] and Shen[25] (theory) and Nesbitt (experimental) reveals that the line shape observed in Figure 5.23d corresponds to a $2p_{3/2}$ Mn in HS Mn^{2+} state.[26]

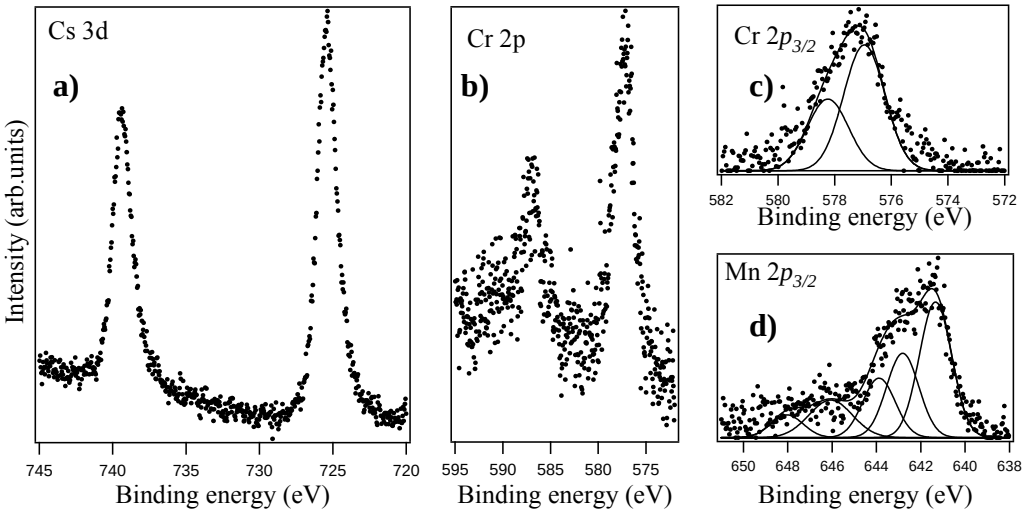

Figure 5.23 Detailed XPS spectra of the Cs *3d* (a), Cr *2p* (b), Cr *2p3/2* after Tougaard background removal, fit and raw data (c) and Mn *2p3/2* after Tougaard background removal, fit and raw data (d) regions of the $CsMn[Cr(CN)_6]$ nanocomposite (**10**).

The carbon *1s* peak testifies to the successful synthesis of **10** as a nominal PVP-CsMnCr composite. Figure 5.24a overleaf shows the carbon signal fitted, as described by Chan et al,[18] with the four different components of pure polyvinylpyrrolidone, namely: (1) $–CH_x-C^*H_2-CH_x-$, (2) $-C^*H_2-(C=O)-$,(3) $–N-C^*H_x-$ and (4) $-C^*=O$. From the difference between the experimental data and the continuous line representing the sum of the four components, it is clear that a fifth component must be added in order to fit the experimental data correctly. This fit is reproduced in Figure 5.24b where the fifth component placed at a binding energy of

285.7 eV, overlapping with the second component of the PVP C *1s*. This fifth component is due to the additional C*≡N bond arising from the PBA nanoparticles.

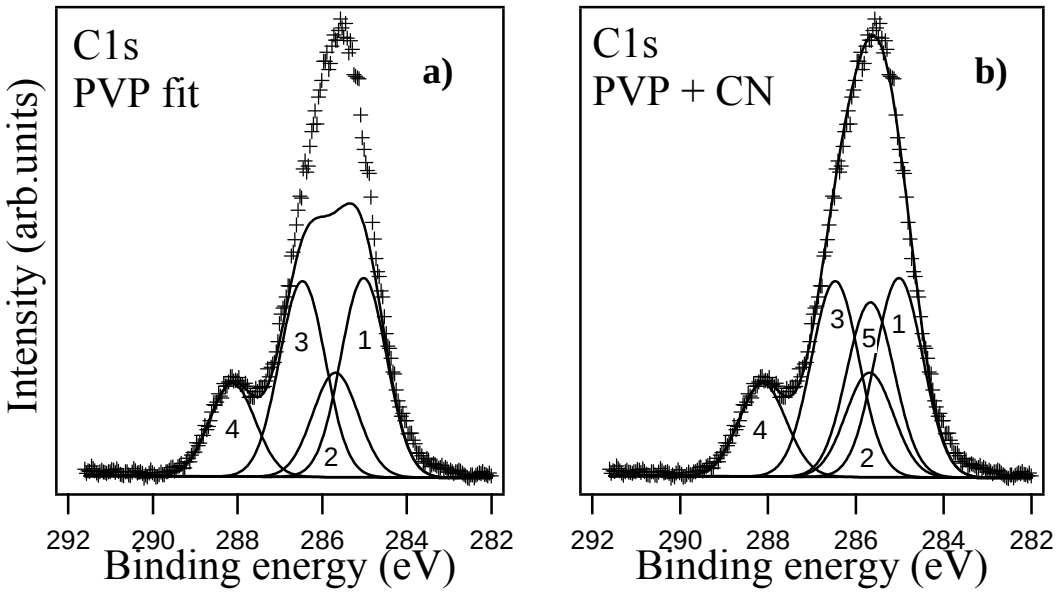

Figure 5.24 a) XPS spectra of C *1s* raw data and the 4 components PVP fit and b) C *1s* raw data 5 components PVP + CN fit.

5.5 Discussion

TEM images of the PVP-protected PBAs reported above typically show well dispersed pseudo-spherical nanoparticles, with mean particle diameters ranging from 7.5 to 16.5 nm. On the basis of these images, particle size and the extent of inter-particle separation within a given family of hexacyanochromate nanoparticles appear to be dependent upon the [PVP]/[M^{2+}] ratio. Mean particle diameters within the copper hexacyanochromates series (samples **1** to **3**) shrink from 13.4 to 8.0 nm as [PVP]/[Cu^{2+}] is increased from 16 to 83, while those of the caesium manganese hexacyanochromates (samples **7** to **9**) decrease from 16.5 to 7.5 nm as [PVP]/[Mn^{2+}] is increased from 8 to 183. The observation that particle size varies systematically with [PVP]/[M^{2+}] holds within a PVP-PBA family; however, inter-family comparisons are not valid since the strength of the cation-polymer interaction is known to be dependent upon the identity of M.[27, 28] The observed decrease of particle size with increasing [PVP]/[M^{2+}] concurs with the findings of previous studies into the influence of polymer concentration on PVP-protected Prussian Blue nanoparticle size[29] and is consistent with the mechanism of stabilization proposed by Uemura et al, where the Fe^{2+} ions bind to the polymer chain to confine growth and inhibit aggregation upon addition of $K_3[Fe(CN)_6]$.[9] It follows that increasing the concentration of PVP can be expected to suppress crystal growth to give smaller nanoparticles.

For ideal non-interacting single-domain nanoparticles which are free from any kind of anisotropy energy the susceptibility is only dependent upon the sample's magnetic moment and the applied field. However, in real systems where anisotropy exists the susceptibility is dependent upon the way in which the low temperature magnetic state is reached.[30, 31] The ZFC curves of **1** to **10** are obtained by cooling the samples from high temperature (where they exhibit superparamagnetic behaviour) to low temperature (where thermal relaxation effects are minimized) in the absence of any applied field before measuring the magnetization at step-wise increments in a small applied field.[32, 33] The FC curves are similarly obtained, except that cooling occurs in the presence of a small applied field, i.e. the FC magnetization is achieved by a

dynamic process. Consequently, the observed FC curve is expected to be strongly influenced by the relaxation behaviour of the nanoparticles under measurement.[34]

The magnetizations of the $Mn_3[Cr(CN)_6]_2$, $CsMn[Cr(CN)_6]$ and $Cu_3[Cr(CN)_6]_2$ nanocomposites recorded in low magnetic fields are quite distinct from those of the equivalent bulk materials which order at 66, 90 and 66 K respectively. All the PVP-protected PBAs reported in this chapter exhibit - or tend towards - a maximum in the ZFC curve (indicative of T_B) and an irreversibility of the ZFC and FC curves at temperatures well below T_C (T_N) of the corresponding bulk PBA. The ZFC maximum is typically observed slightly below the temperature of irreversibility. These distinct features are not exclusive to superparamagnetic systems; they may also be observed in nanoparticle systems exhibiting spin-glass behaviour. The latter scenario arises where interactions between nanoparticles are non-negligible. For example, in a dense ensemble of single domain nanoparticles the interparticle interaction may dominate over single particle blocking giving rise to collective freezing of the superspins into a spin glass phase below a critical temperature (T_g).[3] To distinguish between these two behaviours it is necessary to examine the AC susceptibility data. In order to simplify the proceeding discussion superparamagnetism will be assumed until AC susceptibility measurements prove otherwise.

The ZFC magnetization of a superparamagnetic system tends towards zero below the blocking temperature because the nanoparticles, and hence the easy axes along which the supermoments are aligned, are randomly orientated and thus tend to cancel each other out. Above this temperature, where there is sufficient thermal energy to overcome the anisotropy barrier, the permanent alignment of the supermoment along a particular axis is destroyed and the material now exhibits paramagnetic type behaviour. Thus the crossover from blocked-to-free is marked by a peak, the characteristics of which may provide an indication of the particle size distribution. A wide distribution of particle sizes gives rise to a range of blocking temperatures, thus we expect the breadth of the ZFC curve and the difference between T_B and T_{irr} to vary directly with the range of particle sizes. This is consistent with our observations

for samples **2-7** which exhibit well defined ZFC maxima and narrow particle size distributions. Consequently, based on the ZFC/FC magnetizations of the manganese hexacyanochromate series we hypothesise that further TEM images will reveal a narrowing of particle size distribution upon going from **4-6.**

The suppression of T_B with contracting particle diameter observed within the copper hexacyanochromate family of nanoparticles is consistent with the direct relationship between the activation energy and particle volume outlined in Equation 5.1. Based upon the particle size distributions determined from TEM images, this relationship does not appear to hold for the caesium manganese hexacyanochromate family. While TEM images indicate that the particle size decreases from **7** to **8** to **9** as expected (that is with increasing PVP concentration) an anomaly seems to exist in the relationship between T_B and mean particle size, with the T_B of **8** being lower than that of **9**. There are a number of factors which may account for this unexpected result. The first of these being that the magnetic properties of single domain assemblies are strongly influenced by interparticle interactions - arising from dipolar coupling between the particles - as well as particle size. For example, Mallah et al found that the blocking temperature of an assembly of PVP protected $CsNi[Cr(CN)_6]$ nanoparticles decreased upon dilution, that is with increasing interparticle separation.[35] However, the nature of the dependence of T_B on interparticle interaction is not well understood, with recent literature suggesting that the particle interactions may either enhance or depress T_B (or equivalently the energy barrier) compared to the non-interacting values.[36, 37]

It is important to note that the TEM derived size information is localized to the areas of grid where the images are obtained. Thus one or more of the TEM images may not be representative of caesium manganese hexacyanochromate nanocomposite from which it was taken. For example, the seemingly anomalously high T_B of **9** may be accounted for if the true mean particle size of **9** is larger than that determined from the TEM images. This hypothesis is supported by estimations of particles size from XRD patterns of **7**, **8** and **9**; application of the Scherrer formula to the (200) reflections suggest that the mean particle size of **8** is smaller than that of both **7** and

9. Furthermore, if the particles are not as widely dispersed as the TEM images suggest then we must consider the influence that that inter-particle interactions can have on T_B. The probability of such misrepresentations occurring can be reduced by maximizing the number of samples analysed and images obtained.

AC susceptibility measurements were employed to investigate the origin of ZFC/FC irreversibility of **2, 5**, **7** and **9**. Frequency dependent behaviour is exhibited in both the $\chi'(T)$ and $\chi''(T)$ susceptibility components for each of the nanoparticle composites, with the temperature of peak susceptibility (T_B) varying directly with the measurement frequency. The magnetization of a nanoparticle will only appear static (blocked) if the measuring time (τ_m) is much shorter than the relaxation time (τ). AC susceptibility measurements performed over a range of different frequencies are essentially a means of studying the relationship between the magnetic response and τ_m, since $\tau = (2\pi f)^{-1}$ (Equation 5.4). Thus by increasing the measurement frequency (*f*) we are effectively reducing τ_m and increasing the threshold of thermal activation energy necessary to observe magnetization fluctuations. It is therefore rational that T_B should be directly related to *f*.

The values of Φ and τ extracted from AC susceptibility measurements of **2, 5** and **9** are consistent with superparamagnetism. The superparamagnetic behaviour of **2** is further verified by the absence of a magnetic hysteresis above T_B. The Φ and τ values of **7** are characteristic of spin-glass freezing, rather than blocking. Such behaviour is not surprising when we consider the densely packed array of nanoparticles shown in the TEM image of **7** (Figure 5.14a). At adequately high packing densities interparticle interactions become non-negligible, modifying the anisotropic energy barriers of every particle in the system. In such instances magnetization reversal is determined by the total free energy of the nanoparticle array, rather than the anisotropic energy barriers of individual particles. At low temperatures the nanoparticles may form a collective state quite distinct from that of the individually blocked nanoparticles. [3]

X-ray photoelectron spectroscopy has proven a useful means of establishing the surface oxidation states and elemental compositions of PBAs. Nevertheless, the XPS analysis of caesium manganese hexacyanochromate nanocomposites reported above is, to the best of our knowledge, the first time the technique has been employed in the characterization of polymer protected PBA nanoparticles. XPS measurements of **10** indicate that manganese and caesium are present within the sample as HS Mn^{2+} and Cs^{+}, whereas chromium is – somewhat surprisingly - present as both Cr^{2+} and Cr^{3+}. The reduction of $[M'^{3+}(CN)_6]^{3-}$ to $[M'^{2+}(CN)_6]^{4-}$ within PBAs typically occurs via an intermetallic charge transfer from M^{2+} to M'^{3+}. If such a process were to account for the $[Cr^{2+}(CN)_6]^{4-}$ moieties of **10**, we would expect to observe the presence Mn^{3+} ions. However, XPS analysis unequivocally shows that manganese ions of **10** exist solely as Mn^{2+} and thus raises speculation as to the origin of the electron which drives the reduction Cr^{3+} to Cr^{2+}. Furthermore, the Cs:Mn:Cr ratio of 1.28:1.56:1 (as determined by XPS measurements) presents a problem of electroneutrality, since the positive charge contributed by Cs^{+} and Mn^{2+} ions is only partially cancelled by the negative charge contributed by the $[Cr^{2+}(CN)_6]^{4-}$ and $[Cr^{3+}(CN)_6]^{3-}$ moieties.

Relatively little is know about the nature of the chemical interaction between PVP and the metal cations of PBAs. The polymer-metal interaction of PVP-stabilized metal nanoparticles has, however, been the subject of several investigations. The results of these studies indicate that PVP not only acts as a stabilizer, but may also modify the electronic structures of the metallic nanoparticles. For example, spectroscopic studies provide evidence of a charge transfer from the C=O groups of PVP to the metal atoms in Au-PVP, Rh-PVP and Pt-PVP nanoparticles.[38, 39] Furthermore, the nature of polymer-metal interaction in the latter nanocomposite has proven to be size-dependent: a charge from the C=O group of PVP to Pt occurs for Pt-PVP particles < 7nm, while for those particles >25 nm a charge transfer from Pt to the PVP side chain is observed.[40] Shen et al exploited the dual functionality of PVP, as a steric stabilizer and reducing reagent, to prepare PB nanocubes and nanospheres using $K_3[Fe(CN)_6]$ as a single-source precursor. The $[Fe(CN)_6]^{3-}$ ions dissociate into Fe^{3+} ions which are subsequently reduced to Fe^{2+} by PVP. In this case the capacity of PVP for reduction was attributed to the hydroxyl (-OH) groups which terminate

the PVP chains.[25] It is feasible that polymer-metal interactions similar to those described above occur in PVP-stabilized PBA nanoparticles. Consequently, it may be necessary to include both the protecting polymer and the PBA core when considering electroneutrality and the source of reductive electrons in PVP-stabilized PBAs.

5.6 Conclusions

Three novel series of PBA nanoparticles based upon the $[Cr(CN)_6]^{3-}$ molecular building block have been successfully prepared by employing PVP to confine growth and inhibit aggregation. TEM images of these nanocomposites redispersed in H_2O show well dispersed, pseudo-spherical nanoparticles, the dimensions of which are found to decrease with increasing polymer concentration. Control over the magnetic properties of these PBAs can be exerted by systematically varying the $[PVP]/[M^{2+}]$ ratio, thus illustrating the strong correlation between particle size and physical properties in the nanoregime.

Each of the samples investigated by means of AC susceptibility exhibited frequency dependence of the blocking temperature. Arrhenius plots of ln τ as a function of the reciprocal blocking temperature demonstrate the existence of superparamagnetism within each of the hexacyanochromate families. The highest recorded blocking temperature of 5.8 K was observed for $Cu_{1.52}[Cr(CN)_6]\{C_6H_9NO\}_{23.63}$ nanoparticles with a mean diameter of 11.9 nm and a 10 mT applied field. Quantification of the frequency dependence of $Cs_{0.81}Mn_{1.07}[Cr(CN)_6](C_6H_9NO)_{8.35}(H_2O)_{5.80}$ nanoparticles (mean particle size = 16.5 nm) is indicative of spin-glass behaviour arising from the presence of interparticle interactions.

X-ray photoemission spectroscopy provided some useful insights into the nature of polymer-metal interactions in PVP-stabilized caesium manganese hexacyanochromate. Our findings lend further support to previous results which indicate that PVP modifies the electronic structure of the nanoparticle cores which it stabilizes. This effect warrants further investigation as it may have serious implications for the rational design of magnetic PBA nanoparticles.

5.7 Bibliography

1. D. L. Leslie-Pelecky and R. D. Rieke, *Chemistry of Materials*, 1996, **8**, 1770-1783.
2. J. Vejpravova, J. Plocek, D. Niznansky, A. Hutlova, J. L. Rehspringer and V. Sechovsky, in *WDS'05 Proceedings of Contributed Papers: Part III*, ed. J. Safrankova, Matfyzpress, Prague, 2005, pp. *518–523*
3. S. Bedanta and W. Kleemann, *Journal of Physics D-Applied Physics*, 2009, **42**, 013001.
4. C. Liu, A. J. Rondinone and Z. J. Zhang, *Pure and Applied Chemistry*, 2000, **72**, 37-45.
5. G. A. Held, G. Grinstein, H. Doyle, S. H. Sun and C. B. Murray, *Physical Review B*, 2001, **64**, 144420.
6. V. Skumryev, S. Stoyanov, Y. Zhang, G. Hadjipanayis, D. Givord and J. Nogues, *Nature*, 2003, **423**, 850-853.
7. R. H. Kodama, *Journal of Magnetism and Magnetic Materials*, 1999, **200**, 359-372.
8. L. Catala, A. Gloter, O. Stephan, G. Rogez and T. Mallah, *Chemical Communications*, 2006, 1018-1020.
9. T. Uemura and S. Kitagawa, *Journal of the American Chemical Society*, 2003, **125**, 7814-7815.
10. J. G. Moore, E. J. Lochner, C. Ramsey, N. S. Dalal and A. E. Stiegman, *Angewandte Chemie-International Edition*, 2003, **42**, 2741-2743.
11. L. Catala, T. Gacoin, J. P. Boilot, E. Riviere, C. Paulsen, E. Lhotel and T. Mallah, *Advanced Materials*, 2003, **15**, 826.
12. W. Kosaka, M. Tozawa, K. Hashimoto and S. I. Ohkoshi, *Inorganic Chemistry Communications*, 2006, **9**, 920-922.
13. Y. Jinli, X. Yan and X. Desheng, *Chemical Physics Letters*, 2007, **435**, 317-321.
14. Q. Kong, X. G. Chen, J. L. Yao and D. S. Xue, *Nanotechnology*, 2005, **16**, 164-168.
15. T. Uemura, M. Ohba and S. Kitagawa, *Inorganic Chemistry*, 2004, **43**, 7339-7345.
16. F. A. Frye, D. M. Pajerowsk, N. E. Anderson, J. Long, J. H. Park, M. W. Meisel and D. R. Talham, *Polyhedron*, 2007, **26**, 2273-2275.
17. P. Zhang, F. Zuo, F. K. Urban, A. Khabari, P. Griffiths and A. Hosseini-Tehrani, *Journal of Magnetism and Magnetic Materials*, 2001, **225**, 337-345.
18. K. Chan, L. E. Kostun, W. E. Tenhaeff and K. K. Gleason, *Polymer*, 2006, **47**, 6941-6947.

19. T. Sven, AVS, 2005, pp. 741-745.

20. D. A. Shirley, *Physical Review B*, 1972, **5**, 4709-4714.

21. H. Borchert, E. V. Shevehenko, A. Robert, I. Mekis, A. Kornowski, G. Grubel and H. Weller, *Langmuir*, 2005, **21**, 1931-1936.

22. J. I. Langford and A. J. C. Wilson, *Journal of Applied Crystallography*, 1978, **11**, 102-113.

23. R. P. Gupta and S. K. Sen, *Physical Review B*, 1975, **12**, 15-19.

24. W. E. Buschmann, S. C. Paulson, C. M. Wynn, M. A. Girtu, A. J. Epstein, H. S. White and J. S. Miller, *Chemistry of Materials*, 1998, **10**, 1386-1395.

25. X. P. Shen, S. K. Wu, Y. Liu, K. Wang, Z. Xu and W. Liu, *Journal of Colloid and Interface Science*, 2009, **329**, 188-195.

26. H. W. Nesbitt and D. Banerjee, *American Mineralogist*, 1998, **83**, 305-315.

27. M. Liu, X. Yan, H. Liu and W. Yu, *Reactive and Functional Polymers*, 2000, **44**, 55-64.

28. E. Diaz, R. B. Valenciano and I. A. Katime, *J Appl Polym Sci*, 2004, **93**, 1512-1518.

29. V. Hornok and I. Dekany, *Journal of Colloid and Interface Science*, 2007, **309**, 176-182.

30. J. Hesse, *Journal of Alloys and Compounds*, 2001, **326**, 205-214.

31. J. Hesse, H. Bremers, O. Hupe, M. Veith, E. W. Fritscher and K. Valtchev, *Journal of Magnetism and Magnetic Materials*, 2000, **212**, 153-167.

32. M. F. Hansen and S. Morup, *Journal of Magnetism and Magnetic Materials*, 1999, **203**, 214-216.

33. C. Papusoi, *Journal of Magnetism and Magnetic Materials*, 1999, **195**, 708-732.

34. R. W. Chantrell, N. Walmsley, J. Gore and M. Maylin, *Physical Review B*, 2001, **6302**.

35. D. Brinzei, L. Catala, N. Louvain, G. Rogez, O. Stephan, A. Gloter and T. Mallah, *Journal of Materials Chemistry*, 2006, **16**, 2593-2599.

36. D. Peddis, C. Cannas, A. Musinu and G. Piccaluga, *Journal of Physical Chemistry C*, 2008, **112**, 5141-5147.

37. J. J. Lu and H. L. Huang, *Chinese Journal of Physics*, 2000, **38**, 81-94.

38. Y. Borodko, S. M. Humphrey, T. D. Tilley, H. Frei and G. A. Somorjai, *Journal of Physical Chemistry C*, 2007, **111**, 6288-6295.

39. H. Tsunoyama, N. Ichikuni, H. Sakurai and T. Tsukuda, *Journal of the American Chemical Society*, submitted **2009.**

40. L. M. Qiu, F. Liu, L. Z. Zhao, W. S. Yang and J. N. Yao, *Langmuir*, 2006, **22**, 4480-4482.

Chapter 6

Conclusions

Molecule-based magnets based upon Prussian Blue analogues, $A_xM^{II}[M'^{III}(CN)_6]$ (where A= alkali metal cation and M, M'= transition-metal cations), exhibit a wealth of exotic electronic and magnetic behaviours. The overall aim of the work described in the preceding chapters was the synthesis and characterization of novel Prussian Blue analogues (PBAs).

The flexibility of the PBA framework structure was exploited to synthesise the novel $Rb_xNi_zMn_{(1-z)}[Fe(CN)_6]\cdot yH_2O$ ($0<z<1$) series, which incorporates both ferromagnetic and antiferromagnetic interactions. The synthesis and characterization of this family of PBAs served to illustrate how relatively minor changes in chemical composition can induce significant changes in magnetic properties. For example, some members exhibited a switch in the sign of the spontaneous magnetization (equivalent to a change in the direction of the magnetic poles in a bar magnet) in response to changes in temperature. In addition, the rare phenomenon of a double magnetic pole inversion was attained by incorporating a small fraction of Fe^{2+} into the $Rb_xNi_zMn_{(1-z)}[Fe(CN)_6]$ lattice.

The "tunability" of PBAs – their potential to switch between electronic and magnetic states upon application of an external stimulus – is of particular interest. Exploration of the way in which these materials react to external perturbations may: 1) provide us with an improved understanding of the inherent nature of these materials and 2) lead to development of commercially attractive PBAs, i.e. those suitable for application in new data storage and information transport devices. The research presented here focused specifically on the use of light and pressure as external stimuli, with a view to developing photo- and piezo-switchable multifunctional PBAs.

Upon X-ray irradiation, several members of the $Rb_xNi_zMn_{1-z}[Fe(CN)_6]$ ($0<x<1$) series underwent cooperative transitions, which in turn led to otherwise inaccessible metastable states. These photo-induced phenomena were observable over a broad

range of temperatures. Hydrostatic pressure proved to be an effective means of tuning magnetic interactions and trapping of novel inaccessible states within this series of PBAs. The $Rb_{0.64}Ni_{0.31}Mn_{0.87}[Fe(CN)_6]\cdot 2.8H_2O$ composition was found to be an extremely responsive pressure sensor, exhibiting pressure-induced sequential multiple magnetic pole inversions and antiferromagnetic/ferromagnetic crossover. Diminishing piezo- and photo-sensitivities observed as the extent of Ni doping increases within the $Rb_xNi^{II}_zMn_{(z-1)}[Fe(CN)_6]\cdot yH_2O$ are attributed to disrupted cooperativity between redox active Fe^{III}(S = 1/2)-CN-Mn^{II}(S = 5/2) units due to the presence of non redox-active Fe^{III}(S = 1/2)-CN-Ni^{II}(S = 4) units.

PBAs incorporating the Cu^{2+} ion were studied with the aim of establishing the influence of structural distortions on the photo-induced electron transfer which has been observed in a number of related compounds. X-ray powder diffraction and absorption measurements of Jahn-Teller distorted caesium copper hexacyanoferrates revealed an unusual and unexpected response to photoirradiation which could not be attributed to any of the reversible phase transitions typically associated with PBAs i.e. spin crossover, charge transfer or cyano flip. Instead photo-irradiation was found to initiate an irreversible chemical transformation which results in the simultaneous reduction of both transition metal centres and the expulsion of cyanide ligands.

Latterly, the miniaturization of electronic devices and the demand for high density data storage has created an interest in nanostructured molecular magnets. However, while the relationship between the unit-cell structure and magnetic properties of PBAs has been extensively studied, few efforts have been made towards understanding and controlling the growth mechanisms of these solids. Thus, one of the key objectives of the research encompassed within this thesis was the preparation of PBA nanoparticles. Three series of transition metal hexacyanochromate nanoparticles were fabricated by means of a polymer protected synthesis, in which poly(vinylpyrroldine) (PVP) is employed as a confining nanoreactor medium. Particle sizes were varied between 7.5 and 16.5 nm, and magnetic responses subsequently tuned, by controlling the feed ratio of M site ions to PVP monomers employed in the synthesis. The PVP-protected PBAs exhibited magnetic behaviours quite distinct from those of the corresponding bulk materials. Superparamagnetism,

which is indicative of single domain magnetic objects, was observed within each nanoparticle series. Whilst the low blocking temperatures of the PBA nanoparticles explored within this work restrict their technological applications, they do serve to illustrate that particle sizes and magnetic behaviours can be controlled with relative ease by varying the concentration of the PVP protectant. Thus applying polymer protected synthesis to PBA building blocks which display higher magnetic ordering temperatures may provide a feasible route to attaining new functional magnetic nanoparticles.

.

Appendix 1 - IR Spectra of $Rb_xNi^{II}_zMn_{(1-z)}[Fe(CN)_6]\cdot yH_2O$ Series

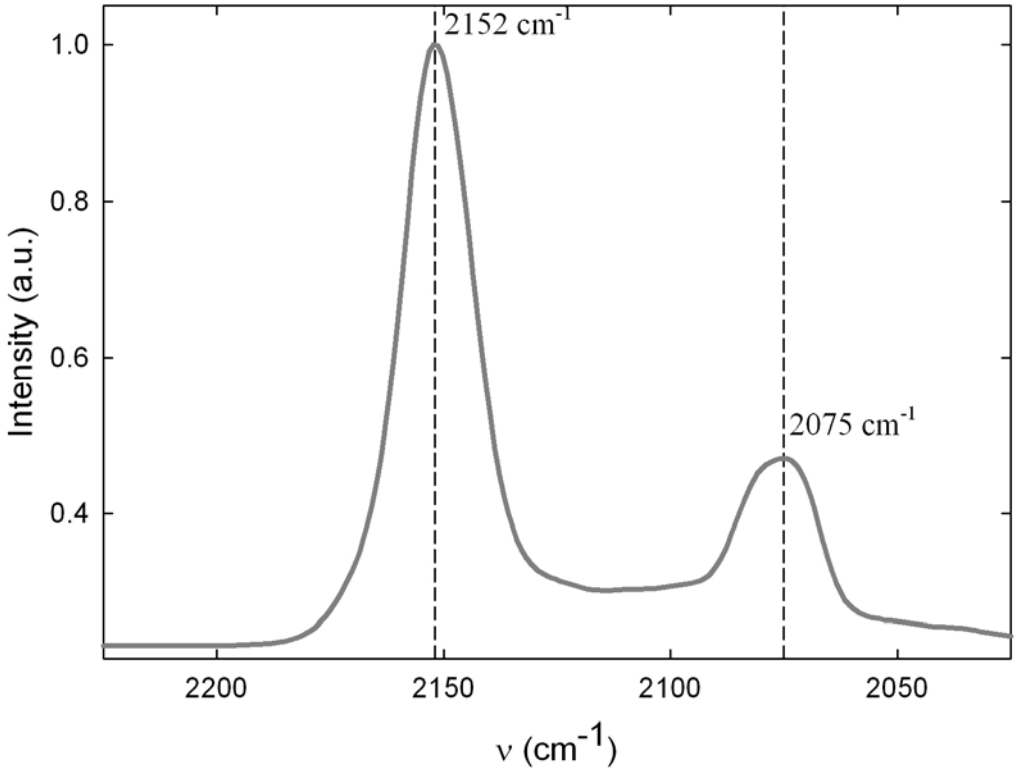

Figure A1.1 IR spectrum of $Rb_{0.59}Ni_{0.13}Mn_{0.97}[Fe(CN)_6]\cdot 1.72H_2O$

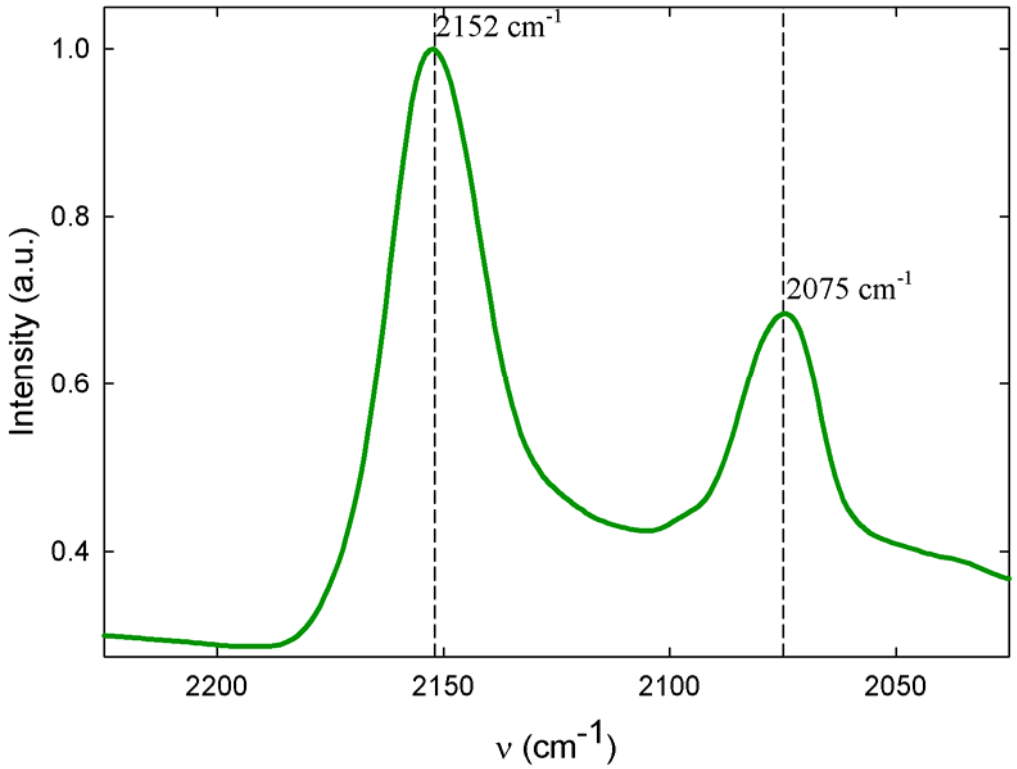

Figure A1.2 IR spectrum of $Rb_{0.78}Ni_{0.23}Mn_{0.88}[Fe(CN)_6]\cdot 1.46H_2O$

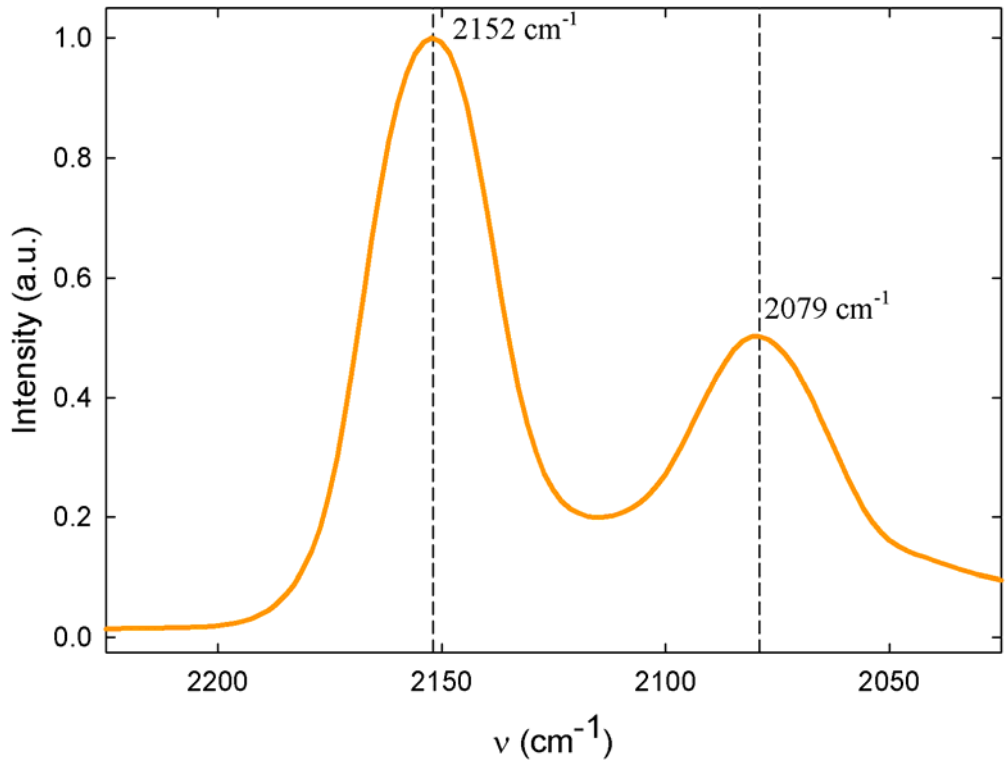

Figure A1.3 IR spectrum of $Rb_{0.64}Ni_{0.31}Mn_{0.87}[Fe(CN)_6]\cdot 2.8H_2O$

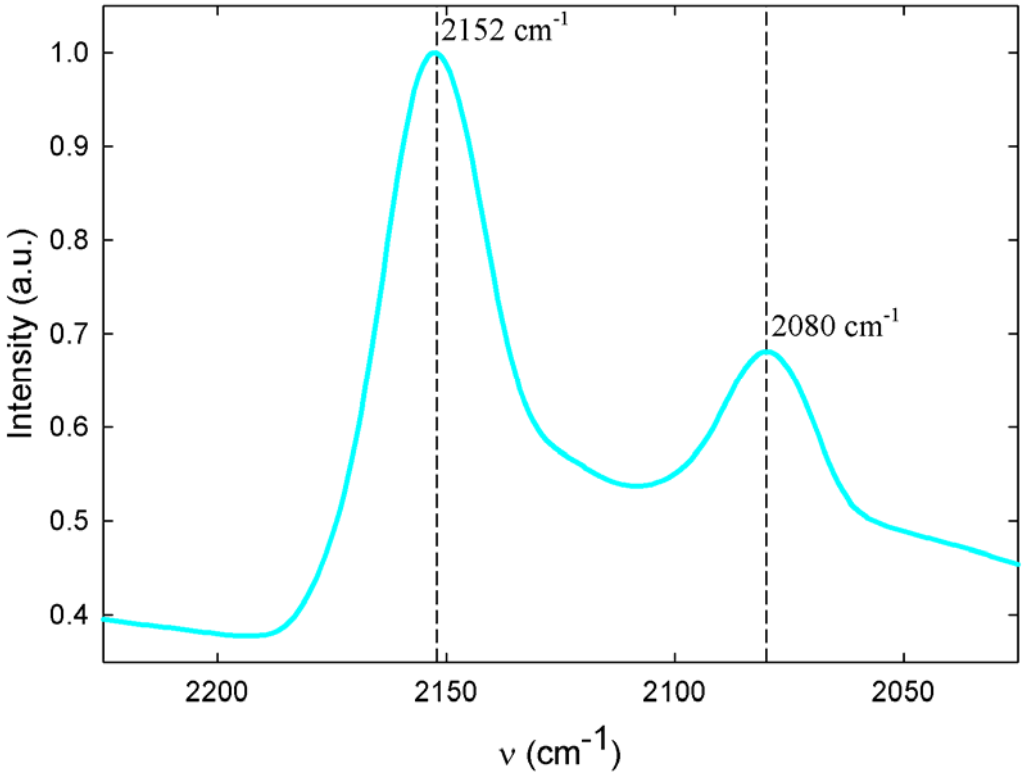

Figure A1.4 IR spectrum of $Rb_{0.54}Ni_{0.34}Mn_{0.75}[Fe(CN)_6]\cdot 3.28H_2O$

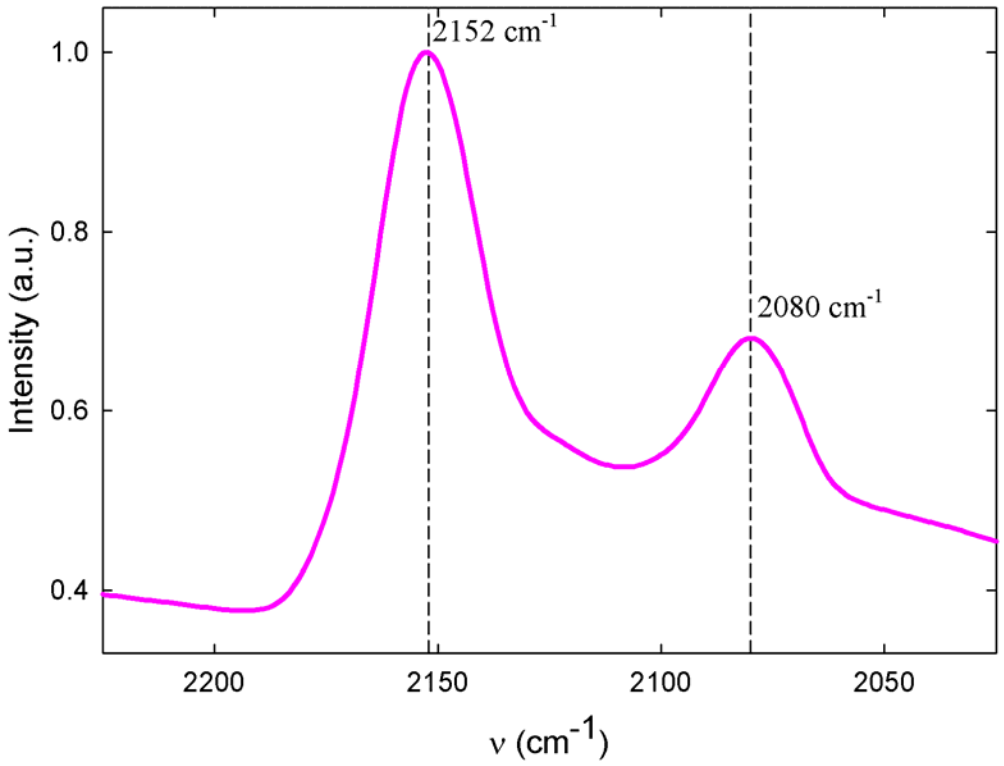

Figure A1.5 IR spectrum of $Rb_{0.64}Ni_{0.45}Mn_{0.66}[Fe(CN)_6]\cdot 2.33H_2O$

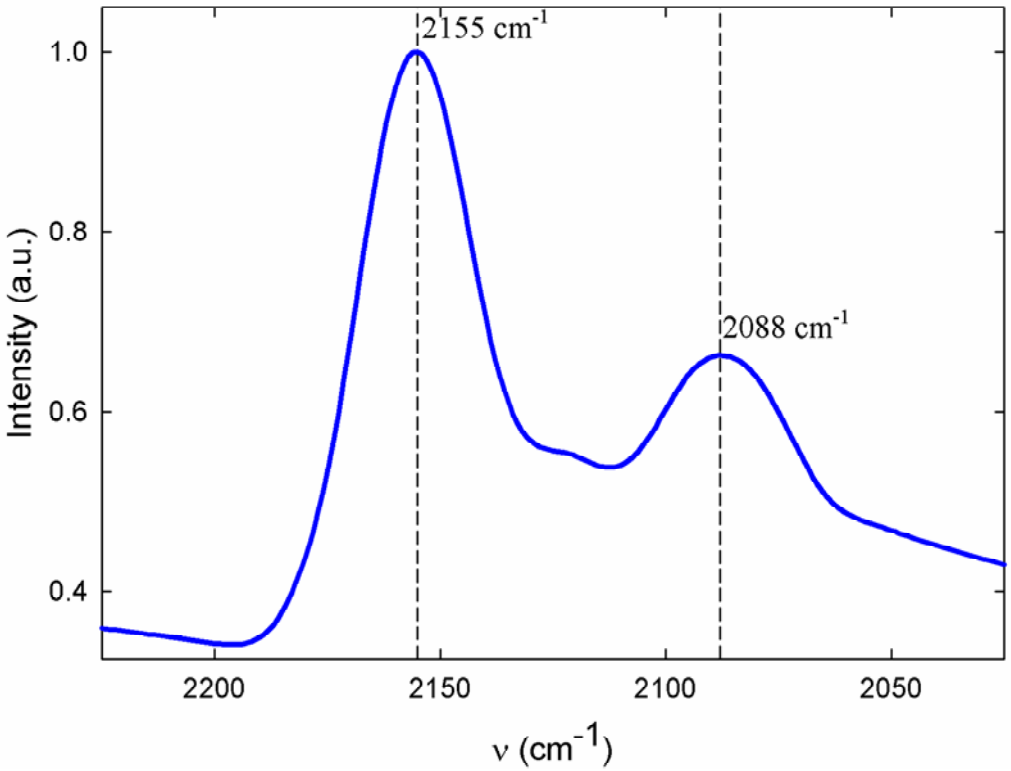

Figure A1.6 IR spectrum of $Rb_{0.67}Ni_{0.52}Mn_{0.53}[Fe(CN)_6]\cdot 2.22H_2O$

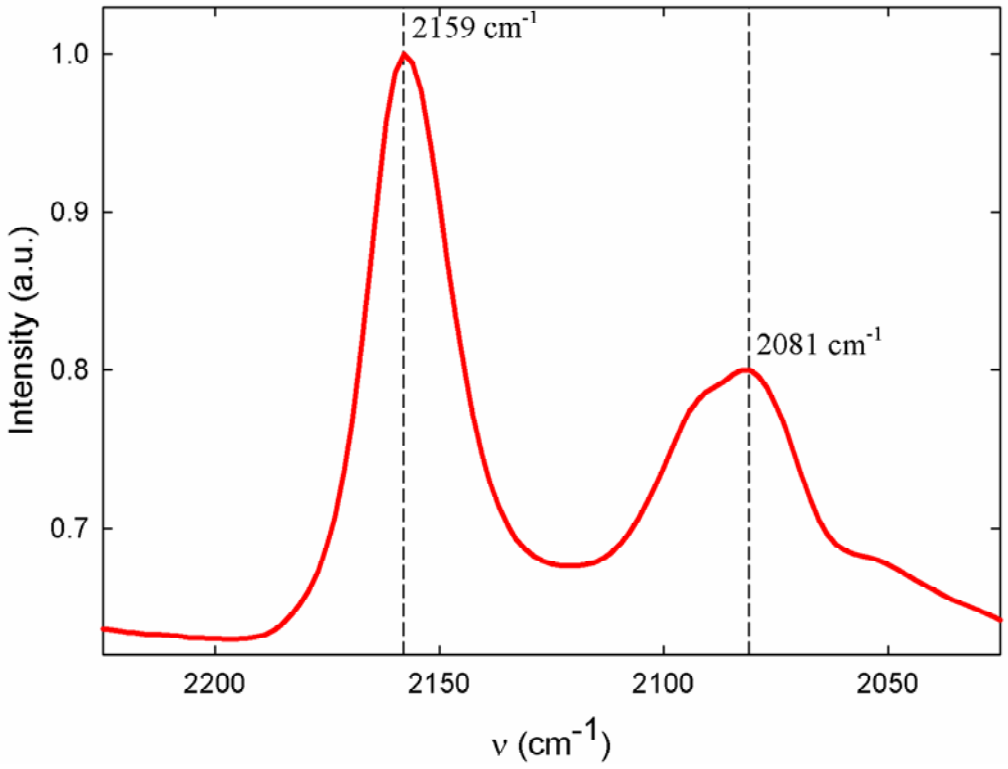

Figure A1.7 IR spectrum of $Rb_{0.64}Ni_{0.62}Mn_{0.42}[Fe(CN)_6]\cdot 2.56H_2O$

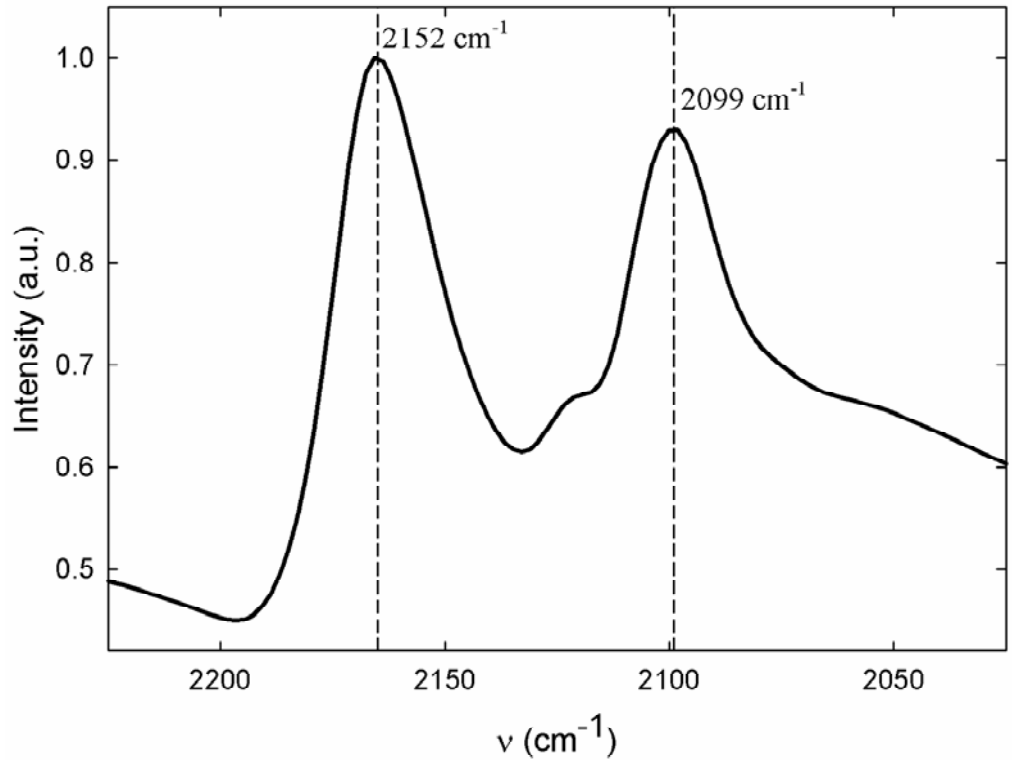

Figure A1.8 IR spectrum of $Rb_{0.65}Ni_{1.06}[Fe(CN)_6]\cdot 3.13H_2O$

Appendix 2

Postgraduate Lectures

CSEC Seminars

School of Chemistry Inorganic, Materials, Structural and Physical Chemistry/Chemical Physics Seminars

School of Chemistry Colloquia

Professional Development Courses

HTML & Web Authoring (26/06/07)

Academic Paper Writing (30/05/06)

EndNote Reference Manager (22/03/06)

Effective Writing (21/02/2006)

Effective Presentations (18/02/06)

Science Communication in Action (19/10/05).

Conferences & Meetings

MagNet Meeting, Cambridge, 2005

MagNet Meeting, Edinburgh, 2006

School of Chemistry Physical Section Meeting, Firbush, 2006

EMRS Spring Meeting, Strasbourg, 2007.

Academic Awards

JSPS Summer Program Fellowship, Department of Chemistry, Graduate School of Science, The University of Tokyo, 17th June – 21st August 2008.

European Network of Excellence MAGMANet award of financial support for the poster presentation, "Laser-induced Phase Transitions & Chemical Modifications in Prussian Blue Analogues Containing the Jahn-Teller Active Cu^{2+} Ion", EMRS Spring Meeting 2007.

Prize winning oral presentation, "Pressure Effects on the Magnetic Properties of Tri-metallic Prussian Blue Analogues", University of Edinburgh Physical Chemistry Graduate School Trip, 2005.

J|A|C|S
COMMUNICATIONS

Published on Web 04/15/2006

Pressure-Induced Sequential Magnetic Pole Inversion and Antiferromagnetic−Ferromagnetic Crossover in a Trimetallic Prussian Blue Analogue

Lindsay Egan,[†,||] Konstantin Kamenev,[‡,||] Dionisis Papanikolaou,[§] Yasuhiro Takabayashi,[§] and Serena Margadonna*[,†,||]

School of Chemistry, School of Engineering & Electronics, and Centre for Science at Extreme Conditions, University of Edinburgh, Edinburgh EH9 3JJ, U.K., and Department of Chemistry, University of Durham, Durham DH1 3LE, U.K.

Received March 4, 2006; E-mail: serena.margadonna@ed.ac.uk

Prussian blue (PB) analogues display a wide range of important magnetic (e.g., room temperature magnetic ordering) and magneto-optical (e.g., piezoelectric ferromagnetism, photoinduced (de)-magnetization) properties.[1] This stems from the flexibility of their framework structure which allows one to adjust at will the composition and tune the total magnetization of the system by selecting appropriate spin sources. In addition, the nature of the magnetic exchange can be anticipated in advance from basic orbital interaction arguments and the structure directing quality of the cyanide bridge. A notable example of this approach has been the design of magnetic materials (Néel's *N* phases)[2] displaying magnetic pole inversion below a compensation temperature, T_{comp}, by using competing ferromagnetic (FM) and antiferromagnetic (AFM) interactions in trimetallic PB analogues, $(Ni_xMn_{1-x})_{1.5}[Cr(CN)_6]\cdot nH_2O$ ($x \sim 0.4$).[3] The reversible change of the sign of the spontaneous magnetization can be also observed as a response to an external stimulus, such as humidity and light irradiation.[4]

The application of hydrostatic pressure is also a powerful tool to modulate the properties of molecular magnets, including PB analogues, which show various responses, such as internal electron transfer, spin state transitions, and linkage isomerism of the cyanide bridge.[5] In addition, pressure strongly influences the ground state magnetic properties by finely tuning the strength of the ligand field and the $d-\pi-d$ exchange interactions. Here we show that pressure can be also employed to induce a series of magnetic pole inversions in an appropriately chosen trimetallic PB ferrimagnet, $Rb_{0.64}Ni_{0.31}Mn_{0.87}[Fe(CN)_6]\cdot 2.8H_2O$ (**1**).[6] Depending on the experimental conditions, the magnetization of **1** can be reversibly switched sequentially from positive to negative and back to positive at very low pressures. At moderate pressures, a reversible internal charge transfer is also induced, leading to a crossover from ferrimagnetic to FM ordering.

1 is a member of the family of mixed ferri-ferromagnets, $Rb_yNi^{II}{}_xMn^{II}{}_{1-x}[Fe^{III}(CN)_6]_z\cdot nH_2O$, which incorporate both FM ($J_{Ni-Fe} > 0$) and AFM ($J_{Mn-Fe} < 0$) interactions and display a change in sign of the spontaneous magnetization for $x \approx 0.35-0.45$ below $T_{comp} \approx 6-8$ K. It was chosen in such a way as to be ferrimagnetic but with a value of x placing it at ambient P near Néel's $R-N$ phase boundary for exhibiting magnetic pole inversion.[2] The magnetic response of **1** is consistent with overall AFM exchange interactions (Weiss temperature, $\theta = -7.5(1)$ K), while both the measured $\chi_M T$ at 300 K (4.53 cm^3 K mol^{-1}) and the saturation magnetization (2.63 μ_B) are consistent with parallel alignment of the Ni^{II} ($S = 1$) and antiparallel alignment of Mn^{II} (HS, $S = 5/2$) spins with the Fe^{III} (LS, $S = 1/2$) spins. **1** is a ferrimagnet, $T_N \approx 16$ K, with the temperature dependence of the spontaneous magnetization showing a double hump (Figure 1a).

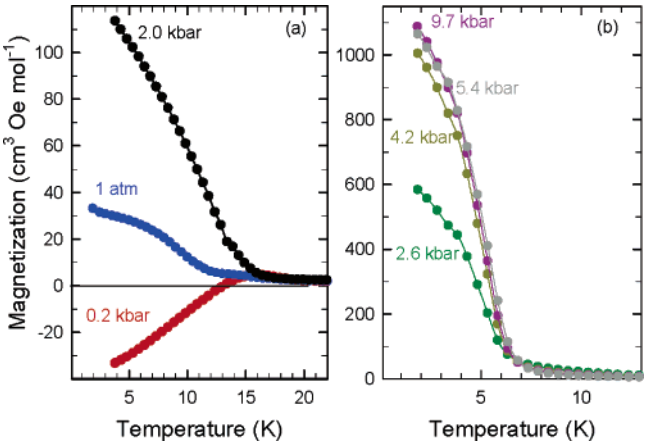

Figure 1. Temperature dependence of the magnetization ($H = 1$ mT, field cooling) of $Rb_{0.64}Ni_{0.31}Mn_{0.87}[Fe(CN)_6]\cdot 2.8H_2O$ as a function of pressure.

The magnetic response of **1** proved extremely sensitive to pressure. Remarkably, upon pressurizing at *only* 0.2 kbar, the material exhibits magnetic pole inversion with the spontaneous magnetization reversing its sign to negative below $T_{comp} = 13$ K (Figure 1a).[7] This is accompanied by an increase of the ordering temperature to 17.5 K and a decrease of both θ (−5.9(1) K) and $\chi_M T$ at 300 K (4.32 cm^3 K mol^{-1}) (Figure 2b). These trends are consistent with the applied pressure enhancing the FM relative to the AFM exchange interactions [$(dJ_{Ni-Fe}/dP) > (d|J_{Mn-Fe}|/dP)$], thereby shifting the material across the $R-N$ phase boundary. The signature of the larger FM pressure coefficient is also evident when the applied pressure is increased further to 0.6 kbar. The low-field magnetization switches back to positive as the FM interactions are further enhanced, and the material crosses now the $N-P$ boundary. The spontaneous magnetization continues to increase rapidly on further raising the pressure to 2.0 kbar as the FM interactions compete more effectively and θ now assuming a small positive value (Figure 1a).

However, the behavior of **1** changes even more dramatically when the pressure reaches 2.6 kbar. The spontaneous magnetization increases at an accelerated rate (Figure 1b), while the measured $\chi_M T$ at 300 K decreases considerably. This pressure-induced transformation is essentially complete by 4.2 kbar when the spontaneous magnetization approaches a value 40 times larger than that at 1 atm and the magnetic ordering temperature is ∼5 K. The Weiss constant assumes a large positive value (+16.4(2) K), and $\chi_M T$ (300 K) collapses to 2.6 cm^3 K mol^{-1}. These changes provide the signature of a sudden switch from ferrimagnetic to FM order and a concomitant change in the metal ion spin configurations. The

† School of Chemistry, University of Edinburgh.
‡ School of Engineering & Electronics, University of Edinburgh.
|| Centre for Science at Extreme Conditions, University of Edinburgh.
§ University of Durham.

10.1021/ja061514m CCC: $33.50

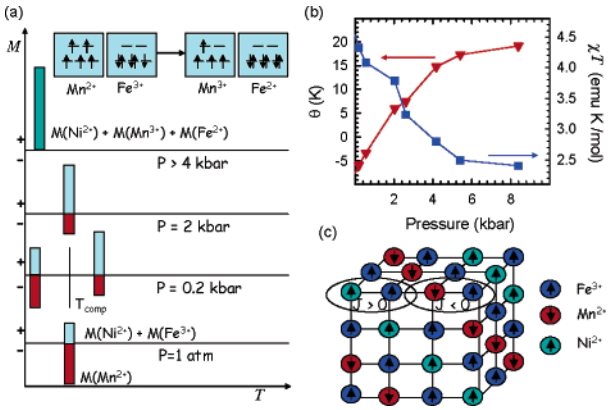

Figure 2. (a) Schematic diagram illustrating positive, $M(Ni^{2+})+M(Fe^{3+})$, and negative, $M(Mn^{2+})$, magnetizations versus the direction of the external magnetic field as a function of temperature and pressure. Following the phase transition driven by the internal redox reaction above 4 kbar, all magnetic sublattices interact ferromagnetically. (b) Pressure dependence of $\chi_M T$ at 300 K (blue squares) and of the Weiss temperature, θ (red triangles), deduced by Curie−Weiss fits to $1/\chi_M(T)$ data between 50 and 300 K. (c) Schematic illustration of the coexistence of both FM and AFM superexchange interactions in the cubic PB-type structure of **1**.

only possible scenario consistent with the decrease in the effective magnetic moment is the internal metal-to-metal charge transfer Mn^{II}(HS, d^5, $S = 5/2$)−NC−Fe^{III}(LS, d^5, $S = 1/2$) → Mn^{III}(HS, d^4, $S = 2$)−NC−Fe^{II}(LS, d^6, $S = 0$),[8] while alternative possibilities, such as metal-centered spin transitions and cyanide ligand flips, can be unambiguously excluded. Such a pressure-induced electronic transformation is also the driving force for the switch to bulk ferromagnetism. At low pressures, the Mn^{II}(HS) and Fe^{III}(LS) centers couple antiferromagnetically. In contrast, in the piezotransformed material, the exchange coupling between near-neighbor Mn^{III}(HS, $t_{2g}^3e_g^1$) ions, as mediated by the Fe^{II}(LS, $t_{2g}^6e_g^0$) t_{2g} orbitals, is FM in nature.[9] As the pressure is increased further to 9.7 kbar, no other major changes are observed with T_C increasing slowly at ∼0.1 K/kbar, reflecting the enhancement of the exchange interactions, which accompanies the decrease in near-neighbor metal−metal distances.

All transformations are fully reversible upon release of the pressure and are accompanied by hysteretic behavior (Figure 2S). The back internal electron transfer, Mn^{III}(HS)−NC−Fe^{II}(LS) → Mn^{II}(HS)−NC−Fe^{III}(LS), is now observed at 3.6 kbar ($\Delta P \sim 0.6$ kbar) as is the reversal of the sign of the spontaneous magnetization just above atmospheric pressure ($\Delta P \sim 0.1$ kbar).

There are several prominent points arising from the present results. Pressure is proven to be an extremely efficient external stimulus for fine-tuning the properties of molecular magnets and for generating hidden electronic and magnetic states. The flexibility of the structure of PB analogues and its ability to incorporate a variety of competing magnetic interactions have allowed the design of mixed ferro-ferrimagnets (Figure 2c), which can span the whole spectrum of magnetic behavior, predicted by Néel,[2] including the rare phenomenon of magnetization reversal (in small magnetic fields) in response to a change in temperature.[3] By synthesizing **1**, which exhibits positive magnetization but lies at the boundary between Néel's *R* and *N* ferrimagnetic phases, we were able to employ hydrostatic pressure to induce multiple reversals of the direction of the spontaneous magnetization. Remarkably, the magnetic response of **1** is so sensitive to pressure that the magnetization flips from positive to negative at only 0.2 kbar and then flips back to positive at 0.6 kbar. Such facile pressure-induced control of the magnetic poles is unprecedented and mirrors the effect of light illumination on the magnetic properties. It can be attributed to the rapid enhancement of the FM interactions with increasing *P*, as also reflected in the substantial increase in the magnetic ordering temperature.

Figure 2a summarizes in a schematic way the evolution of the competition between the metal sublattice magnetizations with increasing pressure. As the applied pressure increases above ∼4 kbar, the material becomes unstable, abruptly transforming to a phase in which an internal redox reaction, Mn^{II}(HS)−Fe^{III}(LS) → Mn^{III}(HS)−Fe^{II}(LS), takes place with the effective magnetic moment at ambient temperature decreasing sharply and the magnetic order switching from ferrimagnetic to bulk FM. Although pressure-induced electron transfer has been observed before in PB analogues, the transformed state is also typically accessible thermally at ambient pressure.[5] This is not the case for **1** as there is no hint of the presence of a thermal hysteresis loop in the χT versus *T* data, and pressure allows access to a hidden electronic state with drastically different magnetic properties.

In conclusion, the trimetallic mixed ferri-ferromagnet **1** shows an extreme (reversible) sensitivity to pressure with facile flipping of the magnetic poles and interconversion between electronic states with differing magnetic properties. The initial results presented here demonstrate that pressure is a powerful stimulus to tune and modulate the magnetic interactions in PB analogues and to allow trapping of novel inaccessible states.

Acknowledgment. We thank K. Prassides (Durham) for discussions, and the Royal Society for a Dorothy Hodgkin Research Fellowship (S.M.).

Supporting Information Available: Synchrotron X-ray powder diffraction profile of **1** at room temperature. Temperature dependence of the spontaneous magnetization obtained on releasing the pressure from 9.7 kbar to ambient. Temperature dependence of $\chi_M T$ and magnetic hysteresis *M* versus *H* loops at various pressures. This material is available free of charge via the Internet at http://pubs.acs.org.

References

(1) (a) Ferlay, S.; Mallah, T.; Ouahes, R.; Veillet, P.; Verdaguer, M. *Nature* **1995**, *378*, 701. (b) Sato, O.; Iyoda, T.; Fujishima, A.; Hashimoto, K. *Science* **1996**, *272*, 704. (c) Nuida, T.; Matsuda, T.; Tokoro, H.; Sakurai, S.; Hashimoto, K.; Ohkoshi, S. *J. Am. Chem. Soc.* **2005**, *127*, 11604.
(2) Néel, L. *Ann. Phys.* **1948**, *3*, 137.
(3) (a) Ohkoshi, S.; Sato, O.; Iyoda, T.; Fujushima, A.; Hashimoto, K *Inorg. Chem.* **1997**, *36*, 268. (b) Ohkoshi, S.; Iyoda, T.; Fujushima, A.; Hashimoto, K. *Phys. Rev. B* **1997**, *56*, 11642.
(4) (a) Ohkoshi, S.; Arai, K.; Sato, Y.; Hashimoto, K. *Nat. Mater.* **2004**, *3*, 857. (b) Ohkoshi, S.; Yorozu S.; Sato, O.; Iyoda, T.; Fujushima, A.; Hashimoto, K. *Appl. Phys. Lett.* **1997**, *70*, 1040.
(5) (a) Ksenofontov, V.; Levchenko, G.; Reiman, S.; Gütlich, P.; Bleuzen, A.; Escax, V.; Verdaguer, M. *Phys. Rev. B* **2003**, *68*, 024415. (b) Moritomo, Y.; Hanawa, M.; Ohishi, Y.; Kato, K.; Takata, M.; Kuriki, A.; Nishibori, E.; Sakata, M.; Ohkoshi, S.; Tokoro, H.; Hashimoto, K. *Phys. Rev. B* **2003**, *68*, 144106. (c) Hanawa, H.; Moritomo, Y.; Tateishi, J.; Ohishi, Y.; Kato, K. *J. Phys. Soc. Jpn.* **2004**, *73*, 2759. (d) Coronado, E.; Gimenez-Lopez, M. C.; Levchenko, G.; Romero, F. M.; Garcia-Baonza V.; Milner, A.; Paz-Pasternak, M. *J. Am. Chem. Soc.* **2005**, *127*, 4580. (e) Awaga, K.; Sekine, T.; Okawa, M.; Fujita, W.; Holmes, S. M.; Girolami, G. S. *Chem. Phys. Lett.* **1998**, *293*, 352.
(6) **1** was prepared as a brown solid by reaction of aqueous solutions of $MnCl_2$ (0.075 M), $NiCl_2$ (0.025 M), RbCl (1 M), and $K_3[Fe(CN)_6]$ (0.1 M), and its stoichiometry was determined by elemental analysis (Rb:Ni:Mn:Fe: H_2O = 0.64:0.31:0.87:1:2.8). X-ray powder diffraction measurements are consistent with a single-phase material (Figure 1S). *T*- and *H*-dependent magnetization was measured in a QD MPMS SQUID magnetometer up to ∼10 kbar. Two piston-cylinder high-pressure cells using Daphne mineral oil as pressure transmitting medium were employed: a home-built one (pressure calibrated by its external diameter) and the easyLab Mcell10 (pressure calibrated with the *P*-dependence of the T_C of Sn). The data were corrected for diamagnetic core contributions.
(7) The required pressure to invert the magnetization direction is so small that it can be also reached by pelleting the material with a hand-operated press.
(8) We restrict ourselves to the electron transfer occurring only between the Fe^{III} and Mn^{II} sublattices. Given the small Ni content, it is not possible to establish unambiguously with the present data whether the Ni^{II} sublattice is also oxidized. This does not affect our subsequent discussion as the coupling between the Ni and Fe sublattices remains always FM.
(9) Mayoh, B.; Day, P. *J. Chem. Soc., Dalton Trans.* **1976**, 1483.

JA061514M

Supporting Information for "Pressure-Induced sequential magnetic pole inversion and antiferromagnetic-ferromagnetic crossover in a trimetallic Prussian Blue Analog"

Lindsay Egan[†], Konstantin Kamenev[‡], Dionisis Papanikolau[§], Yasuhiro Takabayashi[§], Serena Margadonna[†*]

[†]*School of Chemistry and Centre for Science at Extreme Conditions, University of Edinburgh, Edinburgh EH9 3JJ, UK,* [‡]*School of Engineering& Electronics and Centre for Science at Extreme Conditions, University of Edinburgh, Edinburgh EH9 3JJ, UK,* [§] *Department of Chemistry, University of Durham, Durham DH1 3LE, UK.*

Figure 1S. Synchrotron X-ray powder diffraction profile of $Rb_{0.64}Ni_{0.31}Mn_{0.87}[Fe(CN)_6]\bullet 2.8H_2O$ at room temperature. The X-ray wavelength is 0.8513 Å. The cubic lattice constant is a = 10.455 Å and the space group is *Fm-3m*.

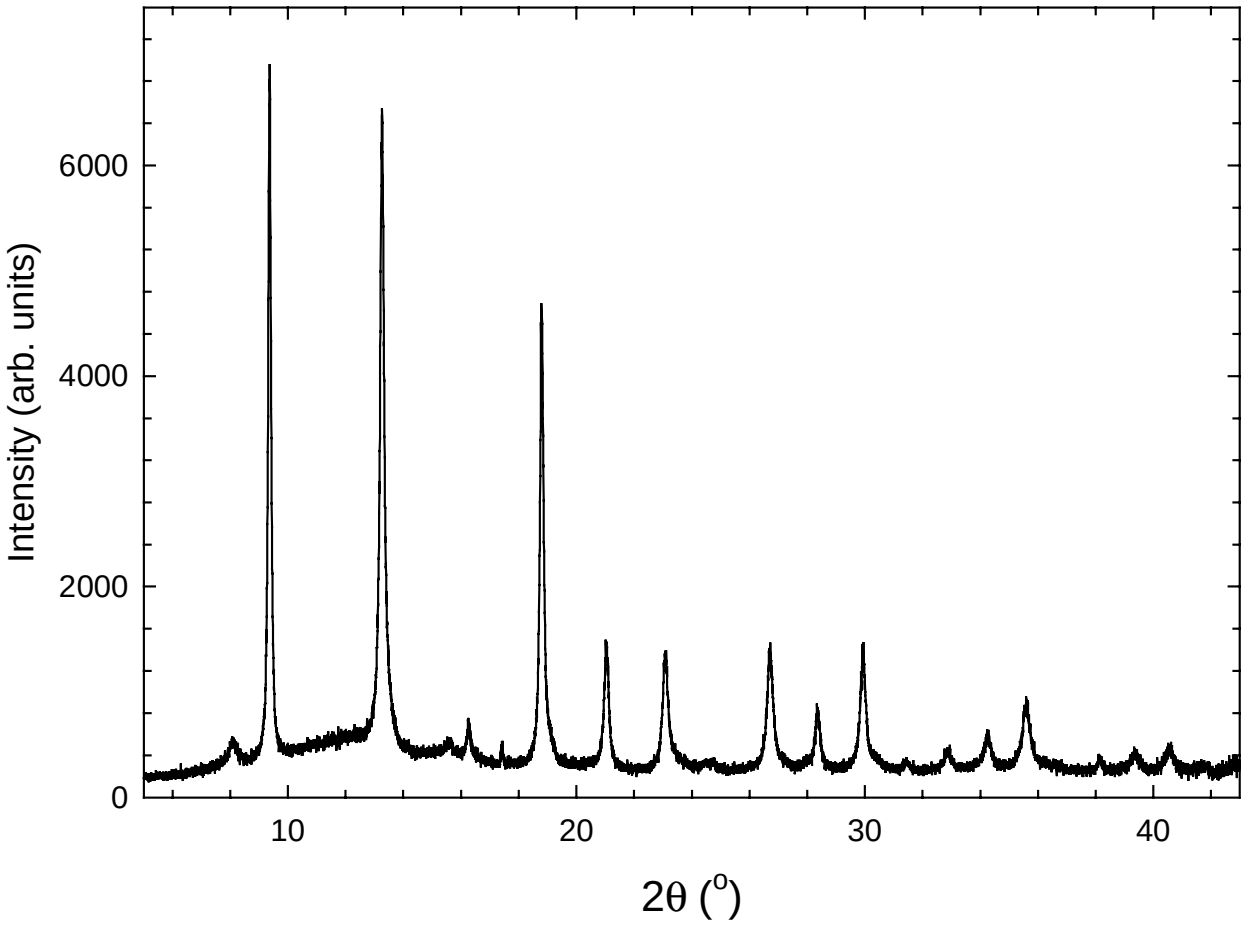

Figure 2S. Temperature dependence of the magnetization (H = 1 mT, field cooling) of $Rb_{0.64}Ni_{0.31}Mn_{0.87}[Fe(CN)_6]\bullet 2.8H_2O$ as a function of pressure. Data were collected on releasing the pressure from 9.7 kbar to ambient. (a) Diamonds: 7.7 kbar, hexagons: 3.6 kbar, triangles down: 2.2 kbar. (b) Circles: 0.4 kbar, triangles up: 0.1 kbar, squares: complete release of pressure.

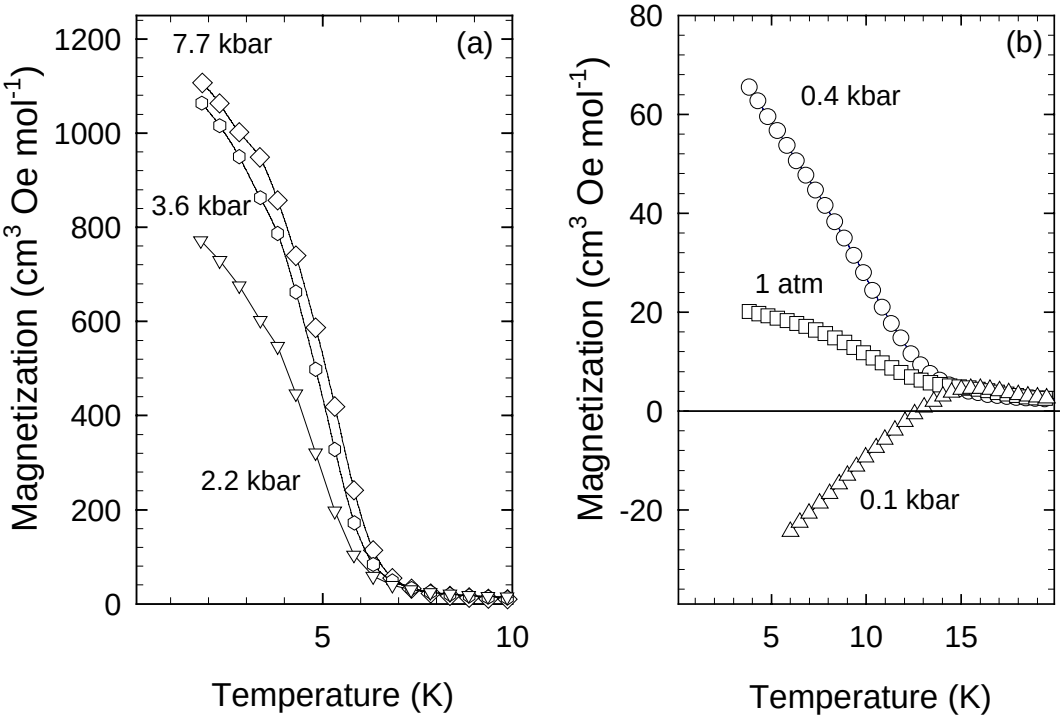

Figure 3S. Temperature evolution of $\chi_M T$ for $Rb_{0.64}Ni_{0.31}Mn_{0.87}[Fe(CN)_6]\bullet 2.8H_2O$ at selected pressures in the temperature range 2 K < T < 90 K. Open circles: 0.6 kbar, triangles up: 2.0 kbar, triangles down: 5.4 kbar, squares: 9.7 kbar. Data were collected on increasing pressure. Inset: same as above but in the temperature range 50 K < T < 300 K.

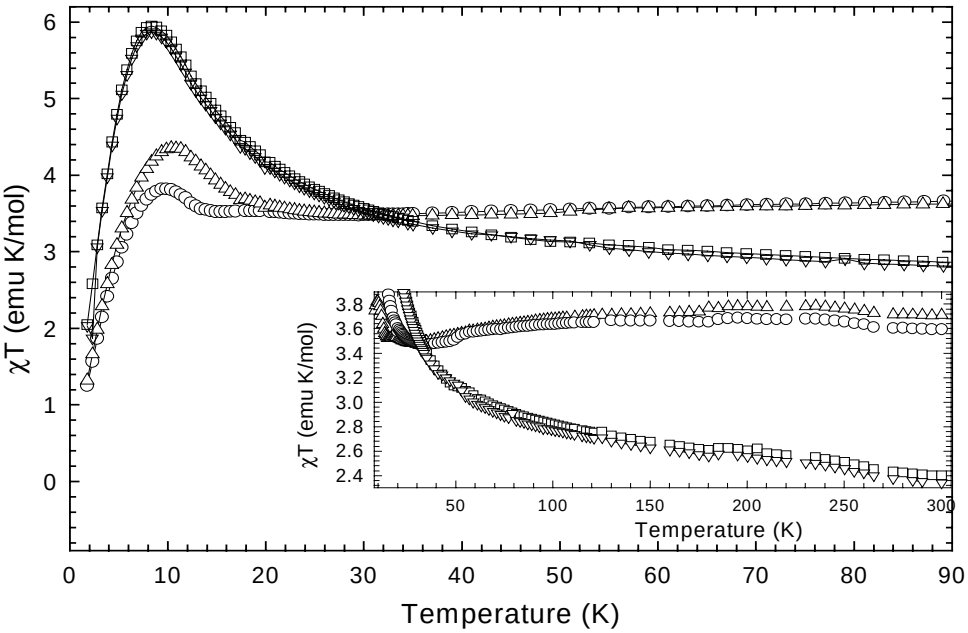

Figure 4S. Temperature evolution of $\chi_M T$ for $Rb_{0.64}Ni_{0.31}Mn_{0.87}[Fe(CN)_6]\bullet 2.8H_2O$ at selected pressures in the temperature range 2 K < T < 90 K. Squares: 7.7 kbar, triangles up: 2.2 kbar, circles : 0.4 kbar Data were collected on releasing pressure. Inset: same as above but in the temperature range 50 K < T < 300 K.

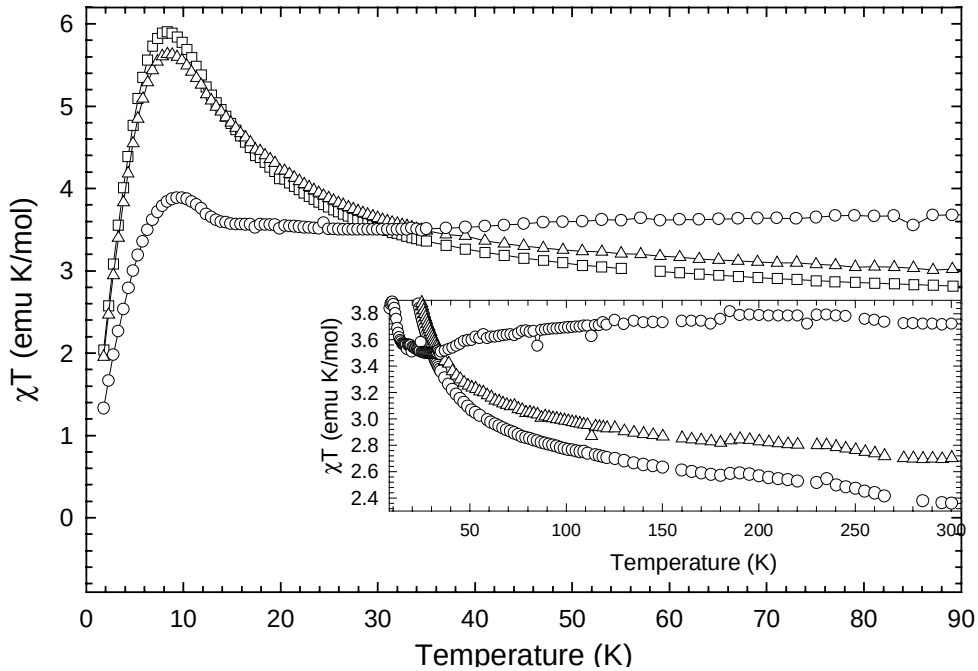

Figure 5S. Magnetic hysteresis loops for $Rb_{0.64}Ni_{0.31}Mn_{0.87}[Fe(CN)_6]\cdot 2.8H_2O$ at 4 K at selected pressures. Right panel - circles: 0.6 kbar, squares: 9.7 kbar. Inset: comparison between ambient conditions (dashed line) and 0.6 kbar (solid line). Left panel - circles: 0.2 kbar. Inset: comparison between ambient conditions (dashed line) and 0.2 kbar (solid line).